

Diss. ETH No. 23176

Multi-Objective Optimization of Inductive Power Transfer Systems for EV Charging

A thesis submitted to attain the degree of

DOCTOR OF SCIENCES of ETH ZURICH
(Dr. sc. ETH Zurich)

presented by

ROMAN BOSSHARD

MSc ETH

born on 20.12.1986

citizen of Oetwil am See, Switzerland

accepted on the recommendation of

Prof. Dr. Johann W. Kolar, examiner

Prof. Dr. William G. Hurley, co-examiner

2015

ETH Zurich
Power Electronic Systems Laboratory
Physikstrasse 3 | ETL H23
8092 Zurich | Switzerland

<http://www.pes.ee.ethz.ch>

© 2015 by Roman Bosshard

Für meine Familie

Acknowledgments

FIRST of all, I would like to thank Prof. Dr. Johann W. Kolar for inviting me to join the Power Electronic Systems Laboratory (PES) at ETH Zurich. It was a great experience to work in this inspiring facility under his supervision. Johann always had a high interest for my work, and I am grateful for his trust and support during my time as a PhD. I want to thank him especially for the opportunity to present my research results as part of international conference tutorials at his side.

I thank Prof. Dr. William Gerard Hurley for his interest in my thesis. I sincerely appreciate that he found time to travel to Zurich shortly before Christmas to be the co-examiner at my PhD defense.

Furthermore, I thank ABB Corporate Research, Switzerland, for their funding of my PhD project. I thank everyone involved for the great interest in my results and for the constructive discussions at our project meetings.

Special thanks belong to Jonas Huber, who was my office colleague for most of the time I worked at PES. The detailed discussions and his support with many aspects of my research were much appreciated. Many thanks also to Jonas Mühlethaler for being my co-supervisor during my initial year as a PhD, I learned a lot from him. Oliver Knecht helped me a lot with the discussions related to IPT. I would like to thank him for his inputs and particularly also for his support in unraveling the mysteries of power electronics hardware. I thank Christoph Gammeter, who supported me regarding the thermal management of my system. Gabriel Ortiz was always a great help and source of inspiration for graphics and presentations, for which I am very grateful. I also thank Arda Tüysüz for his support with the FEM simulations and for always keeping up the good mood. Furthermore, I thank all of my students for their contribution to my work. Special thanks belong to Jonas Pfaff for his great work and to Ugaitz Iruretagoyena, who supported me during the final phase of my PhD and even invited me to visit his family in the Basque Country.

The excellent spirit of work at PES is a result of the great collaboration and mutual support among its team members. I thank everyone for their company: Daniel Rothmund, David Boillat, Dominik Bortis, Dominik Neumayr, Florian Krismer, Lukas Schrittwieser, Mario Mauerer, Matthias Kasper, Maurus Kaufmann, Michael Flankl, Michael Leibl, Pedro Bezerra, Ralph Burkart, Thomas Guillod, Toke Andersen, Uwe Badstübner, and Yanick Lobsiger. I enjoyed the time we spent together

at PES, during our trips to conferences, or at the various events that we organized outside of work. In addition, I would like to express my gratitude to the permanent staff of PES: Monica Kohn, Roswitha Coccia, Prisca Maurantonio, Damaris Egger, Yvonne Schnyder-Liebherr, Beat Seiler, Peter Seitz, Peter Albrecht, and Claudia Stucki. Their names do not appear on our scientific publications, but without their support, many achievements would not have been possible.

Finally, I would like to thank my parents Silvia and Werner, my brother Adrian, my girlfriend Michèle, and all of my friends for their support during this intense phase of my life. Without you, I would not be who I am today.

Zurich, December 2015

Roman Bosshard

Abstract

ELECTRIC mobility is rapidly gaining popularity owing to the increasing CO₂-awareness and the lower total cost of ownership of Electric Vehicles (EV). Rising market shares of EV among newly sold vehicles document the trend towards more sustainable ways of transportation. Nevertheless, further improvement is still required to remove technological barriers that currently hinder a widespread adoption. On one hand, the development of electrical energy storage systems with ever higher energy and power densities addresses the limited electrical driving range and long battery charging time of today's EV. On the other hand, innovative charging concepts increase the acceptance of the technology among consumers and accelerate the transition from traditional to electric mobility.

Unique advantages result from the contactless transmission of the battery charging energy by Inductive Power Transfer (IPT) across the air gap between a charging platform embedded in the road surface and a receiver coil on the EV. The elimination of the galvanic connection between the charging station and the vehicle simplifies the charging process and removes safety concerns related to the handling of the electrical equipment. In addition, an automatically established power transfer without the need for moving mechanical components is particularly attractive for the charging of public transportation EV. It enables the integration of the charging process with the regular vehicle operation by *opportunity charging* at bus stations, taxicab stands, or traffic lights along the route. Owing to the reduced dwell times for recharging at the depot, operators can lower the number of fleet vehicles and the related operating costs. Furthermore, the more frequent recharging reduces the depth of discharge of the battery. This extends the battery lifetime and allows dimensioning the EV with a smaller on-board energy storage capacity and consequently with lower initial costs.

The fundamental working principles of contactless charging systems and the key challenges in their optimization are derived from the analysis of a conventional conductive EV charger in the first part of this thesis. It is shown that the design of contactless EV battery charging systems is characterized by multiple competing optimization objectives. The limited construction volume on the vehicle demands for a high power density of the on-board power electronics equipment, particularly of the transmission coils. Moreover, a high efficiency is required for the charging process to minimize energy costs and to simplify the thermal

management of the components. Low electromagnetic stray fields and a high coil positioning tolerance are required in addition. The analysis of the physical limitations and the interdependencies between these performance factors is the main topic of the thesis. A multi-objective optimization process is proposed for taking into account multiple design objectives simultaneously. A combination of analytical models with electromagnetic finite element method calculations is employed for the calculation of the power losses, the stray field, and the necessary construction volume of the IPT coils. Based on the mathematical models, the physical performance limits are calculated. The results show that trade-offs are encountered between the efficiency of the power transfer, the power density of the transmission coils, and the magnetic stray field, which are described by Pareto fronts at the physical performance limit.

In a first step, the proposed multi-objective IPT optimization process is theoretically and experimentally validated by the design of a scaled prototype. A DC-to-DC efficiency of 96.5% is achieved for the transmission of 5 kW across an air gap of 52 mm with 210 mm diameter coils. In a second step, the approach is applied to the optimization of a contactless EV charger with 50 kW charging power. The realized transmission coils have a volumetric power density of 2.7 kW/dm³ and a gravimetric power density of 2.0 kW/kg. Thereafter, the design of the power electronic converter is discussed. An all-SiC MOSFET solution comprising multiple parallel-interleaved converter modules with coupled magnetic components is optimized for high compactness and high efficiency. The power density of the presented 50 kW/800 V/85 kHz hardware prototype is 9.5 kW/dm³ at a calculated DC-to-AC efficiency of 98.62%. The thesis ends with a comprehensive experimental investigation of the full-scale 50 kW IPT system and the verification of the presented calculation models. The DC-to-DC efficiency is measured as 95.8%, including the IPT resonant system as well as all power electronic conversion stages. In addition, measurements of the magnetic stray field document that the presented 50 kW prototype system fulfills the ICNIRP 2010 guidelines at 800 mm lateral distance from the coil center.

The thesis is concluded by a critical assessment of the physical limits and the technical feasibility of contactless EV charging systems. Thereupon, recommendations are given for future research areas that could help overcoming today's limitations of the technology.

Kurzfassung

DIE ELEKTROMOBILITÄT gewinnt auf Grund des erhöhten CO₂-Bewusstseins und der geringeren Gesamtbetriebskosten von Elektrofahrzeugen (Electric Vehicles, EV) zunehmend an Popularität. Der ansteigende Marktanteil von Elektrofahrzeugen an den Neuzulassungen belegt den Trend in Richtung nachhaltiger Transportmittel. Es besteht jedoch weiterhin Verbesserungspotential zur Überwindung technologischer Hürden, welche momentan eine umfassende Verbreitung behindern. Einerseits ermöglicht die Entwicklung elektrischer Energiespeicher mit immer höherer Energie- und Leistungsdichte eine Erweiterung der elektrischen Reichweite und eine Verkürzung der Batterieladedauer heutiger Fahrzeuge. Andererseits können innovative Ladekonzepte die Akzeptanz der Technologie bei den Konsumenten fördern und dadurch den Übergang von der traditionellen zur elektrischen Mobilität beschleunigen.

Einzigartige Vorteile ergeben sich aus der berührungslosen Übertragung der Batterieladeenergie mittels induktiver Leistungsübertragung (Inductive Power Transfer, IPT) durch den Luftspalt zwischen einer in die Strassenoberfläche eingebetteten Ladeplattform und einer fahrzeugseitigen Empfängerspule. Die Entfernung der galvanischen Verbindung zwischen der Ladestation und dem Fahrzeug vereinfacht den Ladeprozess und beseitigt Sicherheitsbedenken im Zusammenhang mit der Handhabung der elektrischen Teile des Ladegeräts. Ein automatischer Leistungstransfer zum Fahrzeug ohne bewegliche mechanische Teile ist ausserdem insbesondere attraktiv für das Laden von Elektrofahrzeugen des öffentlichen Verkehrs. Die Technologie eröffnet die Möglichkeit einer Integration des Ladeprozesses in den regulären Betrieb mittels *Gelegenheitsladung* an Bushaltestellen, Taxiständen oder an Verkehrsampeln entlang der Fahrzeugroute. Auf Grund der reduzierten Stehzeit für das Batterieladen im Depot, kann der Betreiber die Anzahl der Flottenfahrzeuge und die damit verbundenen Betriebskosten reduzieren. Zudem kann durch die regelmässigeren Aufladung die Entladetiefe der Batterien reduziert werden. Dies ermöglicht eine Erhöhung der Batteriebensdauer sowie eine Auslegung der Elektrofahrzeuge mit einem kleineren Energiespeicher, was eine Senkung der Investitionskosten zur Folge hat.

Im ersten Teil dieser Dissertation werden die grundsätzliche Funktionsweise eines berührungslosen Ladesystems und die Hauptherausforderungen in dessen Auslegung von der Analyse eines konventionel-

len, kabelgebundenen Ladegeräts abgeleitet. Es wird aufgezeigt, dass die Dimensionierung eines berührungslosen Ladesystems durch mehrere konkurrierende Optimierungsziele erschwert wird. Der beschränkte verfügbare Bauraum im Fahrzeug verlangt nach einer hohen Leistungsdichte der fahrzeugseitigen leistungselektronischen Komponenten, insbesondere der Empfängerspule. Ausserdem wird zur Minimierung der Energiekosten und zur Vereinfachung der thermischen Auslegung der Komponenten eine hohe Effizienz benötigt. Weiter sind möglichst geringe elektromagnetische Streufelder und eine hohe Toleranz bezüglich der Spulenpositionierung erforderlich. Die Analyse der physikalischen Grenzen und der Verknüpfungen zwischen den genannten Kenngrössen bildet das Kernthema der Dissertation. Ein Mehrkriterienoptimierungsverfahren wird vorgestellt, welches die simultane Betrachtung mehrerer Dimensionierungsziele ermöglicht. Eine Kombination von analytischen Modellen und elektromagnetischen Berechnungen mit Hilfe der Finite-Elemente-Methode wird für die Abschätzung der auftretenden Verluste, des Streufelds und des benötigten Bauraums der Ladespulen eingesetzt. Basierend auf den mathematischen Modellen werden die physikalischen Grenzen bestimmt. Die Berechnungsergebnisse zeigen Zielkonflikte zwischen der Übertragungseffizienz, der Leistungsdichte der Ladespulen und dem magnetischen Streufeld auf, welche an der physikalischen Grenze durch Pareto-Fronten beschrieben werden.

In einem ersten Schritt wird das vorgeschlagene Mehrkriterienoptimierungsverfahren anhand der Entwicklung eines skalierten Prototypen theoretisch und experimentell verifiziert. Dabei wird für die Übertragung von 5 kW über einen Luftspalt von 52 mm mittels Spulen von 210 mm Durchmesser eine DC-bis-DC Effizienz von 96.5% erreicht. In einem zweiten Schritt wird das Verfahren für die Optimierung eines berührungslosen Ladegeräts für Elektrofahrzeuge mit einer Ladeleistung von 50 kW angewendet. Die realisierten Übertragerspulen weisen eine volumetrische Leistungsdichte von 2.7 kW/dm³ und eine gravimetrische Leistungsdichte von 2.0 kW/kg auf. Anschliessend wird die Optimierung des leistungselektronischen Konverters besprochen. Eine Lösung mit ausschliesslich Silizium-Karbid Leistungshalbleitern, bestehend aus mehreren, parallel geschalteten Konvertermodulen mit zeitversetzter Taktung und gekoppelten magnetischen Komponenten, wird auf eine hohe Kompaktheit und eine hohe Effizienz ausgelegt. Die Leistungsdichte des vorgestellten 50 kW/800 V/85 kHz Hardwareprototypen beträgt 9.5 kW/dm³ bei einer berechneten DC-bis-AC Effizienz von 98.62%. Die

Dissertation wird abgeschlossen durch eine umfassende experimentelle Untersuchung des 50 kW Ladesystems und die Verifikation der vorgestellten Berechnungsmodelle. Die gemessene DC-bis-DC Effizienz beträgt 95.8%, einschliesslich der berührungslosen Übertragung und aller leistungselektronischen Wandlerstufen. Ausserdem belegt die Messung des magnetischen Streufelds des 50 kW Prototypen die Erfüllung der ICNIRP 2010 Richtlinien in einem lateralen Abstand von 800 mm vom Spulenmittelpunkt.

Die Dissertation wird abgerundet durch eine kritische Untersuchung der physikalischen Grenzen und der technischen Machbarkeit von berührungslosen Ladesystemen für Elektrofahrzeuge. Darauf basierend werden Themengebiete für weitergehende Forschungsarbeiten vorgeschlagen, welche einen Betrag zur Überwindung der heute bestehenden Grenzen der Technologie leisten können.

Abbreviations

2D	Two Dimensional
3D	Three Dimensional
AC	Alternating Current
ADC	Analog-to-Digital
BEV	Battery Electric Vehicle
CAD	Computer Aided Design
CAN	Controller Area Network
CM	Common Mode
CNC	Computerized Numerical Control
DC	Direct Current
DCI	Direct-Coupled Inductor
DM	Differential Mode
DOI	Digital Object Identifier
DSP	Digital Signal Processor
EMC	Electromagnetic Compatibility
ESR	Equivalent Series Resistance
EV	Electric Vehicle (incl. BEV and PHEV)
EVI	Electric Vehicles Initiative
FC	Frequency Control
FEM	Finite Element Method
FFT	Fast Fourier Transform
FPGA	Field Programmable Gate Array
HEV	Hybrid Electric Vehicle
ICI	Inverse-Coupled Inductor
ICNIRP	International Commission on Non-Ionizing Radiation Protection
IEEE	Institute of Electrical and Electronics Engineers
IGBT	Insulated-Gate Bipolar Transistor
IPT	Inductive Power Transfer
MOSFET	Metal-Oxide Semiconductor Field-Effect Transistor
OEM	Original Equipment Manufacturer
OFC	Oxygen-Free Copper
OP	Operating Point
PHEV	Plug-in Hybrid Electric Vehicle
PC	Personal Computer
PCB	Printed Circuit Board

Abbreviations

PFC	Power Factor Correction
PI	Proportional-Integral
POM	Polyoxymethylene
PWM	Pulse-Width Modulation
SAE	Society of Automotive Engineers
Si	Silicon
SiC	Silicon Carbide
SOC	Self-Oscillating Control
VC	Voltage Control
ZCS	Zero Current Switching
ZVS	Zero Voltage Switching

Contents

Abstract	vii
Kurzfassung	ix
Abbreviations	xiii
1 Introduction	1
1.1 Limitations & Technology Drivers	2
1.2 Opportunities for IPT in Electric Public Transportation	5
1.2.1 Existing Industry Solutions	8
1.3 Key Engineering Challenges	9
1.3.1 High Efficiency and High Power Density	9
1.3.2 High Tolerance to Coil Misalignment	12
1.3.3 Minimum Cooling Requirements	13
1.3.4 Low Electromagnetic Stray Fields & High Oper- ational Safety	13
1.3.5 High Reliability & Low Cost	14
1.3.6 Interoperability	15
1.4 Goals and Contributions of the Thesis	15
1.5 Outline of the Thesis	16
2 Fundamentals of Inductive Power Transfer	19
2.1 Isolated DC-DC Converter for Conductive EV Charging	19
2.1.1 Transformer Equivalent Circuit	20
2.1.2 Basic Operation of the Converter	23
2.1.3 Series Resonant Compensation of the Leakage Inductance	25
2.1.4 Fundamental Frequency Modeling	27
2.2 Transition to an Inductive Power Transfer (IPT) System	29
2.2.1 Series-Series Resonant Compensation	30
2.2.2 Pole-Splitting (or Bifurcation)	33
2.2.3 Efficiency Limit of the Resonant Circuit	34
2.2.4 Design Rules for Series-Series Compensation . .	38
2.2.5 Alternative Compensation Topologies	39
2.3 Efficiency Optimal System Operation	41
2.3.1 Zero Voltage Switching of the MOSFET Full-Bridge Inverter	41
2.3.2 ZVS Conditions for the IPT System	44
	xv

2.3.3	Synchronous Rectification at the Receiver	45
2.3.4	Maximum Efficiency Control Concept	46
2.3.5	Comparison to Alternative Control Methods	50
2.4	Summary of the Chapter	54
3	Multi-Objective IPT Optimization Process	55
3.1	Scaled IPT System Specifications	56
3.2	Modeling & Calculation of Power Losses in IPT Coils	58
3.2.1	Coil Geometry Selection	58
3.2.2	Axis-Symmetric FEM Simulation Models	60
3.2.3	FEM-Based IPT Coil Loss Modeling	62
3.2.4	Resonant Capacitors Loss Model	66
3.2.5	Simplified Thermal Model	66
3.3	Multi-Objective Optimization Process	67
3.3.1	Optimization Methodology	68
3.3.2	Discussion of Optimization Results	72
3.4	Validation of the FEM-Calculated Magnetic Field	78
3.4.1	Design of a Magnetic Field Probe	78
3.4.2	Comparison to a Commercial Field Probe	80
3.4.3	Validation of the FEM Simulation Results	81
3.5	Experimental Verification	82
3.5.1	Equivalent Circuit Parameters	83
3.5.2	Thermal Measurements	84
3.5.3	Measured Power Losses and DC-to-DC Efficiency	86
3.6	Summary of the Chapter	89
4	Optimization of the Transmission Coils	91
4.1	High-Power IPT Battery Charger	92
4.1.1	E-Type Transmission Coil with Rectangular Footprint	94
4.1.2	Considered Coil Materials	96
4.2	Multi-Objective Coil Optimization	103
4.2.1	Power Loss Calculation Models	103
4.2.2	Thermal Model	109
4.2.3	Optimization Methodology	111
4.2.4	Discussion of the Optimization Results	115
4.2.5	Selected Design for the Prototype	120
4.2.6	Coil Positioning Tolerance	121
4.2.7	Comparison to the Scaled Prototype	125
4.3	Realization of the Prototype	126
4.3.1	Mechanical Construction Details	127

4.3.2	Forced-Air Cooling System of the Transmission Coils	129
4.3.3	Design of the Resonant Capacitor	132
4.4	Summary of the Chapter	136
5	Power Electronic Converter & Control	139
5.1	Selection of the Converter Topology	141
5.2	ZVS Full-Bridge Inverter Stage	143
5.2.1	Paralleling of SiC MOSFETs	145
5.2.2	Power Circuit Layout for Symmetrical Current Distribution	146
5.2.3	Gate Driver Concept	150
5.2.4	Inverter Stage Assembly	151
5.3	Modular Buck+Boost-Type DC-DC Conversion Stage .	152
5.3.1	Inverse-Coupled and Direct-Coupled Magnetic Components	153
5.3.2	Steady-State Converter Operation	155
5.3.3	Design of the Magnetic Components	158
5.4	Power Electronics Control	168
5.4.1	Control of the IPT System Output Power	168
5.4.2	Feedback Control of the DC-Link Voltage	169
5.4.3	Synchronous Rectification at the Receiver	172
5.5	Realized Hardware Prototype	174
5.5.1	Realized DC-DC Converter Module	174
5.5.2	Final Assembly of the All-SiC IPT Power Converter	177
5.6	Summary of the Chapter	179
6	Experimental Verification	181
6.1	Experimental Analysis of the Power Electronic Converter	182
6.1.1	Switching Performance and Current Sharing of the ZVS Full-Bridge	182
6.1.2	Efficiency of the Buck+Boost-Type DC-DC Converter Modules	185
6.2	Experimental Verification of the IPT System Performance	190
6.2.1	IPT Test Setup with Energy Feedback	190
6.2.2	Synchronous Rectification at the Receiver	193
6.2.3	DC-to-DC Efficiency Measurement	195
6.2.4	DC-to-DC Efficiency Measurement with Coil Misalignment	197

6.2.5	Component Temperatures During Continuous Operation	198
6.2.6	Measurement of the Magnetic Stray Field	198
6.3	Summary of the Chapter	201
7	Conclusion & Outlook	205
7.1	Results & Conclusions	205
7.2	Future Research Areas	209
	List of Publications	211
	Bibliography	215
	Curriculum Vitae	233

1

Introduction

INCREASING public awareness of the environmental impact of greenhouse gas emissions together with the development of modern lithium-ion batteries has triggered a renewed interest in electric mobility worldwide [1]. Together with an environmentally sustainable energy production using renewable energy sources, Electric Vehicles and Plug-in Hybrid Electric Vehicles (EV/PHEV¹) can have a significantly smaller CO₂-footprint compared to traditional vehicles that exclusively rely on internal combustion engines. As an additional advantage, the total cost of ownership over the lifetime of EV is lower than that of traditional vehicles despite the higher initial purchase price [2]. Hence, vehicle markets of the developed world have seen EV sales rapidly increasing over the past five years (cf. **Fig. 1.1**).

However, despite the rapidly increasing sales, the absolute number of EV is still small compared to that of their fossil-fueled competitors. Only in a small number of countries their market share among newly sold passenger cars is higher than 1%, including Norway, the Netherlands, the US, Sweden, and Switzerland [3, 4]. For Switzerland, the EV market share is currently at 4.1% [3]. To support further growth, governments of the developed world are imposing policies that encourage customers to purchase EV instead of fossil fuel-based alternatives. In addition to fiscal incentives, CO₂-regulations for new passenger cars are being established worldwide [5], with the goal of reducing the greenhouse gas emissions of the transportation sector to reach climate targets [6]. This further promotes research and development among vehicle manufacturers as well as in academia. Additionally, public and semi-

¹For better readability, only the abbreviation EV is used for all battery-powered electric vehicles with an interface for recharging from an external electrical supply.

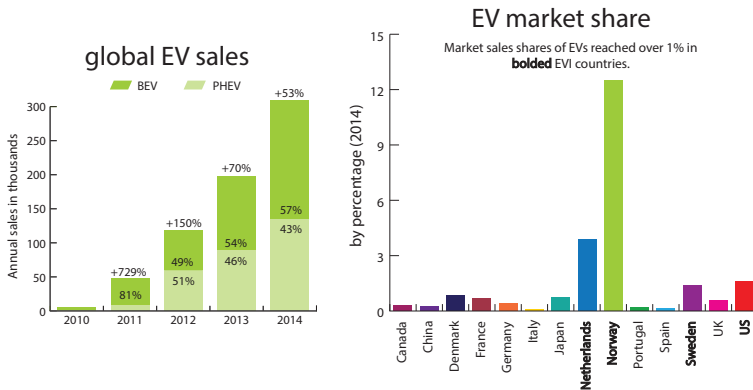


Fig. 1.1: Global annual Battery Electric Vehicle (BEV) and PHEV sales and market shares in the member countries of the Electric Vehicles Initiative (EVI). In Switzerland, the EV market share among newly sold cars is 4.1% [3]. Figure reproduced from [4], © OECD/IEA/EVI 2015, *EV Outlook 2015*, IEA Publishing, License: www.iea.org/t&c.

public charging infrastructure is being deployed on a large scale in order to enable battery-powered electric travel over ever longer distances [2,4].

1.1 Limitations & Technology Drivers

Despite the rapid developments of the recent past, a number of technical limitations that impede widespread EV adoption still remain. According to [2], the main technological challenges are

- ▶ **Cost and performance of the battery**
In typical passenger EV, the battery represents up to 30 % of the total cost while battery lifetime is still limited.
- ▶ **Limited driving range**
Even if the battery capacity of most EV exceeds the average daily travel distance of typical consumers, the lower range compared to traditional vehicles is still a barrier.
- ▶ **Safety and reliability**
Electrical and battery-related failures in the recent past show that the safety and reliability of EV is an important factor.

Hence, battery technology can be considered as one of the key driving factors for the future development of EV. Further improvements of the energy density and the lifetime of the lithium-ion battery will reduce cost and increase the driving range. They also offer potential to limit the weight and volume increase that results from battery-electric instead of fossil fuel energy storage.

In addition to battery technology, widespread deployment of charging equipment of different power levels in public or semi-public areas will promote EV. Shorter charging times of only minutes instead of hours for a full recharge with modern fast charging stations reduce the driving range limitation [7, 8]. Hence, the ongoing implementation of fast charging networks will eventually increase electrical travel distances to the level of traditional fossil fuel based transportation. Taking these factors into account, EV charging infrastructure can be identified as a second technology driver.

Therefore, innovative concepts such as contactless battery charging by Inductive Power Transfer (IPT) [9–15] have the potential to accelerate technology adoption. The main aim of this technology is a simplification of the charging process in order to make EV charging stations more accessible and user friendly. In this system, the charging cable of a conventional battery charger is replaced by an IPT receiver coil mounted to the underfloor of the vehicle and an inductively coupled transmitter coil embedded in the road surface. Therefore, the user does not need to handle a power connector anymore. This increases convenience and, most importantly, it eliminates the safety concerns related to the high-power electrical equipment.

As another key advantage, contactless charging allows starting the charging process fully automated, without the need for interaction with the EV user. Therefore, the charging process can be initiated within much shorter time compared to a conventional battery charger, for instance if the vehicle is stationary at a charging platform only for a short period of time. This makes IPT technology particularly attractive for the implementation of a distributed charging network. Charging platforms can be installed at locations where vehicles stop during normal commutation, e. g., at traffic lights, at bus stations, or at taxicab stands. In this *opportunity charging* setup, small amounts of charging energy are supplied to the battery every time the vehicle reaches a charging platform during its normal operation. As a result of the short but frequent charging periods, the time required for the complete recharging

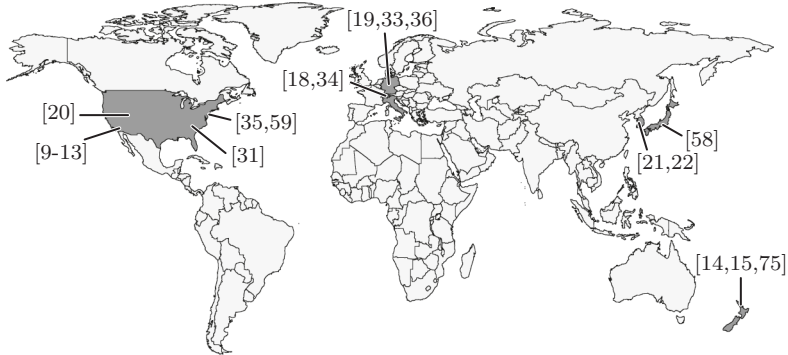


Fig. 1.2: Geographical overview of selected research and development activities on IPT for contactless EV battery charging in industry and academia.

of the battery can be reduced. This is of particular advantage for public transportation systems. The long charging times for the recharging of the large batteries of electric buses can be significantly reduced or even eliminated by distributing the charging process along bus lines. Moreover, the shorter standing times of the vehicles allow reducing the number of fleet vehicles needed to operate a transportation network. Therefore, the total cost of operation is reduced.

These opportunities have triggered a high number of research projects in industry as well as in academia around the world. A geographical overview of selected IPT research activities is shown in **Fig. 1.2**. On one hand, several start-up companies, university spin-offs, and research institutions have focused their attention on the subject. On the other hand, also established vehicle manufacturers in Germany and Japan as well as Original Equipment Manufacturers (OEM) have announced activity in the area. As a result, the number of scientific publications and filed patents on the subject has been increasing rapidly over the past years (cf. **Fig. 1.3**).

Most of the published research is focused on specific aspects of the design or the control of IPT systems for private transportation, mainly because the lower power level simplifies implementation and testing. A number of projects are also concerned with public transportation where IPT offers additional advantages, particularly in terms of operation costs. This is also where the investigations presented in this thesis are mainly aimed. In order to provide the context of the presented re-

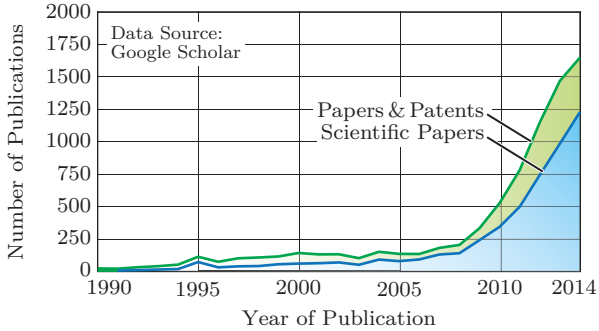


Fig. 1.3: Publication numbers as obtained from the Google Scholar search query: *power inductive OR contactless "electric vehicle" -"induction motor" -"induction machine"* (the last part excludes electrical machine research with similar titles).

search findings, the main opportunities and design challenges are briefly reviewed in the following.

1.2 Opportunities for IPT in Electric Public Transportation

Compared to the private transportation sector, in public transportation EV and Hybrid Electric Vehicle (HEV) technology is much more driven by operating costs. A lower total cost of ownership and lower fuel price volatility results from using electrical energy instead of Diesel fuel or petroleum as primary energy source. Moreover, battery powered solutions do not require a continuous power supply by overhead lines. This makes them particularly attractive for urban transportation, where any visible infrastructure equipment is undesirable. Moreover, electric transportation also causes significantly lower noise emissions, another beneficial feature in an urban environment.

In contrast, the dwell time that is needed for frequent battery charging adds operating costs. Furthermore, high-power charging capability and a large storage capacity for long continuous operation add volume and weight to the on-board battery pack and thereby increase the power consumption of the vehicle. Hence, the shorter dwell time and the possibility to operate with a reduced on-board energy storage capacity make

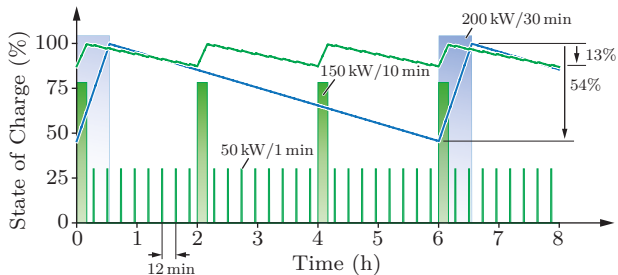


Fig. 1.4: Battery state of charge for charging with 200 kW for 30 min in a depot and for *opportunity charging* with 50 kW/1 min intervals combined with 150 kW/10 min bursts. The depth of discharge is reduced from 54% to 13% and the dwell time is shortened from 30 to 10 min for this scenario.

opportunity charging with charging stations along bus lines particularly attractive.

A possible *opportunity charging* scenario is shown in **Fig. 1.4**. Short 50 kW/1 min charging intervals are used in combination with longer 150 kW/10 min intervals every two hours. In this calculation, a battery capacity of 200 kWh, an average consumption of 1 kWh/km, and an average speed of 20 km/h are assumed for the electric bus². In addition, a conventional charging scheme is shown in which the battery is recharged at a power level of 200 kW for 30 min every 6 h at a bus depot. The comparison of the two scenarios shows that the depth of discharge is reduced from 54% to 13% for the listed assumptions, because the charging energy is supplied more continuously.

A lower depth of discharge increases the battery lifetime [16] and can be utilized for a weight and volume reduction of the on-board energy storage. As a result of the reduced dwell time of 10 min compared to 30 min, the number of fleet vehicles required to operate a particular route is potentially lower for the *opportunity charging* scheme compared to the conventional charging scenario. These aspects imply a lower total cost of ownership for the EV and lower operating costs, which makes the concept highly attractive for public transportation operators.

A comparison of the power conversion chains from the three-phase mains to the high-voltage battery of the vehicle is shown in **Fig. 1.5** for a high-power isolated conductive EV battery charger and a contact-

²Estimated values for a battery-electric public bus in an urban environment.

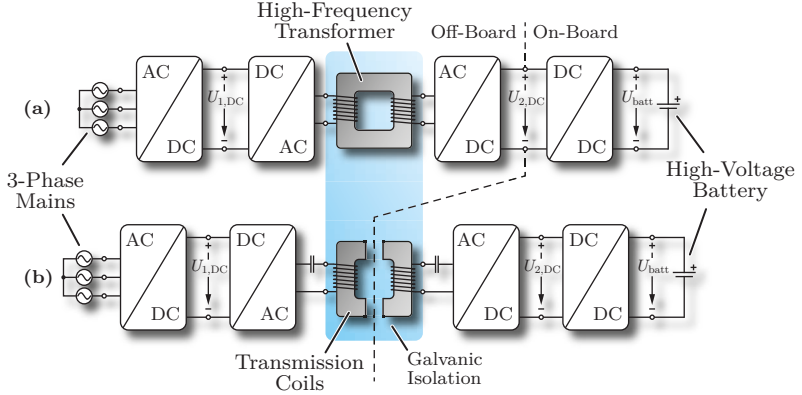


Fig. 1.5: (a) Power conversion chain of a conventional conductive EV charger and (b) a contactless battery charger using IPT.

less solution using IPT. A typical layout for a conductive charger is to connect the vehicle-side power electronics directly to the output of a DC-DC converter stage that incorporates a high-frequency isolation transformer. In this way, the major part of the power electronics is located in the stationary charging station. Typically, only a DC-DC converter for controlling the battery current is required on board. The connection can also be made at other stages of the power conversion chain, for instance directly at the three-phase mains. However, this solution increases the amount of on-board equipment and is therefore typically not preferred.

In the case of a contactless charger, the on-board and off-board components are clearly separated by the air gap of the IPT system. As shown in detail in Section 2.2.1, the IPT coils form a transformer with a large air gap and, consequently, a high leakage inductance. No additional transformer is needed as galvanic isolation is already provided by the contactless power transmission. The high leakage inductance, which would normally cause an output power reduction and a low efficiency, is typically compensated using resonant capacitors [17]. In this way, a high efficiency is achieved even for larger transmission distances. Therefore, the approach enables the design of contactless chargers with the ability to transmit a high output power across the air gap that is needed for the vehicle ground clearance [18–22]. This feature has attracted significant industry attention.

Tab. 1.1: Existing IPT prototype solutions for electric buses intended for public transportation applications [18–22].

Conductix IPT Charge	Bombardier Primove	KAIST OLEV	Wave IPT
			
60-120 kW $\delta = 40 \text{ mm}^1$ $\eta > 90\%$	150-200 kW air gap n/a ¹ $\eta > 90\%$	25 kW $\delta = 200 \text{ mm}$ $\eta > 80\%$	50 kW $\delta = 200 \text{ mm}$ $\eta > 90\%$

¹receiver coil is lowered during charging

1.2.1 Existing Industry Solutions

Recently, several technical solutions for *opportunity charging* at bus stops have been presented. Innovative conductive charging systems have been designed for power levels of several hundred kilowatts [23–27]. In these systems, mechanical contact arms or pantographs are used to establish a galvanic connection between the vehicle and the charging station. Since they are mostly based on existing technology, such systems are readily implemented. However, they include moving mechanical parts that are subject to wear and fatigue. In addition, the exposed copper connectors suffer from corrosion, which is accelerated by the sparking that might occur when connecting or disconnecting the galvanic contacts. Therefore, contactless charging solutions based on IPT have been developed as an alternative solution with reduced visible infrastructure [18, 19] and without moving mechanical parts [20–22]. For the system presented in [21, 22], the power is transmitted via a power track embedded in the road surface while the vehicle is in motion. This concept potentially simplifies the charging process even further, but a realization with low material effort and low installation costs is especially challenging in practice. **Tab. 1.1** shows the key specifications of the realized prototype vehicles. At present time, the listed prototypes are being tested under real world conditions and might lead to commercial products in the near future.

1.3 Key Engineering Challenges

Despite the rapid development of first IPT prototype systems, several design aspects need further investigation by academic and industry research. Therefore, the key engineering challenges for IPT systems are briefly discussed in the following section.

1.3.1 High Efficiency and High Power Density

For passenger vehicles or electric buses, a ground clearance between 100 and 250 mm is typical. Hence, an IPT system without moving mechanical components must be able to transmit power over an air gap of similar width. This poses a major challenge in the design. As shown in full detail in Section 2.2.3, the weak magnetic coupling between the transmission and the receiver coil implies an inherent physical efficiency limit for the power transfer, even if resonant elements are used to compensate the high transformer leakage inductance. The magnetic coupling can be increased only if the transmitter and receiver coils are dimensioned large compared to the air gap. Hence, a low power density results for the main power components of an IPT charging system if the IPT coils are designed for an efficiency above 90%.

For instance the 3.7 kW receiver coil in [34] has a power density of 1.6 kW/dm³ and an efficiency of approximately 90% with 130 mm air gap³. The gravimetric power density is calculated as 0.9 kW/kg. The 3.3 kW receiver coil in [35] has an AC-to-AC efficiency of up to 97%⁴ and, depending on the power electronics, a DC-to-DC efficiency between 93% and 85% at an air gap of 100-150 mm. The volumetric power density is 1.83 kW/dm³ and for the gravimetric power density 0.8 kW/kg can be estimated. The numbers for the volumetric power density and the gravimetric power density do not include the transmitter coil and the power electronics, which contribute another 30 kg in both examples. For the 200 kW system in [19], the volumetric power density⁵ is 1 kW/dm³ and the gravimetric power density is 0.6 kW/kg.

³Upon request, the manufacturer stated that the data sheet efficiency is measured between the mains and the battery, i. e. from AC to DC.

⁴The coil-to-coil efficiency in the data sheet does not include the power electronics. The DC-to-DC efficiency was obtained from the manufacturer upon request.

⁵Upon request, the receiver coil dimensions 2.2 x 0.9 x 0.1 m and a weight of 340 kg were indicated by the manufacturer.

Tab. 1.2: Overview of state-of-the-art conductive on-board chargers and industrially available contactless EV chargers.

	Source	P (kW)	V (dm³)	m (kg)	η (%)	ρ (kW/dm³)	γ (kW/kg)
Conductive	Whitaker ¹ <i>et al.</i> [28]	6.1	1.22	1.6	95.0	5.0	3.8
	J. Everts [29]	3.7	1.85	2.68	95.6	2.0	1.38
	Gautam <i>et al.</i> [30]	3.3	5.46	6.2	93.6	0.60	0.53
	GM Chevrolet Volt [31]	3.3	6.71	10.1	89.6	0.49	0.33
	Nissan Leaf 2013 [32]	3.3	10.9	16.3	85	0.3	0.2
	Toyota Prius 2010 [28]	2.9	6.4	6.6	n/a	0.45	0.44
Contactless	Primove-200 ^{2,3} [19]	200	198	340	90.0	1.0	0.59
	this work ⁴	50	18.5	25	95.8	2.7	2.0
	Goeldi ⁴ <i>et al.</i> [33]	22	22.4	n/a	97.0	0.98	n/a
	Chinthalali <i>et al.</i> [31]	6.6	7.2	12.3	85.0	0.92	0.54
	Brusa ICS115 ² [34]	3.7	2.3	4.0	90.0	1.60	0.93
	WiTricity Wit3300 ² [35]	3.3	1.8	4.0	89.0	1.83	0.83
	Diekhans ^{4,5} <i>et al.</i> [36]	3.0	8.5	3.2	95.8	0.35	0.93

Remarks: for all contactless chargers, only the dimensions and the weight of the receiver coil is included.

¹Designed with SiC MOSFET devices. ²Data obtained from manufacturer upon request. ³Receiver

is lowered to street during charging. ⁴DC-to-DC efficiency. ⁵No coil housing included.

As a comparison, the data of existing on-board conductive EV chargers are collected in **Tab. 1.2**. The listed numbers for the conductive chargers include the complete power conversion chain from the mains to the EV high-voltage battery. For the contactless chargers, only the receiver coil is included for the volumetric and gravimetric power density. The numbers clearly indicate that the required component volume, weight, and material cost for the IPT on-board components are higher than for a conventional solution. For instance, in [28] a state-of-the-art isolated 6.1 kW conductive on-board EV charger is shown with a power density of 5 kW/dm³, an efficiency higher than 95%, and a gravimetric power density of 3.8 kW/kg. These numbers imply a volume of only 1.2 dm³ and a weight of just 1.8 kg. This best-in-class performance is achieved mainly by the beneficial utilization of Silicon Carbide (SiC) instead of conventional Silicon (Si) power semiconductor technology for the miniaturization of the passive system components. The comparison of this best-in-class systems to the industrially available IPT prototypes in **Fig. 1.6** demonstrates that a compact realization of IPT systems with a high volumetric and gravimetric power density is a major challenge. For completeness also the result of this thesis is included in the figure, even though the details of the design and the experimental results are presented later in the thesis. It must be noted that no mains interface is included in the system presented herein. Instead, the transmitter-side power electronics include a DC-DC conversion stage, which in a future design step could be replaced by a three-phase buck-type mains interface. The mains interface is expected to reduce the efficiency by around 1-2 percentage points, depending on the employed power electronics solution [37]. For complete transparency, it must also be pointed out that the listed commercial systems include all necessary structural elements of mounting the coil on the vehicle and are fully compliant with automotive standards. For the work of this thesis further modifications are required to fulfill all automotive requirements.

The analysis of the listed data highlights that the efficiency of the contactless EV chargers is reduced by up to approximately 5%-points compared the latest conductive EV chargers. This is mainly due to the limited construction volume for the receiver coil on the vehicle. Small receiver coils lead to a low magnetic coupling, even if as in [34] a significantly larger transmitter coil is used. As a result, a comparably low transmission efficiency must be accepted for a contactless EV charger.

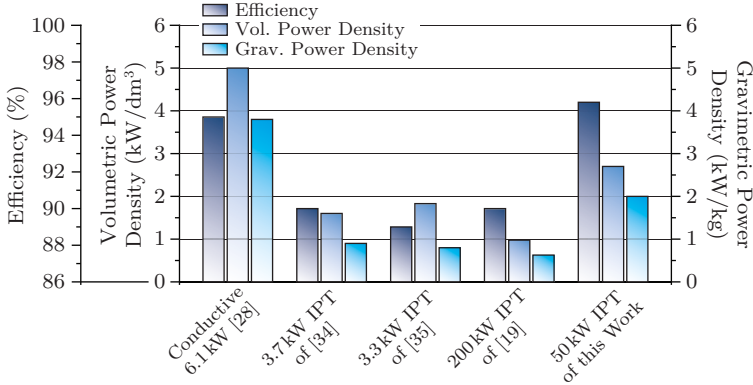


Fig. 1.6: Comparison of the main performance factors for a conductive EV charger [28], for industrially available IPT chargers [19,34,35], and the system presented in this work. The power density for the IPT systems only includes the receiver coil, whereas for [28] the complete system is included.

1.3.2 High Tolerance to Coil Misalignment

Because the magnetic coupling of the IPT transmission coils depends on their relative positioning, the efficiency of the power transfer as well as the impedance characteristics of the resonant system are affected by coil misalignment. Nevertheless, an EV battery charging system is expected to tolerate coil misalignment in the order of 50-150 mm without significantly affected charging times. Therefore, the power electronics must be dimensioned such that a high output power can be maintained even at a system efficiency that is lower than for ideal coil positioning. Additionally, the control system must be robust with respect to the modified impedance characteristics of the resonant system. It must also be able to identify the parameters that are needed for the adaptation of the control algorithm. These requirements impose another design constraint for the IPT coils. A significant reduction of the magnetic coupling variations can typically only be achieved if the coils are designed sufficiently large, which further obstructs the realization of a compact system.

1.3.3 Minimum Cooling Requirements

During operation, conduction losses in the copper wires and hysteresis losses in the core elements of the transmission coils occur. Hence, a passive or active cooling concept is required in order to prevent excessive heating. Passive cooling is challenging, because conventional heat sink elements are electrically conductive parts. High eddy current losses and partial field cancellation due to the counteracting magnetic flux prohibits exposing such parts directly to the high-frequency magnetic field of the IPT coils. For the same reason, also liquid cooling with metal cooling plates is difficult. Forced-air cooling remains as the only option. However, the high reliability requirements of automotive applications might restrict the use of cooling fans, because the rotating parts are subject to wear and may negatively affect the lifetime of the charging system.

Clearly, the thermal management of IPT coils is a key challenge for the designer. The approach pursued in this work, is to ensure minimum losses in the coils by optimizing the transmission coils as well as the power electronics and the control scheme. This alleviates the problem to some extent.

1.3.4 Low Electromagnetic Stray Fields & High Operational Safety

The high-frequency magnetic and electric fields required for the contactless power transfer raise major concerns about the safety and electromagnetic compatibility of such systems. A number of standards and norms specify reference levels regarding the exposure of humans to electromagnetic fields, such as the guidelines published by the International Commission on Non-Ionizing Radiation Protection (ICNIRP) in 1998 and 2010 [38, 39], and the IEEE Standard C95.1-2005 [40]. The upcoming Standard J2954 by the Society of Automotive Engineers (SAE) [41–43], which is concerned with contactless charging of EV, is at present time expected to name the ICNIRP 2010 guidelines as the reference for contactless EV charging related stray field exposure.

One option for reducing the stray fields around the vehicle is to lower the receiver coil towards the charging platform in order to completely cover the transmitter coil as in [18, 19]. This confines the fields to the active area of the power transfer while at the same time increasing the efficiency of the power transfer due to the improved magnetic coupling.

However, such a solution cannot fully profit from the potential of the technology, because moving mechanical parts are required. Alternative options include the use of high-permeability materials for guiding the magnetic flux and electromagnetic shielding. At a sufficiently high conductivity, eddy currents in a conductive shielding produce a counteracting magnetic field, which can be exploited for field cancellation. Such components, however, add weight to the IPT transmission coils and potentially increase the power losses. Reaching an efficiency and power density that is comparable with that of conventional conductive EV chargers becomes therefore even more challenging.

Additional safety concerns arise from the ability of the high-frequency magnetic fields to cause heating of objects located within or close to the active area of the IPT system. For instance metalized paper, a common packaging material, may ignite if positioned directly below the vehicle [42]. Detecting foreign objects in the air gap is therefore of crucial importance to ensure a high operational safety of a practical IPT system.

1.3.5 High Reliability & Low Cost

Challenges regarding component reliability arise from the mounting position of the IPT receiver coil underneath the vehicle. At this location, the receiver coil is constantly exposed to moisture, dirt, and debris from the road surface. If the transmitter coil is embedded in the road surface, a mechanical stability of several tons is required as heavy vehicles might drive across the charging platform. Additionally, if the electronic components are located in a sealed underground cabinet high operating temperatures can result from heating due to power losses and due to sunlight heating the road surface. Therefore, the coil housings and all contained components must be designed sufficiently rugged to withstand these environmental factors.

Due to the lower power density and particularly also because of the need for sufficiently robust housings, high material costs for the power components may result. In addition, embedding a transmitter coil within the road surface could potentially have additional installation costs compared to a conventional charging station installed overground. A compact and cost-effective coil design with a low material effort is therefore of high interest.

1.3.6 Interoperability

For contactless or conventional conductive EV chargers alike, interoperability between the products of different manufacturers is crucial for the success of the technology. While IPT charging technology is still at an early stage, the SAE has announced to specify a common transmission frequency band around 85 kHz as part of the upcoming Standard J2954 with the goal of simplifying interoperability [43]. At its final publication, the Standard is expected to bring further clarification regarding, e. g., charging power levels, geometrical requirements for the transmission coils, communication interfaces, safety features, and test procedures.

1.4 Goals and Contributions of the Thesis

As outlined above, the design of an IPT system for EV charging is an engineering problem where multiple competing objectives must be taken into account. Therefore, a fundamental understanding of the interdependencies between the different performance factors is of crucial importance. However, a multi-objective design method is still missing in literature and it has not been clarified in detail how the different performance factors are related. Moreover, the physical and technological limitations of IPT have not yet been fully analyzed and a benchmark demonstration of what overall system performance can be reached if all system components are fully optimized cannot be found at present time. Therefore, the main goal of this thesis is to provide an improved understanding of the design trade-offs and to clarify the physical and technological boundaries of IPT technology.

The main scientific contribution of the thesis is the holistic design approach, in which all components of the power conversion chain are included. The IPT coils and the resonant circuit, but also the power electronic converter and the control system are considered. A multi-objective optimization approach is proposed, which allows taking into account several performance criteria simultaneously. The trade-offs between different performance factors, such as the system efficiency, the power density, or the stray fields, are highlighted in order to provide insight into the parameter interdependencies within the system. Based on the optimization of a scaled 5 kW and a full-scale 50 kW IPT system intended for public transportation EV charging, the effects of different

design variables are studied. The influence of parameters, such as the coil size, the air gap, the transmission frequency, or the topology and control scheme of the power electronics, are analyzed in detail in order to provide a more profound understanding of their influence on the overall system performance.

The realized prototype system is optimized for performance at the physical efficiency limit given by the weak magnetic coupling of the IPT coils. The transmission coils reach a high area-related, volumetric, and gravimetric power density⁶, as well as a high efficiency, while respecting the reference levels of the ICNIRP 2010 guideline for the magnetic stray field [39]. The power electronic converter is realized using the latest commercially available SiC power semiconductor technology in order to achieve highest compactness and a high efficiency of the complete power conversion chain⁷. By optimizing all aspects of the system for the best performance, the prototype demonstrates the technological limits of IPT for EV battery charging applications.

1.5 Outline of the Thesis

With the goal of providing the reader with a fundamental understanding of the topic, the main results are presented towards the end of the thesis in favor of a detailed introduction. The content is divided into seven chapters, which are briefly outlined in the following.

In order to bridge the knowledge gap between conventional conductive and contactless EV charging systems, **Chapter 2** begins with a review of an isolated EV battery charger known from literature. Based on the results, the fundamental working principles of an IPT system are derived. The key design equations for the transmission coils and the resonant system are analyzed and the most important aspects for a high efficiency of the complete power conversion chain are discussed, including also the power electronic converter and the control.

After the introduction of the basic principles, a multi-objective optimization procedure for IPT systems is developed in **Chapter 3**. Physical models for the estimation of the power losses in IPT coils based on analytical calculations and Finite Element Methods (FEM) are presented and used in the exemplary optimization of a scaled 5 kW IPT

⁶The power densities are 1.6 kW/dm², 2.7 kW/dm³, and 2.0 kW/kg, respectively.

⁷A power density of 9.5 kW/dm³ is reached for the power electronic converter and DC-to-DC efficiency of 95.8% is measured for the complete IPT system.

prototype system. Insights into the interdependencies between the performance factors efficiency, power density, and magnetic stray field of the coils are obtained from the optimization results. The encountered design trade-offs as well as the physical performance limits are discussed in detail. The chapter ends with a detailed experimental verification of the models used during the optimization of the 5 kW prototype system.

In **Chapter 4**, the multi-objective optimization procedure is applied to the design of the full-scale 50 kW transmission coils. First, necessary adaptations to the previously presented power loss models are discussed for the selected IPT coil geometry. Afterwards, a multi-objective optimization with respect to the performance criteria efficiency, area-related and gravimetric power density, and stray field is conducted. Towards the end of the chapter, details of the practical realization including the shielding and the thermal management of the IPT coils are discussed.

Based on the findings for the power electronics in Chapter 2, an all-SiC power electronic converter for the 50 kW IPT system is presented in **Chapter 5**. Details on the realization of the inverter-stage with paralleled MOSFET devices and of the DC-DC conversion stage comprising parallel interleaved converter modules with coupled inductors are given. The chapter ends with the presentation of the realized prototype hardware.

In **Chapter 6** the measurement setup for the experimental verification of the 50 kW IPT system design is described. The presented measurement results include the efficiency for the power converter on its own and DC-to-DC conversion efficiency measurements for the IPT system. Additionally, measured magnetic stray fields are compared to the FEM simulations to verify compliance with the ICNIRP 2010 guidelines.

At the end of each chapter, short summaries of the obtained results are given and the key findings are highlighted. Final conclusions obtained from the presented study are summarized in **Chapter 7**. The achieved performance is critically discussed in light of the physical and technical limitations of IPT systems in EV battery charging applications. Thereafter, the thesis is concluded by suggestions for potential future research areas.

Several parts of the research findings presented in this thesis have been published at international conferences, in the form of papers or presentations, or as papers in scientific journals. Where appropriate, the respective publications have been cited in the document. Additionally,

a list of the publications developed in the course of this work is given at the end of the thesis.

2

Fundamentals of Inductive Power Transfer

TO BRIDGE the knowledge gap between conventional conductive and contactless EV charging systems, this chapter begins with a review of the isolated on-board EV battery charger presented in [44]. In Section 2.1, the basic functionality and the principal advantages of the power converter are described and the influence of an air gap in the core of the high-frequency isolation transformer on the DC output characteristics are analyzed. After the introduction of the concept of resonant compensation and the fundamental frequency model of the resulting resonant converter, in Section 2.2 the transition is made towards an IPT system. In the discussion, the key design challenges and the conditions for an efficient operation of the IPT system become apparent. In Section 2.3, the analysis is extended to include the power electronic converter and its interaction with the resonant system. Conditions for low converter losses are derived and an efficiency optimal control concept is presented.

2.1 Isolated DC-DC Converter for Conductive EV Charging

In this section, the isolated DC-DC converter for conductive EV charging described in [44] is reviewed. The converter topology is shown in **Fig. 2.1(a)**, together with the principal converter waveforms in **Fig. 2.1(b)** and a photograph of one out of three 1 kW converter modules in **Fig. 2.1(c)**. It must be noted that the converter concept is

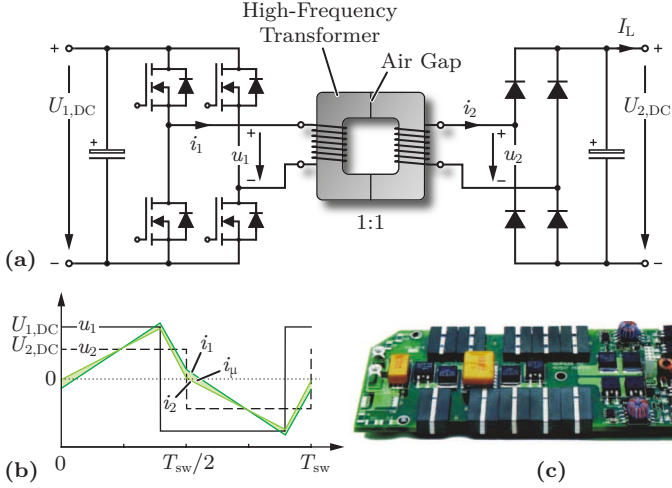


Fig. 2.1: Isolated DC-DC converter for conductive EV charging: (a) power circuit topology, (b) principal waveforms (i_μ not drawn to scale), and (c) photograph of one out of three 1 kW converter modules presented in [44].

applied here for a 400 V/5 kW system for better comparability with the IPT system discussed later in this chapter. Therefore, the used parameter values (cf. **Tab. 2.1**) do not correspond to the original publication [44].

2.1.1 Transformer Equivalent Circuit

For a better understanding of the circuit, in a first step the transformer equivalent circuit and the used notation is introduced. **Fig. 2.2(a)** shows a transformer equivalent circuit, where the transformer differential equations

$$\begin{aligned} u_1 &= L_1 \frac{di_1}{dt} - M \frac{di_2}{dt} \\ u_2 &= M \frac{di_1}{dt} - L_2 \frac{di_2}{dt} \end{aligned} \quad (2.1)$$

are represented by the circuit elements L_1 and L_2 for the primary-side and secondary-side self-inductances, and the mutual inductance M . The ideal transformer with transformation ratio $n = 1$ merely

Tab. 2.1: Parameters of the conductive EV charger.

Parameter	Variable	Value
DC Input Voltage	$U_{1,DC}$	400 V
DC Output Voltage	$U_{2,DC}$	≤ 400 V
Output Power	P_2	≤ 5 kW
Switching Frequency	f_{sw}	48 kHz
Primary Self-Inductance	L_1	3 mH
Secondary Self-Inductance	L_2	3 mH
Turns Ratio	$N_1:N_2$	15:15
Magnetic Coupling	k	0.99 (initially)

represents the galvanic isolation. The primary-side and secondary-side transformer voltages are denoted by u_1, u_2 while i_1, i_2 stand for the transformer currents. The transformer differential equations are fully captured by the three circuit elements L_1, L_2 and M .

The transformer equivalent circuit in **Fig. 2.2(a)** may be extended to general values $n \neq 1$ as long as the terminal behavior remains unaffected. Comparing the circuit equations for both cases, this results in the equivalent circuit **Fig. 2.2(b)**, which is valid for any value of the transformation ratio n . Since the transformer is now represented by four parameters instead of just three, one parameter can be selected arbitrarily while the model remains valid. Hence, the transformation ratio n can be used to modify the equivalent circuit in a way that simplifies further calculations. For instance the selection

$$n = k\sqrt{\frac{L_1}{L_2}}, \quad (2.2)$$

where the variable k represents the magnetic coupling of the two windings,

$$k = \frac{M}{\sqrt{L_1 L_2}}, \quad (2.3)$$

allows eliminating the second series inductance from the equivalent circuit as shown in **Fig. 2.2(c)**.

The three required measurement steps to determine the three parameters of this equivalent circuit are illustrated in **Fig. 2.2(d)**. In

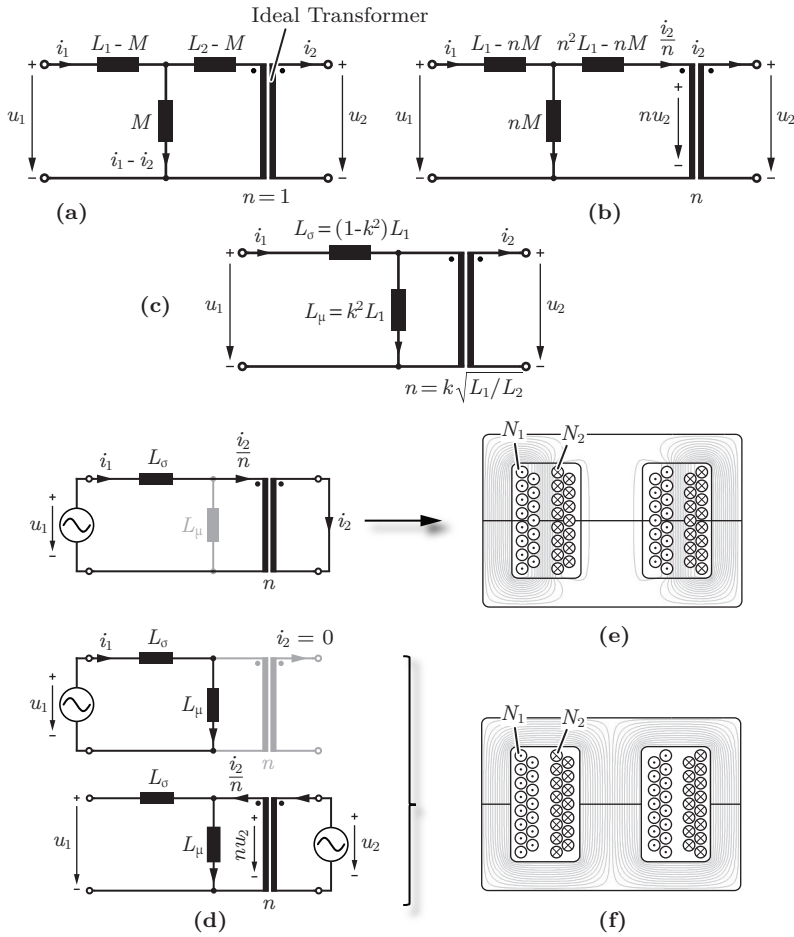


Fig. 2.2: (a) Transformer equivalent circuit with transformation ratio $n = 1$, and (b) for a general transformation ratio n . (c) The selection $n = k\sqrt{L_1/L_2}$ results in the transformer equivalent circuit with the leakage inductance referred to the primary side. (d) Measurement steps to determine the leakage inductance L_σ , magnetizing inductance L_μ , and the transformation ratio n . (e),(f) FEM-calculated magnetic flux lines in the transformer during the measurement steps.

a first step, the secondary winding is shorted while a sinusoidal voltage with angular frequency ω is applied to the primary-side terminals. From a measurement of the primary current i_1 , the leakage inductance L_σ is determined by

$$L_\sigma = \frac{\hat{U}_1}{\omega \hat{I}_1} \Big|_{u_2=0} \quad (2.4)$$

The magnetizing inductance L_μ is determined with a measurement of the secondary-side voltage with open secondary winding and

$$L_\mu = \frac{\hat{U}_2}{\omega \hat{I}_1} \Big|_{i_2=0} \quad (2.5)$$

In a last step, the transformation ratio n can be measured if the voltage source is connected to the secondary-side windings and the primary-side voltage is measured

$$n = \frac{\hat{U}_1}{\hat{U}_2} \Big|_{i_1=0} \quad (2.6)$$

It is interesting to note that the energy of the transformer leakage field (cf. **Fig. 2.2(e)**) is fully modeled by the leakage inductance L_σ on the primary side. Initially the energy was divided into two (not necessarily equal) shares represented by the two series inductances $L_1 - M$ and $L_2 - M$ of the original equivalent circuit in **Fig. 2.2(a)**. This demonstrates that the division of the transformer leakage is arbitrary and that the leakage field cannot be associated with any particular side of the transformer.

2.1.2 Basic Operation of the Converter

After the transformer equivalent circuit has been introduced, the basic functionality of the isolated DC-DC converter is discussed next. A system without losses and with ideal components is assumed throughout the derivation.

The bridge-legs of the full-bridge inverter on the primary side of the converter are operated with a constant 50% duty cycle and 180° phase shift, as shown in **Fig. 2.1(b)**. During the time interval where both transformer terminal voltages u_1, u_2 show positive polarity, a positive

voltage difference is applied to the transformer leakage inductance L_σ and the primary current i_1 rises linearly. Assuming a high magnetic coupling and therefore a large magnetizing inductance L_μ , the magnetizing current i_μ is small and the secondary current i_2 closely follows i_1 (in **Fig. 2.1(b)** the difference $i_\mu = i_1 - i_2$ is not drawn to scale). As soon as the inverter switches the polarity of u_1 , a negative voltage difference is applied to L_σ and the primary current i_1 starts falling. When the secondary current i_2 reverses direction, the diode bridge switches the polarity of the secondary voltage, which completes the first half of the switching cycle.

Neglecting the magnetizing current of the transformer, the load current is calculated by taking the average value of the secondary-side current i_2 over one half of the switching cycle. This results in [45]

$$I_L = \frac{nU_{1,\text{DC}}}{8L_\sigma f_{\text{sw}}} \left(1 - \left(\frac{nU_{2,\text{DC}}}{U_{1,\text{DC}}} \right)^2 \right), \quad (2.7)$$

where f_{sw} is the switching frequency and $U_{1,\text{DC}}, U_{2,\text{DC}}$ are the primary- and secondary-side DC-link voltages of the converter. **Fig. 2.3(a)** shows the DC output voltage $U_{2,\text{DC}}$ in function of the load current I_L with the magnetic coupling k of the transformer as parameter. For the no-load case $I_L = 0$, the output voltage $U_{2,\text{DC}}$ takes the value of the input voltage $U_{1,\text{DC}} = 400$ V. As I_L is increased, a load-dependent difference between the DC-link voltages at the primary and secondary occurs. This is a result of the leakage inductance L_σ , which limits the slope of the primary current and therefore the current average value that can be reached every half-cycle.

The effect becomes more pronounced if the magnetic coupling k of the transformer is reduced and L_σ becomes larger, for instance as a result of an air gap in the transformer core. The converter waveforms for the two operating points $k = 0.99$ and $k = 0.97$, labeled operating points OP₁ and OP₂ in the figures, are shown in **Fig. 2.3(b)**. As a result of the higher leakage inductance, the slope of the transformer currents is lower for OP₂, despite equal input and output voltages. Due to the lower slopes, the current average values are reduced and, consequently, also the load current I_L is lower for OP₂ as shown in **Fig. 2.3(a)**.

The key advantages of this circuit are a result of the described triangular current waveforms. The inductive current in the primary transformer winding enables Zero Voltage Switching (ZVS) of the Metal-

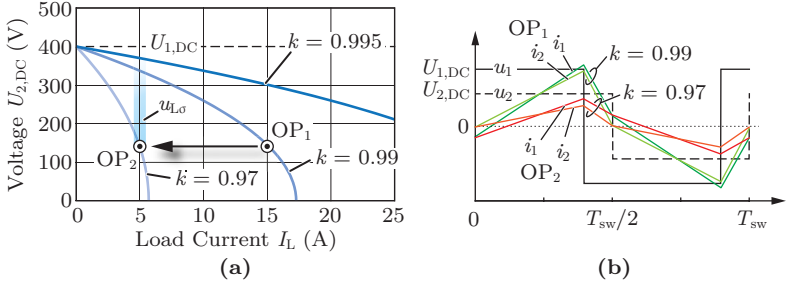


Fig. 2.3: Effects of an air gap in the transformer core on (a) the load characteristics of the converter and (b) on the converter waveforms (i_μ not drawn to scale).

Oxide Semiconductor Field-Effect Transistors (MOSFETs), which practically eliminates switching losses in the primary-side full-bridge inverter. The triangular shape of the secondary current allows Zero Current Switching (ZCS) of the secondary-side rectifier diodes and low reverse recovery losses. Moreover, the soft switching transitions lead to slower voltage slopes at the inverter terminals and hence reduce the required EMC filtering effort [44]. Additionally, since the secondary side consists of only a diode rectifier and the output capacitor, the number of actively controlled switches is small and the overall complexity of the converter is kept as low as possible. It is, therefore, clearly a viable candidate for an on-board EV battery charger with a high compactness and low cost. However, the comparably high RMS current in the transformer windings due to the triangular current waveforms must be noted as a disadvantage in addition to the load-dependent output characteristics.

2.1.3 Series Resonant Compensation of the Leakage Inductance

In order to reduce the effect of the leakage inductance L_σ of the transformer, a series resonant compensation capacitor can be introduced as shown in **Fig. 2.4(a)**. If the capacitance C_1 is selected such that the series resonant frequency

$$f_s = \frac{1}{2\pi} \frac{1}{\sqrt{L_\sigma C_1}} \quad (2.8)$$

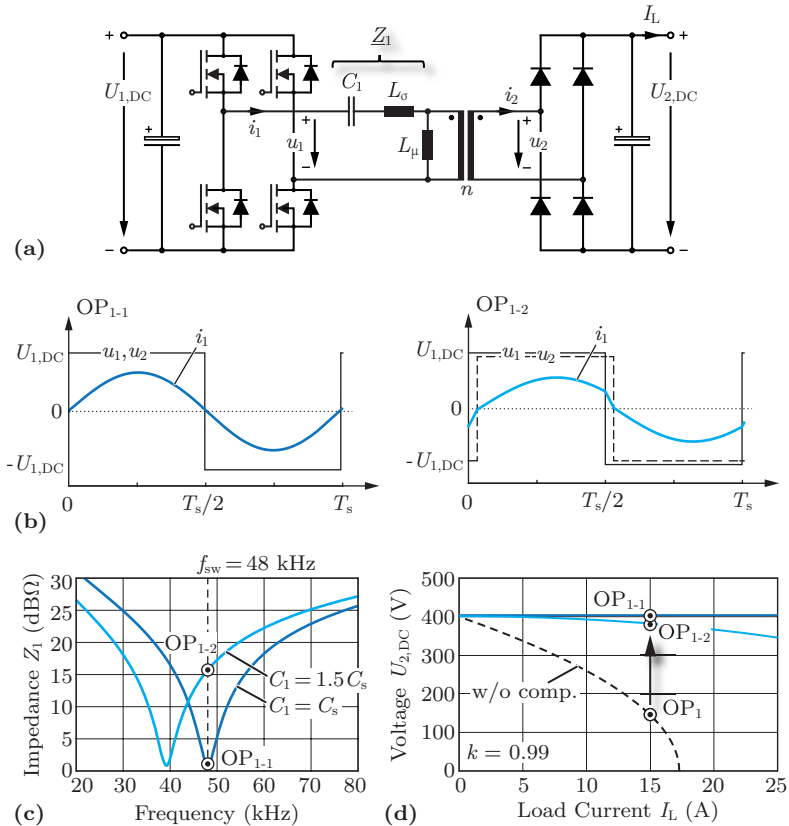


Fig. 2.4: (a) Converter topology with series capacitor C_1 for the resonant compensation of the transformer leakage inductance L_σ . (b) Converter waveforms for an exact compensation with $C_1 = C_s$ and for an over-compensation with a larger capacitance $C_1 = 1.5C_s$. (c) Magnitude of the series impedance Z_1 in function of the frequency, and (d) output characteristics of the converter corresponding to the two capacitance values.

is equal to the converter switching frequency, i.e., if the capacitance C_1 is equal to $C_s = 1/((2\pi f_{\text{sw}})^2 L_\sigma)$, the voltage across the leakage inductance and the voltage across the compensation capacitor become 180° phase-shifted and cancel out during operation. This completely eliminates the load dependency of the converter output characteristics and a constant secondary DC-link voltage $U_{2,\text{DC}}$ is achieved. The resulting converter waveforms and the output characteristics are shown in **Fig. 2.4(b)** for two values of the compensation capacitance C_1 . An exact compensation with $C_1 = C_s$ (labeled OP₁₋₁) is compared to an over-compensation with a larger capacitance of $C_1 = 1.5C_s$ (labeled OP₁₋₂).

As shown in **Fig. 2.4(c)**, if a larger capacitance is selected, the resonant frequency is lower than for an exact compensation. Therefore, a series impedance $Z_1 > 0$ remains at the switching frequency f_{sw} and a small drop of the output voltage $U_{2,\text{DC}}$ occurs in the output characteristics shown in **Fig. 2.4(d)**. However, as will be discussed in Section 2.3, an inductive primary current is necessary for ZVS of the full-bridge inverter. Therefore, this slight over-compensation (OP₁₋₂) and the remaining load-dependency of the output characteristics is accepted because it allows significantly reducing the switching losses.

2.1.4 Fundamental Frequency Modeling

In the converter waveforms of **Fig. 2.4(b)**, the initially triangular current has become almost sinusoidal. The reason for the change in current shape is the frequency characteristic of the series impedance Z_1 , which are shown in **Fig. 2.5(b)**. In the region of the switching frequency f_{sw} , the impedance rises with approximately +20 dB/dec. The inverter is switched with a constant 50% duty cycle. Therefore the amplitude spectrum of the inverter output voltage u_1 , which is also shown in **Fig. 2.5(b)**, is given by

$$\hat{U}_{1(n)} = \frac{4}{\pi} \frac{U_{1,\text{DC}}}{n}, \text{ for } n = 1, 3, 5, \dots \quad (2.9)$$

Since the spectrum of u_1 decays with -20 dB/dec and the impedance rises with approximately +20 dB/dec, the spectrum of the primary current $\hat{I}_{1(n)}$ decays with -40 dB/dec as shown in **Fig. 2.5(b)**. The third harmonic component is already approximately 25 dB smaller than the fundamental component and the fifth harmonic component is another

$$R_{L,\text{eq}} = \frac{8}{\pi^2} \frac{U_{2,\text{DC}}^2}{P_2}, \quad (2.10)$$

where P_2 is the converter output power. The power dissipation in the equivalent load resistance $R_{L,\text{eq}}$ represents the power that flows through the diode rectifier bridge into a DC load with resistance value $R_L = U_{2,\text{DC}}^2/P_2$ in the actual converter.

The remaining equivalent circuit of **Fig. 2.5(a)** can be analyzed using only basic AC circuit calculations instead of solving the differential equations of the initial converter circuit. With this simplification, the transition towards an IPT system is straight-forward as shown in the following section.

2.2 Transition to an Inductive Power Transfer (IPT) System

The two main effects of an increasingly large air gap in the transformer core can be understood directly from the circuit of **Fig. 2.5(a)**. As the air gap in the transformer core becomes larger, the magnetic coupling k between the primary and the secondary core halves is reduced. Hence, the transformer leakage inductance, which is calculated by

$$L_\sigma = (1 - k^2)L_1, \quad (2.11)$$

becomes larger and the magnetizing inductance, which is given by

$$L_\mu = k^2L_1, \quad (2.12)$$

is reduced. From these observations, two main effects of an increased air gap become apparent:

► **Shifting Resonant Frequency**

As the leakage inductance L_σ becomes larger, the resonant point (2.8) is moved towards lower frequencies and the series resonant circuit becomes under-compensated. Similar to what is shown in **Fig. 2.4(c)**, the series impedance Z_1 is not zero anymore at the switching frequency f_{sw} and a series voltage drop across the leakage inductance remains. Therefore, the output voltage $U_{2,\text{DC}}$ becomes again load dependent as in **Fig. 2.4(d)**.

► **Increasing Reactive Power Demand**

Due to the reduced magnetic coupling k , the reactive current $i_{\mu(1)}$ in the magnetizing inductance L_{μ} increases. Therefore, additional reactive power must be delivered by the voltage source $\underline{u}_{1(1)}$ to supply the same amount of active power to the load $R_{L,eq}$. Therefore, the efficiency of the power transfer is reduced.

The first listed aspect could be counteracted by adjusting the compensation capacitance C_1 according to the higher value of the leakage inductance using (2.8). This is possible as long as the magnetic coupling is not variable during operation. However, the magnetic coupling depends on the air gap and the relative positioning of the transmitter and the receiver coil. Therefore, for EV charging the compensation capacitance C_1 would need to be adjustable for every vehicle position, which is not practical.

Nevertheless, the compensation method described above is a good solution to guarantee a load-independent output voltage in IPT systems with fixed coil positions, where the magnetic coupling is constant. Possible applications could be a power supply through the rotating joints of a robot [47], or to a rotating spindle [48]. Alternatively, the air gap of the IPT system can be used as isolation distance. Further examples are the power supply of an isolated gate driver [49], or auxiliary power supplies in a modular multi-level converter, where a large isolation distance is needed due to the high potential difference [50].

A resonant frequency that is constant independently of the relative positioning of the coils is a desirable feature for the contactless EV charging system, because it reduces the required control effort. This can be achieved by introducing a second compensation capacitor C_2 on the receiver-side. The resulting series-series resonant compensation is discussed in the following.

2.2.1 Series-Series Resonant Compensation

In **Fig. 2.6(a)**, the converter topology for an IPT system with compensation capacitors on both sides of the contactless transformer is shown. The transformer equivalent circuit of **Fig. 2.2(a)** with transformation ratio $n = 1$ simplifies the understanding of the series-series compensated resonant circuit. In **Fig. 2.6(b)**, the fundamental frequency model including the transformer equivalent circuit is shown with the leakage

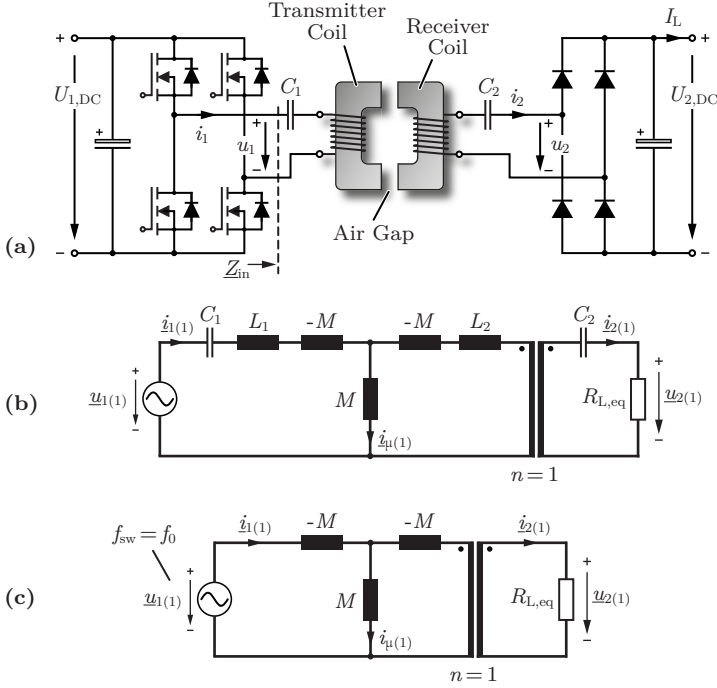


Fig. 2.6: (a) Converter topology of the series-series compensated IPT system. (b) Fundamental frequency model of the converter including the transformer equivalent circuit. (c) Remaining equivalent circuit at the resonant frequency f_0 of the reactive elements L_1, C_1 and L_2, C_2 .

inductances $L_1 - M$ and $L_2 - M$ of the original circuit separated into individual reactances.

The values C_1 and C_2 are selected such that the resonant frequency f_0 , given by the capacitances and the transformer self-inductances, is equal to the switching frequency of the full-bridge inverter

$$f_{sw} = \frac{1}{2\pi} \frac{1}{\sqrt{L_1 C_1}} = \frac{1}{2\pi} \frac{1}{\sqrt{L_2 C_2}} \quad (2.13)$$

The remaining parts of the circuit at resonance are shown in **Fig. 2.6(c)**. From this circuit, the input impedance as seen by the source is calculated as

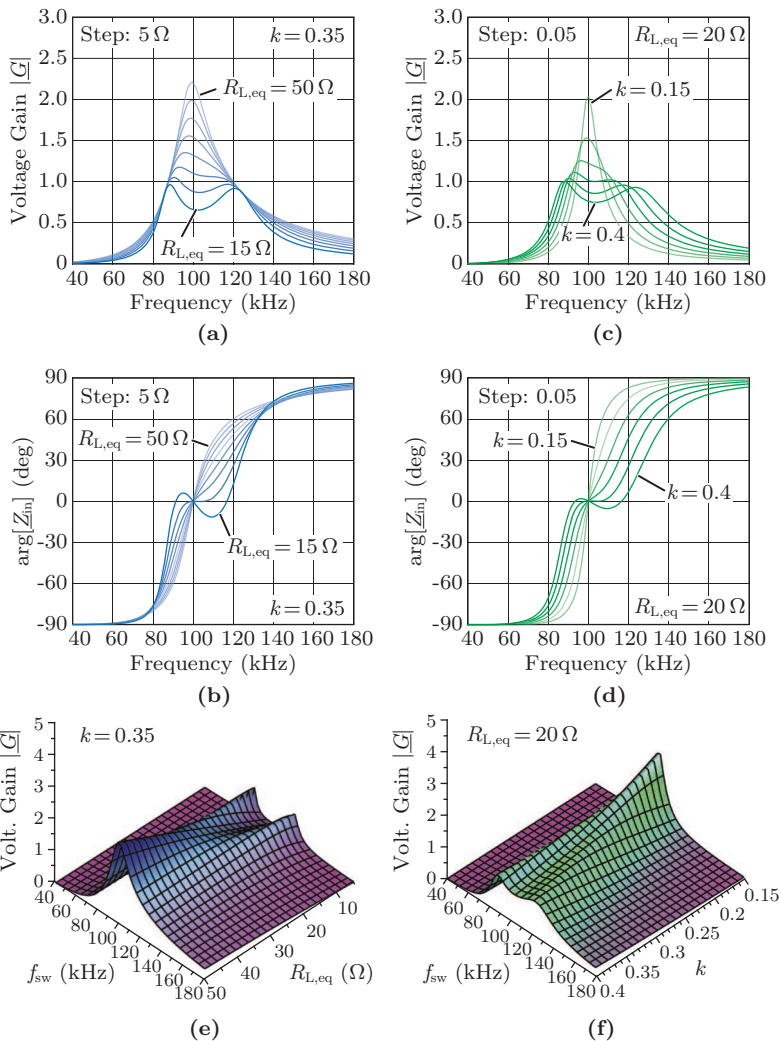


Fig. 2.7: Frequency characteristics of the 5 kW IPT system discussed in Chapter 3: voltage gain $|G| = |u_2/u_1|$ and phase angle of the input impedance Z_{in} shown as a function of the switching frequency and with (a)-(b) the load $R_{L,eq}$ and (c)-(d) the magnetic coupling k as parameter. Surface plots of the voltage gain with (e) the load $R_{L,eq}$ and (f) the magnetic coupling k as parameter.

$$\underline{Z}_{\text{in}} = \frac{\omega_0^2 M^2}{R_{\text{L,eq}}}, \quad (2.14)$$

which is purely real, independently of the magnetic coupling or the load.

Figs. 2.7(a)-(d) show the resulting dependency of the voltage gain $|\underline{G}| = |u_2/u_1|$ and the phase angle of the input impedance $\arg[\underline{Z}_{\text{in}}]$ on the equivalent load resistance $R_{\text{L,eq}}$ and the magnetic coupling k for the parameters of the scaled 5 kW IPT system presented in Chapter 3. As shown in **Fig. 2.7(b)** the resonant frequency is constant, independently of the equivalent load resistance $R_{\text{L,eq}}$. Similar characteristics are observed for a variation of the magnetic coupling k in **Fig. 2.7(d)**. Hence, with the series-series resonant compensation, the resonant frequency does not change in function of the relative coil positioning or the load, which is a principal advantage over other compensation methods.

2.2.2 Pole-Splitting (or Bifurcation)

It is interesting to note that for certain parameter values, the phase angle of the input impedance shown in **Fig. 2.7(b)** or **(d)** has three instead of just one zero crossing. For the same parameters, the voltage gain $|\underline{G}|$ shows two peaks instead of just one peak. This effect is termed pole-splitting or bifurcation in literature [51–53].

For the series-series compensated IPT system discussed here, a pole-splitting occurs if [51, 54]

$$k > \frac{R_{\text{L,eq}}}{\omega_0 L_2} \quad (2.15)$$

As soon as the two initially weakly coupled resonant circuits formed by L_1, C_1 and L_2, C_2 become coupled more strongly, the resonant circuits start interacting with each other and the two poles separate. This reminds of a similar effect that is known from two-stage Electromagnetic Compatibility (EMC) filters that consist of two cascaded second-order LC -circuits. Each stage on its own shows a single peak at the resonant frequency given by the values L and C , whereas the cascaded filter, which corresponds to two strongly coupled resonant circuits, exhibits two peaks. One peak is shifted slightly below and the second peak appears above the resonant frequency of the single stage. The same holds true for the pole-splitting in the IPT resonant circuit. At the point where the condition (2.15) is fulfilled, either by a decreasing

equivalent load resistance $R_{L,\text{eq}}$ (increasing output power P_2) or by an increasing magnetic coupling k , the voltage gain exhibits two peaks that are located above and below the resonant frequency $f_0 = 100$ kHz (cf. **Figs. 2.7(e)-(d)**).

The pole-splitting is discussed further in Section 2.3, where the conditions for soft-switching of the full-bridge inverter are derived. Because the condition (2.15) coincides with the design rules for the IPT coil self inductances derived in the next section, design adaptations are needed to ensure an inductive transmitter current and ZVS of the inverter stage.

2.2.3 Efficiency Limit of the Resonant Circuit

In the following, the efficiency limit of the series-series compensated IPT system is derived. For a simplified calculation, the notation used in [55, 56] is introduced. Using the definition in [57], the transmitter and receiver coil quality factors are given as

$$Q_i = 2\pi \frac{W_{Li}}{P_{\text{loss},i}/f_0} \approx \frac{\omega_0 L_i}{R_{i,\text{AC}}}, \quad (2.16)$$

where $i = 1, 2$ stands for the transmitter the receiver coil, respectively. W_{Li} represents the peak energy stored in the inductor L_i , and $P_{\text{loss},i}$ is the corresponding average power loss. The given approximation is valid under the assumption that the losses in the core material of the IPT coils are small compared to the copper losses. Under this condition, the power loss in the IPT coils can be modeled by the parasitic AC resistances $R_{i,\text{AC}}$ connected in series to the self-inductance of each coil (cf. **Fig. 2.8(a)**). It will become clear in later parts of this thesis that this simplification is valid for the presented IPT designs.

For the series-series compensation method discussed above, the capacitance values are given by

$$C_1 = \frac{1}{\omega_0^2 L_1} \quad \text{and} \quad C_2 = \frac{1}{\omega_0^2 L_2} \quad (2.17)$$

Using these values, the total loss factor is given by

$$\lambda = \frac{P_{\text{loss}}}{P_2} = \frac{1}{\gamma Q_1 k^2} \left(\gamma + \frac{1}{Q_2} \right)^2 + \frac{1}{\gamma Q_2}, \quad (2.18)$$

where the load factor γ was introduced for the ratio

2.2. Transition to an Inductive Power Transfer (IPT) System

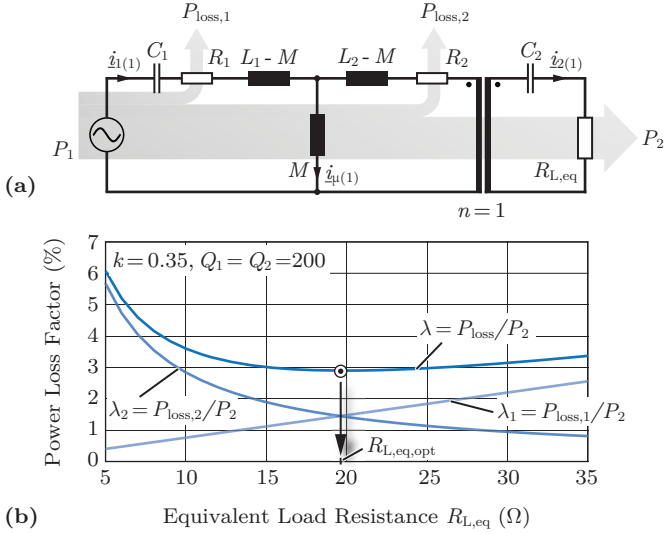


Fig. 2.8: (a) Equivalent circuit for the efficiency calculation. (b) Power loss factors as a function of the equivalent load resistance $R_{L,eq}$.

$$\gamma = \frac{R_{L,eq}}{\omega_0 L_2} \quad (2.19)$$

The total loss factor λ as given in (2.18) depends only on the magnetic coupling k , the two quality factors Q_1, Q_2 and the load factor γ .

The total loss factor λ is shown in **Fig. 2.8(b)** in function of the equivalent load resistance $R_{L,eq}$ for assumed quality factors $Q_1 = Q_2 = 200$, a magnetic coupling $k = 0.35$, and with the values of the 5 kW IPT system described in Chapter 3 for the remaining parameters. The total loss factor has a minimum where the two separate loss factors λ_1, λ_2 of the IPT coils are equal. At the minimum of the total loss factor λ , the optimum load factor is found as

$$\gamma_{opt} = \frac{1}{Q_2} \sqrt{1 + k^2 Q_1 Q_2} \quad (2.20)$$

Inserting the result into (2.18) and solving for the transmission efficiency η yields [17, 55, 56]

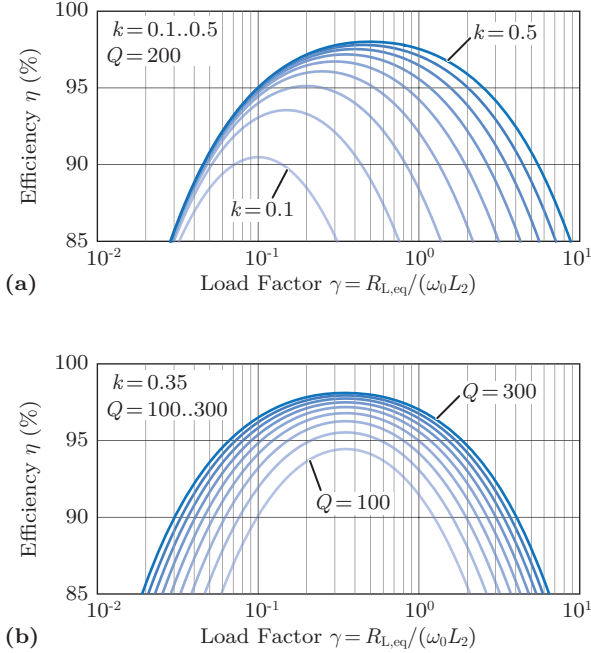


Fig. 2.9: Transmission efficiency η of a series-series resonant compensated IPT system as a function of the load factor γ and the parameters (a) magnetic coupling ($k = 0.1, \dots, 0.5$) and (b) quality factor ($Q = 100 \dots 300$).

$$\eta_{\max} = \frac{k^2 Q^2}{\left(1 + \sqrt{1 + k^2 Q^2}\right)^2} \approx 1 - \frac{2}{kQ}, \quad (2.21)$$

where the quality factor $Q = \sqrt{Q_1 Q_2}$ is introduced for the geometric mean of the individual quality factors.

From (2.21), it becomes apparent that the maximum efficiency of an IPT system is limited by the product of the magnetic coupling k and the quality factor Q . Therefore, the product

$$FOM = kQ \quad (2.22)$$

is termed the Figure-of-Merit (FOM) of IPT systems [55, 56].

As an illustration of the effects of the different variables, **Fig. 2.9** shows the transmission efficiency η as a function of the load factor γ with the magnetic coupling k and the quality factor Q as parameters. It is interesting to note that the load factor γ where the maximum of the transmission efficiency occurs depends on the magnetic coupling k , but not on the quality factor Q . This property becomes important for the design rules for the IPT coil self-inductances given below.

The *FOM* clearly shows that two methods exist for improving the transmission efficiency of an IPT system:

► **Maximization of the Magnetic Coupling:**

Improving the magnetic coupling k is possible by an optimization of the coil geometry. Particularly, the ratio of the coil size compared to the width of the air gap determines how well the transmitter coil and the receiver coil are coupled. Additional practical measures may include systems that ensure the correct positioning of the two coils with respect to each other. For an EV charging system, this can be achieved using modern automated vehicle parking systems or a detection mechanism that instructs the driver how to park the vehicle for an optimum efficiency of the power transfer [58].

► **Maximization of the Quality Factor:**

The quality factors $Q_i \approx \omega_0 L_i / R_{i,AC}$ can to some extent be optimized by increasing the transmission frequency. This approach is pursued by what is often termed *magnetic resonant* or *highly resonant wireless power transfer* (as opposed to *inductive* power transfer) in recent publications [59]. In this approach, often coils without external compensation are used at their self-resonant frequency. The main benefit is that due to very high quality factors, the magnetic coupling, i. e., the coil positioning, becomes less important and a higher freedom of position is achieved. As a drawback, typically comparably high operating frequency is needed.

A similar calculation can be made also for series-parallel compensated IPT systems. In [17, 56, 60], it is shown that the result for the maximum transmission efficiency η_{\max} is identical for series-series compensated and for series-parallel compensated IPT system. The *FOM* is therefore valid for both resonant compensation methods.

2.2.4 Design Rules for Series-Series Compensation

It was shown above, that the transmission efficiency of the series-series compensated IPT system is limited to the maximum value η_{\max} as given by (2.21). The maximum transmission efficiency η_{\max} is reached for a design if the load factor γ fulfills (2.20). Using the assumption of large quality factors¹ for the transmitter and the receiver coils, (2.20) simplifies to

$$\gamma_{\text{opt}} = \left(\frac{R_{L,\text{eq}}}{\omega_0 L_2} \right)_{\text{opt}} \approx k \quad (2.23)$$

The equivalent load resistance as defined in (2.10) is a fixed parameter that depends on the specifications for the output power P_2 and the receiver-side DC-link voltage $U_{2,\text{DC}}$. If the switching frequency of the inverter is also fixed, the condition (2.23) must be fulfilled by designing the receiver self-inductance such that

$$L_2 \approx L_{2,\text{opt}} = \frac{R_{L,\text{eq}}}{\omega_0 k} \quad (2.24)$$

The transmitter self-inductance L_1 is designed to obtain the desired voltage transfer ratio at the resonant frequency

$$|\underline{G}(f_0)| = \frac{U_{2,\text{DC}}}{U_{1,\text{DC}}} = \frac{R_{L,\text{eq}}}{\omega_0 M} = \frac{\gamma}{k} \sqrt{\frac{L_2}{L_1}} \quad (2.25)$$

Using the approximation $\gamma_{\text{opt}} \approx k$ from (2.23), this result can be simplified to the condition

$$\frac{U_{2,\text{DC}}}{U_{1,\text{DC}}} \approx \sqrt{\frac{L_2}{L_1}}, \quad (2.26)$$

from which the design equation for L_1 follows as [56]

$$L_1 = L_{1,\text{opt}} = L_{2,\text{opt}} \cdot \left(\frac{U_{1,\text{DC}}}{U_{2,\text{DC}}} \right)^2 \quad (2.27)$$

With this design, the transmission efficiency η at the output power P_2 , the frequency f_0 , and DC-link voltages $U_{1,\text{DC}}, U_{2,\text{DC}}$ is equal to the physical efficiency limit η_{\max} of the resonant circuit.

¹For typical values, the assumption holds starting from $Q \approx 100$.

Comparing the design rule (2.24) for the receiver self-inductance to the pole-splitting condition given by (2.15) reveals that an efficiency optimal design of the IPT resonant circuit is achieved exactly at the limit to a pole-splitting [51, 54]. It is discussed in detail in Section 2.3 that the small or even negative phase angle above the resonant frequency that results in the case of a pole-splitting can lead to hard-switching of the transmitter-side full-bridge inverter. Hence, in a practical design it is beneficial to avoid a pole-splitting by adapting the design rules.

In order to avoid the pole-splitting, the receiver self-inductance L_2 is selected smaller than the optimal value obtained from (2.24) by a margin of approximately $m_{\text{ps}} \approx 15\text{-}25\%$

$$L_2 \approx (1 - m_{\text{ps}}) \cdot L_{2,\text{opt}} \quad (2.28)$$

It follows from (2.25), that for keeping the voltage gain at the resonant frequency equal to $|G(f_0)| = U_{2,\text{DC}}/U_{2,\text{DC}}$ the inverse modification

$$L_1 = \frac{L_{1,\text{opt}}}{(1 - m_{\text{ps}})} \quad (2.29)$$

must be applied to the transmitter self-inductance L_1 . In this way, the mutual inductance $M = k\sqrt{L_1 L_2}$ and therefore the voltage gain remains unchanged.

As shown in [61], the efficiency reduction that results from this adaptation is small, because the maxima of the transmission efficiency in **Fig. 2.9** are relatively flat. The compromise is acceptable, because of the lower switching losses and the more compact design of the power electronics that are possible if load-independent ZVS of the full-bridge inverter is ensured.

It must be noted that during the initial phase of a design process the magnetic coupling k is not known and the above equations can only be evaluated using values that are exemplary for the investigated coil arrangement. Later on, these equations can be used in an iterative optimization algorithm in combination with, e. g., analytical inductance calculation methods or FEM simulations.

2.2.5 Alternative Compensation Topologies

Apart from the series-series compensation topology discussed above, also other topologies are used for the resonant compensation of the

IPT coils [17]. An often used alternative topology results if the receiver-side compensation capacitor is connected in parallel to the receiver coil instead of in series.

The main advantage of a parallel compensation of the receiver is the lower voltage across the resonant elements L_2 and C_2 , which reduces insulation requirements and leads to a lower electric stray field [62]. A disadvantage of this topology is the circulating reactive current in the receiver-side parallel resonant circuit. The circulating current shows only little dependency on the loading of the IPT system. Due to the additional losses that result in the receiver coil and the resonant capacitor, the transmission efficiency is reduced in partial load situations. Depending on the turns numbers, the higher current in the receiver coil also increases the magnetic stray field. Furthermore, without additional measures, the resonant frequency of a parallel compensated IPT systems depends on the load or on the magnetic coupling. This complicates the control and might lead to hard-switching of the full-bridge inverter for certain load cases or coil positions.

A parallel compensation of the transmitter coil is also possible [52, 53], but requires an additional inductor connected in series between the resonant circuit and the power converter to achieve soft-switching of the full-bridge inverter. This topology is mainly useful for contactless power distribution networks, where a constant current is controlled in a power track that supplies multiple receivers. This has been used in the mining industry [63] or at industrial sites [14, 64, 65]. In these applications, IPT systems were originally implemented to eliminate the carbon brushes used in the power supply of transportation carts and conveyor vehicles. For a system with only one receiver, the power losses in the additional inductor, which must carry the full load current, can be avoided by using a series compensation of the transmitter coil [56].

For the work presented in this thesis, a series-series compensation of the IPT system is chosen mainly for the higher transmission efficiency during partial load conditions and for the load- and magnetic coupling-independent resonant frequency. Nevertheless, the presented multi-objective IPT design procedure could also be applied to a system with a different compensation topology with only minor adaptations.

2.3 Efficiency Optimal System Operation

After the analysis of the design conditions for a high transmission efficiency of the IPT system, in this section the discussion is extended to include the power electronics. In the first part, the conditions for ZVS of the full-bridge inverter are reviewed. Afterwards, an efficiency-optimal control of the transferred power is proposed and compared to existing control schemes.

2.3.1 Zero Voltage Switching of the MOSFET Full-Bridge Inverter

Despite the rapid development of wide band gap semiconductors in recent years, a large share of the power losses in a hard-switched power electronic converter are still attributed to switching losses. Therefore, soft-switching is crucial for the full-bridge inverter supplying the transmitter coil for achieving a high system efficiency. In order to reduce the switching losses of power MOSFETs, typically ZVS techniques are applied. A fundamental requirement for ZVS of a MOSFET half-bridge is a sufficiently high impressed current at the switch node. This is commonly realized with an inductive element such as the leakage inductance of a transformer. In the case of the IPT system, inductive input characteristics can be achieved by an over-compensation of the resonant circuit as discussed above (cf. **Fig. 2.4**).

The converter topology of the series-series compensated IPT system is repeated in **Fig. 2.10(a)** for the discussion of a ZVS transition of the highlighted half-bridge A. For the analysis, the switching frequency is assumed to be selected above the resonant frequency in the inductive region of the input impedance Z_{in} of the IPT system. In **Fig. 2.10(b)**, the approximately sinusoidal transmitter coil current i_1 flowing out of the switch node of half-bridge A is shown. At the time $t = t_0$, the full-bridge switches the output voltage u_1 from positive to negative polarity. Due to the inductive phase angle φ of the output current i_1 with respect to u_1 , the current is still positive at the time of the transition.

Figs. 2.10(c)-(f) show the current commutation in half-bridge A of the full-bridge inverter during the ZVS transition. The current i_1 initially flows through the switch T_1 and is commutated to switch T_2 during the discussed switching transition. As the gate voltage $u_{\text{GS},1}$ is removed from switch T_1 to initiate the switching transition, the im-

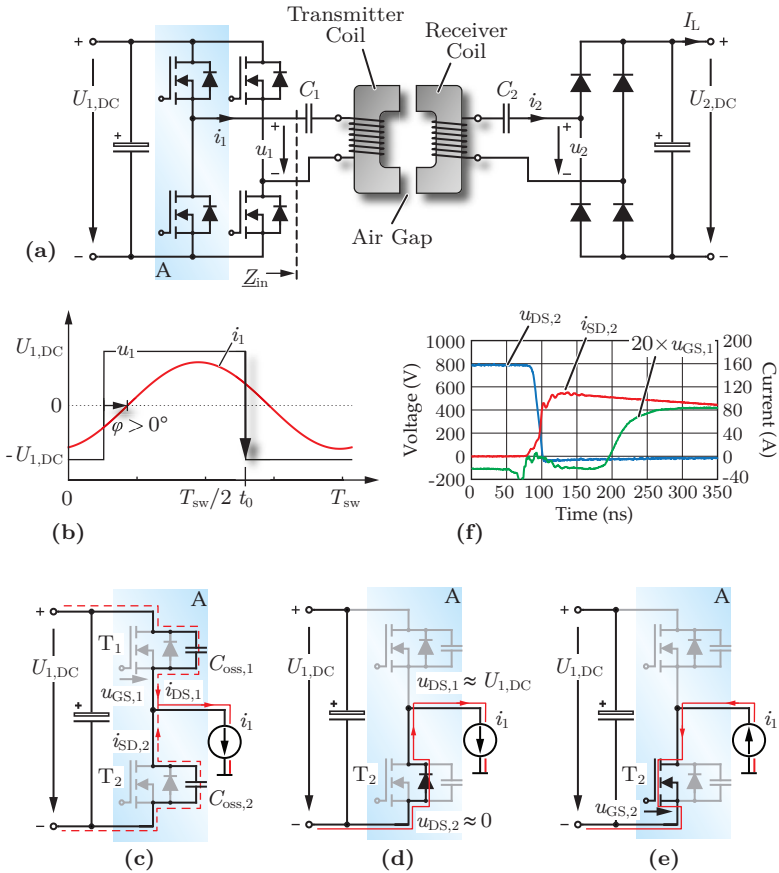


Fig. 2.10: (a) Series-series compensated IPT converter topology. (b) Schematic waveforms of the full-bridge inverter output voltage u_1 and the transmitter current i_1 . (c)-(d) Current paths during a ZVS transition of half-bridges A. (e) Measured gate-to-source voltage u_{GS} , drain-to-source voltage u_{DS} , and source-to-drain current i_{SD} during a ZVS transition of a SiC MOSFET half-bridge of the power electronic converter presented in Chapter 5.

pressed output current i_1 starts to charge the output capacitance $C_{\text{oss},1}$ of T_1 from initially approximately 0 V to $U_{1,\text{DC}}$ and to discharge the capacitance $C_{\text{oss},2}$ of T_2 from $U_{1,\text{DC}}$ to approximately 0 V.

During the ZVS transition, the charge that is needed to charge $C_{\text{oss},1}$ and to discharge $C_{\text{oss},2}$ must be supplied by the load current i_1 . Because the bridge-legs are operated with 50% duty cycle and 180° phase shift, both bridge-legs are switched at the same time. Hence, the required charge is equal to twice the charge Q_{oss} stored in the output capacitance C_{oss} of the MOSFET at $U_{1,\text{DC}}$. Since the capacitance characteristics of the MOSFET are non-linear, the required charge Q_{oss} must be calculated by integration [66, 67]

$$Q_{\text{oss}}(U_{1,\text{DC}}) = \int_0^{U_{1,\text{DC}}} C_{\text{oss}}(u) du \quad (2.30)$$

If the capacitance $C_{\text{oss},2}$ is fully discharged while the current i_1 is still positive, the current transitions to the body-diode of switch T_2 and the transition of the output voltage u_1 is completed (cf. **Fig. 2.10(d)**). As soon as the body-diode of T_2 is conducting the load current, the switch can be turned on with zero voltage across the channel and consequently without significant switching losses. After a positive gate-to-source voltage $u_{\text{GS},2}$ is applied, the channel T_2 takes over the current from the body-diode as shown in **Fig. 2.10(e)**.

A ZVS transition measured in a SiC MOSFET² half-bridge of the power converter presented in Chapter 5 is shown in **Fig. 2.10(f)**. The waveforms show that the drain-to-source voltage $u_{\text{DS},2}$ of switch T_2 has fully completed the transition from $U_{1,\text{DC}} = 800$ V to 0 V and the source-to-drain current $i_{\text{SD},2}$ rises before the gate voltage $u_{\text{GS},2}$ is applied. Since the MOSFET body-diode is already conducting the load current when the gate voltage is applied, this ZVS transition results in almost zero switching losses.

In practice, ZVS can still cause losses if the current supplied by the gate driver of the switch that is turning off (T_1 in the above example) is not sufficient to cut off the inversion layer in the MOSFET channel before the drain-to-source voltage $u_{\text{DS},1}$ rises. In this case, an overlap of current and voltage occurs in the channel, which causes switching losses. Additionally, there are ohmic losses during the charging/discharging process of the output capacitances, which in practice lead to dissipation

²Cree SiC MOSFET C2M0080120D, 1.2 kV/80 mΩ.

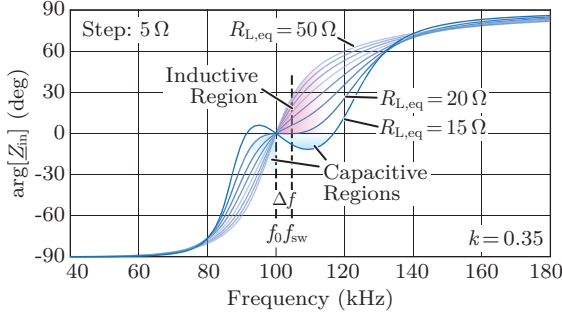


Fig. 2.11: Phase angle of the input impedance Z_{in} of the resonant circuit as seen by the full-bridge inverter for the parameters of the scaled 5 kW IPT system presented in Chapter 3. Switching in the inductive region leads to ZVS of the full-bridge, while in the capacitive regions hard-switching occurs.

of a part of the energy stored in the output capacitance of the switch [67].

2.3.2 ZVS Conditions for the IPT System

As shown in the above discussion, the condition for a ZVS transition is an inductive output current that is able to supply a sufficient amount of charge ($\geq 2 \cdot Q_{\text{oss}}$) to charge and discharge the drain-to-source capacitances of all switches involved in the transition.

Using the fundamental frequency model, the phase difference φ between the fundamental components of the inverter output voltage $\underline{u}_{1(1)}$ at the AC terminals of the full-bridge and the transmitter coil current $\underline{i}_{1(1)}$ is given by

$$\varphi = \arg[\underline{u}_{1(1)}] - \arg[\underline{i}_{1(1)}] = \arg[\underline{Z}_{\text{in}}], \quad (2.31)$$

In **Fig. 2.11**, the previously shown dependency of the phase angle of the input impedance Z_{in} of the resonant circuit on the frequency and on the equivalent load resistance $R_{L,\text{eq}}$ is repeated. Given (2.31), an inductive current results at the inverter output terminals for a positive phase angle of the input impedance Z_{in} . This is achieved by selecting a switching frequency $f_{\text{sw}} = f_0 + \Delta f$ above the resonant frequency $f_0 = 100$ kHz as indicated in the figure.

As described in Section 2.2, a pole-splitting can occur due to an over-loading of the resonant circuit (low $R_{L,\text{eq}}$) or if the magnetic coupling is higher than anticipated. Then, the phase angle of the input impedance $\underline{Z}_{\text{in}}$ becomes capacitive in the region above the resonant frequency that is marked in **Fig. 2.11**. If the switching frequency f_{sw} lies in that region, the current at the full-bridge inverter output is no longer inductive and ZVS is lost.

In order to avoid hard-switching of the full-bridge inverter, the pole-splitting can be prevented in the design. This requires a maximum value of the magnetic coupling k_{max} , which can be obtained from a calculation at the minimum separation between the transmitter coil and the receiver coil. In addition, the load conditions that lead to the minimum of the equivalent load resistance (maximum output power) must be considered. Then, the efficiency optimal design conditions (2.24)-(2.27) must be adapted such that the condition (2.15) for pole-splitting is not fulfilled. In practice, this requires introducing a margin of approximately $m_{\text{ps}} \approx 15 - 25\%$ to the design rules, which results in the modified design rules (2.28)-(2.29). The slight loss increase in the resonant circuit is outweighed by the advantage of load-independent ZVS of the full-bridge inverter, because the maximum of the transmission efficiency is relatively flat.

The frequency separation Δf between the switching frequency and the resonant frequency is iteratively determined for the operation at maximum load (minimum $R_{L,\text{eq}}$), where the phase angle φ is smallest. For these calculations, the exact waveform of the transmitter coil current i_1 and the characteristics of the non-linear output capacitance of the used MOSFET device are needed. A detailed model for this calculation can be found in [68], where a similar series-series compensated IPT system is used as power supply of an artificial heart implant.

2.3.3 Synchronous Rectification at the Receiver

In **Fig. 2.10(a)**, a diode bridge is shown for the receiver-side rectifier. Due to the approximately sinusoidal shape of the receiver coil current i_2 , the diodes are switched at zero current, which leads to low switching losses on the receiver-side³.

In order to achieve a further reduction of the power semiconductor

³The losses due to the diode reverse-recovery are small due to the slow di/dt during the switching transition and are therefore not discussed further.

losses, active rectification with switches instead of diodes in the rectifier can be used to lower the on-state conduction losses of the devices. For the 50 kW IPT charger designed in the later chapters of this thesis, SiC MOSFETs are used for the receiver-side rectifier. The high forward voltage drop of the SiC body-diode makes an active solution particularly important. Therefore, synchronous rectification is implemented in the IPT demonstrator system using a current transformer and a detection circuit of the zero crossings of the receiver coil current. A controller implemented in a Field-Programmable Gate Array (FPGA) is used to turn on the MOSFETs of the rectifier as soon as a current is detected in the respective body-diode. More details regarding the synchronous rectification are given in Section 5.4.3.

2.3.4 Maximum Efficiency Control Concept

After the discussion of the efficiency optimal design of the IPT resonant circuit and the operation of the power electronics with lowest losses, also an efficient control concept is needed. A particular challenge for the IPT system is to reach a high efficiency not only at maximum output power, but also at light load conditions. In addition, the positioning of the IPT coils affects the transfer characteristics of the resonant circuit, which poses another challenge for the control system. Therefore, the last part of this chapter is concerned with a control scheme for the IPT system that is optimized for a high partial load efficiency and insensitivity to coil misalignment.

To clarify the degrees-of-freedom available for the control, **Fig. 2.12** shows the complete power conversion chain from the three-phase mains to the high-voltage battery of the EV. The mains interface with active Power Factor Correction (PFC) controls the DC link voltage $U_{1,DC}$ that is supplied to the inverter stage of the transmitter. PFC converters with boost capability are the most common type in industry, but also solutions with buck and buck+boost capabilities are known in literature [37, 69]. On the vehicle, a rectifier and a DC-DC converter are used to regulate the charging current. Since at the resonant frequency, the IPT resonant circuit acts as a current source, supplying a constant current

$$\underline{i}_{2(1)} = j \frac{u_{1(1)}}{\omega_0 M} \quad (2.32)$$

to the equivalent load resistance $R_{L,eq}$, the receiver-side DC-link voltage can be externally impressed by the DC-DC converter.

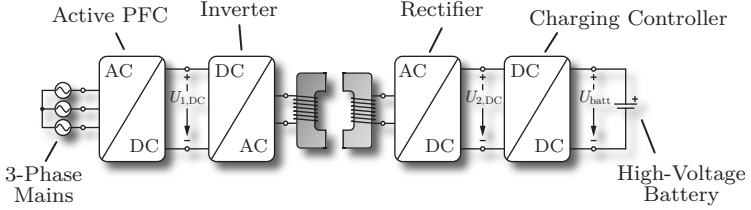


Fig. 2.12: Complete power conversion chain of a high-power IPT system supplying a EV battery from the 3-phase mains.

If all power losses in the system are neglected and ideal components are assumed, the output power P_2 is given by

$$P_2 = \frac{1}{2} R_{L,\text{eq}} |i_{2(1)}|^2 \quad (2.33)$$

Based on the definition of the equivalent load resistance $R_{L,\text{eq}}$ in (2.10), this can be rearranged to

$$P_2 = \frac{8}{\pi^2} \frac{U_{1,\text{DC}} U_{2,\text{DC}}}{\omega_0 M}, \quad (2.34)$$

which constitutes the basis of the efficiency optimal control scheme proposed in the following [61].

In the considered power circuit topology, both DC link voltages $U_{1,\text{DC}}$ and $U_{2,\text{DC}}$ of the IPT system are externally impressed⁴. Therefore, the power transfer of the IPT system can be controlled based on (2.34) by adjusting one or both of the DC link voltages. This allows operating the resonant circuit constantly under optimum conditions, while the full-bridge inverter at the transmitter-side as well as the receiver-side rectifier still achieve soft-switching.

An intuitive choice is to adjust the two DC link voltages proportionally⁵ $U_{1,\text{DC}} \propto U_{2,\text{DC}}$ [33, 61, 70]. Then, according to (2.34), the output power is proportional to the DC link voltage squared $P_2 \propto U_{2,\text{DC}}^2$. This means that according to (2.10) the equivalent load resistance $R_{L,\text{eq}} \propto U_{2,\text{DC}}^2 / P_2$ remains constant for all load conditions. Therefore, also the load factor $\gamma = R_{L,\text{eq}} / (\omega_0 L_2) \approx k$ remains unchanged during

⁴If the receiver-side rectifier is connected directly to the battery without DC-DC converter, $U_{2,\text{DC}}$ in (2.34) is replaced by U_{batt} , because then the voltage is impressed by the battery itself.

⁵Because the voltages are externally impressed, also different choices are possible.

operation. Hence, the transmission efficiency is constantly maintained at the maximum for all load conditions.

However, if the IPT coils are not positioned as initially anticipated and the actual magnetic coupling k' during operation is lower than the magnetic coupling k for which the receiver self-inductance L_2 was designed, the maximum efficiency condition (2.23) is violated as $\gamma \neq k'$. The goal of the presented optimal control scheme is therefore to restore maximum efficiency conditions by adjusting the load factor γ to the optimum value k' in the misaligned position. This can be implemented with a control that acts on the DC-link voltage $U_{1,DC}$ and $U_{2,DC}$.

In a first step the control adapts the receiver-side DC-link voltage $U_{2,DC}$ according to the reference value

$$U_{2,DC}^* = \sqrt{\frac{\pi^2}{8} k' \omega_0 L_2 P_2^*}, \quad (2.35)$$

where P_2^* denotes the controller reference value for the output power, and k' stands for a measurement or an estimate of the magnetic coupling in the misaligned position. This adjustment ensures an optimal load factor for all load conditions despite IPT coil misalignment, i. e., for all values of the magnetic coupling k' and the output power P_2^* .

In a second step, the output power P_2 must be controlled to the reference value P_2^* . For this purpose, the control adjusts the transmitter-side DC link voltage $U_{1,DC}$. The reference value

$$U_{1,DC}^* = \sqrt{\frac{L_1}{L_2}} \cdot U_{2,DC}^* \quad (2.36)$$

follows from the voltage gain at resonance (2.25). Due to the neglected power losses and the parameter uncertainties in the system, this value is not exact in practice. However, it can serve as a feedforward for improving the control dynamics.

Depending on the ratio of the battery voltage U_{batt} and the expected values for $U_{2,DC}^*$, boost or buck+boost functionality is required for the receiver-side DC-DC converter. Additionally, the transmitter-side power electronics require buck capability in order to provide the requested DC link voltage $U_{1,DC}$ at reduced coupling or during light load conditions. The control functionality could be directly obtained from a buck-type mains interface [37, 71]. Alternatively, a conventional boost-type PFC rectifier with a series-connected DC-DC converter could be used for the power electronics of the transmitter.

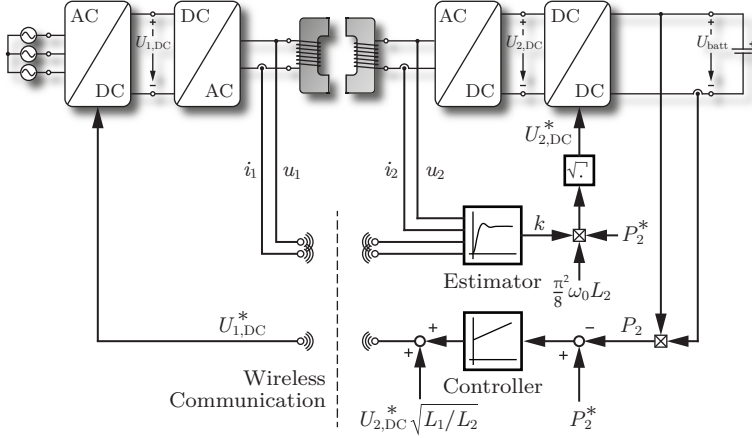


Fig. 2.13: Block diagram of the proposed efficiency optimal control.

In order to calculate the reference value $U_{2,DC}^*$ in (2.35), a measurement or an estimation of the magnetic coupling k' of the IPT coils is needed. A measurement of the magnetic coupling could be realized using a defined sequence of test pulses that are applied to the resonant circuit before the power transfer is initiated. For estimating the magnetic coupling, current and voltage measurements could be implemented at both sides of the resonant circuit. From the current and voltage information and the known impedances of the resonant circuit, the magnetic coupling can be estimated during operation. Alternatively, the ratio of the IPT coil current RMS values could be used as an indicator. During operation, the DC voltages could be iteratively adapted until the pre-calculated optimum ratio of the RMS currents for minimum total losses is found.

In **Fig. 2.13**, a possible realization of a feedback controller using the proposed efficiency optimal control scheme is shown. The key parts of the control are implemented on the receiver-side, which is able to closely monitor and if necessary protect the battery. The necessary communication consists of the measurements for the estimation of the magnetic coupling and the transmission of the reference value $U_{1,DC}^*$.

The proposed control scheme allows operating the IPT system, the *weakest link* of the power conversion chain, constantly at its natural efficiency optimum. The control functionality is moved to the power

electronics at the transmitter and the receiver side, where the required features can be realized in an efficient manner. In this way, the power losses in the IPT coils and in the resonant capacitors are reduced and partly shifted to power electronic components. Particularly at light load conditions, this brings an efficiency advantage [61].

A disadvantage is the additional complexity of the power electronics. Alternative control methods with a lower complexity are discussed in the following.

2.3.5 Comparison to Alternative Control Methods

Several alternative control methods that are known for conventional resonant converters can also be applied to IPT systems. If the DC link voltages are not available for the control, two degrees-of-freedom remain for the control of the power transmission:

► **Inverter- and Rectifier-Stage Duty Cycles:**

In the presented discussion, operation with a constant 50% duty cycle was assumed for the full-bridge inverter at the transmitter. Furthermore, a passive diode rectifier was considered for the receiver. However, the duty cycles of the inverter-stage and of an active receiver-side rectifier can also be used to control the fundamental amplitudes $\hat{U}_{1,(1)}$ and $\hat{U}_{2,(1)}$ that are applied to the resonant circuit [36]. With this approach, the complexity of the power electronics is significantly reduced, because the control principles discussed above can be applied via the duty cycles instead of via controllable DC link voltages. Therefore, the DC-DC converter on the receiver side is not needed and no buck capability of the mains interface is required. As a restriction, the maximum voltage that can be applied to the receiver-side terminals is limited by the battery voltage, which varies with the state of charge of the battery among other factors [72, 73]. For low battery voltages and high charging power levels, the higher current in the receiver coil is a potential disadvantage of such a design. However, the key advantage of the decoupling of the IPT system from the battery voltage is preserved and the resonant circuit can be operated constantly in the efficiency optimum [36]. The drawback that results from the complexity reduction is switching losses in the power electronics of the transmitter and the receiver. Particularly if operation at a transmission frequency of 85 kHz as proposed by

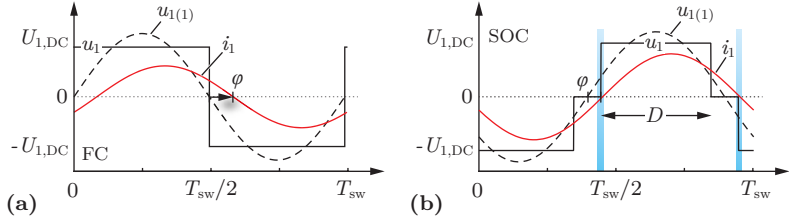


Fig. 2.14: Schematic waveforms for (a) the FC and (b) the SOC methods.

the upcoming IPT standard SAE J2954 [43] is targeted, the additional switching losses could have a high impact on the overall system performance. For this reason, the additional hardware effort is accepted in this work, but addressed with a power electronic converter design with high efficiency and high compactness thanks to the use of wide band gap power semiconductors and optimized magnetic components for the DC-DC conversion-stage (cf. Chapter 5).

► **Inverter-Stage Switching Frequency:**

The switching frequency of the full-bridge inverter can be used to control the power transfer. If the switching frequency is shifted further away from the resonant frequency into the inductive region of the input impedance (cf. **Fig. 2.11**), the transmitted output power is reduced. A schematic waveform for this control method is shown in **Fig. 2.14(a)**. Because of its simplicity, the Frequency Control (FC) is a common method of controlling the power flow in IPT systems [74, 75]. However, it has the disadvantage of an increased circulating reactive power that results from the frequency detuning. It is shown below, that this implies an almost load-independent transmitter coil current and therefore a reduced efficiency in partial load conditions.

► **Combined Duty Cycle and Frequency Control:**

As a third option, the duty cycle and the switching frequency can be controlled simultaneously. Such a control scheme is known in literature as Self-Oscillating Control (SOC) [76, 77] or dual control [78–80]. A current measurement and a controller are used to synchronize the gate signals of the full-bridge inverter to the zero crossings of the transmitter coil current. A schematic wave-

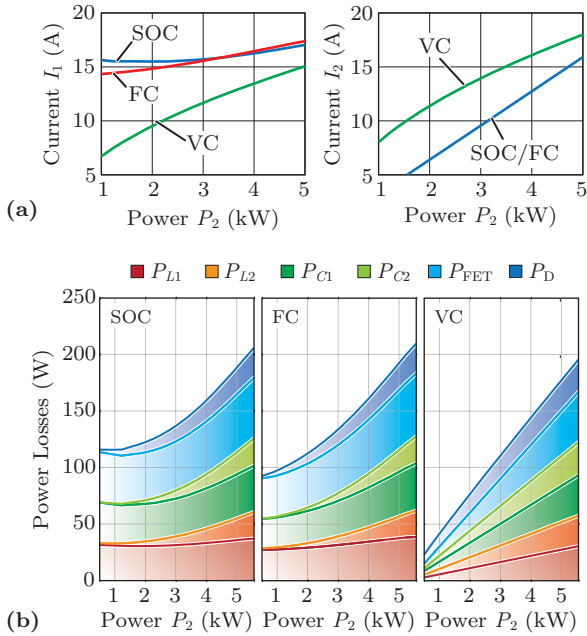


Fig. 2.15: (a) Calculated RMS currents in the IPT coils and (b) calculated power losses for the SOC, FC, and voltage control (VC) methods for the parameters of the scaled 5 kW IPT system presented in Chapter 3.

form for this method is shown in **Fig. 2.14(b)**. Starting from a free-wheeling state and a negative transmitter coil current i_1 , the inverter output voltage u_1 is switched to positive polarity at the zero crossing of i_1 . This results in a ZCS transition. To achieve ZVS, the favorable option for MOSFET devices, a counter in the controller can be used to predict the next zero crossing and to initiate the switching transition shortly before the zero crossing occurs. After the transition, the output voltage is maintained at positive polarity for the time given by the duty cycle D , or as soon as the next zero crossing of the transmitter current occurs. The second switching action is a ZVS transition to a free-wheeling state with $u_1 \approx 0$. After the detection of the next zero crossing, the switching cycle is repeated with inverse polarity.

In [61], the FC, SOC, and DC-link voltage control (VC) schemes

are compared for the 5 kW IPT system described in Chapter 3. The calculated RMS current in the transmitter coil I_1 and in the receiver coil I_2 are shown in **Fig. 2.15(a)**, respectively. For the SOC and the FC methods, the RMS value of the current in the transmitter coil remains almost constant, while the current in the receiver coil is reduced. Consequently, the power losses in the transmitter coil are also almost constant at reduced output power. This is a result of the increased reactive power that has to be supplied to the resonant circuit with the FC and SOC methods. They require operation further above from the resonant frequency, where the circuit becomes more and more inductive. As described above, the VC method is able to operate at a fixed switching frequency and constantly at the efficiency optimum of the resonant circuit. The (close to) ohmic input characteristics are always maintained, independent of the load. For this reason, the currents in the IPT coils are reduced linearly with the output power. For the VC method, the current in the receiver coil is slightly increased as a result of the decreasing receiver-side DC link voltage. This is needed to balance the power losses between the transmitter and the receiver coil, which according to the above discussion is fundamentally required to reach the power loss minimum.

The calculated power losses for the two control methods are shown in **Fig. 2.15(b)**. For the calculation of the power losses $P_{L1/2}$ in the coils, a FEM tool is used as described in Section 3.2.3 and [61, 81]. The losses in the resonant capacitors $P_{C1/2}$ are estimated based on the manufacturer data given in [82]. For the power losses of the MOSFETs of the inverter P_{FET} and of the receiver-side rectifier diodes P_{D} , conduction losses are calculated based on the manufacturer data sheet. Because of the ZVS operation, no switching losses are included. For the FC and the SOC methods, the losses in the transmitter coil P_{L1} , the transmitter-side resonant capacitor P_{C1} , and the transmitter-side power semiconductors P_{FET} are almost constant as the output power is reduced. This is a result of the ohmic losses due to the almost constant RMS current in the transmitter coil. This characteristic fundamentally impairs the efficiency of the system at light load for these methods. In contrast, the VC benefits from the linear decrease of the coil currents. The power losses decrease almost linearly as the output power is reduced. Hence, the efficiency characteristic is drastically improved at light load conditions.

2.4 Summary of the Chapter

In this chapter, the working principles of a contactless EV charger using IPT were derived from a conventional conductive EV charger known from literature. This approach was chosen to provide an easy-to-follow introduction into the concepts of IPT for readers who are not familiar with the subject. A thorough revision of the main operating principles and design challenges for the IPT coils as well as for the power electronics, and a critical discussion of the performance limits of this technology was presented. At the end of the chapter, an efficiency optimal control scheme was proposed and compared to other existing control methods.

The main results of this chapter are summarized as follows:

- ▶ Introduction of the transformer equivalent circuit and derivation of the fundamental frequency model that are used throughout the thesis as tools for a simplified analysis of the IPT system.
- ▶ Analysis of the series-series compensated resonant circuit including the derivation of the $FOM = kQ$ and the efficiency limit it imposes on IPT system.
- ▶ Design guidelines for maximum transmission efficiency between the IPT coils and minimum power losses in the power electronic converters on both sides of the air gap.
- ▶ Proposal of an efficiency optimal control method for IPT using the transmitter- and receiver-side DC link voltages for the control. The method allows constantly operating the IPT resonant circuit at its natural efficiency optimum, while the control functionality is shifted to the power electronics.

After providing an understanding of the fundamental principles, the next step is the derivation of calculation models that accurately quantify the performance of the main system components. Afterwards, the models can be used in a multi-objective IPT design procedure for the contactless EV charger.

3

Multi-Objective IPT Optimization Process

AUTOMOTIVE applications impose a number of constructive boundary conditions on the design of a contactless EV battery charger. If no additional mechanical positioning aids for the alignment of the coils are desired, the air gap is given by the construction of the vehicle and the layout of the charging station. The space for the receiver coil on the underfloor of the vehicle and the allowable weight of the components are typically limited. Therefore, a high power density of the converter systems and, particularly, a high area-related power density α of the IPT coils is required. Additionally, the transmission efficiency η should be as high as possible to simplify the thermal management of the systems. Another design constraint arises from the limitation of the magnetic stray field in the vicinity of the coils. In order to prevent health risks resulting from induced electric fields in human tissue, specifically in the brain and the retina, the stray field is limited by standards [38–40]. Due to the high power level of EV battery charging systems, this becomes a challenge in the system design.

As shown in Section 2.2.3, the Figure-of-Merit $FOM = kQ$ limits the maximum efficiency of the power transmission to approximately $\eta_{\max} \approx 1 - 2/(kQ)$, where k stands for the magnetic coupling of the transmission and the receiver coil and Q for the quality factor of the coils. Therefore, a high transmission efficiency can be achieved if large coils with a high magnetic coupling are used, but this implies a low power density. A higher power density can be achieved if smaller coils are used and instead the quality factor is increased, e. g., by means of a higher transmission frequency. However, only a reduced efficiency can

be reached despite the higher quality factor, because of increasing losses in the power electronics and in the core materials that are typically used for flux guidance [56]. Hence, the two performance indices efficiency η and area-related power density α are related in a trade-off that must be addressed in the optimization of the transmission coils for IPT systems, similar as with other power electronic systems [83].

The trade-off is best described by the η - α -Pareto front, which is a physical performance boundary given by the set of designs for which an increase of one of the performance indices η or α results in a decrease of the other. This set of designs is termed the Pareto-optimal designs. Even though a number of magnetic structures for IPT coils have been proposed in literature, no systematic way for optimizing the magnetic design of IPT coils under consideration of the trade-off between the multiple performance objectives has been presented so far. Therefore, this chapter provides the framework for a multi-objective IPT optimization process which allows finding the Pareto-optimal designs in a systematic manner.

For a validation of the multi-objective design approach, a scaled IPT system with 5 kW output power is optimized for the specifications given in Section 3.1. In Section 3.2, FEM-based models for calculating the power losses and the magnetic stray field of IPT coils as well as calculation methods for the power losses in the remaining system components are provided [56]. Based on these models, the multi-objective optimization process for IPT systems is presented in Section 3.3. Because the component models rely on FEM calculations of the magnetic field, a validation of the accuracy of these methods is required. Therefore, in Section 3.4 the design of a high-bandwidth, low-cost magnetic field probe is presented and used for an experimental verification of the FEM calculations. The experimental validation of the calculation models and the design process for the realized 5 kW hardware prototype is presented in Section 3.5.

3.1 Scaled IPT System Specifications

In this chapter, a scaled IPT system is designed to demonstrate and experimentally verify the multi-objective IPT optimization process. In order to simplify the practical realization of the optimized design, a lower power level is selected. The main specifications of the scaled IPT system are summarized in **Tab. 3.1**.

Tab. 3.1: Specifications of the scaled IPT prototype system.

Parameter	Variable	Value
Output Power	P_2	5000 W
Air Gap	δ	50 mm
Max. Coil Diameter	D_{\max}	300 mm
Transmitter-Side DC-Link Voltage	$U_{1,DC}$	400 V
Receiver-Side DC-Link Voltage	$U_{2,DC}$	350 V
Battery Voltage	U_{batt}	350 V

Typical charging power levels for single-phase EV chargers interfacing the European AC grid vary between 3 kW and 7.4 kW. Therefore, a power level of 5 kW is selected for the scaled IPT system. A single-phase rectifier with buck capability operating from the European 230 V/50 Hz grid is assumed as the power supply for the 5 kW. Single-phase PFC rectifiers are typically designed for a nominal output voltage of 400 V and realized with standard 600 V power semiconductors. Consequently, this is also the specified input DC-link voltage $U_{1,DC}$ of the IPT system. Traction batteries for private transportation EV typically have nominal voltages of 300-400 V. Hence, the IPT system presented in this chapter is designed for an output voltage $U_{2,DC}$ of 350 V.

The air gap, over which the power has to be transmitted, and the maximum coil size are given by the geometrical constraints of the application at hand and cannot be changed in the design process. In this chapter, an air gap of 50 mm is assumed. For the size constraint, a maximum diameter of 300 mm is assumed for both coils. This constraint is generous considering the air gap of 50 mm, but it will help to highlight the trade-offs encountered in the selection of a coil size, which will be discussed in detail in Section 3.3, where the prototype system is designed with a coil diameter of 210 mm.

For the power electronics, the series-series compensated topology is used and the control of the output power is implemented by regulation of the input and output side DC-link voltages as proposed in Section 2.3.4. The main advantages of this topology are the load- and magnetic coupling-independent resonant frequency and the high efficiency at light load conditions, which will be demonstrated in the course of the experimental investigation at the end of this chapter.

3.2 Modeling & Calculation of Power Losses in IPT Coils

The design of an IPT coil starts with the selection of a coil geometry that is suitable for the application at hand. After the selection of a coil geometry for the scaled IPT prototype in the first part of this section, quantitative models for estimating the power losses and the magnetic stray field of the IPT coil are developed based on frequency domain FEM calculations. Additionally, details on the thermal model of the IPT coils are given. At the end of the section, the employed loss model for the film capacitors that are employed for the resonant compensation are given.

3.2.1 Coil Geometry Selection

Early literature on IPT is mainly concerned with transcutaneous power transfer to biomedical implants [84, 85]. For these applications, flat spiral coils without magnetic core are typically employed. Even if magnetic core material would help increasing the magnetic coupling, core-less designs are preferred due to the higher mechanical flexibility [68]. Inductance calculations for air coils are well documented in literature [86–88].

Spiral coils have also been used for IPT systems intended for EV charging [33, 89], mainly because of their low profile. In these applications, typically core materials are employed for flux guidance and shielding of the stray field. An illustrative drawing of a spiral coil on a ferrite core is shown in **Fig. 3.1(b)**. As an additional advantage for the designer, modeling is possible with Two Dimensional (2D) FEM calculations owing to the axial symmetry. This significantly shortens calculation times compared to Three Dimensional (3D) FEM models.

Based on the E-shaped core structures that are widely used for power electronic transformers, also IPT coils based on transformer E-cores have been designed [21, 22, 90]. In reference to the path of the mutual flux ϕ_{12} highlighted in **Fig. 3.1(a)**, both E-core coils and spiral-shaped coils can be classified as E-type IPT coils.

As an alternative to the E-core structure, C-cores can be used for the design of power electronic transformers as shown in **Fig. 3.1(d)**. Based on this transformer geometry, two additional IPT coil geometries can be derived by introducing an air gap in the transformer core. As a first option, the legs of the C-core are completely removed while the

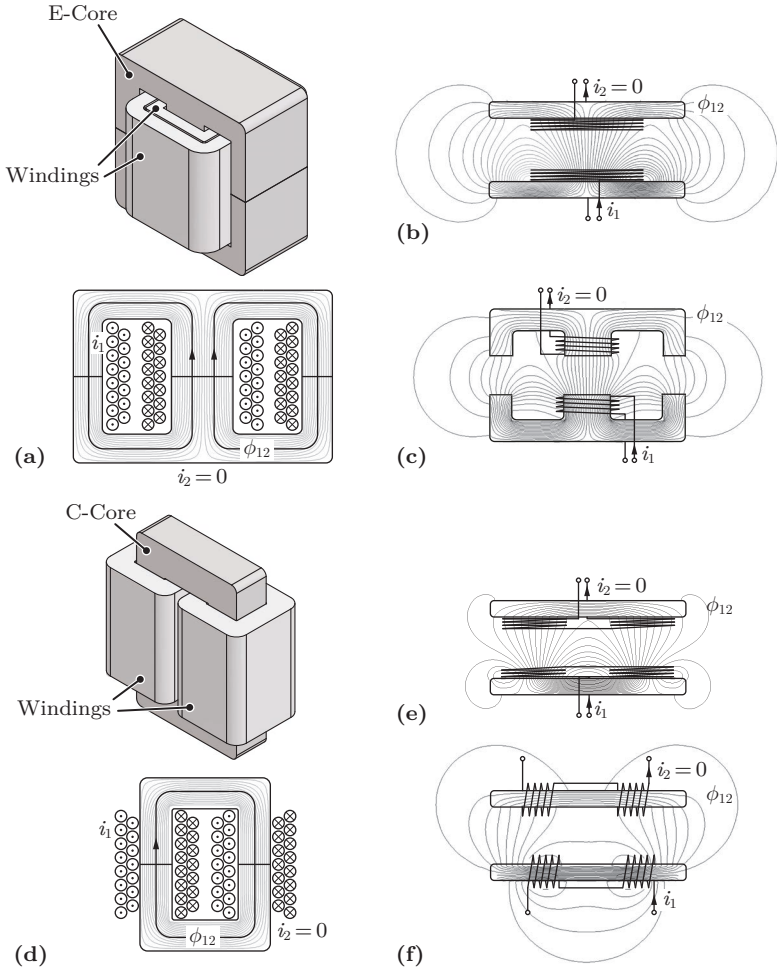


Fig. 3.1: Classification of IPT coil geometries according to the path of the coupling flux ϕ_{12} : (a) Conventional E-core transformer, (b) E-core IPT coil, (c) spiral IPT coil on planar core, (d) Conventional C-core transformer, (e) solenoid IPT coil, (f) double-loop IPT coil on planar core.

transformer windings are left in place as in **Fig. 3.1(e)**. The resulting IPT coil geometry was proposed in [91–94], where it is called the *double-D* coil. As an alternative, the windings can be wound around the remaining core element as shown in **Fig. 3.1(f)**. Such solenoid inductor structures have been investigated for instance in [95–97].

The study of previous literature does not reveal an immediate advantage of any of the discussed coil geometries in terms of the transmission efficiency or the power density. The main factor that determines the magnetic coupling is the area covered by the coil in relation to the air gap distance. The exact shape of the transmission coils has only a minor effect [98]. Therefore, in order to reach a high magnetic coupling and a high transmission efficiency in a practical application, the coil shape needs to be adjusted to the shape, aspect ratio, and size of the available mounting area on the EV.

The main purpose of the scaled 5 kW IPT prototype is to develop and experimentally verify models in perspective of the optimization of a 50 kW EV charger later in this thesis. Therefore, a spiral coil geometry is preferred at this stage, because the axial symmetry enables a more efficient evaluation of FEM models. This becomes a significant advantage during the multi-objective optimization presented in Section 3.3.

3.2.2 Axis-Symmetric FEM Simulation Models

For coil designs that include core materials or that have unconventional geometric shapes, FEM tools are required for the optimization as analytical calculations are hardly possible. These tools allow calculating equivalent circuit parameters of the coil and predicting the electromagnetic losses in the used materials. They can also be used for the dimensioning of the core to avoid saturation as well as for the calculation of the stray fields. Before the detailed discussion of the developed power loss calculation methods, the FEM simulation models are briefly described.

The coil design that was chosen for the IPT prototype presented in the previous section is axis-symmetric. Hence, two dimensional FEM models are sufficient for the calculation. As an additional simplification, all models are solved in the frequency domain at the fundamental switching frequency of the power converter. The approximately sinusoidal current waveforms in the IPT coils described in Section 2.1.4 validate this simplification.

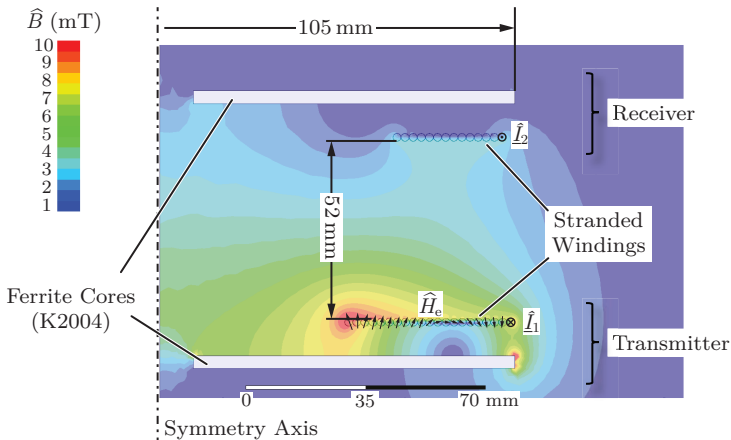


Fig. 3.2: Visualization of the magnetic flux density \hat{B} in the axis-symmetric FEM model. Schematically drawn is the vector of the external magnetic field \hat{H}_e in the transmitter windings (not to scale).

Fig. 3.2 shows the simulation model used in the FEM tool FEMM¹ and in the commercially available FEM software ANSYS Maxwell². The litz wire winding is modeled as cylinders of stranded wire with a uniform current density as in the DC case. This prevents the time-intensive calculation of eddy currents in the windings. Both of the used FEM tools offer this functionality to accelerate their frequency-domain calculation modules. The approximation is valid because

- ▶ a litz wire with sufficiently small strand diameter is chosen to reduce the high-frequency effects to a minimum,
- ▶ the current distribution inside the windings has only little influence on the magnetic field on the outside for the investigated geometry,
- ▶ in the following the losses in the windings are calculated using analytical equations together with field values obtained from the FEM results and not with the tools provided by the FEM simulation packages.

¹Version 4.2, freeware available at www.femm.info (25.9.2015).

²Version 2014, available at www.ansys.com (25.9.2015).

In order to increase the magnetic coupling of the coils, a ferrite core is added to the coil arrangement. The core is modeled by the relative permeability of the used material (K2004, $\mu_r = 2000$). The conductivity of the core material is low ($\sigma < 1 \text{ S/m}$). Therefore, it is neglected in the FEM model. All magnetically inactive materials are not modeled, because capacitive effects are excluded from the calculations.

In both tools, the simulated space is bounded by a sphere with a radius that is several times larger than the coil radius. The sphere radius was determined from a sequence of simulations where the size of the bounding sphere was increased stepwise until no further change in the simulation results could be observed. This process resulted in a sphere radius four times larger than the coil radius. A mixed Dirichlet/Neumann boundary condition on the border of the sphere is chosen to model unbounded, open space. In FEMM, this can be achieved by setting up an appropriate mixed boundary condition manually [99].

Automatic meshing is used in both FEM tools, which leads to a skin depth based mesh in all materials. To increase the accuracy of the stray field calculation, a maximum mesh size of 5 mm was specified along a radial axis, which has its origin in the center of the air gap. The stray field is then evaluated along this axis for the experimental verification presented in the last part of this chapter.

3.2.3 FEM-Based IPT Coil Loss Modeling

After the selection of a coil geometry, the theoretical considerations of the previous parts are extended with physical component models, which are subsequently used for the IPT coil optimization presented later in this chapter. The calculations for the loss estimation in magnetic core elements and litz wire are discussed in detail, closely following [56].

Power Losses in High-Frequency Litz Wire

Contactless EV chargers typically operate above 20 kHz to reduce acoustic noise emissions. The upcoming standard SAE J2954 [43] proposes an even higher frequency of 85 kHz for interoperability among components from different manufacturers. Due to the high operating frequency, typically high-frequency copper litz wire is used for the transmission coils. Since the calculation of the power loss in litz wires is not supported by some FEM tools, a combination of analytical and FE-assisted calculations is applied for the loss estimation.

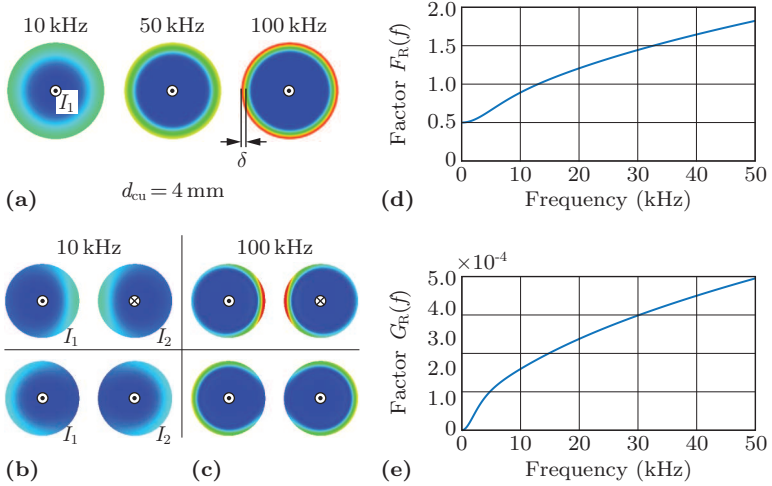


Fig. 3.3: (a) FEM-calculated current distribution in a single conductor and (b)-(c) in neighboring conductors with equal currents in both conductors and for currents with opposite direction. (d) Factors $F_R(f)$ and (e) $G_R(f)$ that model the power losses due to the skin- and the proximity effect, respectively.

The copper losses in the litz wire windings due to the skin effect, including the DC losses, can be approximated by integrating the power loss density [100]

$$p_{\text{skin}} = n \cdot R_{\text{DC}} \cdot F_R(f) \cdot \left(\frac{\hat{I}}{n} \right)^2 \quad (3.1)$$

over the total length of the conductors. The variable n denotes the number of isolated strands in the litz wire, R_{DC} is the DC resistance per unit length of a single strand, \hat{I} is the current peak value, f is the frequency, and $F_R(f)$ is a frequency-dependent factor that models the skin effect in round conductors. An estimation of the power loss density due to the proximity effect is given by [100]

$$p_{\text{prox}} = n \cdot R_{\text{DC}} \cdot G_R(f) \cdot \left(\hat{H}_e^2 + \frac{\hat{I}^2}{2\pi^2 d_o^2} \right), \quad (3.2)$$

where d_o is the outer diameter of the litz wire and $G_R(f)$ denotes a frequency-dependent factor that models the proximity effect in round

conductors. The first proximity loss component is termed the external proximity effect, because it results from the external magnetic field \hat{H}_e . The external magnetic field \hat{H}_e results from the superposition of the magnetic fields produced by the neighboring conductors in the same winding and by the conductors of the opposite IPT coil. It must be evaluated separately for each conductor during the calculation of the proximity losses. The second proximity loss component is termed the internal proximity effect. It depends only on the peak value of the total current in the litz wire \hat{I} .

FEM-simulated current distributions in a single conductor and in neighboring conductors carrying equal currents or currents with opposite phase are shown in **Figs. 3.3(a)-(c)**. The frequency dependency of the factors $F_R(f)$ and $G_R(f)$ that model the power losses associated with the skin- and the proximity effect, respectively, are shown for the conductor diameter $d_{cu} = 4$ mm in **Figs. 3.3(d)-(e)**. The complete analytical derivation and the necessary equations for the calculation of these factors is found in [100–102].

Contrary to the calculation of the losses associated with the skin effect, the calculation of the losses due to the proximity effect requires knowledge of the external magnetic field \hat{H}_e for each conductor. For a conventional transformer with litz wire windings, the calculation of the magnetic field in the winding window is straightforward with Ampère's law

$$\oint_{\partial A} \vec{H} d\vec{l} = \iint_A \vec{J} d\vec{A}, \quad (3.3)$$

where \vec{J} is the current density crossing the surface A bounded by the closed curve ∂A shown in **Fig. 3.4**. For the calculation of $\hat{H}(x)$, a uniform current density in the winding window is assumed. The required values for the external magnetic field \hat{H}_e can then be approximated with good accuracy by evaluating the result $\hat{H}(x)$ at the position x of each conductor. A more thorough analysis of the high-frequency power losses in the litz wires windings of a conventional transformer is found for instance in [103–105]. For designs with solid wire or foil windings instead of litz wire, the self-shielding of the winding and the resulting non-uniform current density in the winding window has to be taken into account for the calculation of the magnetic field [103, 106].

For the IPT coil modeled in this chapter, an analytical calculation is difficult mainly because magnetic materials are used. Particularly,

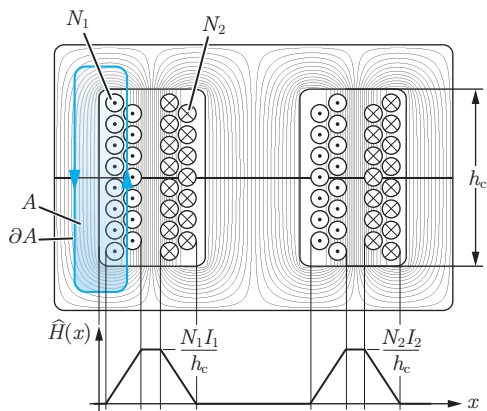


Fig. 3.4: Calculation of the magnetic field in the winding window of a conventional transformer with litz wire windings using Ampère's law.

the field distortions around the edges of the cores in **Fig. 3.2** are hard to capture using an analytical approach. For these reasons, the FEM simulation model described above is used to calculate the power losses due to the proximity effect.

As a good approximation for the selected axis-symmetric coil geometry, the magnetic field is assumed as homogeneous over the total length of one turn of the inductor. Like for a conventional transformer, the external magnetic field \hat{H}_e differs from turn to turn (cf. **Fig. 3.2** and **Fig. 3.4**). Therefore, it must be evaluated in the center of each turn individually in order to calculate the power loss density p_{prox} accurately for each turn. The power loss density p_{prox} is multiplied with the length of the individual turn to obtain the total proximity losses of each conductor. In a three dimensional design, an integration along each turn would be required. Finally, the total power losses due to the proximity effect can be calculated by adding up the power losses of all turns in a coil.

Core Loss Model

As discussed in Section 2.1.4, the currents in the transmitter and in the receiver coil of an IPT system are approximately sinusoidal. Therefore, no advanced core loss calculation methods are required [100]. The core

loss can be estimated by integrating the core loss density according to the Steinmetz equation

$$p_{\text{core}} = \kappa \cdot f_0^\alpha \cdot \hat{B}^\beta \quad (3.4)$$

over the volumes of the cores of the transmitter and the receiver coil. The parameters α , β , and κ are the Steinmetz parameters of the core material ($\alpha = 1.32$, $\beta = 2$, $\kappa = 6.47$ for the material K2004 used in the prototype designed in this chapter).

3.2.4 Resonant Capacitors Loss Model

For the resonant compensation of the coils, film capacitors of the B32653 and B32654 series from Epcos are considered for the scaled 5 kW prototype coil. The capacitors are dimensioned according to their specified maximum RMS current and the required capacitance that is obtained from the transformer equivalent circuit model of IPT coil. A safety margin of two with respect to the rated power loss is included to take the reduced heat dissipation due to the arrangement of multiple capacitors in an array into account.

The power loss in the resonant capacitors is estimated according to

$$P_{\text{cap}} = \frac{\tan \delta(f_0)}{\omega_0 C} I^2 \quad (3.5)$$

where $\tan \delta(f)$ is a fit over frequency of the $\tan \delta$ indicated in the data sheets by the manufacturer [82], and I is the RMS current. The power loss in the resonant capacitors is always included in the results presented in the following.

3.2.5 Simplified Thermal Model

Additional to the models for the power loss estimation, a thermal model is required to analyze the thermal feasibility of the coil design. Unfortunately, a fully coupled electromagnetic and thermal simulation of the coil designs is time-intensive and is therefore rarely possible. Alternatively, a detailed analytical thermal model could be derived for the selected coil geometry using mathematical models for heat conduction and natural or forced convection cooling as documented in literature [107]. This is a difficult task and it is unlikely to yield results of general validity that could be transported to other coil geometries, such as the one

used for the 50 kW transmission coils designed in Chapter 4. Therefore, a simplified approach is adopted.

Since the coil housings must contain only non-conductive materials in order to avoid eddy current losses, plastics are considered for all structural elements of the transmission coils. However, for plastic materials deformation and melting occurs at temperatures significantly below the rated operating temperatures of, e. g., litz wires or ferrite cores. For Polyvinyl Chloride (PVC) and for acrylic glass (PMMA), which is considered as a transparent cover for the coil, the maximum operating temperatures are approximately 60-80 °C. Therefore, the structural elements of the housing and not the active parts are the thermally critical components of the transmission coils.

In order to estimate the temperature at the housing surface, the surface-related power loss density is considered. Typical surface heat transfer coefficients for natural and forced-air convection cooling can be found in [108]. For a surface temperature rise of $\Delta T = 30$ °C above the specified ambient temperature of $T_{\text{amb}} = 45$ °C, the maximum allowable surface related power loss density is 15 mW/cm² for natural convection cooling with a heat transfer coefficient of 5 W/(K m²). With forced-air cooling, a heat transfer coefficient of 50 W/(K m²) is well achievable. For the same ΔT , a maximum surface related power loss density of $p_{\text{surf,max}} = 0.2$ W/cm² is obtained. As an approximative thermal model for the optimization, the coil designs that exceed the maximum surface-related power loss density $p_{\text{surf,max}}$ for forced-air convection cooling are removed from the calculated results. For the calculation of the copper losses without thermal feedback, an average temperature of the winding of 80 °C is assumed for all designs during the optimization.

3.3 Multi-Objective Optimization Process

The magnetic design of the transmission coils is of key importance in order to satisfy the requirements of a high transmission efficiency η and a high power density of the IPT system. Due to the low profile of IPT coils, particularly the area-related power density α , which relates the output power to the required footprint area for the coil, is of interest. In addition, for a contactless EV charger that is installed at a location that is accessible by humans, e. g., a parking garage or a bus station, the stray fields caused by the IPT system must be as low as possible. Limit values for the maximum acceptable field levels are specified in standards such

Tab. 3.2: Parameter space for the multi-objective IPT optimization.

Parameter	Variable	Min.	Max.	# Points
Outer Coil Diameter	D_{coil}	100 mm	300 mm	60
Copper Cross-Section	A_{cu}	1 mm ²	4.7 mm ²	10
Design Frequency ¹	f_0^*	50 kHz	200 kHz	5

¹The actual resonant frequency is not an input parameter, but results from (3.6) during the optimization.

as [38–40]. Therefore, these limits must be taken into account during the design of the IPT coils as another performance factor.

Using the FEM-based calculation methods presented in the previous section, in this section a multi-objective optimization with respect to the area-related power density α , the transmission efficiency η , and the magnetic stray field is performed for the IPT coils of the scaled 5 kW system. The η - α -Pareto front as well as the trade-off between the coil size, the efficiency, and the stray field are discussed in detail. Based on the discussion, insight is obtained into the most important parameter interdependencies for IPT systems. The conclusions are used for the subsequent optimization of the full-scale 50 kW EV charger presented in the later chapters.

3.3.1 Optimization Methodology

Considering the system specifications in **Tab. 3.1**, the coil designs with the diameters, copper cross-sections, and design frequencies listed in **Tab. 3.2** are evaluated in an iterative parameter sweep, similar to the optimization of the medium-frequency transformer in [109]. Only single-layer spiral windings are considered, because flat coil designs are preferred for EV applications to simplify the mounting of the device, and because the parasitic capacitance of this coil design is mainly determined by the number of layers.

The optimization process follows the steps outlined in **Fig. 3.5**. The optimization starts with the definition of the system specifications, the selection of a coil geometry and materials, and the definition of a parameter space (steps 1-4). In the first phase of the coil parameter optimization, a large look-up table is generated (step 5). For each coil size listed in **Tab. 3.2**, all turns numbers that can be realized for a

3.3. Multi-Objective Optimization Process

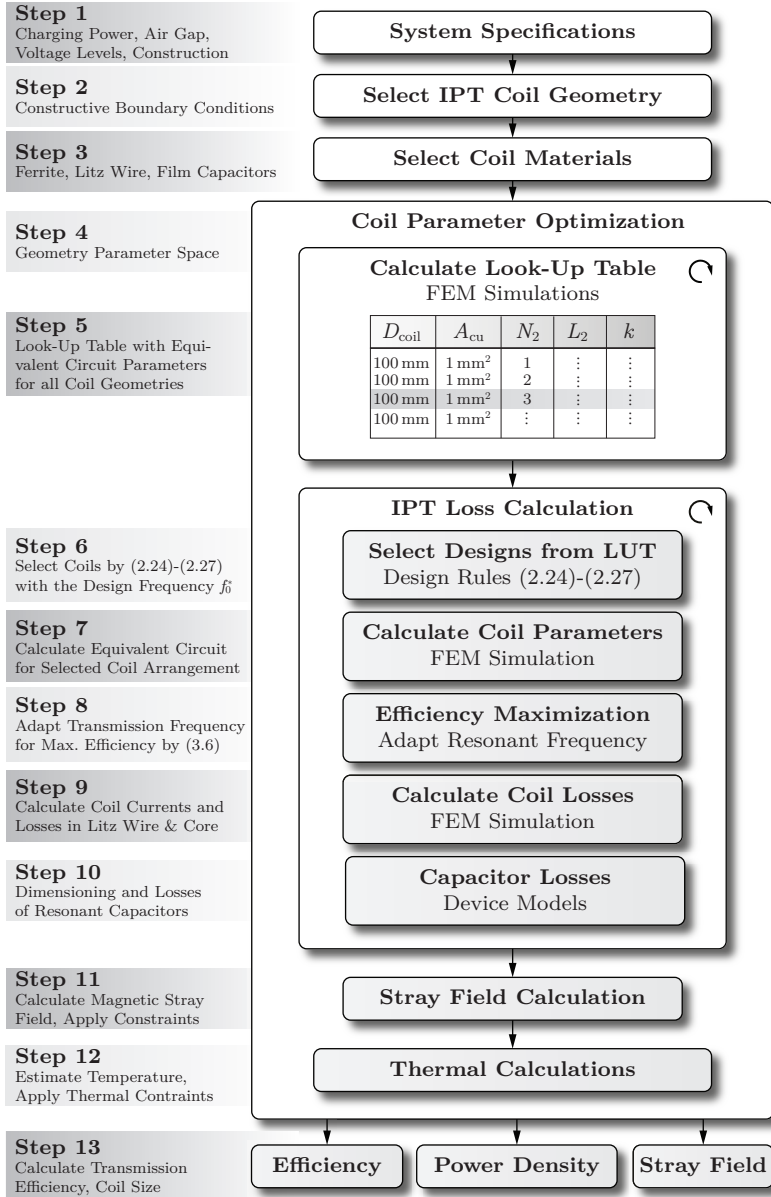


Fig. 3.5: Multi-objective IPT optimization process for the 5 kW prototype.

certain copper cross section are calculated. An FEM model is generated for each coil design. In the FEM model, the turns are always placed starting from the outer edge of the spiral coil and filling up towards the coil center to maximize the magnetic coupling [56]. Then, the self-inductances of the coils are calculated with the FEM tool. For evaluating the design rules (2.24)-(2.27), a first estimate of the magnetic coupling is needed in addition. Therefore, the FEM model is extended with another, identical IPT coil, which acts as the receiver. The magnetic coupling is calculated for the two identical coils and stored in the look-up table. This process is repeated for all specified copper cross-sections and coil diameters. During the later steps of the optimization, IPT transmitter and receiver coils that are not identical are considered as well. For such designs, the estimate for the magnetic coupling obtained in this step is not valid. Therefore, in steps 7-8, a correction is made for the final coil arrangement.

In step 6, the design rules (2.24)-(2.27) are used to select all suitable transmitter and receiver coil pairs from the previously generated look-up table for each design frequency f_0^* in the parameters space of **Tab. 3.2**. The design rules are evaluated using the estimated coupling factor that is stored in the look-up table during step 5. As described in Section 2.2.4, the design rules ensure an optimal loading of the resonant circuit by adapting the IPT coil self-inductances to the equivalent load resistance of the receiver. This leads to the minimum total losses and the maximum transmission efficiency of the IPT system.

The estimate of the magnetic coupling is calculated for identical transmitter and receiver coils during the generation of the look-up table in step 5. However, the design rules used in step 6 do not necessarily yield identical transmitter and receiver coil pairs if the DC-link voltages $U_{1,DC}$ and $U_{2,DC}$ are not equal. Therefore, the self-inductances, the mutual inductance, and the magnetic coupling must be re-calculated for the selected IPT coil arrangements in another FEM simulation (step 7).

Since the transformer equivalent circuit parameters of the actual coil arrangements differ from the original estimates used in step 6, the operation of the selected coils with the DC-link voltages $U_{1,DC}$ and $U_{2,DC}$ would not lead to the desired output power P_2 at the design frequency f_0^* . Therefore, in step 8, the resonant frequency is adapted for each design in order to obtain the correct output power. The resonant frequency f_0 that leads to the output power P_2 , given the DC-link

voltages and the mutual inductance of the actual IPT coil arrangement, follows from (2.34) as

$$f_0 = \frac{1}{2\pi} \frac{8}{\pi^2} \frac{U_{1,\text{DC}} U_{2,\text{DC}}}{P_2 M}, \quad (3.6)$$

This adjustment ensures that all the system specifications in **Tab. 3.1** are fulfilled by the simulated designs. It can be shown that with this adjustment also the optimal load factor is achieved.

Next, the currents in the windings are calculated and the strand diameter of the litz wire is adapted to one fourth of the skin depth at the adapted resonant frequency f_0 to minimize the AC losses. A final FEM simulation in the frequency domain at the adjusted resonant frequency f_0 is used to calculate the power losses of the IPT coils with the models described above (step 9). The resonant compensation capacitors C_1 and C_2 are dimensioned as described in Section 2.2.1 (step 10). Suitable devices are selected from a list of available film capacitors with the calculated RMS currents, taking into account a safety margin regarding the arrangement of multiple capacitors in an array as discussed in Section 3.2.4. Always the smallest realization of the needed capacitance value is selected from the list of possible configurations. From the results of the final FEM simulation, the magnetic stray field of the coil arrangement is extracted at a specified observation point and stored together with the design (step 11).

In the last step, the surface-related power loss density is calculated for each design to approximate the surface temperature of the coil housing (step 12). The designs with a power loss density higher than $p_{\text{surf,max}} = 0.2 \text{ W/cm}^2$ are excluded from the optimization results. Similar to the thermal constraint of the design, also designs where the stray field exceeds a certain maximum value could be removed from the optimization results during step 11. Reference values for the stray field are given in [38, 39], however, the limits which must be respected strongly depend on the target application. Therefore, no restriction is made for the optimization presented in this chapter, but the RMS stray field is extracted from the simulation results and discussed below.

Finally, the transmission efficiency of the IPT system including the power losses in all system components is evaluated and the power density of the coil design is calculated (step 13). The feasible results are stored in a database, from which a suitable design can be selected for the realization of a prototype.

3.3.2 Discussion of Optimization Results

The calculated transmission efficiency η , including the power losses in the core, the copper litz wire windings, and the resonant capacitors, of the evaluated designs is shown in **Fig. 3.6** as a function of the area-related power density α . The η - α -Pareto front which describes the physical trade-off between the transmission efficiency η and the area-related power density α is clearly visible. The coloring in **Fig. 3.6** corresponds to the calculated magnetic coupling. In **Fig. 3.7**, the coloring corresponds to the quality factor. As the coil size is decreased, i.e., at an increasing power density, the magnetic coupling is reduced. However, a high efficiency can still be reached if the quality factor is increased and a high $FOM = kQ$ is obtained despite the reduced magnetic coupling. In **Fig. 3.8**, the Pareto fronts for seven frequencies are outlined. They clearly show that a higher transmission frequency results in a higher quality factor and a high transmission efficiency, even at a high power density of the coils (cf. **Fig. 3.7**).

For the construction of the prototype, a core with a diameter of 210 mm is selected from the limited number of available ferrite cores with a suitable shape. The area-related power density of the prototype is thereby selected as 1.47 kW/dm². For the selection of the transmission frequency, the power losses of the coil designs with a power density of 1.47 kW/dm² are extracted from the optimization results as shown in **Fig. 3.9(a)**. It can be seen that the winding losses decrease with increasing transmission frequency.

At a higher frequency, the design rules (2.24) and (2.27) show that lower self-inductances are needed to reach the maximum transmission efficiency. Hence, coil designs with lower turns numbers and therefore lower AC resistance are needed at a higher frequency. As expected from the Steinmetz equation and the increasing equivalent series resistance of the resonant capacitors described in [82], the losses in the core and the resonant capacitors increase at high frequencies. As a result, up to about 200 kHz the total losses of the designs decrease.

However, the improvement above 100 kHz is small when considering also the frequency-dependent losses of the power electronics. For instance, the gate driver losses and the switching losses that occur despite ZVS of the four MOSFETs and the rectifier diodes double if the switching frequency is increased from 100 kHz to 200 kHz. Hence, 100 kHz is used as the transmission frequency of the prototype system, because of the limited benefit from a further frequency increase.

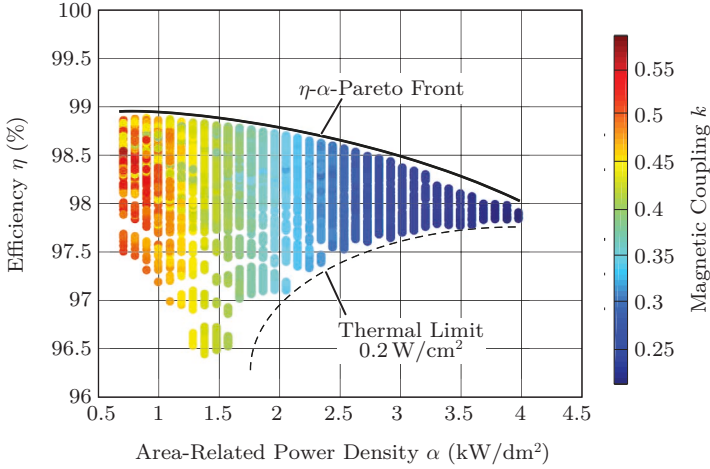


Fig. 3.6: Results of the η - α -Pareto optimization shown with the magnetic coupling k as parameter for the coloring. A higher power density of the coils leads to a lower magnetic coupling and a reduced transmission efficiency.

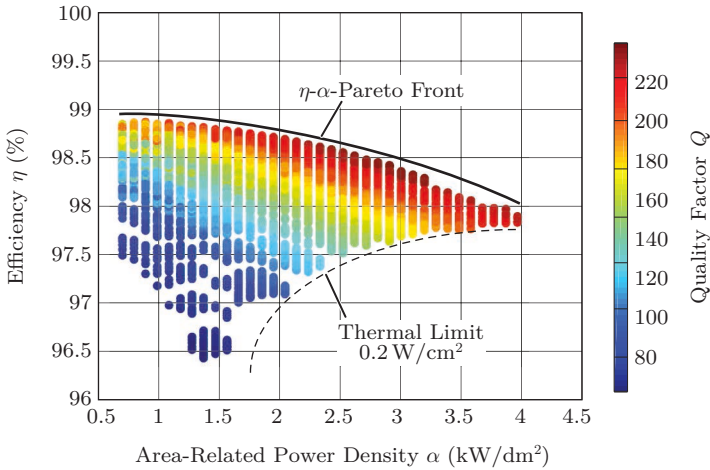


Fig. 3.7: Data points of **Fig. 3.6**, but with the quality factor Q as coloring parameter. A high quality factor (due to the higher transmission frequencies) leads to a high transmission efficiency even for a low magnetic coupling.

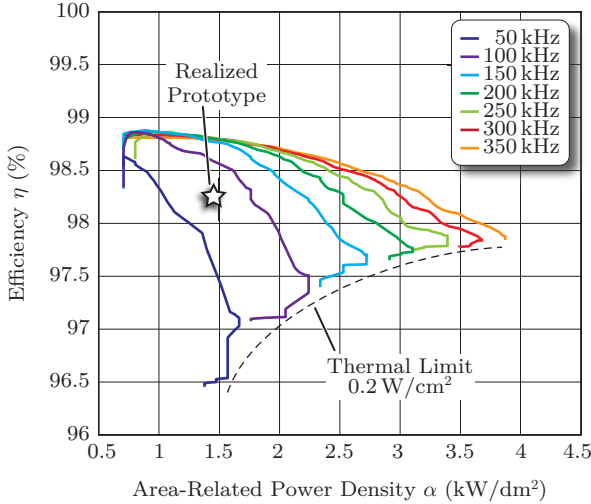


Fig. 3.8: η - α -Pareto fronts for transmission frequencies between 50 kHz and 350 kHz. For a given power density, a higher efficiency is possible with a higher transmission frequency.

A number of further trade-offs and limitations must be considered when selecting a high transmission frequency in a practical design. First, there are technical limitations on how thin the litz wire strands can be manufactured. Commercially available copper litz wires reach minimal strand diameters of around $30\ \mu\text{m}$. At the same time, the packing factor of litz wires decreases with decreasing strand diameter because the required amount of insulation material becomes large compared to the copper cross-section. This leads either to higher copper losses or to a lower power density, if the outer diameter of the wire is increased to maintain a constant copper cross-section. Additionally, with too thin strand diameters, the wires may become fragile. Strands might break during the production or the coil assembly, which reduces the effective copper cross-section. Moreover, the higher price and limited availability of litz wires with extremely thin strands and large copper cross-section must be considered.

As a second limitation, the losses in the power semiconductor of the power electronic converters must be considered. If Insulated-Gate Bipolar Transistors (IGBTs) are used as switches, the switching losses

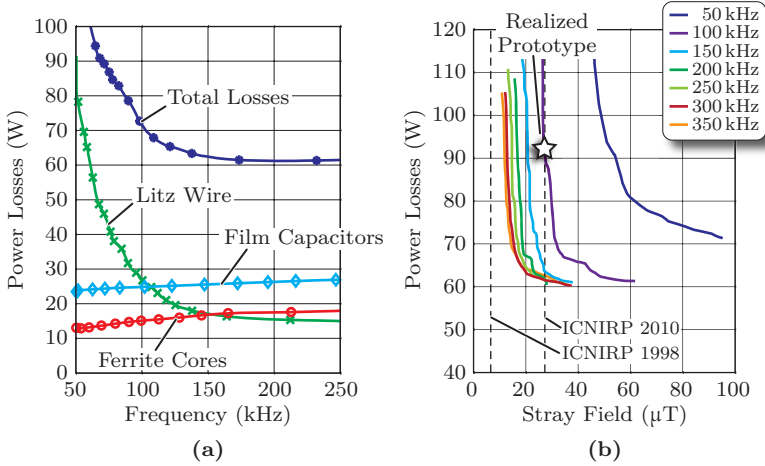


Fig. 3.9: (a) Power losses of designs with a power density of 1.47 kW/dm^2 (power density of the presented prototype). (b) Power loss as a function of the stray field at a distance of 300 mm from the coil center, shown for transmission frequencies between 50 kHz and 350 kHz.

due to the stored charge that occur despite the zero current switching conditions need to be taken into account in a trade-off analysis [110–112]. Even if MOSFETs are used, there are certain frequency dependent losses in the converter, e. g., the mentioned losses of the gate driver or losses in the devices due to incomplete ZVS [67]. Additionally, the switching speed and required interlock time of the used devices become critical as soon as the switching period reaches the order of magnitude of the current and voltage rise-times during turn-on and turn-off of the devices. Moreover, low self-inductance and compensation capacitance values are needed in the resonant circuit at high frequencies. Therefore, parasitics in the power electronic converter and the IPT coils become more and more important. For instance, the stray inductance of the converter layout and of the wires connecting the power converter with the coils is added to the leakage inductance of the IPT coil system. This results in a reduction of the effective magnetic coupling and thus leads to a lower efficiency. Moreover, the self-capacitances of the IPT coils must be taken into account at high frequencies by extending the presented models accordingly.

Another trade-off in the design of IPT coils is shown in **Fig. 3.9(b)**,

where the power loss is depicted as a function of the minimum achieved RMS stray field observed at a distance of 300 mm from the coil center at seven selected frequencies. Similar to the η - α -Pareto front, a trade-off exists for the power loss and the stray field. The stray field at a given observation point can be reduced if smaller IPT coils are used for the power transmission, i.e., the distance of the observation point to the coil windings becomes larger. However, a higher power loss results due to the required increase of the power density of the coils. As shown in **Fig. 3.8**, the power loss can be reduced if the transmission frequency is increased, but the described trade-off exists nonetheless.

With the coil geometry investigated in this chapter, the ICNIRP 2010 guideline [39] can only be fulfilled if a transmission frequency above 50 kHz is used. It is not possible to comply with the ICNIRP 1998 guideline [38] at the observation distance of 300 mm, even with a frequency as high as 350 kHz. As an alternative solution, passive or active shielding could be included in the coil design to reduce the stray field. Then, also the losses due to eddy currents in the shielding elements must be taken into account in the FEM tools. Since shielding is not needed for the scaled prototype designed in this chapter, this is not investigated further at this point. However, for the 50 kW transmission coil designed in Chapter 4, the losses of an eddy current shielding are included in the multi-objective optimization.

Taking everything into account, a prototype IPT system is constructed for the experimental verification of the calculation models. The parameters of the prototype are listed in **Tab. 3.3** and a photograph of the coil assembly is shown in **Fig. 3.10**. A transmission frequency of 100 kHz is used and a copper litz wire with 630 strands with strand diameter 71 μm is chosen based on the skin depth at the selected frequency. The selected design lies approximately 0.3% below the Pareto front for 100 kHz as indicated in **Fig. 3.8**, because of a reduction of the self-inductances by 15% away from their optimal value. This adjustment is needed to avoid a pole-splitting, which could potentially result in high switching losses due to loss of ZVS of the transmitter-side power semiconductors (see discussion in Section 2.3.2 and [51, 52, 54]). From the calculations, a transmission efficiency of 98.25% is expected at the area-related power density of $\alpha \approx 1.47 \text{ kW}/\text{dm}^2$. The expected stray field of the prototype system is 26.16 μT at a distance of 300 mm on a radial axis starting in the coil center, located on a plane parallel to the coil surface in the center of the air gap.

Tab. 3.3: Parameters of the selected design for the scaled prototype system.

Parameter	Variable	Value
Coil Diameter	D_{coil}	210 mm
Copper Cross-Section	A_{cu}	2.49 mm ²
Resonant Frequency	f_0	100 kHz
Litz Wire Strand Diameter	d_i	71 μm
Power Density	α	1.47 kW/dm ²
Transmission Efficiency	η	98.25%
Magnetic Stray Field	B_{stray}	26.16 μT

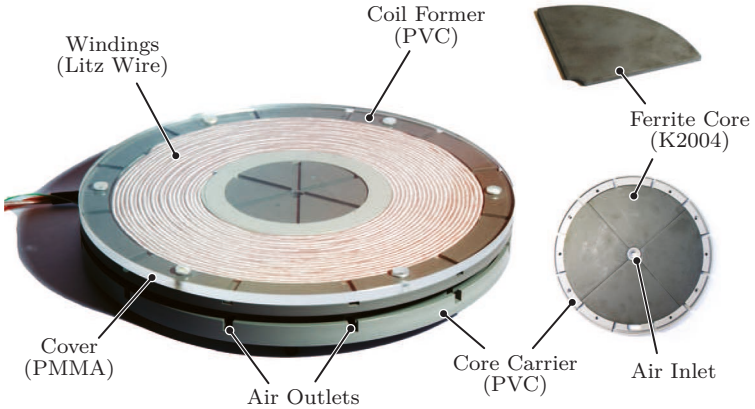


Fig. 3.10: Photograph of the constructed 5kW IPT coil, designed for transmission across an air gap of 50 mm with a coil diameter of 210 mm, and a transmission frequency of 100 kHz. The windings are made from copper litz wire with 630 strands of 71 μm diameter. A forced-air cooling system with compressed air is used for the thermal management.

3.4 Validation of the FEM-Calculated Magnetic Field

The component models presented above rely on FEM tools for the calculation of the magnetic field data for the estimation of the power losses in the litz wire and in the core, as well as for the prediction of the magnetic stray field. Therefore, the magnetic field calculation results of the FEM tools are experimentally verified using a custom-made magnetic field probe that is described in the first part of this section [81].

3.4.1 Design of a Magnetic Field Probe

Several sensor technologies exist for measurements of magnetic fields, which differ largely in terms of sensitivity, bandwidth, and cost [113]. Even though Hall effect sensors would offer a cost advantage and would allow for a highly integrated design of the probe, their sensitivity and bandwidth is typically lower than for induced voltage sensors. Therefore, for the design frequency of 100 kHz, a field probe based on measurements of induced voltage is implemented. For the measurement of the induced voltage caused by the three spatial components of the magnetic flux density vector, three sensor windings are arranged perpendicularly on a cubic supporter made from PMMA as shown in **Fig. 3.11(a)**.

The geometrical size and the number of turns N of the probe are chosen such that a sensitivity of approximately 10-15 mV/ μ T is reached at the design frequency of 100 kHz. For the estimated magnetic fields between 5 and 250 μ T, the induced voltages are in a range suitable for state-of-the-art measurement electronics. In order to reach a high measurement bandwidth, the parasitic capacitance of the winding must be limited. Therefore, a low number of turns is desirable. Hence, a larger area must be enclosed by the windings to reach a sufficiently large signal amplitude. Because a compact design is preferred for precise point-measurements of the magnetic flux density, the side length of the PMMA supporter is chosen as 30 mm considering the trade-off. The windings are placed in 5 mm wide grooves that are milled onto the faces of the supporter. The resulting winding area is approximately $A = 576 \text{ mm}^2$ as indicated in **Fig. 3.11(b)**.

Under the assumption of an approximately constant flux density over the whole winding area, the voltage induced in the winding with spatial orientation $i \in [x, y, z]$ can be calculated from Faraday's law

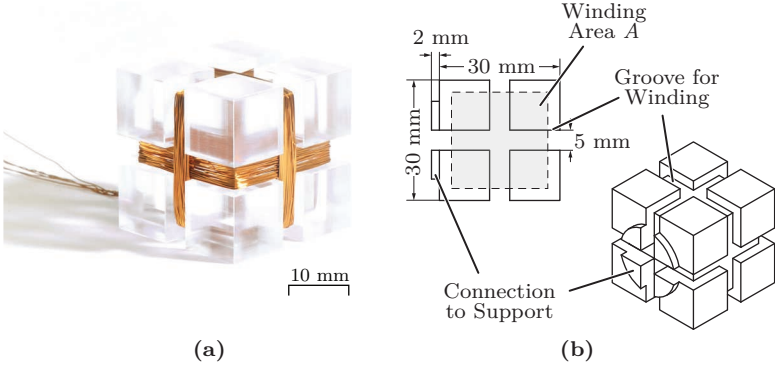


Fig. 3.11: (a) Photograph and (b) construction drawing of the field probe designed for the verification of the FEM-calculated magnetic field of the IPT prototype system. A machined PMMA cube is used to support windings with 40 turns for each spatial component of the field vector.

$$u_{\text{ind},i} = -N \frac{d}{dt} \iint_{A_i} \vec{B} \cdot d\vec{A}_i \approx -NA \cdot \frac{d}{dt} B_i, \quad (3.7)$$

where $\vec{B} = [B_x, B_y, B_z]^T$ denotes the magnetic flux density vector crossing the winding area A . The differential element $d\vec{A}_i$ stands for an orthogonal unit vector on each considered winding area A . In the frequency domain, it can be shown that

$$\hat{U}_{\text{ind},i} = \omega NA \hat{B}_i, \quad (3.8)$$

Thus, the turns number $N = 40$ leads to a measurement sensitivity of $\hat{U}_{\text{ind},i}/\hat{B}_i = 14.5 \text{ mV}/\mu\text{T}$ at the fundamental frequency of 100 kHz. The sensor windings are made from copper wire with a diameter of 0.2 mm. The turns are arranged on two layers in order to obtain an approximately concentrated winding, which is desirable for a measurement of the magnetic flux density at a specific point. For this arrangement, a bandwidth of approximately 2 MHz was measured [81]. The evaluation of a second prototype with the same number of turns and the same copper cross section, but with a single-layer winding indicated that the reduced parasitic capacitance and the higher bandwidth are of limited benefit, due to the increased measurement error caused by the

geometrically less concentrated winding arrangement.

From a measurement of the induced voltage, the corresponding magnetic flux density is determined using

$$|\vec{B}| \approx \frac{1}{\omega N A} \sqrt{\sum_{i \in [x, y, z]} \hat{U}_{\text{ind}, i}^2} \quad (3.9)$$

For an accurate measurement of the voltage at the winding terminals, a voltage-follower circuit is implemented with one operational amplifier³ for each spatial dimension on a measurement PCB. The voltage-follower configuration is used for its high input impedance, which results in a high impedance measurement. This is needed because any loading of the sensor windings would lead to a distortion of the measurement result. The measurement electronics are placed at a distance of approximately 50 mm from the sensor windings to avoid possible field disturbances, e. g., due to the electronic components, or the ground plane of the PCB.

The output signals of the operational amplifiers are connected to a high-bandwidth oscilloscope, where the signals are recorded at a high sampling rate. In order to extract the fundamental frequency components of the induced voltages in the sensor windings and the subsequent calculation of the flux density, the Fast Fourier Transform (FFT) of the numerics tool Mathworks MATLAB⁴ is used.

3.4.2 Comparison to a Commercial Field Probe

In order to verify the functionality of the field probe, measurements of the magnetic flux density are performed on the measurement setup shown in **Fig. 3.12(a)** while the prototype IPT system is active. Measurements are taken with the presented field probe along the indicated x -axis. Additionally, measurements with a commercially available field probe⁵ are taken at the same locations. The measurement is executed once during the transmission of 1 kW and repeated for 5 kW power transmission. A comparison of the measurement results obtained from both probes is shown in **Fig. 3.12(b)**. The deviation of the measurements obtained from the probe presented in this chapter with respect

³OPA820 by Texas Instruments is used for its high bandwidth.

⁴Version 2015a, available at www.mathworks.com (20.10.2015).

⁵Narda ELT-400, available www.narda-sts.com (20.10.2015).

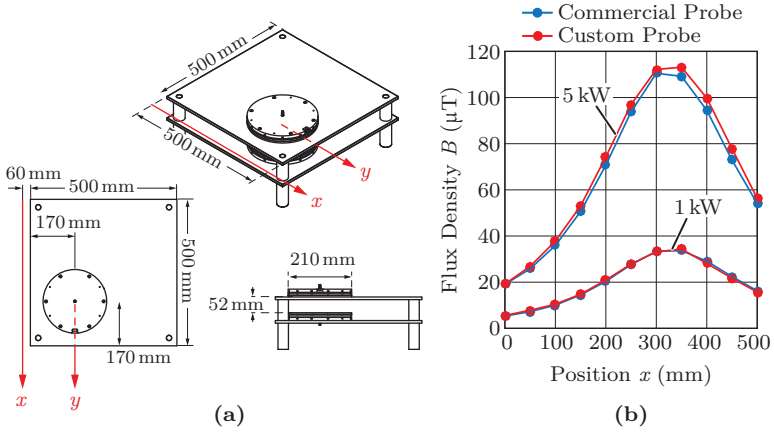


Fig. 3.12: (a) Measurement setup including the IPT coils. The axes used for the reference measurements is marked in red. (b) Comparison of field measurements taken once with a commercial device and once the presented custom-made field probe along the axis denoted x , during the transmission of 1 kW and 5 kW.

to the commercial device is below 5% for all positions, even for flux density values as low as 5 μT .

A part of this error likely results from the significantly larger size of the commercial field probe. The probe head of the commercial device has a diameter of 120 mm, while the winding area of the custom-made probe designed in this section is much smaller. Therefore, for the commercial device, the magnetic flux density is averaged over a larger area. Additionally, the mechanical positioning of the two probes at identical locations is difficult in practice. Hence, the obtained results validate the quality of the custom probe. Therefore, the probe is used for the verification of the FEM-calculated magnetic fields.

3.4.3 Validation of the FEM Simulation Results

To verify the accuracy of the FEM field calculations, field measurements are taken with the designed field probe [56, 81]. The probe is moved along the radial axis denoted y in **Fig. 3.12**. The origin of the y -axis is located in the center of the air gap and it runs on a plane parallel to the IPT coil surface. The measurements are taken while the prototype

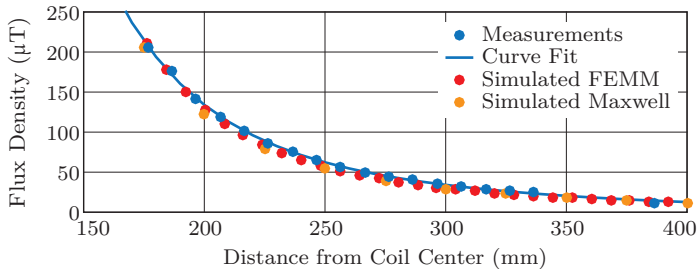


Fig. 3.13: Comparison of the FEM-calculated and measured magnetic flux density along the axis denoted y in **Fig. 3.12**. The average absolute value of the relative error with respect to the measurements is 9.3% for FEMM and 11.6% for Ansys Maxwell.

IPT system is active and transmitting 5 kW.

The measured RMS magnetic flux density is shown in **Fig. 3.13**, together with the values calculated by the two FEM tools FEMM and Ansys Maxwell. If the relative error of the calculation is averaged in absolute value, the tool FEMM shows a deviation of 9.3%. The commercial FEM tool deviates by 11.5% from the measured field values. This is considered a good agreement of the FEM-calculated and the measured field values. Hence, the accuracy of the stray field calculations used for the η - α -Pareto optimization presented above is verified with the presented experiment. The accuracy of the estimated power losses of the presented IPT prototype is verified in the next section.

3.5 Experimental Verification

For the experimental verification of the power loss calculation models, the power converter shown in **Fig. 3.14** is used. Even though for the measurements a DC-link voltage of 400 V is used, the converter is realized with 1.2 kV SiC MOSFETs⁶, which have higher conduction losses when compared to a design with 600 V devices. However, the higher blocking voltage will also allow future experiments with higher DC-link voltages, e.g., 800 V supplied from the three-phase grid. Moreover, also switching frequencies higher than 100 kHz are possible owing to the low

⁶Cree CMF2012D, 1.2 kV/42 A has $R_{DS,on} = 80 \text{ m}\Omega$ at 75 °C.

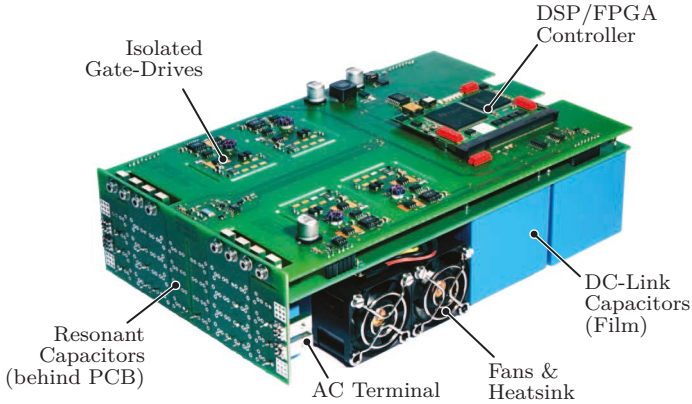


Fig. 3.14: 5 kW power converter designed for the measurements presented in this chapter. The converter is designed with 1.2 kV SiC MOSFET devices for operation at switching frequencies ≥ 100 kHz and up to 800 V DC-link voltage.

capacitance and high switching speed of the used devices. This flexibility of the test setup is preferred over the additional loss reduction that could result from devices with lower blocking voltage rating.

A waveform of the transmitter-side inverter output voltage u_1 , the receiver-side rectifier input voltage u_2 , and the IPT coil currents i_1 and i_2 at a transmission of 5 kW output power are shown in **Fig. 3.15**. The close to sinusoidal shape of the inductor currents supports the fundamental frequency model presented in Section 2.1.4.

In order to assess the quality of the FEM-based component models presented above, an extensive experimental verification is performed. In the following, the measurement results are compared to the calculated values.

3.5.1 Equivalent Circuit Parameters

Tab. 3.4 shows the circuit parameters measured at an air gap of 52 mm and those obtained from the FEM tools. Indicated in brackets is the calculation error relative to the measured values. It can be seen, that the self-inductances are calculated accurately by both of the used FEM tools. The magnetic coupling is also accurate with an error of less than 10%. The highest error appears for the mutual inductance, because

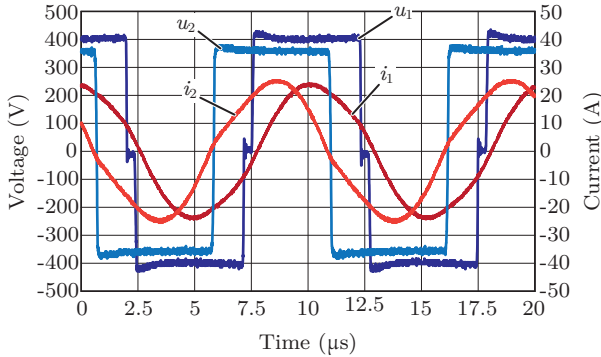


Fig. 3.15: Principal converter waveforms of the IPT system measured during the transmission of 5 kW with 400 V DC input voltage and 350 V DC output voltage across an air gap of 52 mm.

Tab. 3.4: Comparison of the measured and FEM-calculated equivalent circuit parameters at an air gap of 52 mm.

Variable	Measured.	FEMM	Ansys Maxwell
L_1	122 μH	129.9 μH (+6.5%)	126.8 μH (+3.9%)
L_2	70.3 μH	72.4 μH (+3%)	71.4 μH (+1.6%)
M	30.6 μH	33.9 μH (+10.7%)	33.3 μH (+8.8%)
k	0.33	0.35 (+6.1%)	0.35 (+6.1%)

in its calculation according to $M = k\sqrt{L_1L_2}$ the errors in the self-inductances and the magnetic coupling are adding up.

3.5.2 Thermal Measurements

In order to experimentally support the assumptions that were made for the simplified thermal model presented above, the component operating temperatures are measured. Two thermocouples (sensors 1-2) are positioned at the locations indicated in **Fig. 3.16(a)**, which shows the result of a thermal simulation of the transmitter coil. Sensor 1 is positioned between the winding and the PMMA cover. Sensor 2 is located on the ferrite core, which is in direct contact with the PVC housing. The temperatures are measured during a first experiment with only natural

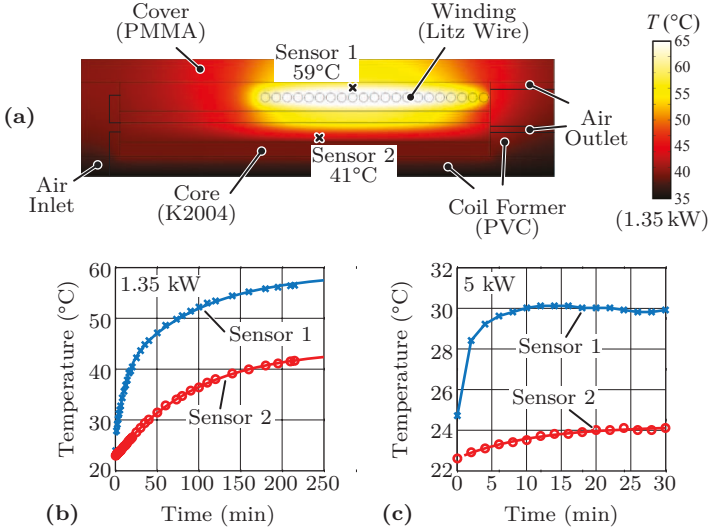


Fig. 3.16: (a) Thermal simulation model of the scaled prototype IPT coil with indicated sensor positions. (b) Temperatures measured with thermocouples at the indicated positions for 1.35 kW output power without cooling. (c) Measured temperatures at 5 kW output power using forced air cooling with compressed air.

convection cooling and during a second experiment, where forced-air cooling with compressed air is used. The measured temperatures for the two experiments are shown in **Figs. 3.16(b)-(c)**.

During the experiment without active cooling, the temperature measured by sensor 1 reaches the maximum rating of the PMMA cover if an output power of 1.35 kW is transmitted. For this operating point, the power losses in the transmitter coil are approximately 7 W and the surface-related power loss density is 10 mW/cm², which comes close to the estimated thermal limit of 15 mW/cm² for natural convection.

During the second experiment, the full output power of 5 kW is transmitted and forced-air cooling with compressed air is applied. The temperature measurement results are shown in **Fig. 3.16(c)**. Due to the active cooling, the steady-state temperatures are reduced significantly. The winding temperature (sensor 1) of 30 °C and the core temperature (sensor 2) of 24 °C are well below the thermal limit of the employed litz wire (150 °C) and the core material (100 °C). The temper-

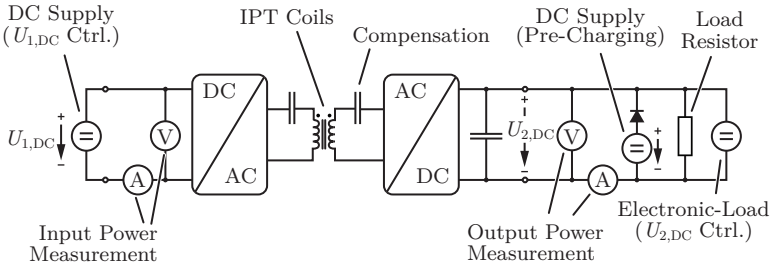


Fig. 3.17: Schematic of the experimental setup used for the DC-to-DC power loss measurements. The input DC-link voltage $U_{1,DC}$ is controlled with a DC supply and the output DC-link voltage $U_{2,DC}$ with an electronic load.

ature of the used PVC coil former and the PMMA cover are also below their maximum operating temperatures. At 5 kW output power, the surface-related loss density of the presented prototype is approximately 37 mW/cm^2 . Given the temperature increase of only 8°C above ambient temperature measured with sensor 1, the assumed thermal limit of 0.2 W/cm^2 for forced-air cooling with compressed air of the coils seems a valid preliminary assumption.

3.5.3 Measured Power Losses and DC-to-DC Efficiency

Due to the high frequency of the currents in the IPT coils and the steep slopes of the switched voltages, it is difficult to reliably measure the power loss in the resonant tank directly. For this reason, only measurements of the DC input power and the DC output power are taken with a power analyzer⁷. The used measurement setup is shown in **Fig. 3.17**. At the transmitter side, a DC supply is connected as the power supply. At the receiver side, a load resistor is used to dissipate the transmitted power. The output voltage is regulated with an electronic load operating in constant voltage mode, which is connected in parallel to the load resistor. The output power of the IPT system is shared between the passive load resistor and the active electronic load. In order to minimize startup transients, the DC-link capacitor at the output is pre-charged with a DC supply. In order to disconnect the pre-charging

⁷Yokogawa Precision Power Analyzer WT3000.

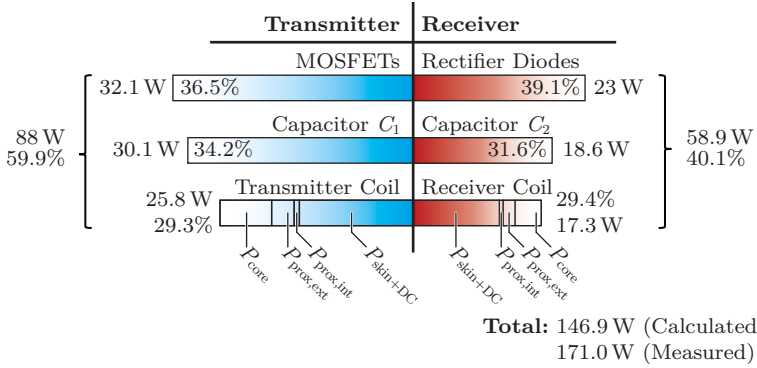


Fig. 3.18: Calculated loss components contributing to the total DC-to-DC conversion losses of the prototype IPT system at 5 kW output power and 52 mm air gap. The FEM-calculated loss components are divided into power losses due to the skin effect P_{skin} (including DC copper loss), the internal and external proximity effect $P_{prox,int}$, $P_{prox,ext}$, and core losses P_{core} .

supply from the rest of the circuit as soon as the power transmission is initiated, a diode is connected in series.

The measured power loss at the rated output power of 5 kW are compared to the sum of the calculated losses in the components of the prototype system in **Fig. 3.18**. The coil and capacitor losses are calculated as outlined in Section 3.2. Owing to the ZVS operation of the MOSFETs and because an external auxiliary supply is used to power the gate drivers, only conduction losses are included for the semiconductor losses of the transmitter-side inverter. Also the rectifier diodes⁸ on the receiver side are soft-switched and therefore only conduction losses have to be calculated for the semiconductor losses of the receiver. A thermal model is used to estimate the junction temperature of the devices for the calculation of the conduction losses based on the measured steady-state temperature of 35 °C of the custom-made heat sink.

The comparison in **Fig. 3.18** shows that the coil losses contribute about 30% of the total losses, while the remaining losses occur to approximately equal parts in the resonant capacitors and in the semiconductor devices. This clearly illustrates that for a holistic optimization of the IPT system, these components must be considered in addi-

⁸IXYS DSEI2x101 fast-recovery Si diodes.

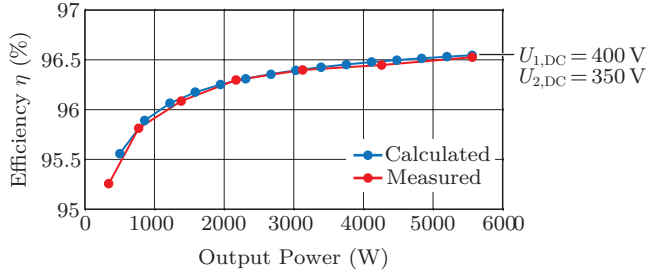


Fig. 3.19: Calculated and measured DC-to-DC efficiency, including losses in the IPT coils, resonant capacitors, and power semiconductors, as a function of the output power at 52 mm air gap. The output power is adjusted by controlling the DC-link voltages on both sides of the resonant circuit.

tion to those of the IPT coils.

The partitioning of the calculated coil losses into skin effect loss (including DC copper loss), proximity effect loss, and core loss is also given in **Fig. 3.18**. It can be seen that thanks to the small strand diameter of the used litz wire (71 μm), the main parts are the DC copper losses. Approximately 24% of the total power losses in the coils result from core losses.

The calculated total loss at 5 kW output power is 146.9 W, which means a calculation error of -14.2% with respect to the measured 171 W DC-to-DC conversion power loss. The calculation of the losses in the resonant capacitors and the semiconductors is assumed to be accurate, because it is based directly on manufacturer data. Therefore, the results indicate a good agreement of the FEM-based component models with the measurements.

To control the output power, the DC-link voltages at the input and the output are adjusted with the supply and the electronic load according to the control method described in Section 2.3. In a practical realization this can be implemented with two additional DC-DC converters on both sides of the IPT system. Since the current in the transmission coil can be decreased significantly below its nominal level during partial load operation, this control method leads to a good performance over a wide operating range as shown in **Fig. 3.19**. The power losses of the additional DC-DC converters required on both sides of the IPT system are not included in the shown results. However, given the high transmission efficiency that can be reached with this control method, it is

expected that the overall conversion efficiency is still higher than what can be achieved with other methods, even if the losses of the required DC-DC converters are included.

The measurements demonstrate a maximum DC-to-DC conversion efficiency of 96.5% of the IPT prototype system at an area-related power density of 1.47 kW/dm^2 , including losses in the IPT coils, the power semiconductors, and the resonant capacitors. This supports the used design principles and the optimization process presented in this chapter. An efficiency above 96% is measured over a wide operating range, which validates the proposed control concept.

3.6 Summary of the Chapter

In this chapter, a multi-objective IPT optimization process was introduced and validated with the design of a 5 kW IPT prototype system with a coil diameter of 210 mm and an air gap of 50 mm. The optimization was performed under consideration of the trade-off between the transmission efficiency η and the area-related power density α in an η - α -Pareto optimization. In addition, the trade-off between the efficiency and the magnetic stray field of the IPT coils was analyzed. An extensive experimental verification of the optimization method that included also a validation of the FEM field calculations used for the power loss estimation, as well as of the employed thermal model was presented in the last part of the chapter.

The main results of this chapter are summarized as follows:

- ▶ Development of FEM-based component models for the estimation of the power losses and the magnetic stray field of IPT coils.
- ▶ Design of a compact high-bandwidth magnetic field probe and experimental validation of the FEM-calculated magnetic fields.
- ▶ Demonstration of the multi-objective IPT optimization process on a scaled 5 kW IPT prototype system and experimental verification of the calculated results.
- ▶ Demonstration of a DC-to-DC efficiency of 96.5% at the maximum output power of 5 kW at an area-related power density of 1.47 kW/dm^2 and a coil diameter of 210 mm.

- ▶ Validation of the control method presented in Section 2.3.4 in the course of the experimental analysis of the scaled 5 kW prototype. Due to the proposed control method, the DC-to-DC efficiency of the prototype is above 96.0% down to 1 kW.

In the following chapter, the experimentally verified component models and the multi-objective IPT optimization process is applied to the design of the transmission coils of the contactless EV charger with 50 kW output power.

4

Optimization of the Transmission Coils

CONTACTLESS battery charging is an attractive solution for public transportation EV. Apart from the lower and less volatile operating costs that result from using electric energy instead of fossil fuels as the main energy source, IPT offers the additional advantage of a reduced standing time for recharging the vehicle batteries. If IPT charging platforms are installed, e. g., at bus stops or at taxicab stands, the battery is partly recharged along the route during regular operation of the vehicle. This significantly reduces the dwell time for a full battery recharge at the depot, and potentially enables a reduction of the number of fleet vehicles that operate a particular line, which leads an additional further cost reduction. As discussed in Section 1.2, this concept is termed *opportunity charging* by numerous OEM [18–20, 23, 26, 27].

The energy consumption of the EV charger has a high impact on the operational costs of a public transportation EV that is operated on a daily basis. Hence, the efficiency of the battery charging system is of high importance, independently of the used charging technology. In addition, particular attention has to be paid to the stray field of an IPT solution for public transportation EV charging. In the final application, the system is installed and operated in a public environment. Therefore, absolute safety of operation must be ensured and interference with other electronic equipment must be limited. Due to the high charging power level, this is particularly challenging. At the same time, the allowable weight and volume for the on-board charging equipment is limited by constructive boundary conditions. Therefore, a high power density is needed.

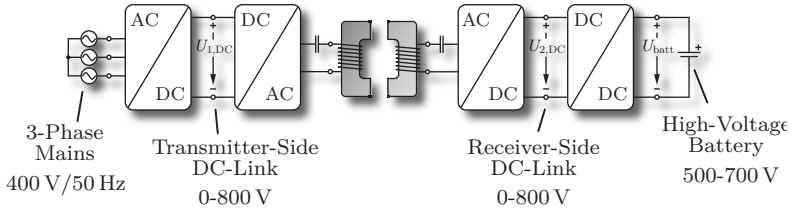


Fig. 4.1: Complete power conversion chain of the high-power IPT battery charger from the three-phase mains to the high-voltage battery of the EV, shown with indicated voltage levels.

It was shown in Section 3.3.2, that these performance factors are related by design trade-offs and the system performance is physically limited by Pareto fronts. Hence, a multi-objective optimization process was developed to take all aspects into account simultaneously. In this chapter, the procedure is applied to the design of a 50 kW contactless EV battery charging system.

The design specifications of the target application are discussed in Section 4.1, where also the most important design considerations for the transmission coil are described. Subsequently, in Section 4.2, the multi-objective optimization of the transmission coils is presented. In Section 4.3, practical design aspects, such as the active cooling system for the coil and the integration of the resonant capacitors, are discussed for the realized prototype system.

4.1 High-Power IPT Battery Charger

For the EV battery charger with a charging power level of 50 kW, a supply from the European 400 V/50 Hz three-phase mains is assumed as shown in **Fig. 4.1**. For the implementation of the control method presented in Section 2.3.4, variable DC-link voltages are needed at both sides of the resonant circuit for the regulation of the power flow and operation at the efficiency optimum. Therefore, a three-phase buck+boost-type mains interface [37, 71, 114] or a two stage solution with a boost-type mains interface and a series-connected DC-DC conversion [33, 70] is assumed for obtaining a controlled DC output voltage at the transmitter-side.

At this power level, mains interfaces are commonly designed with

Tab. 4.1: Specifications of the example IPT system.

Parameter	Variable	Value
Output Power	P_2	50 kW
Transmitter-Side DC-Link Voltage	$U_{1,DC}$	0-800 V
Receiver-Side DC-Link Voltage	$U_{2,DC}$	0-800 V
Battery Voltage	U_{batt}	500-700 V
Air Gap	δ	100-200 mm
Misalignment Tolerance	$\Delta x, y$	± 100 mm
Transmission Frequency	f_0	85 kHz

a DC-link voltage of 600-800 V, using 1.2 kV power semiconductor devices. A high DC-link voltage results in low currents in the transmission coils for a given power level. This lowers the conduction losses in the coils and depending on the number of turns also the magnetic stray field is reduced. Therefore, a nominal DC-link voltage of $U_{1,DC} = 800$ V is used at the transmitter-side of the IPT system.

At the receiver-side, a dedicated DC-DC conversion stage is considered for the regulation of the DC-link voltage. For obtaining a symmetrical system, a nominal DC-link voltage of $U_{2,DC} = 800$ V is desired also for the receiver-side. However, voltage levels of batteries designed for applications where high power and energy demands exist simultaneously, such as public transportation EV, are typically 500-700 V [115, 116]. Therefore, a power electronics topology with buck+boost capability is needed for the DC-DC conversion stage at the receiver. Such a solution is shown in Section 5.3, where the design of the DC-DC conversion stage for the full-scale hardware prototype is presented in detail.

The ground clearance of an electric bus is expected as 100-200 mm if also the pneumatic kneeling function of modern vehicles is taken into account. These values are used as reference for the width of the air gap of the IPT system. Additionally, a tolerance for the coil positioning of at least ± 100 mm is needed in all directions. The power electronic converter presented in Chapter 5 is dimensioned such that the full power of 50 kW can be transmitted at least up to this worst-case positioning.

As discussed in Section 1.3.6, the upcoming SAE standard J2954 is expected to specify a common transmission frequency band around 85 kHz to simplify interoperability between contactless EV battery

charging systems from different manufacturers [43]. For compliance with the upcoming standard and with the goal of demonstrating the physical efficiency limit that it implies, a transmission frequency of 85 kHz is considered.

A summary of the specifications of the presented contactless EV charger is given in **Tab. 4.1**. In the remainder of this section, the proposed geometry for the IPT coil is presented and the aspects that influences the material and component selection are discussed.

4.1.1 E-Type Transmission Coil with Rectangular Footprint

Several options for the IPT coil geometry were discussed in Section 3.2 and classified into E-type and C-type transmission coils regarding the path they provide for the coupled magnetic flux. It was discussed that for a given width of the air gap the area covered by the transmission coils is the determining factor for the magnetic coupling k , which together with the quality factor Q defines the Figure-of-Merit $FOM = kQ$. Therefore, it is important to optimally use the available construction volume by adapting the coil geometry to the geometric shape of the available space on the EV.

For the application discussed in this thesis, the coil geometry in **Fig. 4.2** is proposed. A rectangular winding is placed centrally on a ferrite core in order to achieve an E-type flux path. The ferrite core is split into several separated ferrite bars [93,94]. In practice the bars are realized by aligning multiple *I*-cores, which are widely available from various manufacturers. This reduces the coil weight significantly when compared to a core that completely covers the backside of the winding and does not significantly alter the field distribution due to the high relative permeability of the core material. To reduce the high-frequency losses in the conductor, copper litz wire is used for the windings.

The proposed orientation of the receiver-coil on the vehicle is such that the direction labeled as longitudinal direction is oriented towards the vehicle front and is therefore the direction of motion of the EV. As shown in detail in Section 4.3, the magnetic coupling reduces faster for a coil misalignment in the longitudinal direction of the IPT coil than in the lateral direction. This is the preferred mounting orientation, because for the driver an accurate positioning of the vehicle over the charging platform is easier in the direction of motion than in the lateral

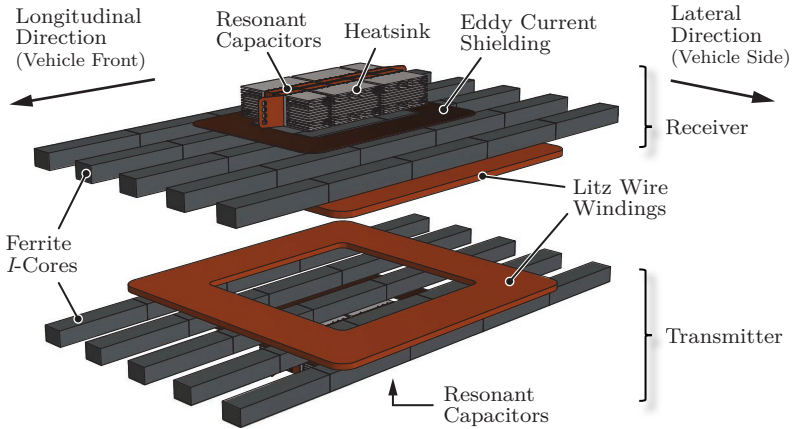


Fig. 4.2: IPT transmission and receiver coil geometry with rectangular footprint (transmitter and receiver are identical). Due to the central positioning of the windings, the flux path is shaped similar than in an E-core transformer.

direction, in which the tolerance therefore needs to be higher.

The transmitter coil and the receiver coil presented in this chapter are designed identically. In order to facilitate the experimental verification at 50 kW, an arrangement with energy feedback through a DC connection between the transmitter-side and receiver-side DC-link terminals is used (cf. Chapter 6). Even if a DC-DC conversion stage is used in both power electronic converters for regulating the output power via variable DC-link voltages, a design with equal nominal DC-link voltages is a favorable option. Hence, also equal inductance values are needed in order to fulfill the design equations (2.24)-(2.27) discussed in Section 2.2.4. In this work, this is achieved by using identical IPT coils. Another practical advantage of this solution is that owing to the equal DC-link voltages also the same power electronics hardware can be used for the transmitter and the receiver (cf. Chapter 5). Despite these simplifications, the results obtained from the multi-objective IPT optimization presented in this thesis can also be applied to a configuration with IPT coils of different size, as might be preferred in order to further reduce the required construction volume on the EV.

The resonant capacitors are mounted directly to the backside of each IPT coil, such that a compact charger module is obtained. The

magnetic field at the location of the resonant capacitor is relatively high despite the ferrite cores. Therefore, a copper plate is placed as an eddy current shielding between the ferrite bars and the capacitors.

A visualization of the field distribution in the proposed coil geometry as obtained from an FEM simulation of a two dimensional projection of the proposed coil geometry is shown in **Fig. 4.3**. Using the equations provided in Section 2.2.4, it can be shown that if all losses in the resonant circuit are neglected a phase shift of exactly 90° results between the current i_1 in the transmitter coil and the current i_2 in the receiver coil. **Figs. 4.3(a)-(d)** show a time sequence of the field distribution for this case. The E-type flux distribution is visible for the time instant where $i_2 = 0$ shown in **Fig. 4.3(a)**. A second interesting effect can be seen in **Fig. 4.3(d)**. Because the currents are equal in magnitude, the mutual flux is fully canceled and no field lines that cross both windings are visible. Nevertheless, the coils are magnetically coupled with $k = 0.33$.

Further details regarding the listed components and materials are given in the following parts. Later in the chapter, the multi-objective optimization of the presented coil geometry is presented.

4.1.2 Considered Coil Materials

Contrary to the optimization example of Chapter 3, the transmission frequency for the 50 kW EV charger is selected as 85 kHz based on a standard and is not a degree-of-freedom of the optimization. Therefore, a number of material parameters that normally result from the optimization can be selected in advance under consideration of the specified frequency. In this way, the number of variables for the multi-objective optimization is reduced and the evaluation process is accelerated.

Copper Litz Wire

The strand diameter of the copper litz wire that is employed for the winding is determined taking into account the skin depth of copper at 85 kHz, which is approximately 0.22 mm at room temperature. The calculated AC resistance per unit length for three different litz wires and a solid wire with equal copper cross-section is shown in **Fig. 4.4**. For the calculation, only the skin effect and the internal proximity effect are considered, i. e., the external magnetic field is assumed as $\vec{H}_e = 0$ [100].

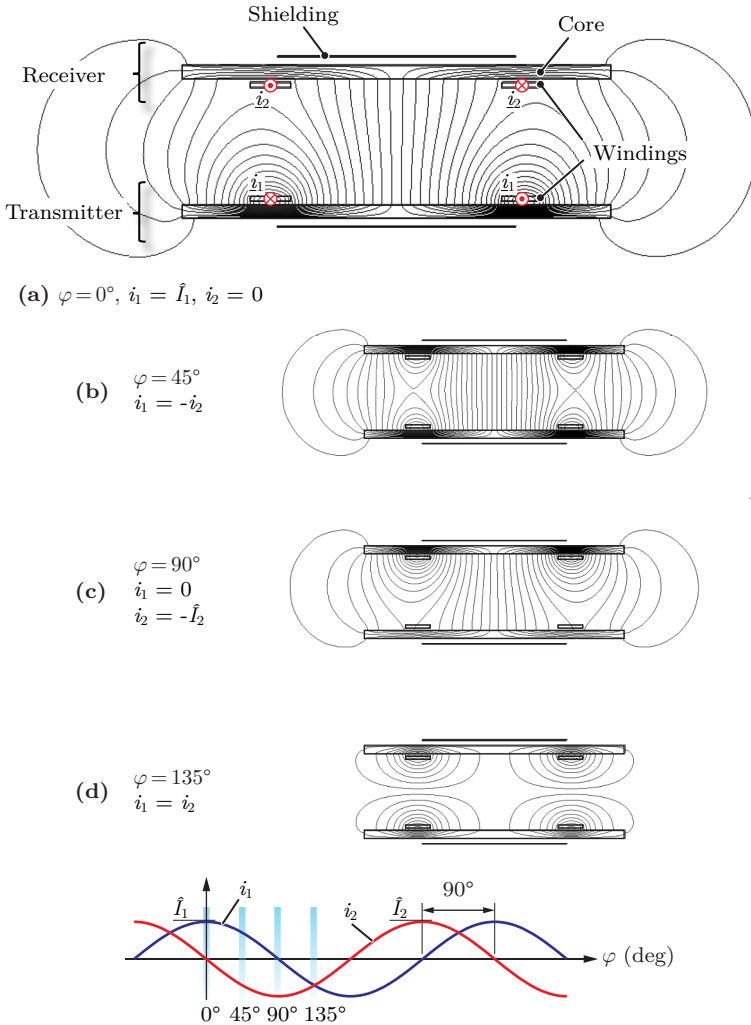


Fig. 4.3: FEM simulation result of a 2D projection of the transmission coil geometry: (a) time instant, where the transmitter current is at the maximum and the receiver current is zero (phase angle $\varphi = 0^\circ$), (b) where the currents have equal magnitude and opposite sign ($\varphi = 45^\circ$), (c) where the transmitter current is zero and the receiver current is at the maximum ($\varphi = 90^\circ$), and (d) where the currents are equal magnitude and sign ($\varphi = 135^\circ$).

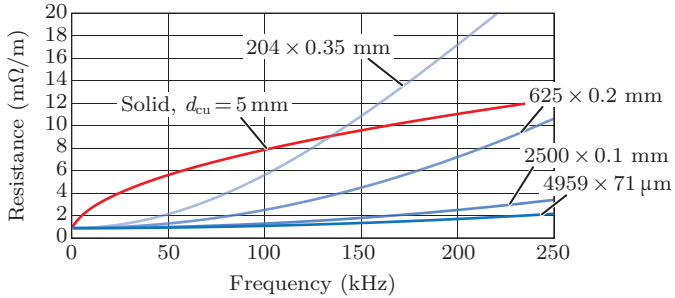


Fig. 4.4: AC resistance of a solid wire and of litz wires with the equal copper cross-section as a function of the frequency. The losses caused by DC conduction, skin effect, and internal proximity effect in the litz wires are considered. The effect of an external magnetic field is not included ($\hat{H}_e = 0$).

Therefore, the rapid increase of the AC resistance for the litz wires is mostly a result of the internal proximity effect in the litz wire bundles.

According to **Fig. 4.4**, choosing for instance a litz wire with strand diameter of 0.35 mm leads to higher power losses than what would occur in a solid wire already below 150 kHz. This is a result of the eddy currents that are induced by the neighboring currents within the litz wire bundle itself, which is termed internal proximity effect. The frequency dependency of the AC resistance suggests that as thin as possible strands are desirable for low losses. However, in the design of a conventional transformer, the choice of the litz wire strand diameter is also limited from below. Finer stranding of litz wires leads to lower packing factors, because an increasing amount of material is needed to isolate the individual strands. Therefore, for a given winding window of the transformer, the current density in the conductors has to be increased at a finer stranding. It is shown in [104], that in this case an optimum strand diameter exists where the reduction of the AC losses is balanced by the increasing DC conduction losses.

For the considered IPT coil geometry the winding cross-section is usually not as strictly limited as for a conventional transformer that has a winding window with fixed dimensions. The available space for the winding in the IPT coil is sufficiently large so that the lower packing factor for finer stranded litz wires does not significantly affect the design. Therefore, a litz wire strand diameter of 0.1 mm is selected for the prototype IPT system presented in this chapter. An even finer

stranding is not considered for manufacturing and cost reasons.

Core Material

Given the considered operating frequency of 85 kHz, power ferrites are considered for their low power losses per unit volume. The particular material employed in the final prototype is the manganese-zinc power ferrite K2004. In addition to the low losses, power ferrite cores are preferred because of their isotropic material properties that result from their manufacturing by pressing and sintering of iron oxides. This is a key difference, e. g., to tape wound cores. Isotropic material properties are of particular importance for IPT transmission coils, because the spatial orientation of the magnetic field exhibits large variations throughout the different core elements and also depends on the relative positioning of the transmitter and the receiver coil. If tape wound cores were used, high eddy current losses would occur where the core flux has spatial vector components orthogonal to the lamination [117]. For the same reason foil windings are not a good alternative to copper litz wire in this application.

Resonant Capacitors

Due to the high-frequency AC currents and the high series resonant voltages that results for the compensation capacitors in the considered series-series compensated topology of the IPT system, film capacitors present the only viable option for the design. High-power polypropylene film capacitors are an established solution for resonant power converters in related applications, for instance in inductive heating. The main reasons are their good thermal stability, the low impact of humidity on their capacitance value, and the excellent loss characteristics up to high frequencies [82].

For the IPT system presented in this thesis, polypropylene film capacitors of type CSP 120-200 from Celem with custom capacitance values are considered. According to the manufacturer, the dissipation factor $\tan \delta$ of these devices is in the range of 0.001 - 0.0014 at 85 kW. When operated at RMS currents above 80-100 A, they must be appropriately cooled via their terminals. For the thermal management of the film capacitors of the prototype system, a capacitor module with forced-air cooling is designed to prevent over-heating of the polypropylene inside the device. The aluminum heat sinks that are mounted to

the capacitor terminals can be seen in **Fig. 4.2**. The design of the resonant capacitor module with active cooling system is presented in Section 4.3.

Design of the Shielding

Since the resonant capacitors are mounted to the backside of the IPT coils (cf. **Fig. 4.2**), a shielding of the capacitor module is required to minimize eddy current losses in the capacitors and in the heat sinks mounted to their terminals. Different options exist for the shielding material, which are briefly outlined in the following.

Firstly, additional ferrite core elements could be employed. However, this would not significantly affect the field distribution at the backside of the coil. The flux that exits at the backside of the ferrite cores and closes far outside the coil can hardly be attracted by placing additional core elements in parallel to the existing low reluctance path.

Secondly, instead of additional ferrite cores a magnetic EMC shielding material such as permalloy could be used. These materials are effective as magnetic shielding due to their very high relative permeability. However, they are mainly intended for shielding DC or low-frequency AC magnetic fields and have limited effect at the considered operating frequency of 85 kHz. In fact, in [118, 119] it is shown that the initially high relative permeability of permalloy is entirely lost at high frequencies (cf. **Fig. 4.5**). Above 40 kHz the permeability of permalloy is approximately equal to that of silicon steel. However, a preliminary FEM-simulation of a silicon steel shielding showed excessively high hysteresis losses due to the high transmission frequency, which prohibit the use of this material as shielding.

As a third option, a conductive instead of a magnetic shielding material can be used. The eddy currents that are induced in a conductive plate produce an opposing magnetic field that counteracts its source. A FEM simulation result of a 2D projection of the considered shielding is shown in **Fig. 4.6(a)**. The effectiveness of the shielding is illustrated in **Fig. 4.6(b)**, where the remaining magnetic flux density at the backside of the receiver coil is shown. An area with a significantly lower magnetic flux density is created for the placement of the capacitor module.

In [89, 93], aluminum plates are proposed for the shielding of IPT coils. In order to determine the most suitable material for the eddy current shielding, a 3D FEM simulation of the designed prototype system is used to calculate the power losses in the shielding as a function of

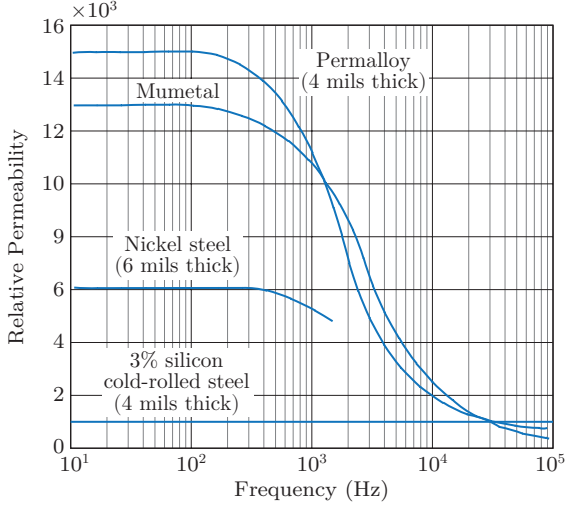


Fig. 4.5: Frequency-dependency of the relative permeability of potential shielding materials. (Figure reproduced from [118,119]. Publisher John Wiley & Sons, Inc., Authors: H. W. Ott, C. Paul, www.wiley.com).

the shielding conductivity σ_{sh} and the transmission frequency f_0 . The results are shown in **Figs. 4.6(c)-(d)**.

The losses in the shielding decrease inversely to the increasing material conductivity. The reason is that at a high conductivity of the material, the eddy currents in the shielding are impressed by the magnetic field of the IPT coil and therefore exhibit current source characteristics. Hence, the resulting power loss is proportional to the product of the source current squared and the eddy current resistance of the shielding. As shown in **Fig. 4.6(a)**, the eddy current in the shielding is concentrated in an area with a width proportional to the skin depth at the excitation frequency f_0 and the height t_{sh} of the shielding. The skin depth δ is given by

$$\delta = \frac{1}{\sqrt{\pi f_0 \sigma_{\text{sh}} \mu_{\text{sh}}}}, \quad (4.1)$$

where σ_{sh} stands for the shielding conductivity and μ_{sh} for the permeability of the shielding. Therefore, the approximate eddy current resistance R'_{eddy} per unit length follows as

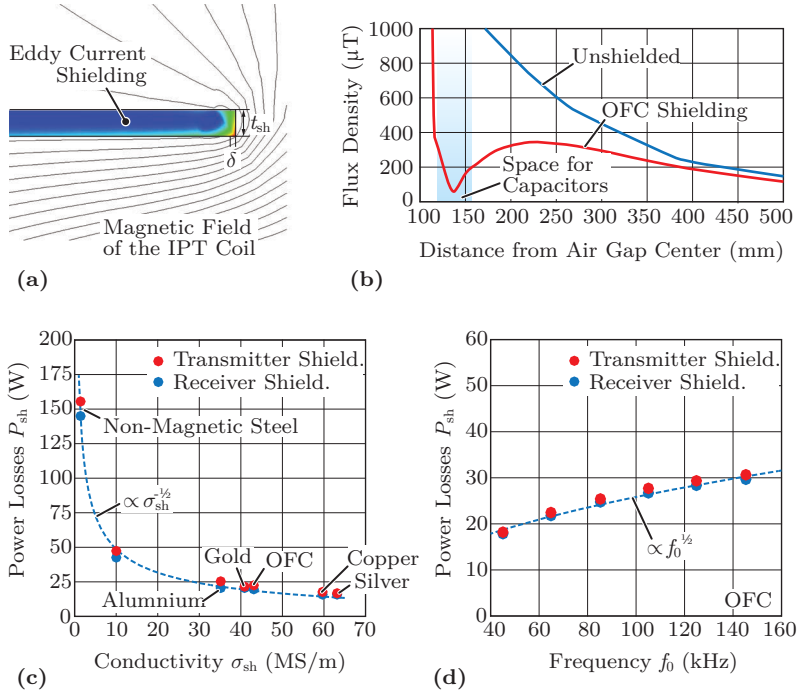


Fig. 4.6: (a) FEM-calculated eddy current density in a 2D projection of the shielding arrangement. (b) Magnetic flux density along a vertical axis positioned centrally on the backside of the receiver-coil, with and without OFC eddy current shielding. (c) 3D FEM-calculated power losses in the eddy current shielding at 85 kHz as a function of the conductivity and (d) of the frequency during the transmission of 50 kW.

$$R'_{\text{eddy}} = \frac{1}{\sigma_{sh} t_{sh} \delta} = \frac{\sqrt{\pi f_0 \mu_{sh}}}{\sqrt{\sigma_{sh} t_{sh}}} \quad (4.2)$$

With the assumption of an impressed eddy current I_{eddy} , a scaling law is found for the losses in the shielding

$$P_{sh} \approx I_{\text{eddy}}^2 R_{\text{eddy}} \propto \sqrt{\frac{f_0}{\sigma_{sh}}} \quad (4.3)$$

In **Figs. 4.6(c)-(d)**, fitted curves confirm this proportionality. A

high conductivity is preferable for the shielding. Particularly non-magnetic steel, as might be used for constructive elements of the vehicle chassis, can cause high power losses if exposed to the magnetic stray field. Therefore, a shielding as it is proposed here for the resonant capacitor module may in practice also be required to prevent power losses in the chassis.

In addition to the eddy current losses, the field cancellation caused by the eddy currents also has an effect on the field distribution in the air gap. This affects the coil self-inductance and causes a reduction of the magnetic coupling [120]. Since the shielding is necessary to prevent eddy currents in the resonant capacitors and their heat sinks, these adverse effects are accepted and taken into account in the design phase.

For the shielding of the prototype presented in this thesis, a sheet of Oxygen-Free Copper (OFC) with a conductivity of approximately 43 MS/m and a thickness t_{sh} of 2 mm is used. As shown in **Figs. 4.6(c)-(d)**, the resulting losses in the shielding are around 25 W at 50 kW output power.

4.2 Multi-Objective Coil Optimization

After the introduction of the components and materials of the proposed transmission coil geometry, in this section the FEM-based multi-objective optimization of the IPT coils is presented. In the first part, necessary adaptations for the power loss estimation in the proposed coil geometry are introduced and the employed thermal model is discussed. In the second part, the optimization results are presented.

4.2.1 Power Loss Calculation Models

Since the proposed coil geometry of **Fig. 4.2** has no 2D symmetry, the prototype coils have to be analyzed with 3D FEM models instead of just 2D models as in the previous chapter. This requires model simplifications for the power loss estimation, because 3D FEM simulations are significantly more computationally intensive.

3D FEM Modeling of the Transmission Coils

A simplification that is common for simulating conventional transformers or electrical machines using FEM tools is to model the copper wind-

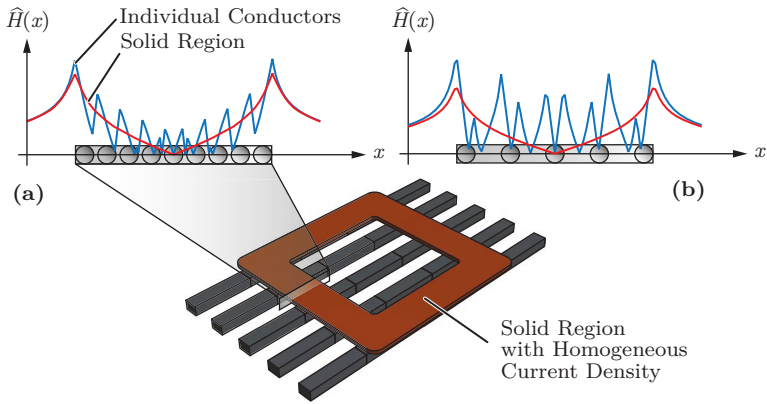


Fig. 4.7: (a) FEM-calculated magnetic field amplitude $\hat{H}(x)$ in a winding modeled with individual conductors and with a solid copper region of equal outer dimensions for a small spacing between the conductors and (b) for a larger spacing.

ings as a solid copper region with the same current density than in the original conductors. The same approximation is also used in the 3D FEM models of the prototype IPT coil designed in this chapter. The main advantage is that because the windings are not modeled in full detail, the required calculation time is lower than for the initially much more complex 3D model. The magnetic losses and the equivalent circuit parameters can still be determined accurately if the geometry of the solid copper regions approximately match the actual windings. For the winding loss calculation an analytical model is needed, because the field distribution inside the solid copper region is not the same as for individual conductors.

In **Fig. 4.7(a)**, the used 3D FEM model and a comparison of the magnetic field \hat{H} in the winding obtained from a 2D FEM simulation is shown for a solid copper region and individual conductors. As expected, the magnetic field inside the winding is not captured accurately if only a solid region is used in the model. Particularly if the spacing between the conductors becomes larger, as shown in **Fig. 4.7(b)**, the current distributions differ more significantly for the two cases and the field inside the windings is modeled inaccurately.

The field outside of the winding is still in good agreement for both

Tab. 4.2: Comparison of the measured and FEM-calculated transformer equivalent circuit parameters of the prototype transmission coils.

Variable	Measured	Calculated	Error
L_1	68.2 μH	71.6 μH	+1.4%
L_2	70.6 μH	71.6 μH	+5.0%
M	15.4 μH	16.5 μH	+7.4%
k	0.2214	0.2318	+4.7%

models. This means that the calculation of the magnetic energy stored in the field is still sufficiently accurate. Hence, the self- and mutual inductances can be predicted with the simplified model. The accuracy is confirmed by the comparison of the FEM-calculated values for the transformer equivalent circuit parameters obtained from the tool Ansys Maxwell and the parameters measured for the realized prototype IPT coils presented in **Tab. 4.2**.

The simplified model of the winding allows an accurate calculation of the magnetic fields only outside of the windings. The results can be used to estimate the equivalent circuit parameters, the losses in the magnetic cores and in the shielding elements, as well as the magnetic stray field of the IPT coils. However, an evaluation of the FEM-calculated fields for the estimation of the losses in the litz wire winding as in Section 3.2.3 is no longer accurately possible due to the necessary model simplifications. Instead, an analytical calculation model is given in the following.

Modified Winding Loss Model

As an alternative to an FEM-based winding loss calculation, a winding loss model based on analytical field calculations in two dimensional projections of the proposed coil geometry is used for the optimization. As shown in **Fig. 4.8(a)**, three cut surfaces (labeled A,B,C) are defined in the 3D model. The magnetic field on the three cut surfaces is calculated approximatively along the axis through the conductor centers, denoted x in **Fig. 4.8(c)**. For the analytical calculation, a number of assumptions are required:

- Corner effects that distort the 3D field distribution cannot be captured with the employed 2D models. The geometry of the cut

surface is assumed as infinitely extended in the direction of the plane and corner effects are therefore neglected.

- ▶ The current distribution within the conductors and hence also the magnetic field is assumed to be the same as for the DC case, because the chosen litz wire strand diameter of 0.1 mm is small in comparison to the skin depth (0.22 mm for 85 kHz).
- ▶ The AC losses are calculated separately for each coil, because the magnetic field caused by the receiver-coil in the windings of the transmitter is significantly smaller than the field that is caused by the current in the neighboring conductors within the transmitter winding itself. Vice versa, the same holds for the receiver-coil.
- ▶ The core elements are assumed to be ideal magnetic conductors of infinite permeability, which is a good approximation given the relative permeability of the ferrite of $\mu_{r,fe} \approx 2000$. Furthermore, the cores are assumed to be non-conductive and field distortions due to eddy currents in the core are neglected.

With these approximations, the magnetic field on the cut surfaces A, B, and C is calculated by solving Ampère's law for each conductor separately and superposition of the results. For cut surface A, the y -component of the magnetic field along the x -axis through the conductor centers [cf. **Fig. 4.8(c)**], caused by conductor $i = 1, 2, \dots, N$ located at position $x = x_i$ and carrying the current \hat{I} , results as

$$\hat{H}_y(x, x_i) = \begin{cases} \hat{I}(x - x_i)/(\frac{1}{2}\pi d_a^2), & \text{for } |x - x_i| < d_a/2 \\ \hat{I}/(2\pi(x - x_i)), & \text{otherwise,} \end{cases} \quad (4.4)$$

where d_a represents the outer diameter of the conductor. The complete magnetic field is given by the superposition of the results for all N conductors. For cut surface A, in which no core elements are contained, this calculation is straightforward and the analytically calculated solution exactly matches the result of the 2D FEM calculation in **Fig. 4.8(f)**.

The surfaces B and C cut through core elements, which alter the field distribution in the winding. To capture the effects of the cores, the *mirroring* or *imaging method* is applied [100,121]. For cut surface B, the winding is mirrored at the core surface as indicated in **Fig. 4.8(d)**. The magnetic field of the mirrored conductors is added to the solution for the

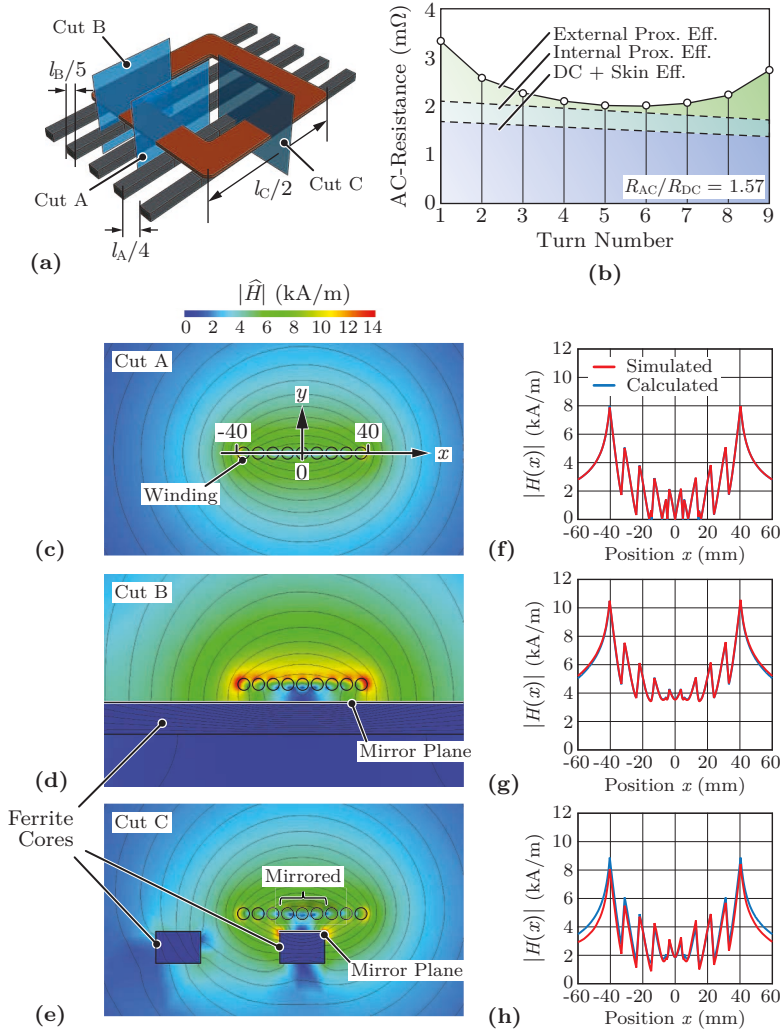


Fig. 4.8: (a) Definition of the cut surfaces A, B, and C used for the estimation of the AC losses. (b) Calculated AC resistance for each turn of the winding of the realized prototype IPT coil. (c)-(e) FEM-calculated magnetic field distribution and (f)-(h) comparison to the analytically calculated magnetic field for a current of 100 A.

cut surface A. This approximation is valid as long as the permeability of the core is significantly higher than that of the surrounding medium. The calculated result is compared to the result of the FEM simulation in **Fig. 4.8(g)**. Also for the calculation on cut surface B, a good agreement with the FEM results is achieved.

For cut surface C, the *imaging method* is applied only for the core that is positioned below the winding. The effect of the second core, which is located outside the winding, is neglected to simplify the analysis. For the example shown in **Fig. 4.8(e)**, the three central conductors of the winding, which are positioned vertically above the core, are mirrored at the core surface. Like for cut surface B, the field of the mirrored conductors is added to the solution for cut surface A. In this case, the agreement between the calculated result and the FEM analysis shown in **Fig. 4.8(g)** is satisfactory, even if it is not as good as for the other two cases.

The AC power losses are calculated for each turn of the winding and for each of the cut surfaces A, B, and C individually. For the estimation of the power losses due to the external proximity effect, the magnetic field obtained from the analytical process described above is evaluated at the center of each conductor. For the internal proximity effect in the litz wires and for the skin effect, the analytical models of [100] are used. The AC resistances per unit length calculated on each cut surface are multiplied by the length contribution l_A , l_B , and l_C of the respective cut surface to the total length of each conductor and added up to obtain the AC resistance of every conductor in the winding (cf. **Fig. 4.8(a)**).

The result of the calculation is shown in **Fig. 4.8(b)** for each of the nine turns in the winding of the coil prototype optimized in this chapter. The partitioning into DC loss and skin effect, internal proximity effect, and external proximity effect is also given. The turn denoted by turn number 9 is the innermost turn of the winding and has therefore the shortest total conductor length and the lowest DC resistance. The total AC resistance of the winding is obtained as $R_{AC} \approx 22.5 \text{ m}\Omega$ by adding up the AC resistance of each turn. The estimated AC-to-DC resistance ratio is $R_{AC}/R_{DC} \approx 1.57$ at 85 kHz for the winding of the coil prototype with a litz wire comprising $2500 \times 0.1 \text{ mm}$ strands and outer diameter $d_a = 7.4 \text{ mm}$.

Power Losses of the Remaining Components

As stated above, the FEM-calculated magnetic fields are accurate outside the simplified solid copper region that is used to replace the individual conductors of the windings. Hence, the power loss density in the employed ferrite cores can be calculated as in Section 3.2.3 by means of the Steinmetz equation. The result is integrated over the core volume within the FEM tool to obtain the total core losses.

Similarly, to determine the losses in the shielding, the power loss density due to the eddy currents can be integrated over the volume of the shielding. In the FEM tool, the mesh of the shielding is refined at the surface for a better resolution of the eddy current calculation and a better accuracy of the power loss estimation.

For the power losses in the resonant capacitors, the dissipation factor $\tan \delta$ obtained from the device manufacturer is used as in Section 3.2.4.

4.2.2 Thermal Model

For the thermal management of the power losses in the transmission coils at 50 kW, a forced-air cooling system is considered. Therefore, for the multi-objective optimization the thermal model shown in **Fig. 4.9** is used. The thermal resistance $R_{\text{th,cu,hs-surf}}$ models the heat conduction from the hotspot inside the winding to the winding surface. The heat transfer on the winding surface due to the forced convection is represented by the thermal resistance $R_{\text{th,cu,surf-amb}}$. Equal models are assumed for the top and bottom winding surface. For the ferrite cores a similar model is assumed. $R_{\text{th,fe,hs-surf}}$ represents the thermal resistance from the hotspot inside the core to the core surface, while the heat transfer by forced convection at the surface is modeled by $R_{\text{th,fe,surf-amb}}$. The model is calculated for the top surface and the surfaces at the sides of the ferrite cores. For the winding as well as for the cores, the respective power losses P_{cu} and P_{fe} are assumed to be uniformly distributed over the whole component volume. A more detailed consideration would require extracting the exact loss distributions from the magnetic FEM simulation and coupling the results to a thermal FEM simulation. This is omitted to accelerate the computations for the power loss estimation. The results that are obtained with the simplified calculation are sufficient to provide a fundamental understanding of the design trade-offs of the IPT system.

The heat transfer via forced convection cooling at the core and wind-

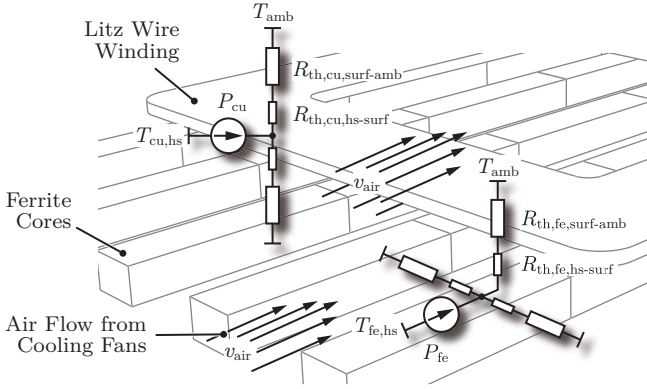


Fig. 4.9: Thermal model considered for the calculation of the hotspot temperatures in the litz wire winding and the ferrite cores of the IPT coils.

ing surfaces is estimated using the models of [122, 123], which have shown highly accurate results for the heat sink modeling presented in [124]. The models allow approximating the surface heat transfer for selected surfaces in the arrangement using the geometric dimension and the characteristics of cooling fans. Assuming that axial cooling fans are placed at both sides of the coil (cf. Section 4.3 for the final coil assembly), the fluid flow in the air channels between the ferrite cores and the winding and between the topside cover of the coil housing and the winding can be approximated by the models of [124].

Based on these models, the heat transfer coefficient at the channel surfaces can be estimated. The average surface heat transfer coefficient for the winding \bar{h}_{cu} and for the ferrite cores \bar{h}_{fe} are estimated for the geometry parameters considered in the optimization presented below. The calculated values for the average surface heat transfer coefficients are $\bar{h}_{cu} \approx 100 \text{ W}/(\text{m}^2 \text{ K})$ for the winding and $\bar{h}_{fe} \approx 100..200 \text{ W}/(\text{m}^2 \text{ K})$ for the ferrite cores. Therefore, as a conservative model, $\bar{h}_{cu} = \bar{h}_{fe} = 100 \text{ W}/(\text{m}^2 \text{ K})$ is used. The maximum surface-related power loss density for the windings and the core is calculated as

$$p_{\text{surf,max}} = \bar{h}_{cu/fe} \cdot (T_{\text{max,cu/fe}} - T_{\text{amb}}), \quad (4.5)$$

and the thermal resistance representing the heat transfer by forced-air convection is given by

$$R_{\text{th,cu/fe,surf-amb}} = \frac{1}{\bar{h}_{\text{cu/fe}} \cdot A_{\text{cu/fe}}} \quad (4.6)$$

where $T_{\text{max,cu/fe}}$ stands for the maximum allowable temperature of the core or winding surface $A_{\text{cu/fe}}$. The ambient temperature is assumed as $T_{\text{amb}} = 45^\circ\text{C}$ for the whole design procedure. The result for $p_{\text{surf,max}}$ is approximately $0.35\text{--}0.75\text{ W/cm}^2$ for maximum surface temperatures between 80°C and 120°C . This is in good agreement with the theory and the experimental measurements presented in Section 3.5.2, as well as with the typical values given in [108].

For the thermal resistances $R_{\text{th,cu/fe,hs-surf}}$ that represent the heat conduction from the hotspots in the winding and in the ferrite cores to the winding and core surfaces, the geometry parameters used in the optimization lead to values that are significantly smaller than the thermal resistance $R_{\text{th,cu/fe,surf-amb}}$ that models the forced convection at the surface. This is mainly a result of the thermal conductivity of the litz wire and the ferrite. Therefore, the thermal resistances $R_{\text{th,cu/fe,hs-surf}}$ are neglected in the following, but the maximum allowable surface temperatures are chosen with a margin of 10°C below the rated maximum temperatures of the components.

4.2.3 Optimization Methodology

After the discussion of the models for the power loss estimation and the thermal analysis, the required modifications to the optimization procedure employed in Chapter 3 are briefly discussed in the following.

Degrees-of-Freedom of the Optimization

The available degrees-of-freedom for the proposed IPT coil geometry are shown in **Fig. 4.10**. For the optimization, the parameters of the coil geometry, namely the number of ferrite cores N_{fe} , outer coil dimensions W_{coil} and L_{coil} , width of the winding w_{cu} , and position of the winding on the core d_{cu} , are evaluated in a parameter sweep similar to the procedure discussed in Section 3.3.1. In **Tab. 4.3**, the parameter space for the considered degrees-of-freedom is listed.

The remaining geometry parameters, height h_{cu} of the winding and dimensions h_{fe} and d_{fe} of the cores, are kept constant in order to limit the number of evaluated parameter sets. For the ferrite cores, the dimensions of a standard I -core are used. Like in Section 3.3.1, only single

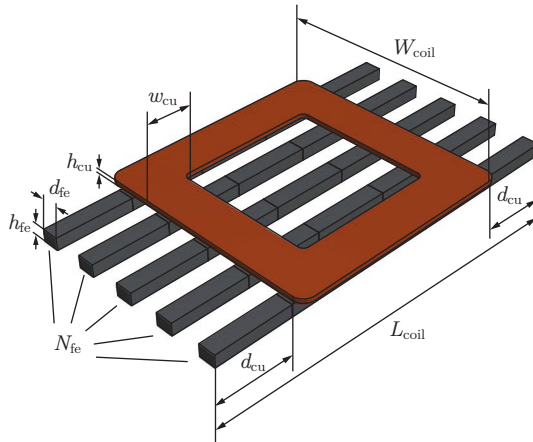


Fig. 4.10: The degrees-of-freedom of the multi-objective optimization are the number of ferrite cores N_{fre} , the coil outer dimensions W_{coil} and L_{coil} , the width of the winding w_{cu} and the position of the winding on the core d_{cu} . The height h_{cu} of the winding and the dimensions h_{fe} and d_{fe} of the cores are kept constant.

layer coils are considered because of their low profile and the lower self-capacitance, which leads to a higher self-resonant frequency. Therefore, the height of the winding h_{cu} is set to the diameter of a standard litz wire with a copper cross-section that would lead to a current density of approximately 5 A/mm^2 . This is a valid simplification, because the height of the windings has only a small influence on the self-inductance values and on the magnetic coupling between the transmitter and the receiver coil.

Optimization Procedure

In the optimization process presented in Section 3.3.1, a large look-up table was used to map coil dimensions and turns numbers to self-inductance and magnetic coupling values. This look-up table was generated with a high number of FEM simulations. During the optimization, the transmitter and the receiver coil were selected from the table separately. Therefore, the magnetic coupling had to be re-calculated and the transmission frequency was adapted to achieve the maximum efficiency. In the optimization presented here, the considerably higher

Tab. 4.3: Parameter space for the multi-objective coil optimization.

Parameter	Variable	Min.	Max.	# Points
Coil Length	L_{coil}	550 mm	700 mm	4
Coil Width	W_{coil}	300 mm	600 mm	7
Winding Position	d_{cu}	40 mm	100 mm	4
Winding Width	w_{cu}	50 mm	150 mm	6
Number of Cores	N_{fe}	3	7	3

computational effort for the 3D instead of axis-symmetric FEM simulations prohibits the generation of a look-up table. Additionally, the transmission frequency is considered a fixed parameter and cannot be changed during the optimization. Therefore, the modified procedure of **Fig. 4.11** that incorporates fewer FEM simulation steps is used. It should be noted that the values for the coil width W_{coil} and the number of cores N_{fe} are selected such that there always remains a gap between the individual ferrite bars. A design with a solid plate of ferrite instead of ferrite bars is not included in the design space.

The optimization starts with the definition of the system specifications, the coil geometry, and the employed coil materials (steps 1-3). Based on the definition of a parameter space, the parameter sweep is started (step 4), in which the performance of every possible combination is evaluated.

In the first FEM simulation, the A_L -value that results for the evaluated coil arrangement is calculated (step 5). The A_L -value is defined as the ratio of the coil self-inductance and the turns number squared $A_L = L_1/N_1^2$. Since the transmitter and the receiver coil are designed identical for equal DC-link voltages at the input and the output, it is unimportant which coil is considered for the calculation of the A_L -value. The magnetic coupling k is also obtained from the first FEM simulation step. Since the magnetic coupling is unaffected by a modification of the turns numbers as long as the winding dimensions remain the same, this value can subsequently be used for the design of the coil self-inductances without re-calculation.

Based on the magnetic coupling k the required self-inductances are calculated according to (2.24)-(2.27), from which the primary and secondary turns numbers $N_1 = N_2$ are derived using the A_L -value (step 6). The resonant capacitors are dimensioned according to the guidelines in

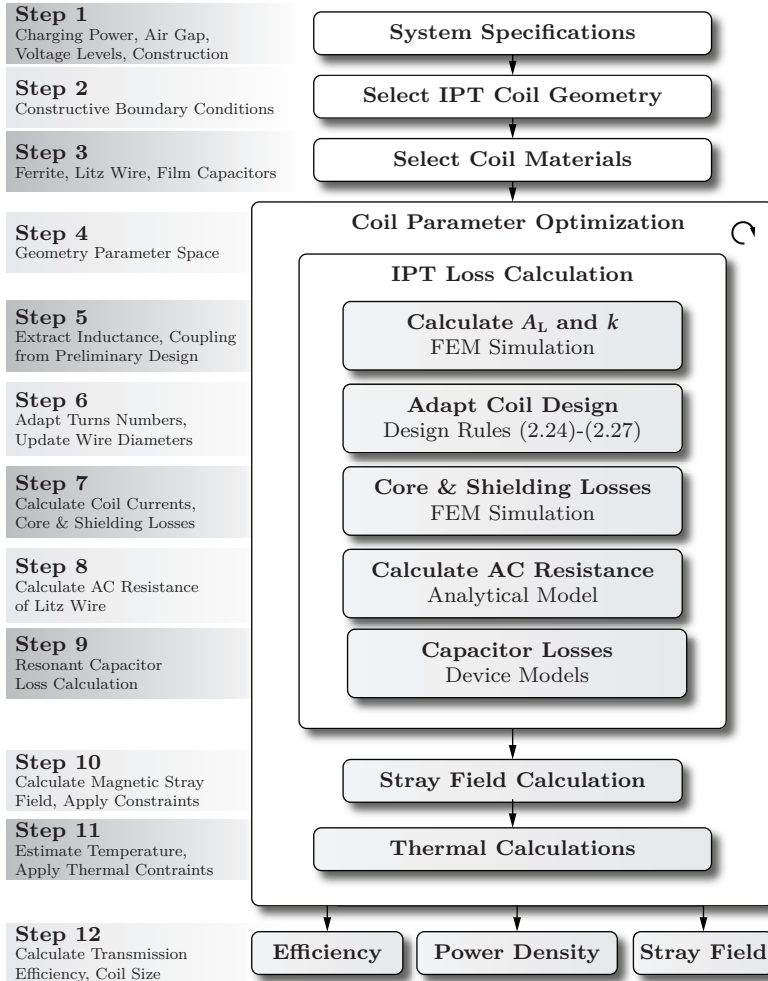


Fig. 4.11: Modified multi-objective optimization process for the IPT coils of the 50 kW EV battery charger (compare to Fig. 3.5).

Section 2.2.1, taking into account the voltage ratings of the selected film capacitors to determine the number of required devices and their weight. With the parameters of the transformer equivalent circuit for the IPT coils and the dimensioned resonant capacitors, the magnitude and the phase of the transmitter and receiver-coil currents can be determined. Then, in a second FEM simulation the losses in the ferrite cores and the eddy current shielding as well as the magnetic stray field are determined at the actual current values (step 7).

For the calculation of the AC losses in the litz wire winding, the analytical winding loss model presented above is used (step 8). The litz wire diameter is chosen such that the width of the winding w_{cu} is the same for the simulated solid copper region and the actual winding with N_1 or N_2 closely spaced individual conductors. If the copper cross-section of the winding with the adapted turns number differs by more than a factor of 1.5 from that of the simulated solid copper region, the considered design is discarded. The number of strands follows from the calculated litz wire diameter, the previously selected strand diameter, and a litz wire packing factor of 0.45 that was estimated based on manufacturer data. The capacitor losses are calculated based on the data sheet values for the power losses as provided by the manufacturer (step 9). This completes the IPT power loss estimation for the selected design.

Based on the result of the power loss calculation, the surface temperatures are calculated with the thermal model discussed above and the design constraints for the copper and ferrite temperatures are applied. Similarly, at this point a constraint for the magnetic stray field could be applied if desired (steps 10-11). A feedback of the calculated device temperatures to the power loss calculation is not included for reducing the required number of FEM simulations. Instead, in the calculation an approximate operating temperature of 80 °C is assumed for the copper and ferrite components.

In the last step, the performance factors for the coil design are extracted and stored in a results database (step 12).

4.2.4 Discussion of the Optimization Results

The calculated transmission efficiency η for the evaluated coil designs is shown in **Fig. 4.12(a)** as a function of the area-related power density α , and as a function of the gravimetric power density γ in **Fig. 4.12(b)**.

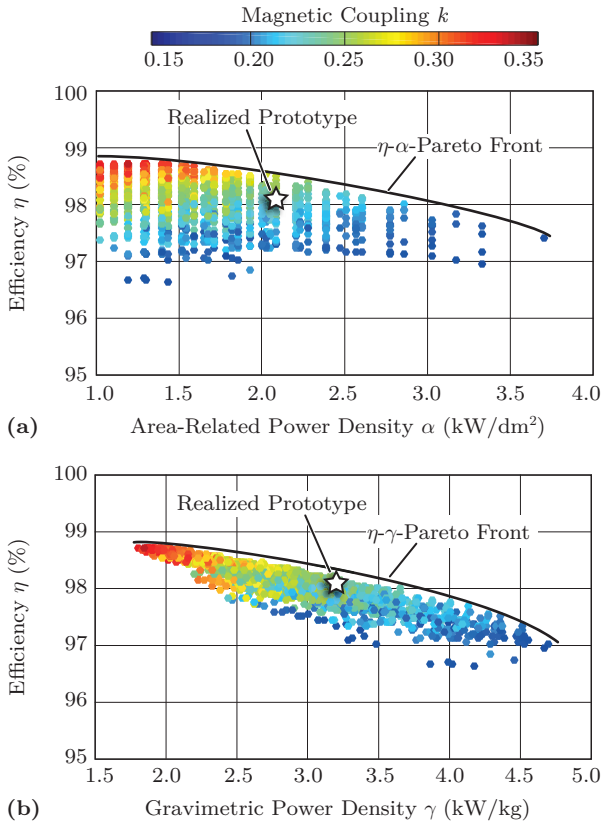


Fig. 4.12: Results of the multi-objective coil optimization: (a) η - α -Pareto front and (b) η - γ -Pareto front for the 50 kW transmission coil design. Included are all losses and component weights of the resonant circuit, i. e., the litz wire windings, the ferrite cores, the eddy current shielding, and the resonant capacitors.

Included are the losses in the litz wire windings, the ferrite core losses, the losses in the resonant capacitors, and the eddy current losses in the shielding. The area-related power density is defined as $\alpha = P_2/A_{\text{coil}}$, where $A_{\text{coil}} = L_{\text{coil}}W_{\text{coil}}$ represents the area covered by the winding and the cores. The gravimetric power density is given by $\gamma = P_2/m_{\text{coil}}$, where m_{coil} stands for the active mass of one IPT coil, including the ferrite cores, the eddy current shielding, the litz wire winding as well as the weight of the resonant capacitors. In both figures, the magnetic coupling k is the parameter for the coloring of the points.

For smaller coils with a higher area-related power density, the magnetic coupling is lower due to the smaller active coil area. Thus, the transmission efficiency is reduced. However, the smaller size of the transmission coils also leads to a lower active mass and, therefore, a higher gravimetric power density. At the performance limit, the area-related power density α or the gravimetric power density γ can only be increased at the cost of a lower transmission efficiency η . This design trade-off is described by the η - α - and the η - γ -Pareto fronts, which are drawn schematically in the figure.

For EV applications, a high area related power density as well as a high gravimetric power density are desirable for the vehicle-side system components. As discussed in Section 1.3.1, for a conductive 6.1 kW EV charger a gravimetric power density of 3.8 kW/kg is achieved in [28] at 95% efficiency from the mains to the battery. Comparing this value to the results shown in **Fig. 4.12(b)**, which include only the receiver coil and not the power electronics, highlights the low compactness as a main design challenge for IPT systems.

A low magnetic stray field presents the third key performance factor for a contactless EV charger. The IPT system must comply with the relevant safety standards for the magnetic field [39–41] in all regions that are accessible to humans, i. e., in the passenger cabin and at all sides of the vehicle. Since the passenger cabin is shielded by the metallic chassis of the EV, the main concern is the stray field around the vehicle. In practice, the magnetic field would be measured with a field probe at test locations within this area, at a fixed distance from the EV specified by a standard.

For the presented multi-objective optimization, the influence of the EV chassis is not included in the sense of a worst case analysis. In analogy to the compliance test measurements and assuming that the IPT coil is mounted centrally below the EV, the magnetic stray field

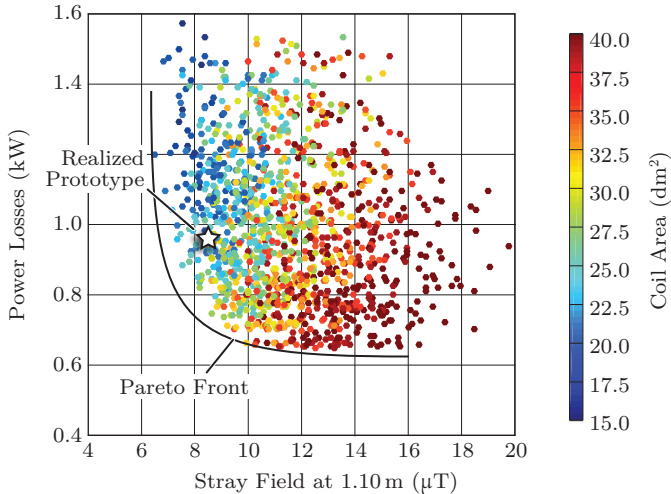


Fig. 4.13: Trade-off between the total losses of the coil designs and the magnetic stray field at a fixed observation point located at a distance of 1.10 m (critical distance in the considered application) on an axis oriented in the lateral direction of the IPT coil. At the Pareto front a further reduction of the magnetic stray field requires smaller IPT coils, which leads to higher power losses.

is sampled at a fixed distance of 1.10 m from the coil center (critical distance in the considered application) on a horizontal axis, which starts at the air gap center point and is oriented in the lateral direction of the IPT coil geometry. The obtained results are shown in **Fig. 4.13**. The coloring represents the coil area of each design. A Pareto front exists at which for a further reduction of the magnetic stray field higher power losses must be accepted. At the boundary, the stray field can only be reduced if the magnetic field source, i.e., the IPT coils, are made smaller and therefore the distance of the current carrying conductors to the fixed observation point becomes larger. Hence, a trade-off is found between the coil size, the power losses, and the magnetic stray field. This is in good agreement with what was observed in Section 3.3.2 for the scaled 5 kW prototype system.

The factors that determine the weight of the transmission coils are highlighted in **Fig. 4.14**. The most significant weight contribution is the weight of the ferrite core material, as shown in **Fig. 4.14(a)**.

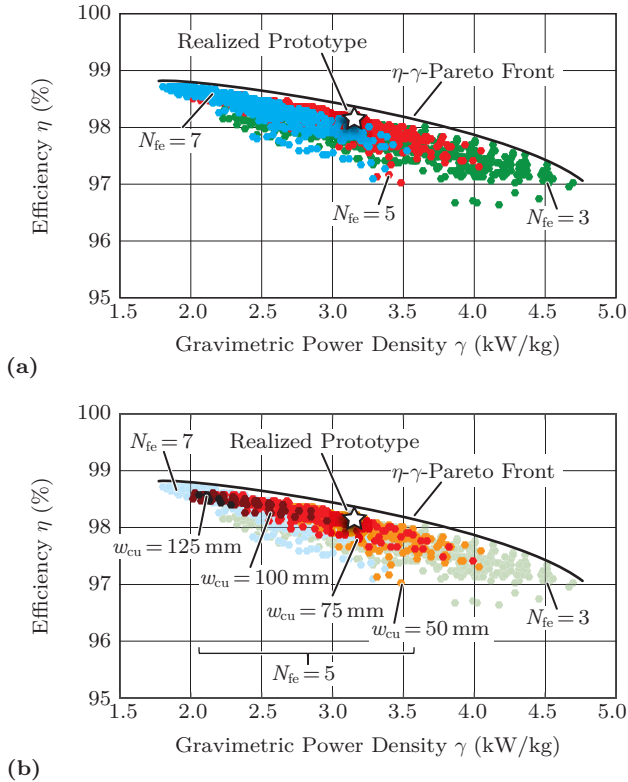


Fig. 4.14: Separation of the design points of the η - γ -Pareto front according to (a) the number of ferrite cores N_{fe} and (b) the width of the winding w_{cu} , which determines the copper mass. The magnetic core elements contribute the largest part of the total coil weight. Lighter coils are realizable with a smaller core or copper cross-section, which lead to a lower transmission efficiency due to increased hysteresis and copper current conduction losses.

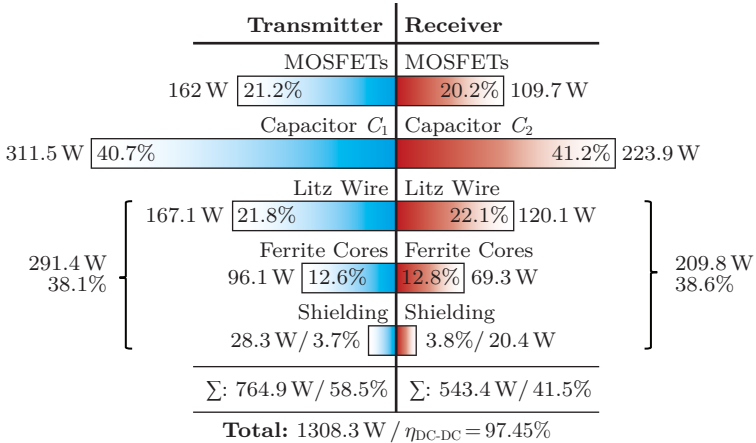


Fig. 4.15: Power loss contributions of the resonant circuit components and of the power semiconductors to the total losses of the IPT system.

This confirms that the division of the core into parallel I -core rods instead of a solid ferrite plate is a useful approach for weight reduction. Despite the reduced core cross-section, the maximum core flux density is below 175 mT for all of the design points shown in the figures. The lower saturation flux density of the ferrite is therefore no limiting factor. Nevertheless, the hysteresis losses in the ferrite are higher for the designs with a lower number of cores N_{fe} due to the higher flux density and consequently the higher power loss density in the cores.

As shown in **Fig. 4.14(b)**, the weight of the litz wire winding is the second main component that determines the weight of the transmission coils. Coils with a lower winding width w_{cu} and consequently with a smaller copper cross-section are lighter, but they have a lower efficiency as a result of the higher copper current conduction losses.

4.2.5 Selected Design for the Prototype

Taking into account the discussed design trade-offs and also practical considerations for the realization, the design with the parameters listed in **Tab. 4.4** is selected for the 50 kW EV charger. The selected design is indicated in **Figs. 4.12 - 4.14**. The modifications required to avoid the pole splitting as well as constructive restrictions resulted in the

selection of a final performance slightly below the Pareto fronts.

The individual contributions of the different components to the total losses are shown in **Fig. 4.15**. For completeness, also the losses in the SiC power semiconductors¹ that are selected for the transmitter-side inverter and the rectifier at the receiver in Section 5.2 are listed.

As expected from the results that were obtained for the scaled system in Section 3.5.3, the loss contribution of the IPT coils and the resonant capacitors is approximately equal. Their share on the total losses of the transmitter is 38% and 41%, respectively. The power semiconductors contribute the remaining 21% of the total losses. For the receiver, the loss distribution is similar. This is a result of the operation close to the efficiency optimum, which implies equal coil losses on both sides of the air gap. Because of the synchronous rectification also similar conduction losses result for the power semiconductors. The total losses amount to 1308.3 W. The calculated DC-to-DC conversion efficiency $\eta_{\text{DC-DC}}$ is 97.45%, including the inverter and the rectifier stage.

4.2.6 Coil Positioning Tolerance

In **Fig. 4.16**, the FEM-calculated magnetic coupling of the selected design is shown together with measurements obtained from the realized hardware prototype as a function of the horizontal misalignment of the IPT coils. In addition, the necessary transmitter-side and receiver-side RMS currents in the IPT coils for the transmission of 50 kW are shown. The maximum efficiency control scheme of Chapter 2 is assumed. The currents are calculated using the highly accurate models presented in [68], which include the losses in the resonant system and also the influence of the non-linear charging processes of the MOSFET capacitances during the ZVS switching transitions for the current calculation.

The magnetic coupling reduces with a steeper slope for a coil misalignment in the longitudinal direction and a smaller slope in the lateral direction (cf. **Fig. 4.2** for axis orientation). For the thermal management of the IPT coils, the resonant capacitors, and the power electronics the worst case (solid lines in **Fig. 4.16**) is used to determine the necessary current carrying capability of the components and the requirements

¹Three parallel connected SiC MOSFET devices of type Cree C2M0025120D, rated for 1.2 kV/90 A with $R_{\text{DS,on}} = 25 \text{ m}\Omega$ at 25 °C.

Tab. 4.4: Design parameters and calculated performance of the IPT transmission coil design selected for the contactless 50 kW/800 V/85 kHz EV charging demonstrator system.

Parameter	Variable	Value
Coil Length	L_{coil}	630 mm
Coil Width	W_{coil}	400 mm
Winding Width	w_{cu}	50 mm
Winding Position	d_{cu}	100 mm
Core Number	N_{fe}	5
Number of Turns	N_1, N_2	9.5
Self-Inductance	L_1, L_2	71.6 μH
Mutual Inductance	M	16.5 μH
Magnetic Coupling	k	0.2299
DC Resistance	R_{DC}	14.3 m Ω
AC Resistance	R_{AC}	22.5 m Ω
Active Material Weight	m_{coil}	15.7 kg
Active Coil Area	A_{coil}	24.0 dm ²
Total Coil Weight ¹	$m_{\text{coil,tot}}$	24.6 kg
Total Coil Area ¹	$A_{\text{coil,tot}}$	31.2 dm ²
Transmitter DC-Link Voltage	$U_{1,\text{DC}}$	800 V
Receiver DC-Link Voltage	$U_{2,\text{DC}}$	800 V
Transmitter RMS Current ²	I_1	87.3 A
Receiver RMS Current ²	I_2	69.7 A
Magnetic Stray Field ³	B_{stray}	8.3 μT
Transmission Efficiency	η	98.0%
Active Area-Rel. Power Density	α	2.1 kW/dm ²
Active Gravimetric Power Density	γ	3.2 kW/kg
DC-to-DC Efficiency ⁴	η_{tot}	97.45%
Area-Related Power Density ¹	α_{tot}	1.6 kW/dm ²
Volumetric Power Density ¹	ρ_{tot}	2.7 kW/dm ³
Gravimetric Power Density ¹	γ_{tot}	2.0 kW/kg

¹Dimensions of final prototype assembly, including all passive components.

²RMS coil currents for ideal coil positioning.

³RMS magnetic flux density at 1.10 m lateral distance from coil center.

⁴Includes the losses of the power semiconductors.

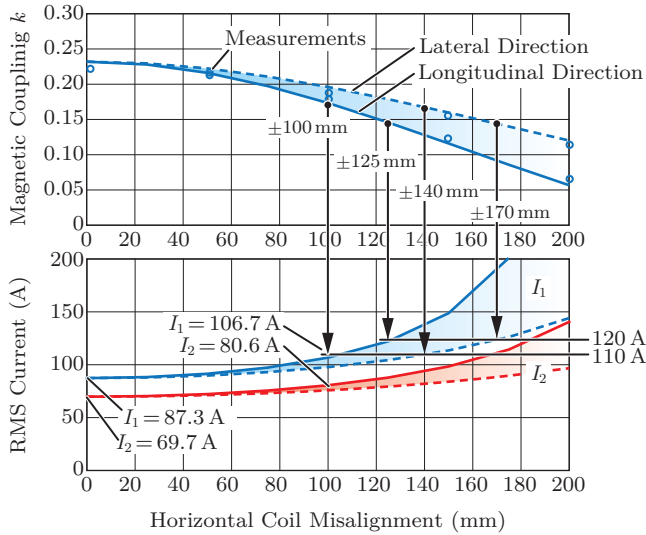


Fig. 4.16: FEM-calculated and measured magnetic coupling k and required transmitter RMS current I_1 and receiver RMS current I_2 for 50 kW power transfer as a function of the horizontal coil misalignment in lateral or longitudinal direction at constant air gap of 160 mm.

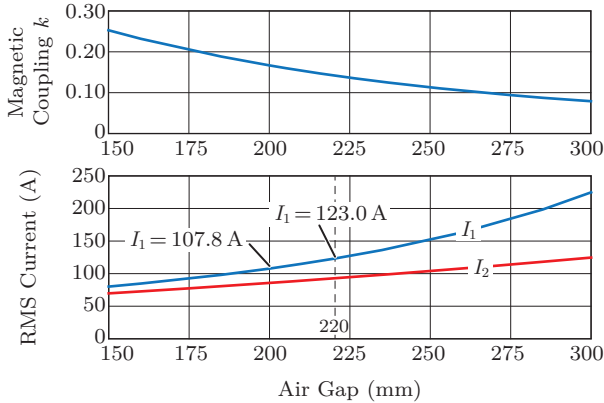


Fig. 4.17: FEM-calculated magnetic coupling k and required transmitter and receiver RMS currents for 50 kW power transfer as a function of the air gap between the IPT coils (without lateral or longitudinal coil misalignment).

for the cooling system. These factors, together with the employed control scheme, ultimately limit the misalignment tolerance of the system. As soon as the maximum currents or the maximum cooling capability is reached during operation, the only option is to limit the coil currents by decreasing the output power, which means charging the EV battery at a lower current and increased charging time.

As indicated in **Fig. 4.16**, the transmitter-side components have to be dimensioned for an RMS current of $I_1 = 106.7$ A and the components of the receiver for $I_2 = 80.6$ A in order to tolerate a coil misalignment of ± 100 mm in the longitudinal direction. The nominal currents are $I_1 = 87.3$ A and $I_2 = 69.7$ A. This implies that the electronics and the cooling system have to be dimensioned for an approximately 22% higher RMS currents. At the coil misalignment of ± 125 mm, a 40% increase of the RMS current ratings is needed or, equivalently, the power losses in IPT coils, the capacitors, and the power semiconductors are approximately doubled compared to ideal coil positioning.

In the direction of motion of the vehicle positioning aids can assist the driver with the accurate positioning the EV. For instance small bumpers could be installed on the road surface as indicators of the correct parking position. Accurate positioning of the vehicle is more difficult in the lateral direction of the EV, because applying position corrections is more involved for the driver. The orientation of the IPT coils with respect to the vehicle is therefore selected such that the misalignment tolerance is higher in the lateral direction of the vehicle, i. e., the direction denoted as the lateral direction of the IPT coil in **Fig. 4.2** corresponds to the lateral direction of the EV. In this case, if the power electronics and the resonant capacitors are dimensioned with a current carrying capability of approximately 120 A, as required for ± 125 mm coil misalignment in the longitudinal direction (direction of motion of the EV), a coil misalignment of up to ± 170 mm in the lateral direction is possible.

Fig. 4.17 shows the FEM-calculated magnetic coupling and the necessary transmitter-side and receiver-side RMS currents for transmitting the full output power of 50 kW as a function of the air gap between the IPT coils². For the maximum transmitter RMS current of 120 A, operation at an air gap of up to 220 mm is possible with the selected coil design. This also fulfills the specifications listed at the beginning of this chapter.

²The air gap is measured between the litz wire windings of the coils.

A higher tolerance with respect to coil misalignment or a larger air gap can be achieved for the selected coil design by a further over-dimensioning of the components. The required current carrying capability and cooling effort for the electronics can be reduced by increasing the size of the IPT coils instead. This increases the magnetic coupling and lowers the required coil currents. Thus, the material effort and possibly the cost is shifted from the electronics to the IPT coils. As a last option, a different coil geometry could be used. However, a comparison to alternative coil geometries known from literature indicates that no large advantage can be expected from fundamentally changing the coil geometry [125].

4.2.7 Comparison to the Scaled Prototype

A comparison of the design parameters and the performance factors for the scaled prototype of Chapter 3 and the presented full-scale transmission coil is given in **Tab. 4.5**.

Despite the large difference in output power, a similar performance is achieved for both systems. As a result of the similar operating frequency and thermal boundary conditions, the area-related and gravimetric power densities of the transmission coils is approximately equal. The volumetric power density of the scaled prototype is higher. The main cause for this difference is that the core of the full-scale system is realized with ferrite rods instead of the flat plates, which was preferred for simplifying the mechanical assembly. The measured DC-to-DC efficiency (cf. Section 3.5.3, Section 6.2.3) is also similar for both cases. This is mainly a result of the similar relative air gap, defined as the ration of the air gap and the square root of the coil area, of approximately 0.28 in both cases. It is interesting to note that also the specific weight of the copper litz wire windings and the ferrite cores is similar in both cases. This is thought to be a result of the similarities between the geometrical arrangements in both designs and the similar operating frequencies.

The consistency of the obtained results for the scaled and the full-scale system validate the proposed multi-objective IPT optimization process at two substantially different power levels. The similarities between the performance factors suggests that the presented numbers can be used as a reference for performance predictions over a wide power range. A key requirement for the scaling to systems with different

Tab. 4.5: Comparison of the design parameters for the scaled 5 kW prototype of Chapter 3 and the presented full-scale 50 kW transmission coil.

Parameter	5 kW System	50 kW System
Input Voltage	400 V	800 V
Output Voltage	350 V	800 V
Output Power	5 kW	50 kW
Transmission Frequency	100 kHz	85 kHz
Air Gap	50 mm	150-200 mm
Coil Size	210 mm diam.	410 x 760 x 60 mm
Coil Weight ¹	2.3 kg	24.6 kg
Relative Air Gap ²	0.279	0.287
Area-Related Power Density	1.47 kW/dm ²	1.6 kW/dm ²
Volumetric Power Density	4.8 kW/dm ³	2.7 kW/dm ³
Gravimetric Power Density ¹	2.2 kW/kg	2.0 kW/kg
DC-to-DC Efficiency ³	96.5%	95.8%
Specific Copper Weight	43 g/kW	52 g/kW
Specific Ferrite Weight	112 g/kW	160 g/kW

¹Includes the weight of the resonant capacitors.

²Defined as the ratio of the air gap to the square root of the coil area.

³Measured value at nominal power.

specifications is the similarity of the ratio of the coil size to the air gap. In addition, the two prototypes are designed for a similar transmission frequency. Hence, frequency scaling is not captured by this comparison and must therefore be carefully considered when making performance predictions.

4.3 Realization of the Prototype

In this section, practical aspects of the prototype realization are discussed. In the first part, the mechanical construction of the IPT coil is explained and the final prototype realization is shown. The design of the active cooling system for the IPT coil is presented and FEM simulations are used to validate the thermal management. Subsequently, the construction of a resonant capacitor module is presented, including

its active forced-air cooling system.

4.3.1 Mechanical Construction Details

Since high additional eddy current losses prohibit the use of metals for the structural elements of the transmission coils, the construction of the prototype relies on high-temperature plastic materials such as Polyoxymethylene (POM), polycarbonate, and teflon.

As indicated in the Computer Aided Design (CAD) construction drawings of **Fig. 4.18**, for the base plate and the coil housing POM parts produced by Computerized Numerical Control (CNC) milling are employed. The ferrite cores are attached to the base plate with polycarbonate fixtures produced by additive manufacturing (3D printing). Seamlessly integrated into the base plate is a core carrier produced from teflon sheets by water jet cutting. The core carrier has a higher temperature rating than the POM base plate and can, therefore, be placed in direct contact with the ferrite cores without any risk of overheating. At the frontside and the backside of the IPT coil, cooling fans are positioned via mounting points integrated into the base plate. To prevent air bleeding, the top of the coil is covered with a transparent polycarbonate plate (not shown in **Fig. 4.18**). The winding is positioned on a CNC milled POM coil former. The coil former surface is realized with a groove structure for guiding the cooling air along the bottom side of the litz wire conductors. Milled guides on the coil former and 3D printed polycarbonate fixture elements are used to hold the conductors in position. The coil former with the attached winding is then positioned on the cores and is directly attached to the coil housing

A photograph of the finished prototype assembly including also the polycarbonate cover is shown in **Fig. 4.19**. Since the transmitter and the receiver coil are identical, only one IPT coil is shown in the photograph.

As a result of the added 9.9 kg passive weight of the coil housing, the total weight of the coil is 24.6 kg including the base plate, the coil housing with the polycarbonate cover, the active cooling system, and the resonant capacitor module with its heat sink. Given the additional space needed for the housing and the cooling system, the coil area is increased from initially 24.0 dm² for only the active components to 31.2 dm² by adding the passive parts. This finally results in an area-related power density of $\alpha_{\text{tot}} = 1.6 \text{ kW/dm}^2$ and a gravimetric power

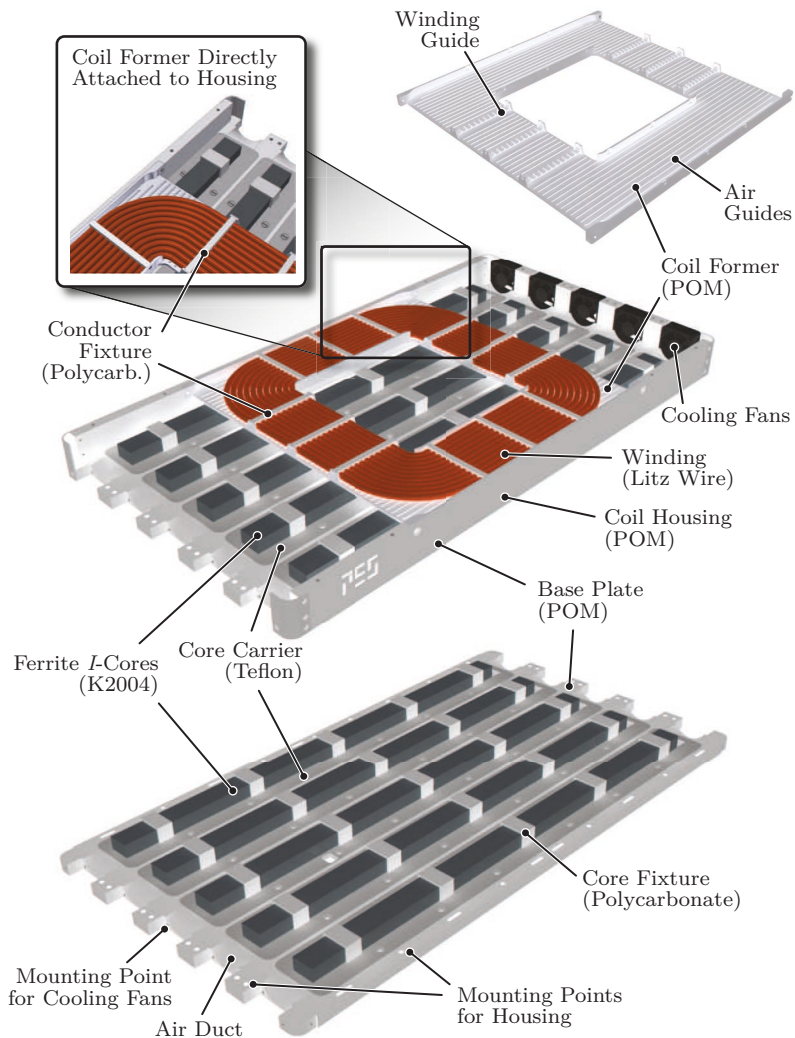


Fig. 4.18: Construction drawings of the realized prototype IPT coil including the structural elements and the coil housing (the polycarbonate cover of the housing is not shown).

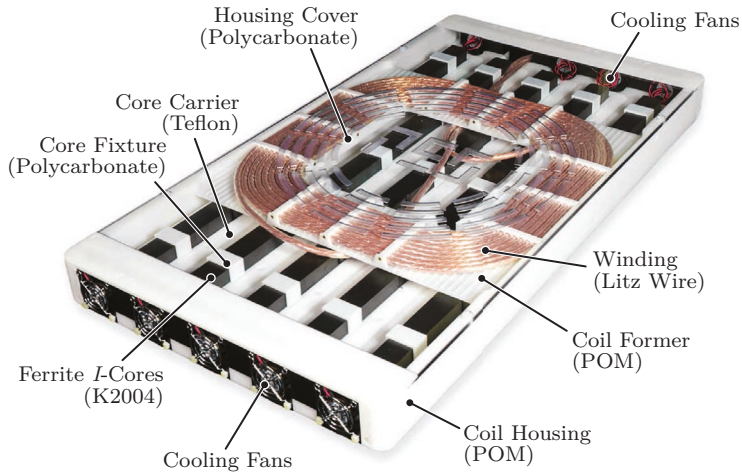


Fig. 4.19: Photograph of the realized forced-air cooled demonstrator IPT coil for EV battery charging at 50 kW/800 V/85 kHz.

density of $\gamma_{\text{tot}} = 2.0 \text{ kW/kg}$ for the realized prototype.

The presented IPT transmission coil is intended for experimental testing in a laboratory environment. The main goal is to provide a performance benchmark that demonstrates the potential of IPT technology under optimum conditions. For the final EV application, additional mechanical structures for mounting the coil on the vehicle, possibly additional eddy current shielding to prevent losses in the vehicle chassis, and a more rugged coil housing are necessary. All of these parts lower the area-related and gravimetric power density in the practical application.

4.3.2 Forced-Air Cooling System of the Transmission Coils

For the thermal management of the transmission coils, an active forced-air cooling system with axial cooling fans is implemented. **Fig. 4.20** shows the open coil housing including the cooling fans and the maximum temperature ratings of the components. In the following, thermal simulations implemented in the FEM tool Comsol Multiphysics³ are

³Version 4.3b, available at www.comsol.com (7.10.2015).

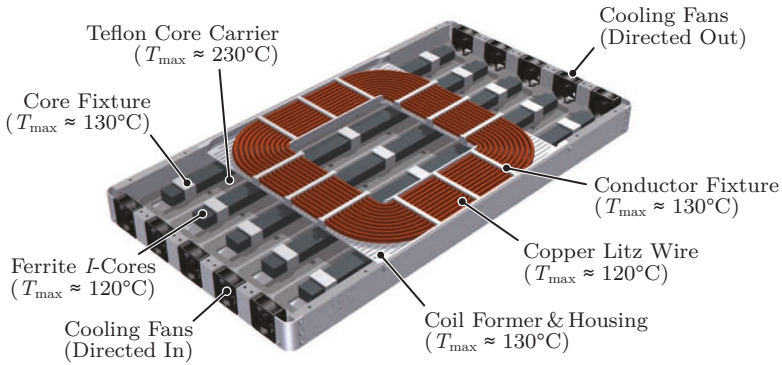


Fig. 4.20: Active cooling system and maximum temperature ratings of the mechanical components of the prototype IPT coil.

used to validate the thermal feasibility of the selected coil design.

To estimate the heat transfer at the surfaces of the windings and the ferrite cores the calculation models presented in [122–124] are used as briefly discussed above. The models allow estimating surface heat transfer based on an analytical calculation of the fluid flow in the air channels between the ferrite cores, between the polycarbonate cover of the housing and the winding, and between the winding and the coil former. The models of [124] are able to estimate the fluid velocities and the resulting heat transfer coefficient at the channel surfaces.

The estimated surface heat transfer coefficients are indicated in **Fig. 4.21(a)**. Due to the space requirements for the structural elements of the prototype, the dissipation of the copper losses is lower between the bottom surface of the winding and the coil former than at the winding top surface. Therefore, different heat transfer coefficients result for the top and bottom surfaces of the winding. The fluid velocity of the cooling air is higher in the region of the winding because the fluid is forced into narrower channels. For this reason, the heat transfer coefficient for the core surfaces is higher below the winding than at the outer ends of the arrangement.

Electromagnetic FEM simulations of the prototype show that the magnetic flux density in the core is significantly higher below the winding than outside. Hence, the core losses occur mostly in that region. Therefore, for the thermal FEM simulation the calculated core losses are attributed only to the cores below the winding and the cores, which are

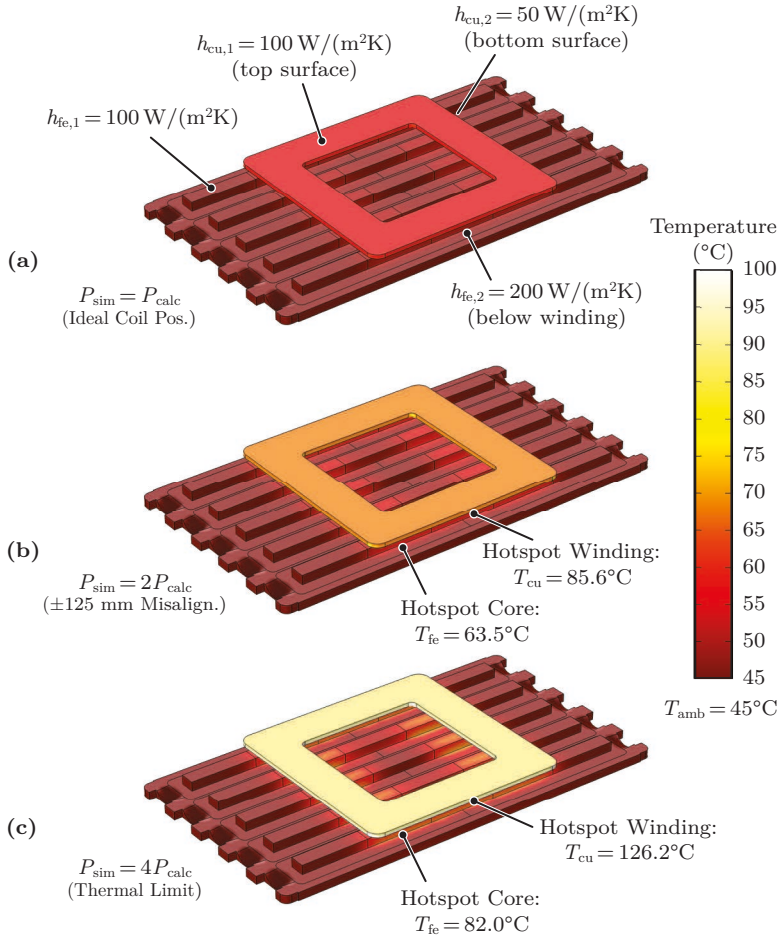


Fig. 4.21: (a) Results of a thermal FEM simulation for approximated surface heat transfer coefficients and the calculated power losses of the coil. In (b) the same simulation is solved with doubled power losses, which approximately occur at the maximum specified coil misalignment. (c) the thermal limit is reached inside the winding at four times higher power losses.

note covered by the winding, are modeled without losses. The winding losses are assumed to occur uniformly in the complete winding.

First, a simulation with the power losses calculated above and the specified ambient temperature of 45 °C is evaluated. Then, for the sake of simplicity, all power losses are increased stepwise by the same factor until the thermal limit is reached in one of the components. The thermal FEM simulation results are shown in **Fig. 4.20** for different power losses. **Fig. 4.20(c)** shows that the maximum temperature for the litz wire winding is reached at four times higher than calculated power losses. This shows that the selected cooling fans provide sufficient cooling and could even be operated with a reduced speed and lower mass flow.

As discussed above, the critical case for the thermal management occurs during operation with misaligned transmission coils, when the losses are increased significantly compared to normal operation. It is shown above, that at a coil misalignment of ± 125 mm the RMS currents in the coils are increased up to 40% for transferring the rated output power. This implies a factor of 2 higher power losses, which corresponds to the case shown in **Fig. 4.20(b)**. The hotspot temperatures in the winding $T_{\text{cu}} = 85.6$ °C and in the core $T_{\text{fe}} = 63.5$ °C are sufficiently below the maximum rating of 120 °C for both materials. Hence, the simulations show that the selected coil design is thermally feasible with sufficient margin to tolerate the specified coil misalignment.

4.3.3 Design of the Resonant Capacitor

As discussed in Section 4.1, polypropylene film capacitors of the series CSP 120-200 by Celeem are used for the resonant capacitors. Due to the high capacitor losses (cf. **Fig. 4.15**), active cooling of the devices is needed. Ideally, liquid cooling is provided at the bus bars that are connected to the capacitor electrodes. For the presented prototype, forced-air cooling is preferred, because a liquid cooling system might not be available on a typical EV.

A construction drawing of the designed resonant capacitor module is shown in **Fig. 4.22(a)**. Due to their voltage rating, a series connection of five devices is required. Milled aluminum heat sink elements are mounted to the capacitor electrodes at both sides of the devices. Axial cooling fans are mounted at both ends of the heat sinks for forced-air cooling. High-voltage isolation between the heat sinks, which are

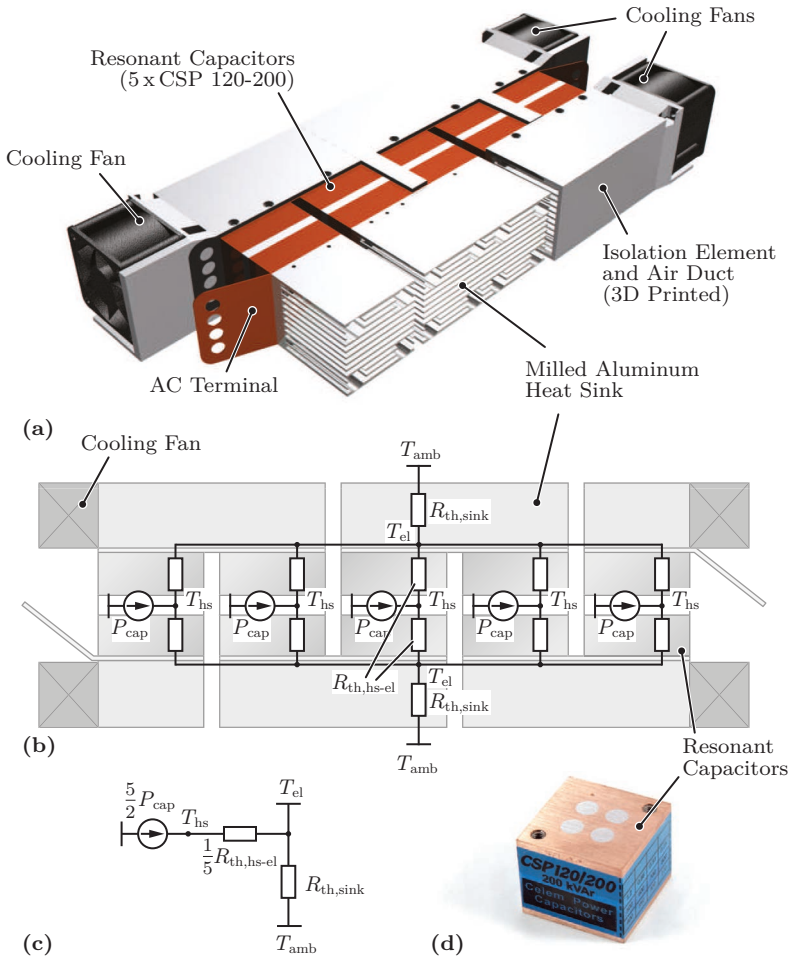


Fig. 4.22: (a) Construction drawing of the resonant capacitor module with forced-air cooling system. (b) Complete thermal model and (c) simplified thermal model of the capacitor module including the cooling system. (d) Photograph of one of the employed high-power polypropylene film capacitors.

electrically connected to the capacitor terminals, is provided by 3D printed polycarbonate isolation elements, which at the same time serve as ducts for the cooling air.

The thermal model used for the design of the cooling system shown in **Fig. 4.22(b)** is briefly outlined in the following. The thermal resistance from the hotspot inside the polypropylene film capacitors to the electrodes is specified as 0.09 K/W for two-sided cooling by the manufacturer. In **Fig. 4.22(b)** the thermal resistance divided into two equal thermal resistances $R_{\text{th,hs-el}} \approx 0.18$ K/W from the hotspot to each electrode. The thermal resistance $R_{\text{th,sink}}$ represents the entire heat sink that is attached at one side of the module, taking into account the two cooling fans. Due to its symmetries, the thermal network can be simplified as shown in **Fig. 4.22(c)**. The simplified thermal network allows calculating the required thermal resistance $R_{\text{th,sink}}$ as

$$R_{\text{th,sink}} = \frac{2}{5} \cdot \frac{T_{\text{hs,max}} - T_{\text{amb}}}{P_{\text{cap}}} - \frac{R_{\text{th,hs-el}}}{5}, \quad (4.7)$$

where $T_{\text{hs,max}} \approx 90$ °C stands for the maximum hotspot temperature inside the device, $T_{\text{amb}} = 45$ °C for the ambient temperature, and P_{cap} for the power losses of a single device.

For the power losses of the resonant capacitors at the transmitter side as calculated in Section 4.2 for ideal positioning of the IPT coils, a thermal resistance $R_{\text{th,sink}} \leq 0.32$ K/W is needed. However, the cooling system is dimensioned for a higher power dissipation, because of the increased RMS currents in the IPT coils during operation with misaligned IPT coils. Using the tools in [124], a thermal resistance as low as $R_{\text{th,hsink}} \approx 0.139$ K/W is reached for the heat sink of the prototype capacitor module. This enables operation with up to 110 A transmitter coil RMS current, which corresponds to a coil misalignment of up to ± 100 mm in the longitudinal direction of the IPT coils and ± 140 mm misalignment in the lateral direction (cf. **Fig. 4.16**). At reduced ambient temperature, e. g., at $T_{\text{amb}} \approx 30$ °C instead of the rated 45 °C, also operation at ± 125 mm coil misalignment in the longitudinal direction and ± 170 mm in the lateral direction is possible.

The fact that the heat sinks are mounted directly to the electrodes of the resonant capacitors could potentially lead to additional heating due to the current density in the aluminum of the heat sink. To quantify the effect, the current density in the heat sink is calculated with a FEM simulation. The effect of the fins of the heat sink is captured by a

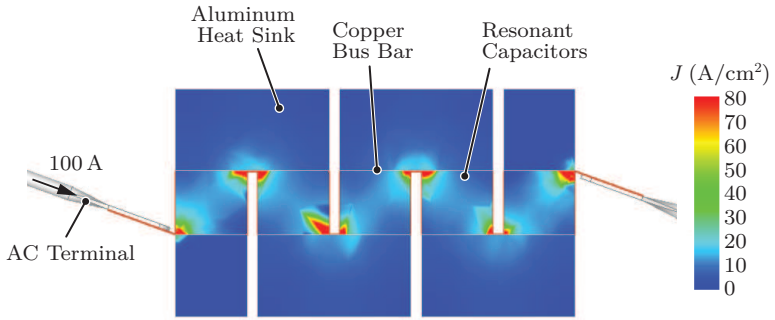


Fig. 4.23: FEM-calculated current density in the capacitor module with aluminum heat sinks connected to the electrodes of the resonant capacitors, shown for a total current of 100 A.

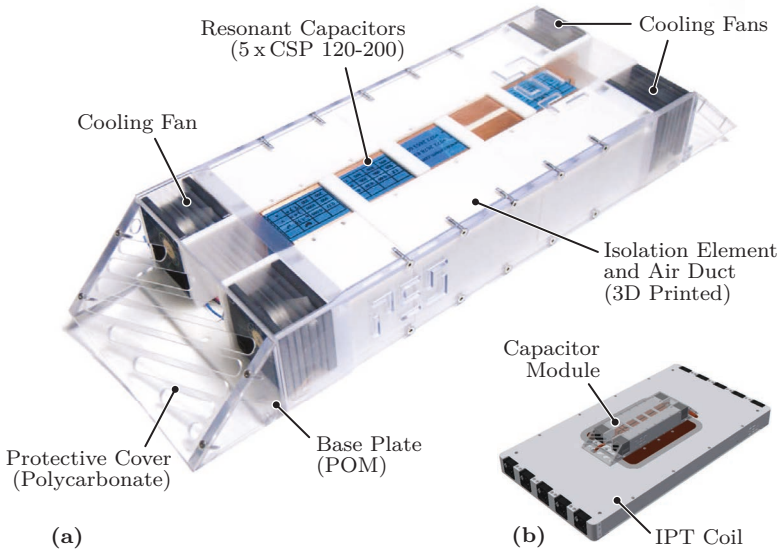


Fig. 4.24: (a) Photograph of the assembled resonant capacitor module with forced-air cooling system and polycarbonate cover. (b) Mounting position of the capacitor module at the backside of the IPT coil.

reduction of the aluminum conductivity by 50%, which approximately corresponds to the ratio of aluminum to air volume. The capacitor electrodes are modeled as copper blocks. The dielectric is not modeled, because of its limited effect on the current distribution in the heat sinks. The FEM simulation result is shown in **Fig. 4.23**. The simulation shows that the current is largely concentrated within the resonant capacitors and the copper bus bars connecting the devices. The estimated power loss in the heat sink due to current conduction is 0.45 W. The effect is therefore of no further concern.

A photograph of the assembled resonant capacitor module is shown in **Fig. 4.24(a)**. A cover made from CNC milled polycarbonate parts is used to cover the copper parts as a safety precaution. Screw terminals in the POM base plate allow mounting the module directly to the backside of the presented IPT coil as shown in **Fig. 4.24(b)**.

4.4 Summary of the Chapter

In this chapter, a novel geometry was proposed for the transmission coils of a contactless EV charging system. The necessary calculation models for estimating the power loss in all components of the proposed IPT coil were presented. Based on the models, a multi-objective optimization of the transmission coils for the contactless 50 kW EV charging system was conducted. The encountered design trade-offs between the transmission efficiency, the area-related power density, the gravimetric power density, and the stray field of the IPT coils were highlighted. The Pareto fronts, which represent the physical performance limits of the technology with respect to the listed performance indices, were analyzed in detail. Taking everything into account, an IPT coil design was selected from the optimization results and a hardware prototype was practically realized.

The key results for the optimized IPT transmission coils are summarized as follows:

- The developed multi-objective IPT optimization process was applied to a 50 kW EV charging system. The optimization results confirmed the key conclusions for the scaled prototype system of Chapter 3. The consistency of the obtained performance of the 5 kW and the 50 kW system validates the approach for a wide power range.

- ▶ The calculated transmission efficiency of the realized IPT prototype is 98.0%, including the losses in the IPT coils, the resonant capacitors, and the shielding elements. If the power semiconductors of the transmitter and the receiver-side power electronics are included as well, the DC-to-DC efficiency is 97.45%.
- ▶ The area-related power density of the realized transmission coils is 2.1 kW/dm², the gravimetric power density is 3.2 kW/kg, and the magnetic stray field fulfills the ICNIRP 2010 guidelines.
- ▶ The outer dimensions of the realized IPT coils are 400 x 630 mm and the weight of the active materials is 15.7 kg. Including the necessary constructive elements, the dimensions of each coil are 60 x 410 x 760 mm and the total weight of the final assembly is 24.6 kg.
- ▶ A thermal analysis of the IPT coil and the resonant capacitor module showed that the resonant components can operate at the full output power of 50 kW with a coil misalignment of ± 100 mm in the longitudinal direction, ± 140 mm in the lateral direction, and with an air gap of up to 200 mm at 45 °C ambient temperature.
- ▶ At an ambient temperature of 30 °C, a coil misalignment of up to ± 125 mm is possible in the longitudinal direction and up to ± 170 mm in the lateral direction. The air gap can be extended up to 220 mm.
- ▶ The required RMS current carrying capability of the power electronics for this positioning tolerance is approximately 120 A at the inverter-stage output and the rectifier-stage input.

After the multi-objective design and the realization of the transmission coils, the next step is the design of the 50 kW power electronics in Chapter 5. The results of an extensive experimental verification of the predicted performance of all IPT system components are subsequently presented in Chapter 6.

5

Power Electronic Converter & Control

POWER electronic converter systems for EV battery charging must provide galvanic isolation and a high power processing capability at a high efficiency. At the same time they are facing automotive requirements, such as high compactness, high reliability, and low cost [28, 126–128]. For a conventional EV charger with a DC connection to the vehicle, only a DC-DC conversion stage is needed on the vehicle for controlling the battery current. For the contactless charging system, the IPT receiver coil and the rectifier-stage have to be integrated into the vehicle in addition to the on-board DC-DC converter. IPT systems suffer from a lower power density of the passive components than conventional conductive EV chargers, due to the physical limitations of the contactless power transmission. Depending on the application, this is an acceptable compromise, given the added functionality of the contactless charging. However, achieving a high compactness while maintaining a high efficiency for the additional on-board power electronics is therefore the main design objective for an overall competitive solution.

It was already demonstrated that the peak efficiency of an IPT system can be comparable with a conventional EV charger if the coils and the power converters are appropriately designed [75]. However, a substantial part of a typical constant current and constant voltage charging profile does not require the full output power from the converter. Especially when the state of charge of the battery is close to the allowed maximum, the charging current must be reduced to protect the cells from over-charging. Therefore, apart from the efficiency at the nominal point, for battery charging systems also the efficiency at partial

load is of importance [61]. For bi-directional systems with vehicle-to-grid power transfer capability [33, 129] the efficiency at partial load is particularly important to make bi-directional energy exchange with the grid financially and ecologically attractive. However, depending on the used control method, IPT systems can exhibit a substantially reduced efficiency at light load conditions [61]. For instance control of the power flow by a frequency detuning of the resonant circuit bears the cost of reactive currents in the IPT coils that do not contribute to the power transfer and lead to a reduced partial load efficiency (cf. Section 2.3.5).

For an improved system performance, the power electronic converter supplying the IPT resonant circuit must provide dedicated control functionality to improve the performance of the *weakest link* in the power conversion chain. As discussed in Section 2.3.4, an extension of the conventional IPT topology with additional DC-DC conversion stages at the transmitter-side and at the receiver-side DC-link of the systems allows constantly operating the IPT system at its natural efficiency optimum [33, 61, 70]. The additional conversion stages allow shifting the control functionality from the resonant circuit to the power electronic converter. This simplifies achieving an efficient control of the power flow, because with the power electronics the required control functionality can be achieved at comparably low additional power losses. Furthermore, due to the introduced degrees-of-freedom, such a solution also allows optimizing the system performance during operation with misaligned IPT transmission coils [61].

By utilizing the improved switching performance and high blocking capability of state-of-the-art SiC MOSFET technology [28, 130–133], a power electronics solution that fulfills the requirements of high power density and high efficiency while implementing the necessary control functionality is designed in this chapter. The realized converter topology, which is introduced in Section 5.1, consists of a ZVS full-bridge inverter that supplies the high-frequency AC voltage to the resonant circuit, and of a non-isolated buck+boost-type DC-DC conversion stage that provides the variable DC-link voltage needed for the power control. Realization details of the ZVS full-bridge inverter are given in Section 5.2. For the DC-DC converter, a parallel interleaved solution is used, which incorporates three identical converter modules that each consist of two sub-interleaved phases and coupled magnetic components. The design of the DC-DC converter modules is presented in Section 5.3, while details regarding the control of the power flow in the DC-DC con-

verter and in the IPT system as a whole are given in Section 5.4. Finally, in Section 5.5, the assembly of the optimized all-SiC power converter is presented.

5.1 Selection of the Converter Topology

Typical IPT power converters employ a ZVS full-bridge inverter for the supply of a high-frequency AC voltage to the resonant circuit at the transmitter side. At the receiver side, a passive or active rectifier is needed [75, 81]. If no further conversion stages are included in the system, this topology allows controlling the power flow either via the inverter switching frequency or the duty cycles of the inverter and the rectifier stage. As shown in Section 2.3.5, detuning the resonant circuit by adapting the switching frequency for the power control leads to circulating reactive currents, which cause conduction losses in the IPT coils and the resonant capacitors. This results in a reduced partial load efficiency.

Solutions where the control functionality is shifted from the resonant system to the power electronics generally lead to a better performance. In [36], a control scheme with a hard-switched modulation of the voltage fundamental components that are applied to the resonant circuit is presented. The method avoids the circulation of reactive power and allows constantly operating the IPT resonant circuit at its natural efficiency optimum [134]. However, the functionality is achieved at the cost of additional switching losses in the power electronics. At the targeted transmission frequency of 85 kHz, as proposed by the upcoming IPT standard SAE J2954 [43], the additional switching losses would have a high impact on the overall system performance.

Recently, also solutions with additional external DC-DC conversion stages have been proposed [33, 61, 70]. The power conversion chain from the three-phase mains to the battery for this approach is shown in **Fig. 5.1(a)**. As discussed in Section 2.3.4, if the two DC-link voltages are used for the control of the power flow at a constant switching frequency, the resonant circuit is operated at its natural efficiency optimum without additional switching losses in the inverter and rectifier stages. Therefore, this solution is preferred in this thesis with the aim of designing an IPT system that demonstrates a benchmark efficiency.

The selected topology for the receiver-side power electronics is shown in **Fig. 5.1(b)**. To simplify the implementation and the experiments

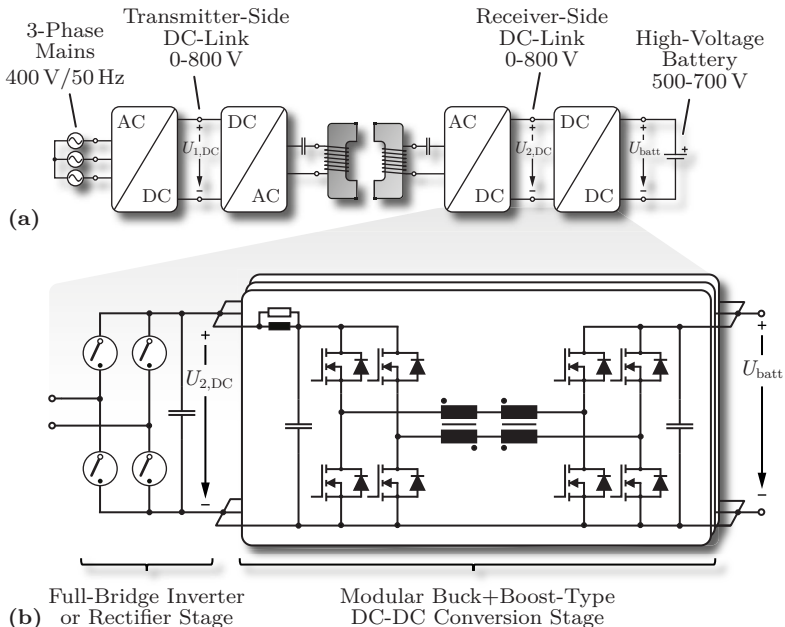


Fig. 5.1: (a) Power conversion chain of a contactless EV battery charger. (b) Selected converter topology with a full-bridge inverter/rectifier stage at the interface towards the coil and a modular buck+boost type DC-DC conversion stage at the battery interface.

presented in Section 6.2, an identical converter is also used for the transmitter. At the transmitter side, the full-bridge inverter stage is used to supply a 85 kHz rectangular voltage with a constant 50% duty cycle to the resonant circuit. At the receiver side, the same full-bridge serves as a synchronous rectifier in order to reduce conduction losses. Details about the implementation of the synchronous rectification are given in Section 5.4.3.

For a moderate current loading of the power electronic converter and the IPT resonant system at 50 kW, nominal DC-link voltages of 800 V supplied by a three-phase mains interface connected to the European 400 V/50 Hz grid are considered. As discussed in Section 4.1, typical voltage levels of traction batteries with high power density and high energy density are typically 500-700 V [115,116]. Therefore, power

semiconductors with 1.2 kV blocking capability are required. Given the transmission frequency of 85 kHz and the comparably high switching losses of IGBTs even under near-zero current switching conditions [110–112], SiC MOSFETs are the preferred option in this work because of their high switching speeds and low ZVS losses.

The selected control scheme requires lowering the DC-link voltages below their nominal values to reduce the output power. Therefore, the listed DC-link and battery voltage levels imply that buck+boost functionality is needed for the DC-DC conversion stage of the receiver. The selected topology for the buck+boost type DC-DC converter is shown in **Fig. 5.1(b)**. The DC-DC conversion stage is implemented as three parallel interleaved converter modules of identical topology. Each DC-DC module is designed for an output power of 20 kW, which results in a total power capability of 60 kW for the DC-DC conversion stage. The ZVS full-bridge is designed for the same power level. This ensures that also the experimental investigation of sub-optimal operating points with high losses at 50 kW output power is possible with the developed hardware. Such operating points occur for instance at a high coil misalignment. The division of the DC-DC conversion stage into three 20 kW modules reduces the current loading of each module to a level where the use of Printed Circuit Board (PCB) technology instead of copper bus bars and discrete power semiconductors instead of power modules are possible. Both aspects are favorable for a highly compact realization. The internal splitting into two parallel phases, which are constantly operated at 180° phase shift, enables the use of coupled inductors, which allows for a further volume reduction [135–140]. In addition, the parallel interleaving of the phases reduces the voltage and current ripples at the output and allows using a smaller DC-link capacitance in the modules.

In the following sections, first the necessary considerations for the ZVS full-bridge inverter stage are discussed in detail. Afterwards the optimization of the 20 kW DC-DC converter modules is presented. At the end of the chapter, the power control for the complete converter is discussed and the final converter assembly is presented.

5.2 ZVS Full-Bridge Inverter Stage

SiC power MOSFETs with 1.2 kV blocking voltage are currently available as discrete devices (approx. 20-60 A), typically packaged in TO-247

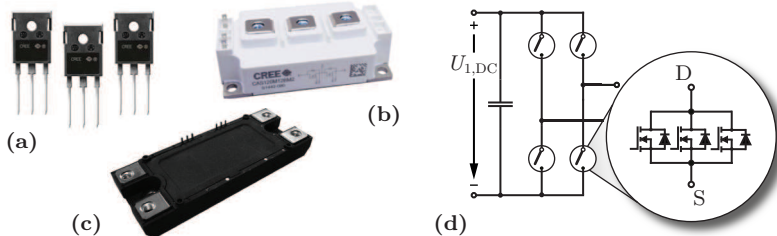


Fig. 5.2: Commercially available packages for SiC MOSFETs: (a) TO-247 package for single chips and (b)-(c) half-bridge modules by Cree and Rhom (images reproduced from manufacturers' websites; not to scale). (d) Parallel connection of three discrete devices for each switch of the full-bridge.

transistor housings, or in the form of power modules (approx. 100-300 A) as shown in **Figs. 5.2(a)-(c)**. For the inverter stage designed here, according to Section 4.2.6 the RMS output current of the full-bridge is expected as approximately 120 A for a misalignment of the IPT coils of ± 125 mm. Therefore, a solution with multiple parallel connected discrete devices for each switch of the full-bridge as shown in **Fig. 5.2(d)**, or the use of half-bridge modules is possible.

At the time of writing, commercially available SiC power modules are typically realized in housings that were originally designed for IGBTs¹ for compatibility with established industry converter layouts. Therefore, these devices have the disadvantage of comparably high commutation and gate inductances², even with a careful design of the internal layout of the module [130, 141, 142]. Under ZVS conditions particularly the source inductance is critical, because the inductive voltage drop caused by the rising or falling drain current in the source inductance reduces the voltage that is effectively applied to the gate. In addition, the gate inductance limits the slope of the gate current. Both effects together determine how fast the gate can be charged or discharged. For a high inductive output current of the half-bridge, high

¹Cree offers 5 m Ω and 12 m Ω half-bridge modules in conventional 62 mm housings (CAS300M12BM2, CAS120M12BM2). Rhom offers a 6.5 m Ω module in a custom package (BSM300D12P2E001). A 3.75 m Ω half-bridge module is available in a 62 mm housing from Semikron (SKM500MB120SC).

²The data sheets of Cree CAS120M12BM2 and CAS300M12BM2 specify a commutation inductance of 15 nH and 14 nH, respectively. The gate inductance is not indicated.

ZVS losses occur if the gate driver is too slow to turn off the MOSFET channel before the drain to source voltage starts rising [67]. Furthermore, a compact realization of the inverter stage is complicated by the comparably large volume of the power module packages. For these reasons, a solution with discrete TO-247 devices is preferred for the power converter designed in this chapter. For low conduction losses at the expected RMS output current of approximately 120 A, three 25 m Ω /60 A devices of type C2M0025120D are used for each switch of the full-bridge inverter as shown in **Fig. 5.2(d)**.

In the following, the design of the full-bridge inverter stage with paralleled discrete SiC MOSFET devices is discussed, including the gate driver concept and layout considerations for the power circuit.

5.2.1 Paralleling of SiC MOSFETs

For a symmetrical utilization of all paralleled devices during commutation as well as during continuous conduction, the internal device characteristics (on-state resistance $R_{DS(on)}$ and threshold voltage) as well as the parasitic elements of the external power circuit layout are of crucial importance [143–145]:

► **Common source inductance³ L_S mismatch:**

As shown in **Fig. 5.3(a)**, the negative feedback of the slope di_{DS}/dt of the drain-to-source current i_{DS} on the gate voltage via the common source inductance L_S leads to a reduction of the effective gate-to-source voltage u_{GS} . In a parallel connection of multiple devices, the slower charging or discharging of the gate capacitance causes a slower switching of the devices with higher L_S . The load current therefore commutates to the faster devices earlier at turn-on and remains longer in the slower devices at turn-off. For a hard-switched converter this results in an uneven distribution of the switching losses among the paralleled devices.

► **Drain-to-source inductance L_{DS} mismatch:**

The parasitic drain-to-source inductance L_{DS} of the semiconductor package and the parasitic inductance of the power circuit layout together are responsible for the voltage overshoot at turn-off of the devices. In addition, as illustrated in **Fig. 5.3(b)**,

³The common source inductance L_S is defined as the part of parasitic device inductance that is shared by the load current and the gate current.

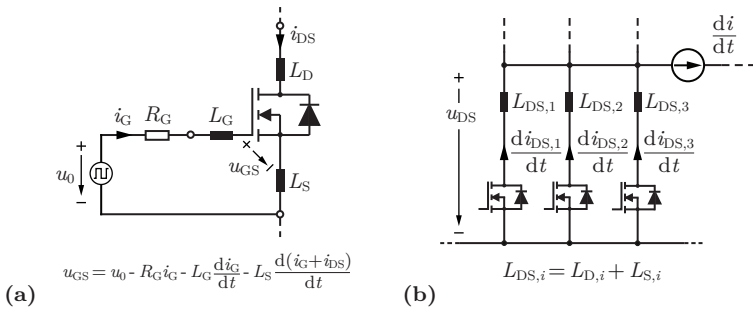


Fig. 5.3: Two effects of the MOSFET package inductances: **(a)** negative feedback of the impressed drain-to-source current i_{DS} via the common source inductance L_S on the gate-to-source voltage u_{GS} during switching transients and **(b)** imbalance of the individual device currents $i_{DS,i}$ due to unequal drain-to-source inductances $L_{DS,i}$. Because the voltage drop u_{DS} is equal for all devices, inductance differences cause unequal slopes $di_{DS,i}/dt$.

a mismatch of L_{DS} among paralleled devices causes an uneven sharing of the inductive load current during the on-state. Assuming a fixed DC-link voltage, equal on-state resistances, and an impressed slope di/dt of the load current, unequal device inductances $L_{DS,i}$ cause unequal slopes $di_{DS,i}/dt$ of the individual drain-to-source currents, because the voltage u_{DS} must be equal for all paralleled devices. Therefore, the inductance differences lead to an asymmetric current distribution during the conduction interval [145].

Therefore, the main design objective for the full-bridge inverter stage with parallel connected devices is a symmetrical layout with small commutation and gate inductances. In addition, a fast driver circuit is needed to achieve ZVS and minimum switching losses. Both of these aspects are discussed in the next sections.

5.2.2 Power Circuit Layout for Symmetrical Current Distribution

If three devices are paralleled for each switch of the full-bridge, a total of twelve power semiconductors results. Therefore, a symmetrical arrangement of the devices is challenging. A possible arrangement with a

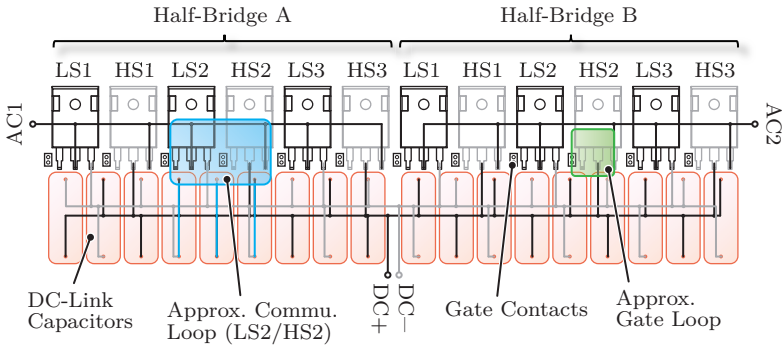


Fig. 5.4: Power board layout with minimum commutation and gate loop for the paralleled devices (HS1-HS3 and LS1-LS3 of each half-bridge). The symmetry of the layout ensures equal current sharing among the devices.

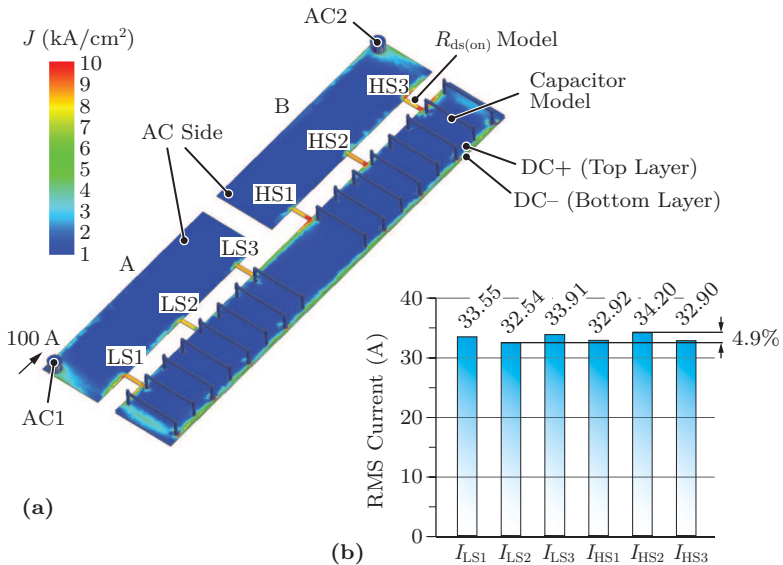


Fig. 5.5: (a) FEM-calculated current distribution in the power board of the full-bridge inverter at 85 kHz. (b) Calculated current sharing among the parallel connected SiC MOSFET devices.

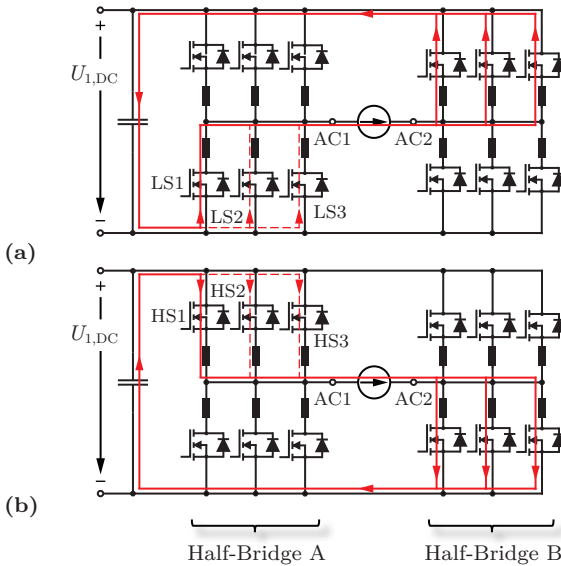


Fig. 5.6: FEM simulation steps for calculating the inductance differences ΔL of the paths through (a) the low-side devices LS1-LS3 and (b) the high-side devices HS1-HS3 of half-bridge A and all complementary devices of half-bridge B.

minimized commutation inductance is shown in **Fig. 5.4**. The symmetrical layout ensures similar inductances for all paralleled devices due to the equal commutation loops indicated in the figure.

To validate the design, an approximative model of the power PCB is analyzed in a FEM simulation. For the power semiconductors that are turned on, a block of material with a resistance that corresponds to the on-state resistance of the devices is inserted. For the devices in off-state, the block is removed. The DC-link capacitors are modeled by a block of material with the same impedance as the capacitors of the final prototype at the switching frequency. The calculated current distribution at 85 kHz for a total current of 100 A is shown in **Fig. 5.5(a)** for the case where the low-side devices LS1, LS2, and LS3 of half-bridge A and the high-side devices HS1, HS2, and HS3 of half-bridge B are turned on.

In order to calculate the inductance differences between the paths

Tab. 5.1: FEM-calculated inductance differences between the current paths through the paralleled SiC MOSFET devices.

Device	LS1	LS2	LS3	HS1	HS2	HS3
ΔL	-7.54 nH	ref.	3.26 nH	-7.56 nH	-0.11 nH	3.37 nH

through the paralleled devices, a sequence of FEM simulations is executed. In each simulation step, one device out of the three paralleled MOSFETs in the low-side switch of half-bridge A is conducting, while all three complimentary high-side devices of half-bridge B are conducting as illustrated in **Fig. 5.6(a)**. The process is repeated analogously for the high-side devices of half-bridge A with all low-side devices of half-bridge B conducting as shown in **Fig. 5.6(b)**. The inductance of the path through device LS2 of half-bridge A and HS1-HS3 of half-bridge B is taken as the reference value for a comparison of the path inductances. The differences of the calculated inductances ΔL between terminal AC1 and terminal AC2⁴ for each configuration with respect to the selected reference are summarized in **Tab. 5.1**. It should be noted that this value does not correspond to the difference in commutation inductance of each device.

As a result of the inductance differences ΔL , different current levels are reached in the paralleled devices at the end of the turn-on switching transient. After the commutation, different slopes of the device currents result due to the different device inductances and the impressed slope of the total load current at the output terminal as described above. Therefore, a small on-state current imbalance is expected among the individual devices. In the FEM simulation, the RMS current in each device is calculated for the case where all low-side devices of half-bridge A and all high-side devices of half-bridge B are conducting. The result is shown in **Fig. 5.5(b)**. The RMS device currents during on-state differ by less than 5%. This is sufficient for an approximately equal distribution of the conduction losses. The inductance differences between the paths listed in **Tab. 5.1** may still cause asymmetric current sharing during commutation. However, for ZVS operation, where ideally

⁴Because only the differences are analyzed, the current return path from terminal AC2 to terminal AC1 has no effect. For the simulation, the return path is modeled with a litz wire arranged similar to the load connections in the final converter setup. For clarity, the wire is not shown in the figure.

no overlapping of the drain current and the drain-to-source voltage of the devices occurs, this is less of a concern than for a hard-switched converter.

Measurement results showing the current sharing among the paralleled devices during continuous conduction and during transients obtained from the final converter setup are presented in Section 6.1.1.

5.2.3 Gate Driver Concept

For the gate drive of the paralleled power MOSFETs, it is crucial to use separate gate resistors as shown in **Fig. 5.7(a)** to prevent oscillations between via the gate-drain path of the paralleled devices [143]. In addition, source connections are placed as close as possible to each device to prevent coupling effects from the load current via the common source inductance to the MOSFET gates [145].

As outlined above, a symmetrical design of all gate-loops is necessary for equal current sharing among the paralleled devices. However, a measurement of the package inductance of a TO-247 housing as shown in **Fig. 5.7(b)** indicates that the exact layout of the gate circuitry is less critical than a tight connection between the device housings and the power board. As long as the gate connections are routed tightly together as co-planar lines on the gate drive PCB, the package inductance contributes the major part of the total gate inductance.

The final layout for the gate drive PCB is shown in **Fig. 5.7(c)**. The high-side and the low-side gate drive circuits are both included on the same four layer board. Both drivers are completely isolated from the control for symmetry reasons. A driver of type 1ED020I12 is used as the signal isolator for its high Common Mode (CM) immunity. The driver is connected to two paralleled push-pull stages, each consisting of a pair of bipolar transistors. The positive and negative gate voltages $+22\text{ V}/-5\text{ V}$ are generated by an isolated supply circuit. The gate resistors and the necessary connections are placed on the top layer and first inner layer for the low-side driver and on the bottom layer and lowest inner layer for the high-side driver. The FR4-core of the PCB provides the necessary isolation distance. The outer dimensions of the gate drive PCB are 35 x 90 mm.

The footprint of the complete switching cell, including the half-bridge with six SiC MOSFET devices and the gate drive PCB, is 35 x 116 mm, which is approximately 40% smaller than the footprint

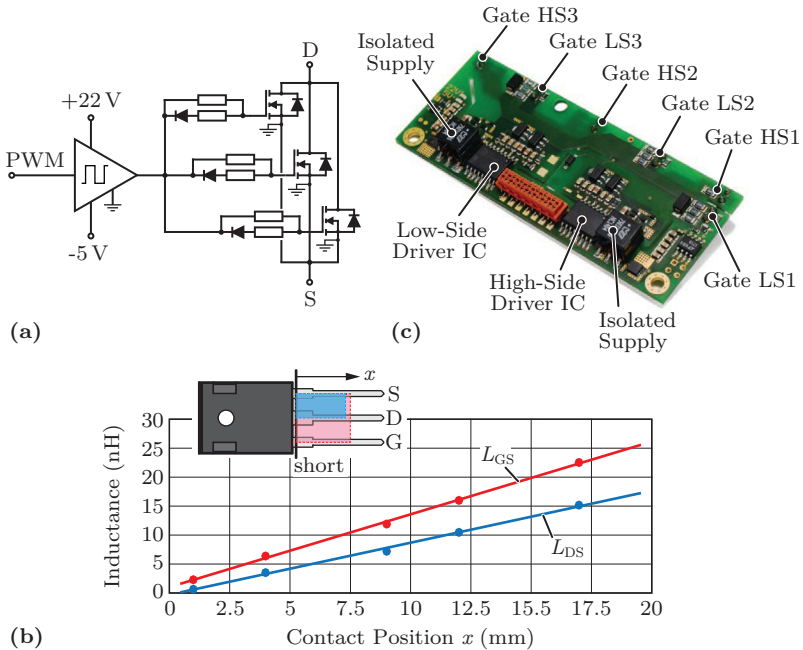


Fig. 5.7: (a) Gate driver circuit with separate gate resistors for each of the paralleled MOSFETs. (b) Measured gate-to-source inductance L_{GS} and drain-to-source inductance L_{DS} of a TO-247 housing in function of the contact position x (internal inductance of wire bonds not included). (c) Photograph of the gate driver PCB. The outer dimensions of the board are 35 x 90 mm.

of a 62 mm half-bridge module at a comparable on-state resistance of 8.3 m Ω for the three paralleled devices. The vertical extension is approximately 20 mm. For comparison, the vertical size of the power module is 30 mm, excluding the additionally required driving circuitry, which adds at least another 10 mm.

5.2.4 Inverter Stage Assembly

The final assembly of the ZVS full-bridge inverter stage is shown in **Fig. 5.8**. An aluminum heat sink with milled fins and axial cooling fans is used for the forced-air cooling of the SiC MOSFET devices. The heat sink is dimensioned using [124] under consideration of the

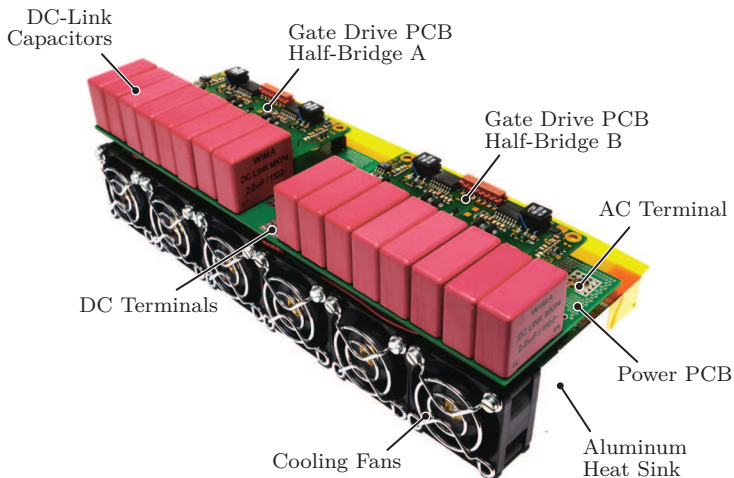


Fig. 5.8: Photograph of the final assembly of the 800 V/120 A/85 kHz ZVS full-bridge inverter stage with a power density of $48 \text{ kW}/\text{dm}^3$. The form factor is optimized for the combination with the three interleaved DC-DC converters.

maximum misalignment of the IPT coils, where the maximum RMS output current of up to 120 A of the inverter stage is reached.

The power density of the realized full-bridge as shown in **Fig. 5.8** is $48 \text{ kW}/\text{dm}^3$, a result of the high switching frequency of 85 kHz that allows for a small DC-link capacitance and the compact realization of the switches with discrete devices instead of power modules. The form factor of the full-bridge assembly is selected considering the combination with the three parallel interleaved DC-DC converters in the assembly of the complete converter (cf. **Fig. 5.23**).

5.3 Modular Buck+Boost-Type DC-DC Conversion Stage

As outlined above, buck+boost capability is required for the DC-DC conversion stage, because of the specified battery and DC-link voltage levels. The selected DC-DC converter topology in **Fig. 5.9(a)** provides the necessary features. Coupled inductors are used for a high power

density of the magnetic components [135–140]. The working principles for the coupled inductors and the detailed operation of the converter are discussed in the first part of this section. Thereafter, the design of the magnetic components is discussed and it is shown that the coupled inductors can be realized with a smaller area product than conventional parallel interleaved inductors. The realized hardware prototype is presented at the end of the chapter.

5.3.1 Inverse-Coupled and Direct-Coupled Magnetic Components

Before the discussion of the converter operation, the necessary conventions for the Inverse-Coupled Inductor (ICI) and the Direct-Coupled Inductor (DCI) that are used as magnetic components in the presented DC-DC converter are introduced. The key advantages of such a solution compared to a conventional parallel interleaved converter are discussed further below.

As shown in **Fig. 5.9(a)**, the ICI and the DCI are connected in series between the half-bridges 1/2 and 3/4 of the DC-DC converter. They therefore share the same winding currents i_{L1} and i_{L2} , which each contribute half of the DC current that is responsible for the power flow through the converter. The windings senses of the two devices are selected such that the DC flux components cancel out in the core of the ICI, while in the core of the DCI the DC flux components add up. Therefore, the core of the DCI is realized with an air gap δ to lower the inductance in order to avoid saturation. The ICI core does not require an air gap, if the winding currents are sufficiently well balanced during operation by the control. The winding sense and the magnetic circuits are illustrated in **Figs. 5.9(b)-(c)**. The turns numbers of the two windings on the ICI core are equal. Therefore, the self-inductance L_{ICI} is equal for each winding of the ICI. Also the turns numbers of the two windings of the DCI are equal and the inductances L_{DCI} are the same for both windings. If as a first approximation an ideal coupling of the two windings is assumed, the transformer equivalent circuits shown in **Figs. 5.9(d)-(e)** result.

From the equivalent circuit diagram of the ICI in **Fig. 5.9(d)**, the slope of the Differential Mode (DM) current i_{DM} follows as

$$\frac{di_{DM}}{dt} = \frac{d}{dt} \frac{i_{L1} - i_{L2}}{2} = \frac{u_{ICI}}{2L_{ICI}} \quad (5.1)$$

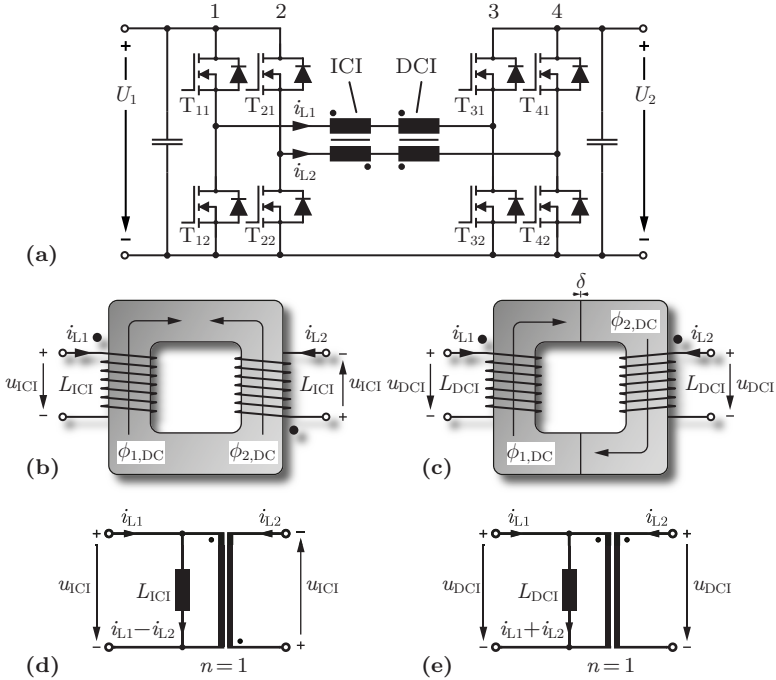


Fig. 5.9: (a) Selected topology for the buck+boost-type DC-DC converter with coupled magnetic components. (b)-(c) Definition of the winding sense and (d)-(e) transformer equivalent circuit diagrams for the ICI and the DCI, respectively.

Therefore, the effective inductance for the DM current ripple $\Delta i_{DM,pp}$ is $2L_{IC1}$. Concerning the total voltage at the ICI windings of $2u_{DM}$ (cf. **Fig. 5.11(c)**), the inductance $4L_{IC1}$ is effective, which is a result of the magnetic coupling of the two windings with individual inductance L_{IC1} .

Equally, from the DCI transformer equivalent circuit diagram of **Fig. 5.9(e)**, the slope of the CM current i_{CM} is calculated as

$$\frac{di_{CM}}{dt} = \frac{d}{dt} \frac{i_{L1} + i_{L2}}{2} = \frac{u_{DC1}}{2L_{DC1}} \quad (5.2)$$

and hence the CM current ripple $\Delta i_{CM,pp}$ results from the effective inductance $2L_{DC1}$ of the DCI. Concerning the output current i_{out} (cf. **Fig. 5.11(b)**), the inductance L_{DC1} is effective.

These relations indicate the main advantage of the coupled magnetic components instead of uncoupled inductors for the parallel interleaved converter. The DM and CM current ripples can be independently adjusted by the design of the inductances L_{ICI} and L_{DCI} . This additional degree-of-freedom in the design is responsible for the smaller required area product of this design option. However, for the derivation of these relations, first the operation of the DC-DC converter needs to be introduced. Therefore, the operation modes of the DC-DC converter are shortly discussed in the following.

5.3.2 Steady-State Converter Operation

The selected topology is configured for boost operation by keeping the switch nodes of the two neighboring bridge legs 1/2 in **Fig. 5.9(a)** constantly clamped to the input voltage U_1 . Alternatively, for the buck configuration, the bridge legs 3/4 are constantly clamped to the output voltage U_2 . In each case, the remaining bridge legs are used to apply a modulated voltage to the series connected ICI and DCI.

Figs. 5.10(a)-(c) shows the switching states and the paths of the inductor currents i_{L1} and i_{L2} for buck operation. The two input-side bridge legs 1/2 are operated with a constant phase shift of 180° and equal duty cycles, while the switch nodes of bridge legs 3/4 at the output side are constantly clamped to the output voltage U_2 . For boost operation, the bridge legs 1/2 are constantly clamped to the input voltage U_1 and the bridge legs 3/4 are switching with 180° phase shift and equal duty cycle as shown in **Figs. 5.10(d)-(f)**. The figure shows only the switching states for duty cycles $D < 0.5$ of the devices T_{11}/T_{21} in buck mode and T_{32}/T_{42} in boost mode. Bi-directional power transfer is possible if the diodes are only used for conduction during the interlock delay time and the gates of the MOSFETs are operated as for synchronous buck or boost operation.

In the following, only the buck mode operation is analyzed while the results apply analogously for operation in boost mode. Following [146], in **Fig. 5.11(a)** an equivalent circuit diagram of the converter is shown where the switch node voltages of the bridge legs 1/2, denoted u_{11} and u_{21} , are replaced by rectangular voltage sources. As shown in [137, 138, 146], the switch node voltages can be divided into a CM and a DM component,

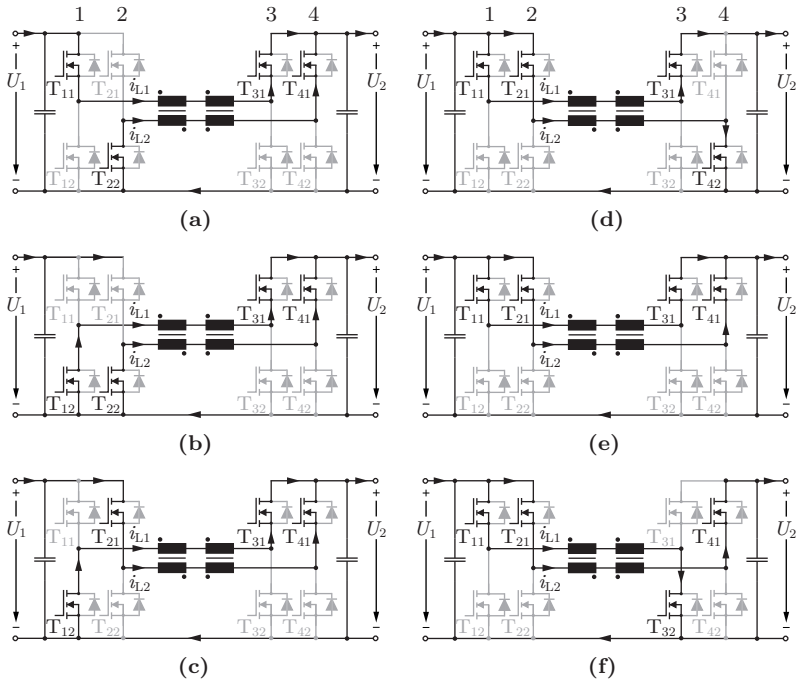


Fig. 5.10: (a)-(c) Switching states and paths of the inductor currents i_{L1} and i_{L2} for operation in synchronous buck mode and (d)-(f) in synchronous boost mode. Only the switching states for duty cycles $D < 0.5$ of the devices T_{11}/T_{21} in buck mode and T_{32}/T_{42} in boost mode are shown.

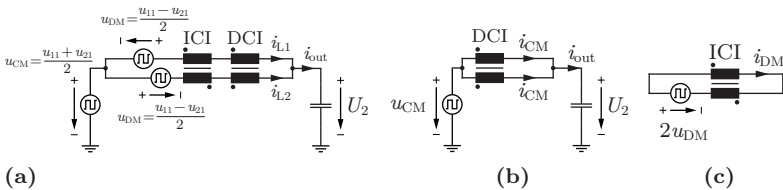


Fig. 5.11: (a) Converter equivalent circuit diagram for synchronous buck operation with replacement of the switch node voltages u_{11} and u_{21} by rectangular voltage sources. Splitting of the circuit into (b) a CM and (c) a DM equivalent circuit [146].

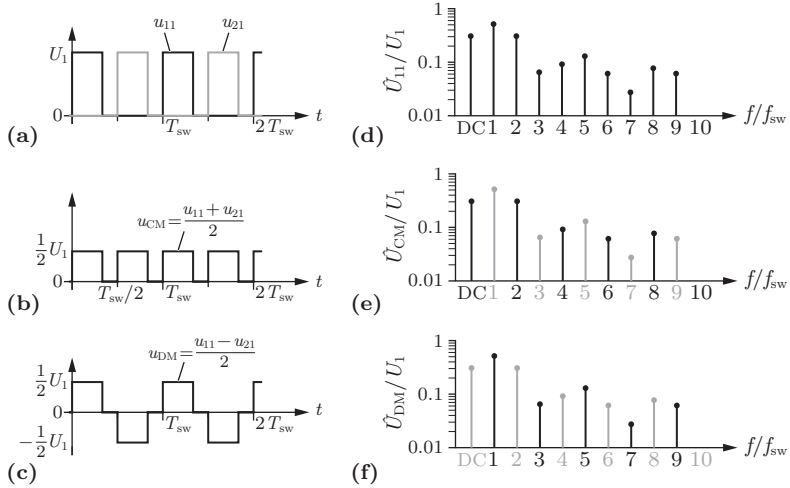


Fig. 5.12: (a) Switch node voltages u_{11}, u_{12} during synchronous buck operation with duty cycle $D = 0.3$ and 180° phase shift. (b) Corresponding CM and (c) DM voltage waveforms. Spectra of (d) the switch node voltage u_{11} , (e) the CM voltage u_{CM} , and (f) the DM voltage u_{DM} [146].

$$\begin{aligned}
 u_{CM} &= \frac{u_{11} + u_{21}}{2} \\
 u_{DM} &= \frac{u_{11} - u_{21}}{2}
 \end{aligned} \tag{5.3}$$

Schematic waveforms of the switch node voltages and the calculated CM and DM voltage components are shown in **Figs. 5.12(a)-(c)** for operation in synchronous buck mode with duty cycle $D = 0.3$.

Considering the opposite winding senses of the ICI and the DCI in the equivalent circuit diagram of **Fig. 5.11(a)**, independent CM and DM equivalent circuit diagrams can be derived as shown in **Figs. 5.11(b)-(c)**. From the simplified equivalent circuits, it becomes apparent that according to Kirchhoff's equations the voltage $u_{DCI} = u_{CM} - U_2$ is applied to each winding of the DCI. Equally, the voltage $u_{ICI} = u_{DM}$ appears at each winding of the ICI.

Spectral Analysis of the ICI and DCI Voltages

The effect of the ICI and DCI can also be understood by comparing the spectrum of the switch node voltage u_{11} and the spectra of the ICI and DCI winding voltages u_{ICI} and u_{DCI} , which are shown in **Figs. 5.12(d)-(f)**. As discussed in [146], the spectrum of the CM spectrum of the switch node voltage contains the DC component and the even harmonics. Consequently, the voltage applied to the DCI windings and the flux in the DCI core exhibit AC components at the even multiples of the switching frequency. Therefore, the even harmonics of the current ripple, which in sum form the CM current ripple Δi_{CM} , are attenuated by the DCI inductance L_{DCI} . Because of the winding sense described above, the DCI flux additionally contains a DC component, which shows that this device must store magnetic energy for the power transfer to the converter output. The DC component is given by the sum of the DC flux caused by the winding currents.

The DM spectrum contains the remaining odd harmonics of the switch node voltage spectrum [146] as shown in **Fig. 5.12(f)**. Hence, the voltage applied to the windings of the ICI and the flux in the ICI core contain components at the converter switching frequency f_{sw} and at its odd multiples. The odd harmonics of the current ripple, i. e. the DM current ripple Δi_{DM} , are attenuated by the inductance L_{ICI} . Similar to a transformer, the ICI flux does not contain a DC component, which shows that the device does not store net magnetic energy. Therefore, the area product of the ICI is small compared to the DCI, as will be discussed in more detail below.

5.3.3 Design of the Magnetic Components

For the design of the magnetic components, in a first step the ripple currents in the inductor windings are calculated. Based on the ripple calculation, a comparison to a converter with parallel interleaved stages with uncoupled inductors is presented at the end of the section.

Calculation of the Ripple Currents

Calculated waveforms for buck operation of the DC-DC converter with ICI and DCI are shown in **Fig. 5.13(a)** for a duty cycle $D = 0.3$ and in **Fig. 5.13(b)** for a duty cycle $D = 0.7$. The calculated DCI and ICI winding voltage amplitudes are indicated in the figures. In

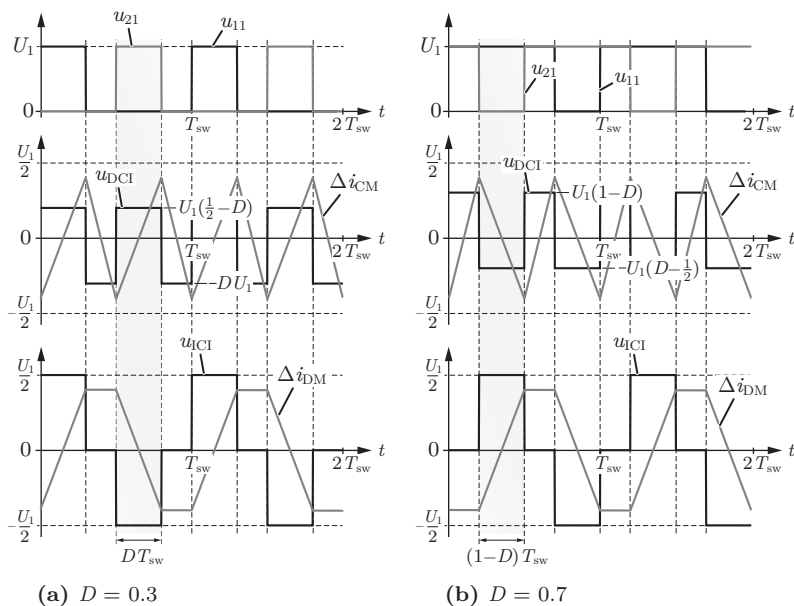


Fig. 5.13: (a) Calculated waveforms for the DC-DC converter with ICI and DCI for duty cycle $D = 0.3$, and (b) $D = 0.7$. The marked intervals are used for the calculation of the CM and DM ripple currents Δi_{CM} , Δi_{DM} .

the marked time intervals, the peak-to-peak values of the CM and DM current ripples are calculated as

$$\begin{aligned} \Delta i_{\text{CM,pp}} &= \frac{U_1 \left(\frac{1}{2} - D_{\text{eff}} \right)}{2L_{\text{DCI}}} \cdot \frac{D_{\text{eff}}}{f_{\text{sw}}} \\ \Delta i_{\text{DM,pp}} &= \frac{\frac{1}{2}U_1}{2L_{\text{ICI}}} \cdot \frac{D_{\text{eff}}}{f_{\text{sw}}}, \end{aligned} \quad (5.4)$$

where the introduction of the effective duty cycle D_{eff}

$$D_{\text{eff}} = \begin{cases} D, & \text{for } 0 \leq D \leq 0.5 \\ 1 - D, & \text{for } 0.5 < D \leq 1 \end{cases} \quad (5.5)$$

serves the purpose of representing the results for $D \leq 0.5$ and $D > 0.5$ in a single equation.

The peak-to-peak CM and DM current ripples are shown in **Fig. 5.14(a)** as functions of the duty cycle. For comparison, also the peak-to-peak current ripple $\Delta i_{L,pp}$ in the windings of two uncoupled inductors is shown [146]. All current ripple values are normalized to the DC-link voltage U_1 , the switching frequency f_{sw} , and the respective inductance. The maximum CM and DM current ripples are obtained at $D = 0.25$ or $D = 0.75$, and at $D = 0.5$, respectively, as

$$\begin{aligned}\Delta i_{CM,pp,max} &= \frac{1}{32} \frac{U_1}{f_{sw} L_{DCI}} \\ \Delta i_{DM,pp,max} &= \frac{1}{8} \frac{U_1}{f_{sw} L_{ICI}}\end{aligned}\quad (5.6)$$

The winding current ripples Δi_{L1} , Δi_{L2} are calculated from the CM and DM current ripples as

$$\begin{aligned}\Delta i_{L1,pp} &= \Delta i_{CM,pp} + \Delta i_{DM,pp} \\ \Delta i_{L2,pp} &= \Delta i_{CM,pp} - \Delta i_{DM,pp}\end{aligned}\quad (5.7)$$

The normalized winding current ripple $\Delta i_{L1,pp}$ is shown in **Fig. 5.15(a)** as a function of the duty cycle and for different inductance ratios L_{ICI} to L_{DCI} . As indicated by the shaded areas, the unconventional shape of the curves results from the superposition of the triangular curve representing the DM current ripple with the CM current ripple of **Fig. 5.14(a)**. **Fig. 5.15(b)** shows the waveforms for the winding current ripples that correspond to the curves in **Fig. 5.15(a)** and the duty cycle $D = 0.3$. For larger values of L_{ICI} , the DM current ripple is attenuated more and more strongly and the winding current ripple becomes smaller. In the ideal case where L_{ICI} is infinitely large, the DM current ripple completely vanishes and only the CM ripple is left in the winding. This means that i_{L1} and i_{L2} become equal, even though the switch node voltages u_{11} and u_{21} are 180° phase shifted.

The ripple of the converter output current $\Delta i_{out,pp}$ follows from the sum of the winding currents as

$$\Delta i_{out,pp} = 2\Delta i_{CM,pp}, \quad (5.8)$$

which is shown in normalized form in **Fig. 5.14(b)** as a function of the duty cycle. The normalized output current $\Delta i_{O,ipp}$ of a converter with two uncoupled inductors is shown as a comparison [146]. The maximum output current ripple appears in both cases at $D = 0.25$ or at $D = 0.75$.

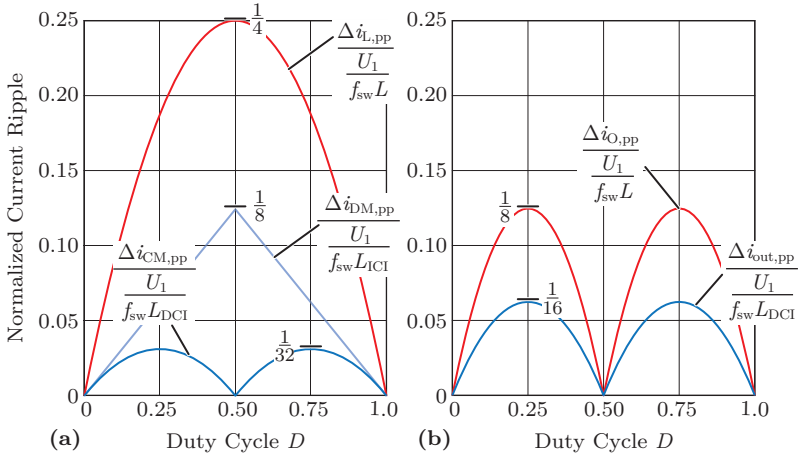


Fig. 5.14: (a) Normalized CM and DM current ripples $\Delta i_{CM,pp}$, $\Delta i_{DM,pp}$ in comparison to the current ripple $\Delta i_{L,pp}$ in the case of two uncoupled inductors. (b) Normalized output current ripple in the case of coupled inductors $\Delta i_{out,pp}$ in comparison to the output current $\Delta i_{O,pp}$ in the case of uncoupled inductors.

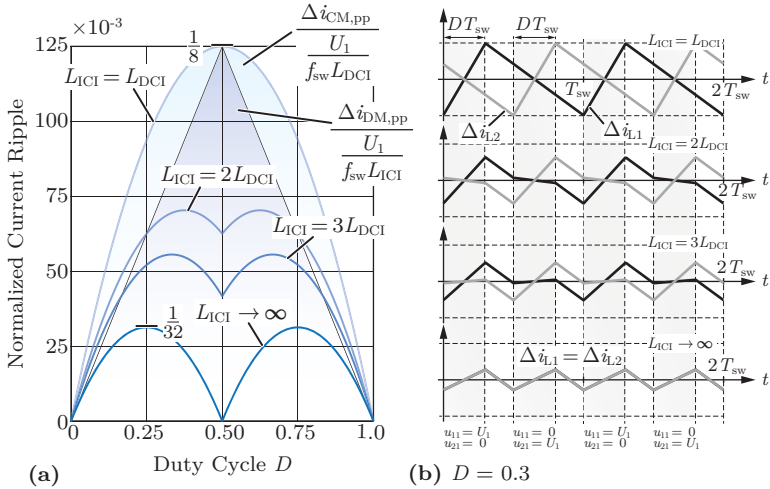


Fig. 5.15: (a) Normalized winding current ripple as a function of the duty cycle D for different ratios of ICI inductance L_{ICI} to DCI inductance L_{DCI} . (b) Waveforms of the winding current ripples $\Delta i_{L,2}$ and $\Delta i_{L,1}$ for $D = 0.3$.

For the converter with coupled inductors, the maximum is calculated as

$$\Delta i_{\text{out,pp,max}} = \frac{1}{16} \frac{U_1}{f_{\text{sw}} L_{\text{DCI}}}, \quad (5.9)$$

whereas for the converter with uncoupled inductors of inductance L , the maximum is [146]

$$\Delta i_{\text{O,pp,max}} = \frac{1}{8} \frac{U_1}{f_{\text{sw}} L} \quad (5.10)$$

This comparison shows that for the same switching frequency and inductance $L = L_{\text{DCI}}$, the output current ripple is reduced by a factor of two by the direct coupling of the parallel interleaved inductors. As shown below in more detail, the current ripple reduction occurs because the stored magnetic energy in the DCI is increased by a factor of two compared to two parallel interleaved inductors of the same inductance as a result of the coupling of the DCI windings. Furthermore, (5.8) shows that the ripple of the output current depends only on the CM current ripple, i.e., on the DCI inductance L_{DCI} , and not on the inductance of the ICI. However, according to (5.7), the winding current ripples depend on both inductance values. Therefore, in the component design the inductance L_{DCI} can be used to fulfill an output current ripple criterion, while the additional degree-of-freedom L_{ICI} is used for the attenuation of undesired DM currents between the interleaved bridges. Thereby, the winding RMS currents, the resistive losses in the coils, as well as conduction and switching losses in the power semiconductors are minimized. This ability is a fundamental advantage of the solution with coupled inductors.

Calculation of the Area Product and the Stored Energy

So far, the differences between the converter with coupled inductors and a converter with uncoupled inductors were discussed in terms of current ripples and inductance values. However, in order to estimate which solution finally leads to the more compact design, a comparison of the total required area products is necessary.

If the current density in the inductor windings is limited to the maximum RMS current density J_{max} , the required DCI or ICI winding window is

$$A_{\text{cu}} = \frac{N(I_{L1} + I_{L2})}{k_{\text{cu}}J_{\text{max}}} = \frac{2NI_{L1}}{k_{\text{cu}}J_{\text{max}}}, \quad (5.11)$$

where N stands for the turns number and k_{cu} is the copper filling factor of the winding window. The given simplification is possible because the RMS values of the winding currents I_{L1} and I_{L2} are equal.

The RMS values of the winding currents depend on the ratio of ICI inductance L_{ICI} and DCI inductance L_{DCI} as shown in **Fig. 5.15(a)**. For the design $L_{\text{ICI}} = L_{\text{DCI}}$, the winding current ripple has a single maximum at $D = 0.5$, which is exactly 50% of the winding current ripple of uncoupled inductors. This choice for the ICI inductance L_{ICI} leads to one half of the winding and output current ripples than for uncoupled inductors at the same switching frequency. For this design, the maximum RMS currents can be extracted at $D = 0.5$, where the CM ripple vanishes. The result is

$$I_{L1} = I_{L2} = \sqrt{\left(\frac{I_{\text{DC}}}{2}\right)^2 + \left(\frac{\Delta i_{\text{DM,pp,max}}}{2\sqrt{3}}\right)^2}, \quad (5.12)$$

where I_{DC} is the total DC output current of the converter. The remaining calculations are not affected by the selection of the L_{ICI} to L_{DCI} ratio.

The peak value of the flux linkage in the DCI is given by

$$\hat{\psi}_{\text{DCI}} = 2L_{\text{DCI}} \left(\frac{I_{\text{DC}}}{2} + \frac{\Delta i_{\text{CM,pp,max}}}{2} \right), \quad (5.13)$$

and the flux linkage of the ICI is calculated as

$$\hat{\psi}_{\text{ICI}} = 2L_{\text{ICI}} \left(\frac{I_{\text{DC,offset}}}{2} + \frac{\Delta i_{\text{DM,pp,max}}}{2} \right), \quad (5.14)$$

if also a DC offset $I_{\text{DC,offset}}$ is taken into account. The DC offset could result for instance from a sensor offset in the current measurement, from the Analog-to-Digital (ADC) conversion, from the discretization for the digital control, from transient or steady-state control errors, or if unbalanced voltage time areas are applied to the circuit by the two interleaved half-bridges. As an approximation, the offset is considered to be proportional to the load current of the converter and $I_{\text{DC,offset}} = 5\% I_{\text{DC}}$ is assumed for the following discussion.

The minimum core cross-section A_{core} needed to limit the flux density in the DCI to the maximum value B_{max} is given by

$$A_{\text{core}} = \frac{\hat{\psi}_{\text{DCI}}}{2NB_{\text{max}}}, \quad (5.15)$$

The combination of this result with (5.11) leads to the DCI area product

$$A_{\text{cu}}A_{\text{core}} = \frac{\hat{\psi}_{\text{DCI}}I_{\text{L1}}}{k_{\text{cu}}J_{\text{max}}B_{\text{max}}}, \quad (5.16)$$

The ICI area product is calculated by replacing the flux linkage $\hat{\psi}_{\text{DCI}}$ by $\hat{\psi}_{\text{DCI}}$ in (5.15) and (5.16).

As a last step, the stored magnetic energy in the devices is calculated with the peak flux density and the peak value of the total current, which for the DCI is given by the sum $i_{\text{L1}} + i_{\text{L2}} = 2i_{\text{CM}}$ and for the ICI by the difference $i_{\text{L1}} - i_{\text{L2}} = 2i_{\text{DM}}$. Hence, the peak value of the stored magnetic energy in the DCI is given by

$$E_{\text{DCI}} = \frac{1}{2}\hat{\psi}_{\text{DCI}} \cdot 2\hat{I}_{\text{CM}}, \quad (5.17)$$

which results in the simplified expression

$$E_{\text{DCI}} = 2L_{\text{DCI}} \left(\frac{I_{\text{DC}}}{2} + \frac{\Delta i_{\text{CM,pp,max}}}{2} \right)^2 \quad (5.18)$$

For the ICI, the peak stored magnetic energy analogously results as

$$E_{\text{ICI}} = 2L_{\text{ICI}} \left(\frac{I_{\text{DC,offset}}}{2} + \frac{\Delta i_{\text{DM,pp,max}}}{2} \right)^2 \quad (5.19)$$

This result can be intuitively understood from a simplified consideration. The magnetic energy in the DCI is given by

$$E_{\text{DCI}} = \frac{1}{2}L_{\text{DCI}}i_{\text{L1}}^2 + \frac{1}{2}L_{\text{DCI}}i_{\text{L2}}^2 + M_{\text{DCI}}i_{\text{L1}}i_{\text{L1}}, \quad (5.20)$$

where M_{DCI} is the mutual inductance of the DCI. If the DCI windings are ideally coupled the mutual inductance is equal to the DCI self-inductance $M_{\text{DCI}} = L_{\text{DCI}}$ as used throughout in the above derivation. Since only the CM current causes a magnetic flux in the core, the winding currents can be replaced by $i_{\text{L1}} = i_{\text{L2}} = i_{\text{CM}}$. Therefore, the peak value of the magnetic energy is

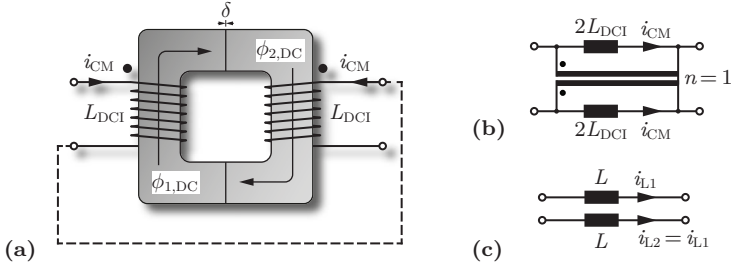


Fig. 5.16: (a) CM magnetic circuit and (b) electric equivalent circuit diagram of the DCI and (c) of two uncoupled inductors used for comparing the stored magnetic energy.

$$E_{DCI} = 2L_{DCI}\hat{I}_{CM}^2 \quad (5.21)$$

This result becomes immediately clear if the equivalent circuit in **Fig. 5.9(e)** is modified as shown in **Fig. 5.16(b)**. Furthermore, the CM magnetic circuit shown in **Fig. 5.16(a)** provides additional insight. If the two DCI winding currents are equal, the windings can be treated as if they were series connected. Because the turns number is doubled, the total inductance of the series connection of two windings with inductance L_{DCI} on a common core is equal to $4L_{DCI}$. Therefore, the peak value of the stored magnetic energy is given by

$$E_{DCI} = \frac{1}{2}(4L_{DCI})\hat{I}_{CM}^2, \quad (5.22)$$

which is equivalent to the result obtained in (5.21).

In contrast, the magnetic energy stored in two uncoupled inductors with equal winding currents $i_{L1} = i_{L2}$ is obtained from **Fig. 5.16(c)** as

$$E_L = \frac{1}{2}L\hat{I}_{L1}^2 + \frac{1}{2}L\hat{I}_{L2}^2 = L\hat{I}_{L1}^2, \quad (5.23)$$

Comparing this result to (5.21) shows, that for the same inductance $L = L_{DCI}$ and current $i_{L1} = i_{CM}$, the energy stored in the DCI is increased by a factor of two as a result of the magnetic coupling of the two windings.

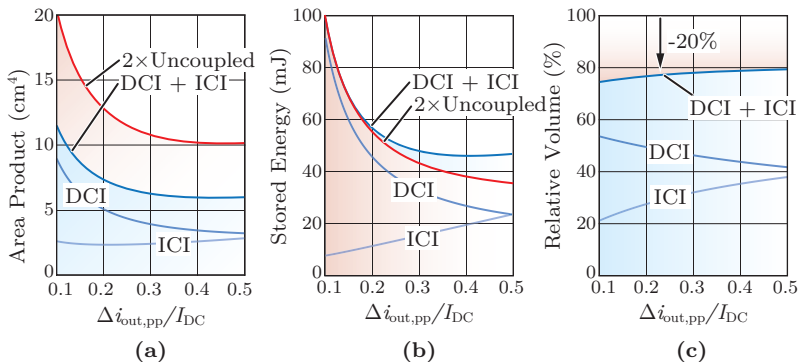


Fig. 5.17: (a) Calculated area products and (b) peak stored magnetic energy for two uncoupled inductors and for coupled magnetic components as a function of the relative output current ripple. (c) Approximate volume of the DCI and ICI solution as percentage of the volume of two uncoupled inductors (estimated from area product).

Comparison to Uncoupled Magnetic Components

A comparison of the area products for the ICI and the DCI to the total area product for two uncoupled inductors is shown in **Fig. 5.17(a)** as a function of the relative current ripple $\Delta i_{out}/I_{DC}$ at the converter output. For the calculation, the values $J_{max} = 2 \text{ A/mm}^2$, $k_{cu} = 0.5$, $B_{max} = 1 \text{ T}$, $f_{sw} = 50 \text{ kHz}$, $U_{DC} = 800 \text{ V}$, and $I_{DC} = 16.7 \text{ A}$ are used with reference to the presented prototype. The peak values of the stored magnetic energy in the devices are compared in **Fig. 5.17(b)**.

At a low relative output current ripple, the DCI inductance has to be large for the required attenuation of the CM current ripple. Due to the linking of the two inductance values by the assumption $L_{ICI} = L_{DCI}$ taken above, the ICI inductance is also higher at a low relative output current ripple. Therefore, the contributions of the decreasing CM and DM current ripples to the flux linkages become smaller and smaller compared to that of the DC components. Hence, the area product is dominated by the stored DC magnetic energy of the components. As shown in **Fig. 5.17(b)**, the magnetic energy stored by the DCI drastically increases at a low relative output current ripple. Because the considered DC offset $I_{DC,offset}$ is much smaller than the DC output current I_{DC} , the area product and the stored energy of the ICI are

significantly smaller than those of the DCI.

As the relative output current ripple is increased, the inductances become smaller. Therefore, the area products of the ICI and the DCI initially decrease. As confirmed by **Fig. 5.17(b)**, the magnetic energy stored in the DCI becomes lower as the inductance reduces. However, for higher relative output current ripples, again due to the underlying assumption $L_{ICI} = L_{DCI}$ also the CM and DM ripple currents increase. The stored magnetic energy in the ICI is dominated by the DM ripple component, because the DC offset $I_{DC,offset}$ is small. Therefore, the stored magnetic energy in the ICI rises proportionally to the relative output current ripple. The same phenomenon could be observed for the DCI as well, but it occurs at a higher output current ripple, because of the large DC current component.

At a certain point, the AC current components caused by the DM and CM current ripples become comparable to the DC components caused by the output current I_{DC} and the DC offset $I_{DC,offset}$. They start dominating the peak values of the flux linkages and the winding RMS current. Therefore, the area product decreases at a reducing rate for the DCI. For the ICI, the area product even has a minimum at $\Delta i_{out,pp}/I_{DC} \approx 0.2$ as shown in **Fig. 5.17(a)**, after which it starts increasing again. At high relative output current ripples, the area products of the ICI becomes comparable to that of the DCI.

All in all, the combined area product of the ICI and the DCI together is more than 40% smaller than the area product for two uncoupled inductors. The total stored magnetic energy at a given relative output current ripple is similar for the coupled magnetic devices and for uncoupled inductors. Hence, as a result of the magnetic coupling, the energy storage capability is increased by approximately a factor of two for a given area product. This observation confirms that the area product and the stored magnetic energy of a magnetic component are typically not directly related. For instance in an inductor, the magnetic energy is stored in the air gap while the core is only needed to guide the flux and to establish the desired field configuration in the air gap [147]. For providing this functionality, a certain core cross-section and winding window are necessary in order to avoid saturation of the core and to limit the current density in the windings. These requirements are characterized by the area product of the inductor. As an alternative example, no energy is stored in a transformer with an ideal core of infinite permeability and with negligible leakage inductance. Nevertheless,

the flux density in the core is not zero and a certain core cross-section is needed to avoid saturation. The area product of the transformer, which results from the core cross-section and the necessary winding window, is therefore not related to a stored magnetic energy.

For a simplified comparison of the component size of the magnetic devices, the volume is assumed to be approximately proportional to the area product to the power of 0.75 [147,148]. The obtained estimates for the DCI and ICI component volumes are shown in **Fig. 5.17(c)** as a percentage of the total volume of two uncoupled inductors. Depending on the specified relative output current ripple, an approximately 20% smaller total magnetics volume is required as a result of the coupling of the magnetic components.

5.4 Power Electronics Control

As outlined in Section 2.3.4, the control of the output power of the IPT system is realized most efficiently by adapting the DC-link voltages of the transmitter-side and the receiver-side power electronic converters. This has the key advantage that the IPT system, which constitutes the *weakest link* of the power conversion chain, is constantly operated at its natural efficiency optimum. Other control schemes typically involve detuning the resonant circuit by increasing the switching frequency of the inverter-stage above the resonant frequency. However, as shown previously, this leads to high reactive currents that circulate in the IPT resonant circuit, without contributing to the power transfer. Alternatively, the duty cycles of the inverter- and the rectifier-stage can be adapted to modulate the fundamental amplitude of the voltage applied to the resonant system at the cost of switching losses in both power electronic converters [36]. With the aim of reaching the maximum possible efficiency for the IPT system, the voltage control scheme is implemented for the measurements presented in this thesis. In the following, a brief overview of the key aspects for the realization of the control of the IPT system is given.

5.4.1 Control of the IPT System Output Power

For the proposed control scheme, the DC-link voltages of the IPT system need to be regulated with the buck+boost-type DC-DC converter. The block diagram of the control system was previously shown in Sec-

tion 2.3.4 and is not repeated here. In the implementation of the control, both voltages $U_{1,DC}$ and $U_{2,DC}$ are adapted simultaneously. Due to the impressed DC-link voltages, the output power approximately follows

$$P_2 = \frac{8}{\pi^2} \frac{U_{1,DC} U_{2,DC}}{\omega_0 M} \quad (5.24)$$

which is given in (2.34) in Section 2.3.4.

The critical parts of the control are implemented at the receiver side, which is closer to the battery and can therefore provide better monitoring and protection. The receiver-side controller computes the reference values for both DC-link voltages $U_{1,DC}^*$ and $U_{2,DC}^*$ as described in Section 2.3.4. The DC-DC conversion stages in the power converters at the transmitter and the receiver side regulate the two DC-link voltages to the calculated reference values. For the necessary communication, the main control board of the power converter is equipped with a wireless communication interface.

In each converter, one out of the three parallel interleaved DC-DC converter modules is used to control the DC-link voltage. In the remaining two modules, current controllers ensure that the load current is shared equally between all parallel interleaved stages. Details on the feedback control of the DC-DC converter with coupled magnetic components are given in the following.

5.4.2 Feedback Control of the DC-Link Voltage

An intuitive solution for the feedback control of the output voltage of the DC-DC converter presented above is to use a cascaded control system as shown in **Fig. 5.18(a)**. An outer feedback loop is implemented for the control of the converter output voltage U_2 and an inner control loop for the control of the two inductor currents i_{L1} and i_{L2} . For a converter with parallel interleaved stages with uncoupled inductors, this is the standard solution.

However, for the selected buck+boost type topology with coupled magnetic components, an individual control of the two winding currents bears the problem that equality of the two currents i_{L1} and i_{L2} is not always given, e. g., during load steps, where a large DM current component could result in a saturation of the ICI. In addition, because the average inductor voltages \bar{u}_{L1} and \bar{u}_{L2} are adjusted independently of each other, transient situations can occur where one converter phase

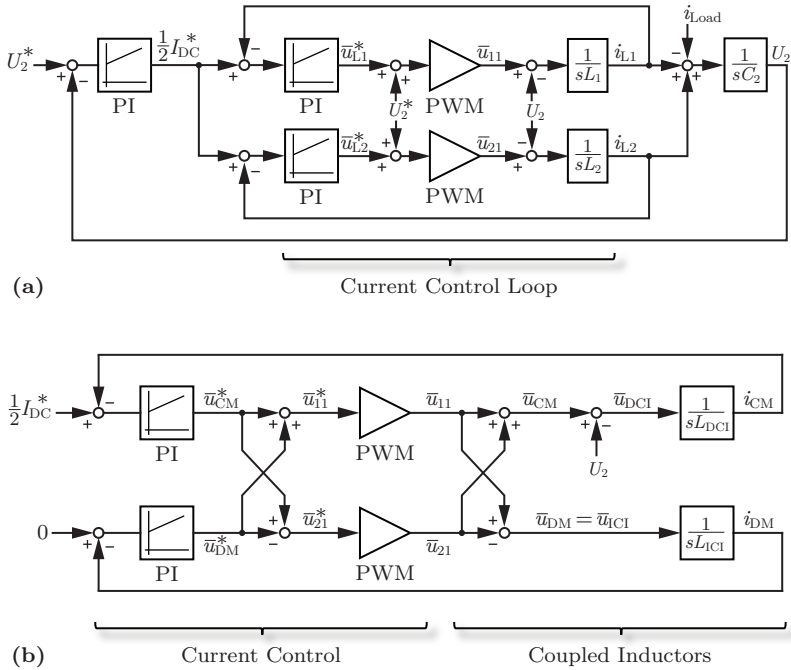


Fig. 5.18: (a) Block diagram of a cascaded voltage and current controller as it could be used in the case of uncoupled inductors. (b) Block diagram with separated current control loops for the CM and DM currents of the converter with coupled inductors.

is switched in boost mode, while the second phase is switched in buck mode. With uncoupled inductors, this is unproblematic. However, an analysis of the ICI and DCI voltages for this situation reveals that the voltages relations are inverted compared to the case that was analyzed above. It was assumed that always only the bridge legs at the same side of the buck+boost-type converter are operated. If this condition is violated and bridge legs at opposite sides of the converter are switched, the CM voltage is applied to the ICI and the DM voltage to the DCI. In a practical setup, this leads to an immediate saturation of the ICI and therefore needs to be prohibited. Thus, an adaption of the conventional cascaded control scheme is necessary in order to take into account the actual voltages applied to the DCI and the ICI.

As a solution, it is proposed to directly control the CM and DM currents i_{CM} and i_{DM} instead of the individual winding currents. The adapted control diagram is shown in **Fig. 5.18(b)**. Given the analysis of the previous section, it is possible to control the CM current via the CM component u_{CM} of the switch node voltages, while the DM current can be controlled via the DM component u_{DM} . Therefore, the output of the Proportional-Integral (PI) controllers for this scheme are reference values for the average CM and the DM voltages \bar{u}_{CM}^* and \bar{u}_{DM}^* . The reference values for the local average values of the switch node voltages are calculated as

$$\begin{aligned}\bar{u}_{11}^* &= \bar{u}_{\text{CM}}^* + \bar{u}_{\text{DM}}^* \\ \bar{u}_{21}^* &= \bar{u}_{\text{CM}}^* - \bar{u}_{\text{DM}}^*\end{aligned}\tag{5.25}$$

The average switch node voltage references are fed to the PWM modulator and applied to the coupled inductors as shown in **Fig. 5.18(b)**. In this way, the control of the DM and CM current components is fully decoupled. By appropriately designing the PI controller, it can be ensured that the average DM current is always actively controlled to zero in order to avoid saturation of the ICI. The output current is controlled via the CM voltage to the reference value I_{DC}^* , which is obtained from the voltage controller in the outer control-loop.

In **Fig. 5.19**, the proposed control scheme is verified by a measurement of the dynamic response of the CM and DM currents of the realized hardware prototype during a step of the CM current reference. First, only the CM current control is activated. As shown in **Fig. 5.19(a)**, a transient DM current is observed, which takes several milliseconds to converge back to its steady-state value. Without the DM control, the steady-state DM current is defined by the different AC resistances and stray inductances of the coupled inductors, as well as by the accuracy of the PWM modulation. The transient deviation from the steady-state is most likely due to an unmodeled cross coupling between the CM and DM currents that results from the nonidealities of the converter, the ADC conversion, and the modulation scheme. During load steps, the observed transient DM current can potentially lead to saturation of the ICI core. The separate PI control of the DM current effectively avoids such transients and prevents core saturation, as confirmed by **Fig. 5.19(b)**. The proportional control gain is set to the same value for both PI controllers in order to achieve a fast disturbance rejection, while the integrator part of the DM current control needs to

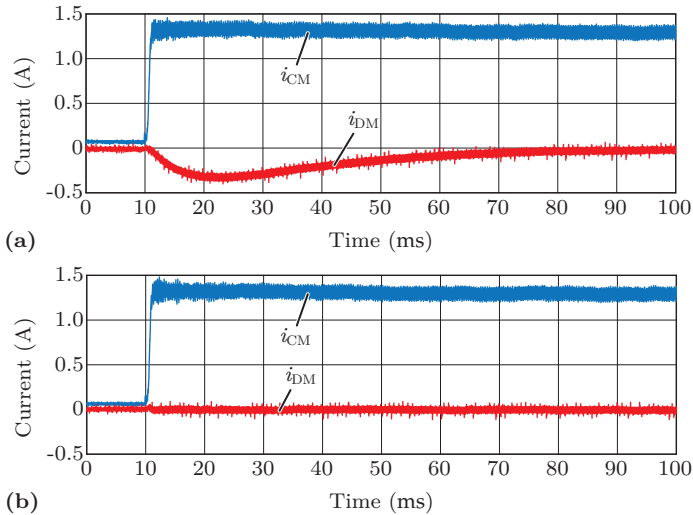


Fig. 5.19: Measured dynamic response of the CM and DM currents during a step of the CM current reference: (a) only the CM current control is activated. (b) both CM and DM current control are active.

be significantly slower for ensuring a dynamic decoupling of the two control loops.

In the final system, one of the three parallel interleaved modules in each power converter is operated with a cascaded voltage control to adjust $U_{1,DC}$ or $U_{2,DC}$ for the regulation of the power flow in the IPT system, and to actively balance the two inductor currents by controlling the DM current to zero. In the remaining two modules only the current control is active. The current reference is calculated by the main control, such that the power is shared equally between all three DC-DC converter modules in steady state. This is implemented by taking the average of all currents and forwarding the result as current reference value to each current-controlled DC-DC converter module.

5.4.3 Synchronous Rectification at the Receiver

A disadvantage of the SiC MOSFETs that are employed in the ZVS full-bridge inverter stage is the comparably high forward voltage drop of the SiC body diode. Therefore, an active rectification is needed to

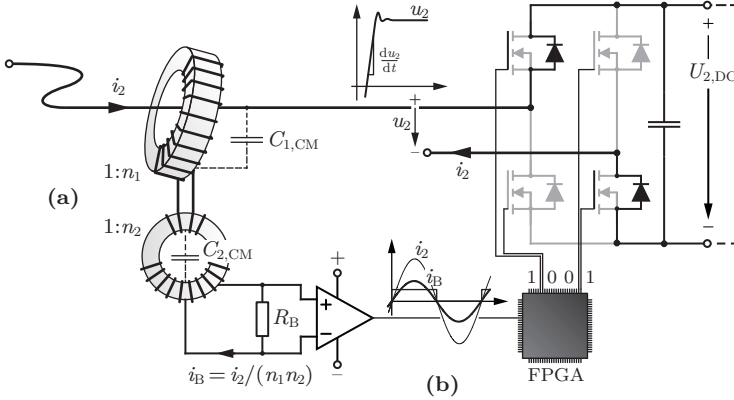


Fig. 5.20: (a) Two-stage AC current measurement with cascaded current transformers to reduce the CM stress and increase the measurement bandwidth. (b) Circuit diagram for the generation of the synchronous gate signals.

reduce the on-state conduction losses of the receiver-side power semiconductors. A synchronous rectification is implemented for the IPT converter based on a measurement of the current in the receiver coil with a two-stage current transformer.

The high receiver coil current at the full output power of 50 kW demands a high transformation ratio for the current transformer, which can be realized with a high turns number on the secondary. However, this limits the bandwidth of the measurement and exposes the signal electronics to a high CM stress. As a result of the high CM capacitance $C_{1,CM}$ between the transformer winding and the primary conductor and the steep voltage slopes at the switch node of the SiC MOSFET full-bridge (up to 60 kV/ μ s), a high CM rejection ratio is required for the measurement circuitry.

A smaller turns number is possible for the current transformer if it is cascaded with a second transformer as shown in **Fig. 5.20(a)**. In this arrangement, the current in the burden resistor i_B is scaled by the product of the transformation ratios of both transformers ($n_1 = 80$, $n_2 = 5$), which reduces the losses in R_B . In addition, the CM capacitances $C_{1,CM} = 2.7$ pF and $C_{2,CM} = 3$ pF of the two transformers are connected in series. Therefore the CM stress for the measurement circuitry is significantly reduced compared to using only a single current

transformer.

For the synchronous rectification, the measurement signal at the burden resistor R_B is connected to a comparator circuit for the detection of the receiver coil current zero crossings as shown in **Fig. 5.20(b)**. The comparator output is fed to the FPGA of the main control board in the IPT converter. There, digital filtering is applied to the incoming signal and synchronous gate signals are derived that activate the gates of the MOSFETs as soon as the conduction state of their respective body diodes is deduced from the receiver coil current measurement. This eliminates the high forward voltage drop of the SiC MOSFET body diode, which drastically reduces the on-state conduction losses of the receiver-side rectifier.

5.5 Realized Hardware Prototype

After the conceptual analysis of the selected converter topology, in this section the hardware implementation of the all-SiC IPT power electronics prototype is discussed.

5.5.1 Realized DC-DC Converter Module

With the aim of a high compactness of the DC-DC converter modules, a design with helical windings is chosen for the magnetic devices. A photograph of the two inductors is shown in **Fig. 5.21**. The helical winding leads to a high copper filling factor of $k_{cu} \approx 0.54$, which reduces the required winding window as well as the total magnetics area product. Both cores of the realized prototype are manufactured from tape wound C-cores.

Because of the different spectral content of the ICI and DCI magnetic flux linkages, it is useful to employ different magnetic materials for the two devices. The DCI has to store a net magnetic energy that is proportional to the output power. The DCI flux therefore mainly consists of a DC component on which a small AC ripple component at the even harmonics of the switching frequency is superimposed. Since the amplitude of the AC flux component excitation is small when compared to the DC component, the AC losses are comparably small. Therefore, the device is realized with an amorphous iron core, because of the high saturation flux density and low cost of this material. The ICI flux does

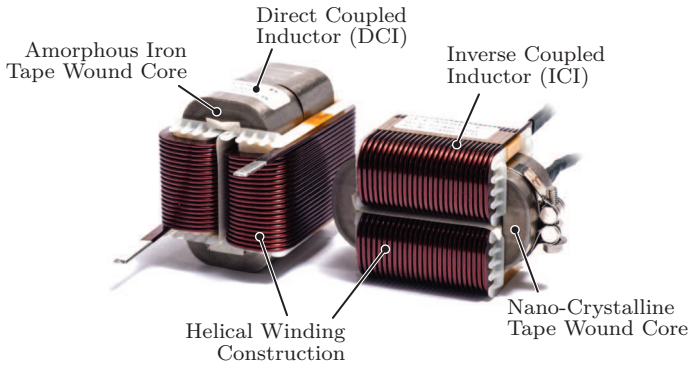


Fig. 5.21: Photograph of the assembled DCI and ICI for the 20 kW buck+boost-type DC-DC converter modules.

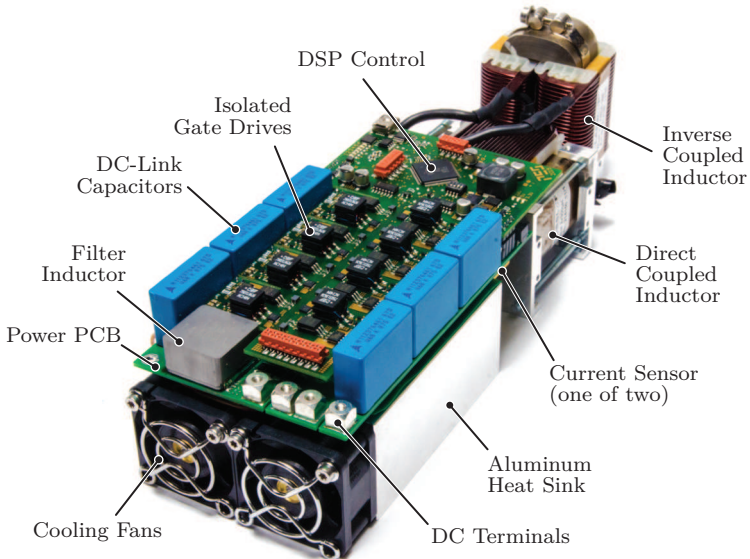


Fig. 5.22: Photograph of the final assembly of the 20 kW/50 kHz/800 V buck+boost type non-isolated DC-DC converter module with coupled magnetic components and a power density of 12.7 kW/dm^3 .

Tab. 5.2: Calculated converter losses at 20 kW power output with $U_1 = 800$ V and $U_2 = 600$ V at 50 kHz switching frequency.

Component	Power Losses
Power Semiconductors	193.7 W
Direct-Coupled Inductor	20 W
Inverse-Coupled Inductor	17.7 W
DC-Link Capacitors	0.5 W
Total Losses	231.9 W
Efficiency	98.85%

not have a DC offset and is excited by the fundamental switching frequency component of the switch node voltage and its odd harmonics. Due to the high inductance, the AC flux excitation and the AC losses are higher when compared to those of the DCI. Therefore, the device needs to be designed with a magnetic material with lower AC losses, such as a nano-crystalline material.

The necessary core size, the turns numbers, and the converter switching frequency are determined from the area products as described above and then iteratively improved based on FEM-calculated core and winding loss data. The power losses of the hard-switched power semiconductors in the converter bridges are calculated from the measured switching loss data of the used devices⁵ given in [149]. For the final design, the inductance values $L_{DCI} = 300$ μ H and $L_{ICI} = 1.5$ mH and the switching frequency $f_{sw} = 50$ kHz are selected. The calculated power losses of a the DC-DC converter module operating at 20 kW with $U_1 = 800$ V and $U_2 = 600$ V at 50 kHz switching frequency are summarized in **Tab. 5.2**.

The forced-air cooling system is dimensioned with the models in [124]. In the final converter arrangement, the coupled magnetic components are arranged in the air stream at the outlet of the heat sink such that they are actively cooled. A photograph of the final converter assembly including the coupled magnetic devices and the forced-air cooling system is shown in **Fig. 5.22**. For the realized DC-DC converter an efficiency close to 99% is achieved at a power density of 12.7 kW/dm³.

⁵Cree C2M0080120D, 1.2 kV/31.6 A with 80 m Ω .

5.5.2 Final Assembly of the all-SiC IPT Power Converter

For the required 50 kW output power of the IPT system, three of the presented 20 kW DC-DC converter module are parallel interleaved. This leaves sufficient margin in power capability for covering the losses of the IPT system during operation at a high coil misalignment. The final converter assembly is shown in **Fig. 5.23**. The power converters at the transmitter and at the receiver are realized with identical hardware.

The DC-DC converter modules are arranged such that the heat sinks of the modules can be combined with the heat sink of the ZVS full-bridge inverter. The forced-air cooling system is designed under consideration of the expected transmitter coil RMS current of up to 120 A that was derived for the operation at maximum coil misalignment in Section 4.2.

An individual Digital Signal Processor (DSP) of type TMS320F28069 (Piccolo) is used in each DC-DC converter module for the cascaded feedback control of the DC-DC converter output voltage and the inductor currents. Another DSP of type TMS320F28335 (Delfino) in combination with an FPGA of type LFXP2-5E is used as the main controller that manages the interaction of the three DC-DC modules and the generation of the gate signals for the ZVS full-bridge. In addition, the main controller is responsible for the generation of the gate signals for the ZVS full-bridge inverter at the transmitter side or for the synchronous rectification at the receiver side, as well as for the ADC sampling and monitoring of the coil currents for protection.

For the communication between the DSPs of the DC-DC converter modules and the main controller, a Controller Area Network (CAN) interface is used. For the communication between the power converter used at the transmitter side and the converter at the receiver side of the IPT system, a wireless communication module is integrated⁶ on the main control board. Furthermore, the main control board also provides a user interface that can be accessed from a Personal Computer (PC) via isolated fiber optic connections.

Owing to the parallel interleaving of multiple DC-DC converter modules, the high switching frequency that can be reached with the employed SiC MOSFET devices, and the use of coupled magnetics in the DC-DC converter stage, a volumetric power density of 9.5 kW/dm³

⁶Roving Networks RN-171 wireless LAN module (WLAN standard 802.11 b/g).

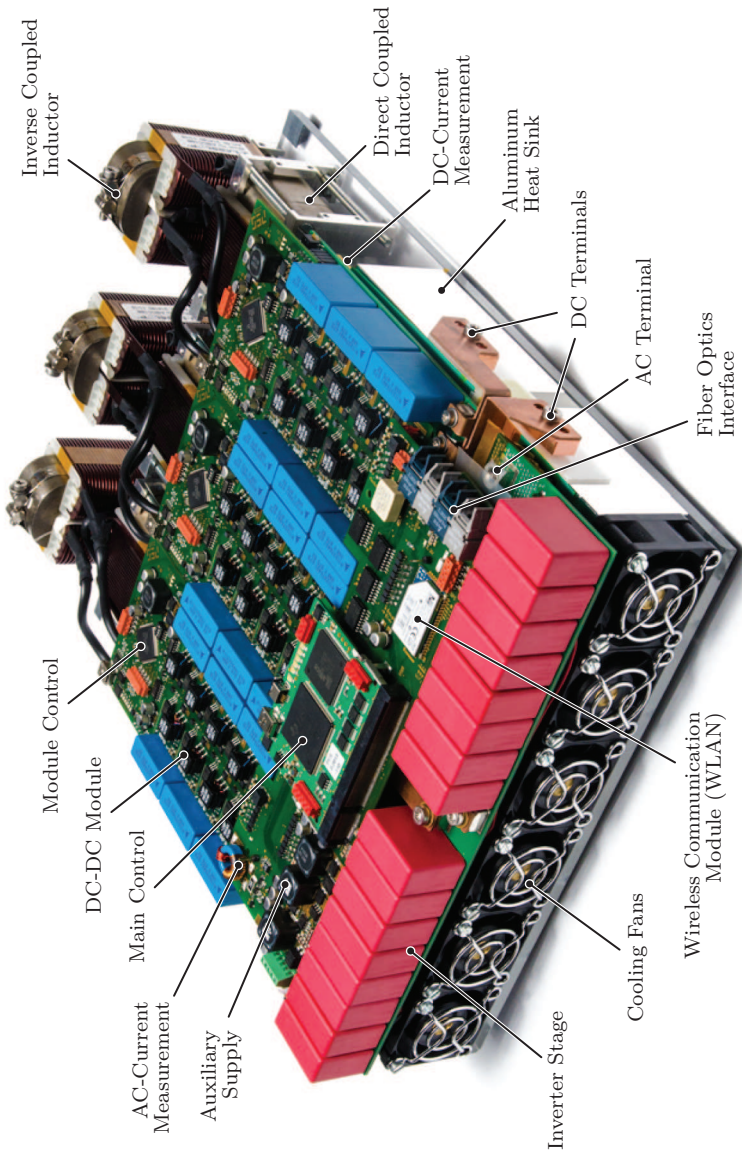


Fig. 5.23: Photograph of the fully assembled all-SiC IPT power electronic converter with 98.62% efficiency and a power density $9.5\text{ kW}/\text{dm}^3$.

and a gravimetric power density of 6.8 kW/kg are achieved for the final converter assembly with a rated power of 60 kW, outer dimensions of 240 x 330 x 80 mm, and a mass of 8.9 kg. The calculated DC-to-AC efficiency for the whole converter operated at 50 kW output power with 600 V input voltage and 800 V in the DC-link is 98.62%, if ZVS losses of the inverter- and rectifier-stage SiC MOSFETs are neglected. This highlights the advantages of the selected design approach.

5.6 Summary of the Chapter

In this chapter, the design of an all-SiC high-efficiency, high-power density power electronic converter for the presented IPT system with 50 kW output power was presented. The ZVS full-bridge inverter- and rectifier-stage is realized with paralleled discrete SiC MOSFET devices. Optimization aspects for symmetrical current sharing among the devices and the design of a single gate driver for all paralleled devices were presented. For the non-isolated DC-DC conversion stage, three parallel interleaved modules with a buck+boost-type converter topology and coupled magnetic components are used. The converter operation with coupled inductors was analyzed in detail and it was shown that the coupling of the parallel interleaved magnetic components is an effective measure to minimize the total magnetics volume. In addition, a novel concept was proposed for the feedback control in the DC-DC converter with coupled inductors and the control of the power flow in the IPT system was discussed. Finally, the realized hardware prototypes of the DC-DC converter module and of the complete IPT power converter were presented.

The key results for the optimized IPT power electronic converter are summarized as follows:

- ▶ As a result of using discrete components for the realization of the full-bridge inverter, the footprint for the power semiconductors and their gate drivers was reduced by approximately 40% compared to today's commercially available SiC MOSFET half-bridge modules. Therefore, a power density of 48 kW/dm³ was achieved for the final assembly of the inverter-stage.
- ▶ Detailed analysis of the buck+boost-type DC-DC converter with coupled inductors showed that the total magnetics area product is 40% smaller than for interleaved converter stages with uncoupled

inductors. For the total magnetics volume, a reduction of 20% is estimated.

- ▶ For the realized hardware prototype of the DC-DC converter module with 50 kHz switching frequency, a power density 12.7 kW/dm^3 was achieved at a calculated efficiency of 98.85%.
- ▶ As a result of the high compactness of each converter component, the power density of the final assembly of the all-SiC IPT power electronics is 9.5 kW/dm^3 and an efficiency of 98.64% is calculated.

With the hardware prototype of the power electronic converter presented in this chapter, the design and realization of the 50 kW IPT system is completed. In the next chapter, an experimental verification of the converter operation and detailed measurement results for the IPT system as a whole are presented.

6

Experimental Verification

THE COMPREHENSIVE experimental evaluation of the IPT system performance is summarized in this chapter. First, an experimental investigation of the power electronic converter is presented in Section 6.1. The switching behavior of the ZVS full-bridge inverter-stage is investigated based on device level voltage and current measurements. The current sharing between the paralleled SiC MOSFETs is analyzed during transients and continuous conduction. Voltage and current waveforms measured at the coupled inductors of the buck+boost-type DC-DC converter are used to validate the design equations. The efficiency of the DC-DC conversion stage is measured in a back-to-back setup of two identical converter modules. After the analysis of the power electronic converter, experiments are conducted for verifying the performance of the IPT system. The used measurement setup comprises an energy feedback from the receiver to the transmitter-side DC-link for circulating the transferred power. This arrangement enables highly accurate direct measurements of the total power losses. The experimental results presented in Section 6.2 include the DC-to-DC conversion efficiency of the IPT system at an ideal coil positioning and with misaligned transmission coils. Measurements of the steady-state device temperatures and the magnetic stray field at different locations conclude the experimental investigation. All measurement results are compared to the calculations of the previous chapters and the employed models are successfully verified.

6.1 Experimental Analysis of the Power Electronic Converter

Before the experimental investigation of the IPT system as a whole, the functionality of each system part is verified individually. Therefore, in this section, the experimental analysis of the power electronic converter is presented. In the first part, the ZVS full-bridge inverter is tested without the DC-DC conversion stage connected. The current sharing between the parallel connected SiC MOSFETs is analyzed based on device-level current and voltage measurements. Later on, two of the realized DC-DC converter modules are connected in a back-to-back arrangement for a measurement of the total power losses and a verification of the calculated efficiency.

6.1.1 Switching Performance and Current Sharing of the ZVS Full-Bridge

In a first experimental test, the switching performance of the ZVS full-bridge is tested without the DC-DC conversion stage connected. For the device level current and voltage measurements presented in the following, the naming conventions shown in **Fig. 6.1(b)** are used. A photograph of the measurement arrangement is shown in **Fig. 6.1(b)**. A low-voltage passive probe is used for the measurement of the low-side gate-to-source voltage $u_{GS,LS}$. Because the measurements are conducted at $U_{1,DC} = 800$ V DC-link voltage, a high-voltage passive probe is used for the measurement of the low-side drain-to-source voltage $u_{DS,LS}$. Both contacts of the passive probes are connected immediately at the leads of a low-side switch, such that the loop between the sensing pin and the ground connection is as small as possible. For the measurement of the individual currents in the paralleled devices, custom high-bandwidth current transformers¹ are positioned around the drain leg of the TO-247 housing of each MOSFET. For the low-side devices, the current is measured as positive if it flows from source-to-drain, while for the high-side the orientation is positive if the current flows from drain-to-source (labeled i_{SD} and i_{DS}) for an improved readability of the figures.

All measurements are preformed at the gate-to-source turn-on and turn-off voltages of +22 V and -5 V, respectively, with the gate driver presented in Section 5.2.3. The gate resistors are selected as 10 Ω for

¹Two stacked R-6 toroidal ferrite cores with 25 turns of the secondary winding.

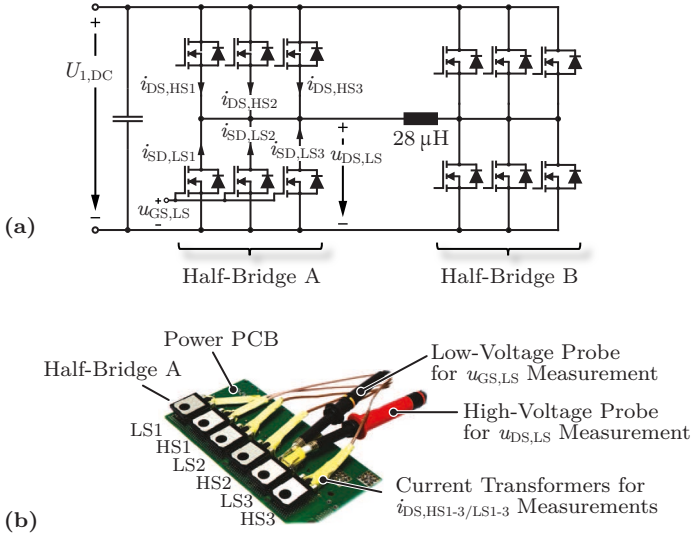


Fig. 6.1: (a) Topology of the ZVS full-bridge inverter with naming conventions. (b) Photograph of the experimental setup for the device level voltage and current measurements.

the turn-on and as $5\ \Omega$ for the turn-off transition. The presented waveforms are obtained from pulse measurements with an inductive load of $28\ \mu\text{H}$, because the employed current transformers are thermally not designed for continuous operation. The signals are sampled with two four-channel oscilloscopes with synchronized triggers. The measured trigger delay of $35\ \text{ns}$ between the two oscilloscopes is compensated in the shown waveforms. For these initial tests, the full-bridge is assembled with devices of type C2M0080120D. In the final setup, devices of type C2M0025120D are used for the lower on-state resistance of only $25\ \text{m}\Omega$ instead of $80\ \text{m}\Omega$. However, similar characteristics are expected for both devices and the conclusions obtained from the measurements performed with the $80\ \text{m}\Omega$ devices are considered equally valid for the final setup.

The measured device voltages u_{GS} and u_{DS} , as well as the individual device currents during a switching transition of inverter half-bridge A are shown in **Fig. 6.2(a)**. The measurement shows a similar behavior of all low-side currents during the transition phase. The high-side currents

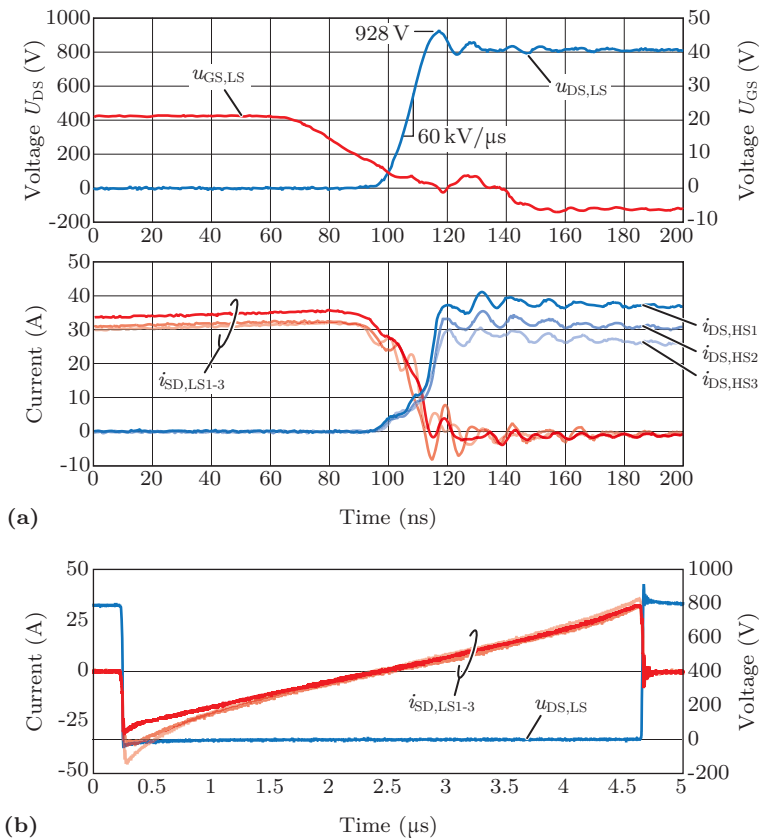


Fig. 6.2: (a) Low-side gate-to-source and drain-to-source voltages and individual currents in the paralleled SiC MOSFETs during a switching transition of half-bridge A. (b) Individual low-side device currents and drain-to-source voltage during continuous conduction with an inductive load.

show differences immediately after the transition. According to [145], this is a result of differences in inductance or on-state resistances along the current paths through the paralleled devices. However, the transient imbalance of the device currents during the switching transition do not have adverse effects on the system performance, because the full-bridge is always operated with ZVS. For hard-switched operation, the asymmetric current distribution could lead to unbalanced switching losses between the devices. For a comprehensive performance evaluation additional measurements of the current sharing during hard switching transitions would be required. The small overshoot of the drain-to-source voltage u_{DS} despite the $60\text{ kV}/\mu\text{s}$ voltage slope confirms that a good trade-off between the symmetrical arrangement of the devices and the commutation loop inductance is achieved.

The complete conduction interval of the low-side switch is shown in **Fig. 6.2(b)**. During the on-state, the current sharing between the paralleled devices is sufficiently symmetric. A similar result is also obtained during the conduction interval of the high-side switch. Therefore, a balancing of the power losses between all of the paralleled devices during continuous operation is expected.

6.1.2 Efficiency of the Buck+Boost-Type DC-DC Converter Modules

In order to confirm the theoretical analysis of the coupled magnetic components, the voltage and current waveforms measured at the coupled inductors are shown in **Fig. 6.3** for an input voltage of 600 V and a duty cycle of $D = 0.25$. The voltage across the ICI and the DCI are measured with two high-voltage differential probes. The winding current ripples are measured with two current probes set to AC-coupling. The measured winding current waveforms of **Fig. 6.3(a)** are mathematically separated into the CM and DM ripple current components shown in **Figs. 6.3(b)-(c)**. As expected, the DCI voltage u_{DCI} defines the CM ripple current Δi_{CM} and the ICI voltage u_{ICI} is responsible for the DM ripple current Δi_{DM} .

The peak-to-peak CM and DM current ripples calculated with the DCI and ICI inductance values and the equations given in Section 5.3.3 are $\Delta i_{CM,pp} = 1.25\text{ A}$ and $\Delta i_{DM,pp} = 0.5\text{ A}$. A comparison of the peak-to-peak current ripples that are extracted from the waveforms to the theoretical calculations confirms the accuracy of the presented circuit

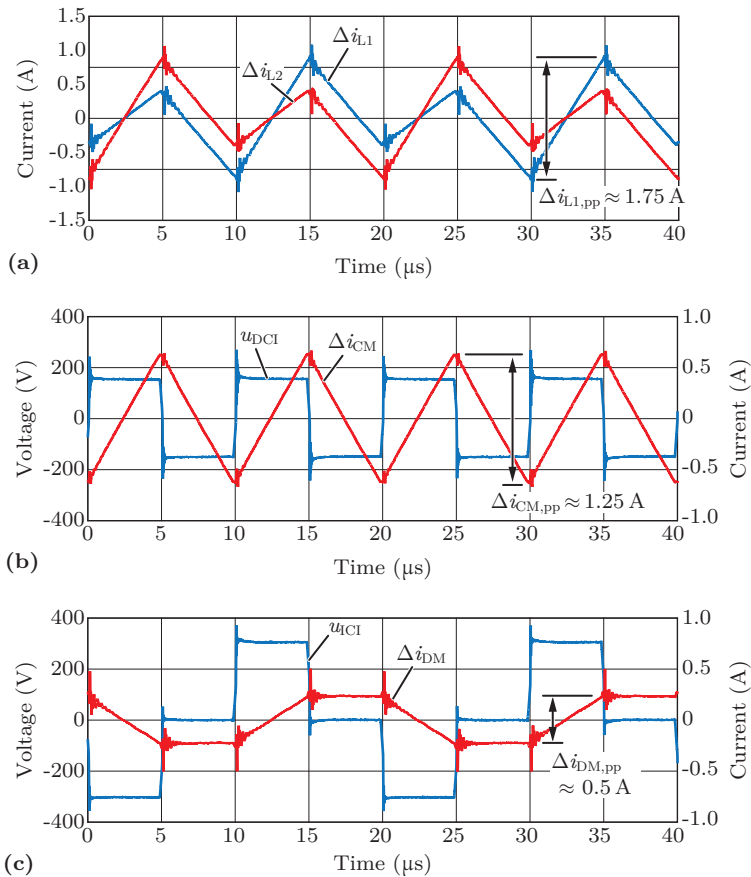


Fig. 6.3: (a) Measured winding ripple current waveforms at the coupled magnetic components of a DC-DC converter module ($U_1 = 600$ V, $D = 0.25$). (b) Mathematically extracted CM current ripple Δi_{CM} and measured DCI voltage u_{DCI} , (c) mathematically extracted DM current ripple Δi_{DM} and measured ICI voltage u_{ICI} .

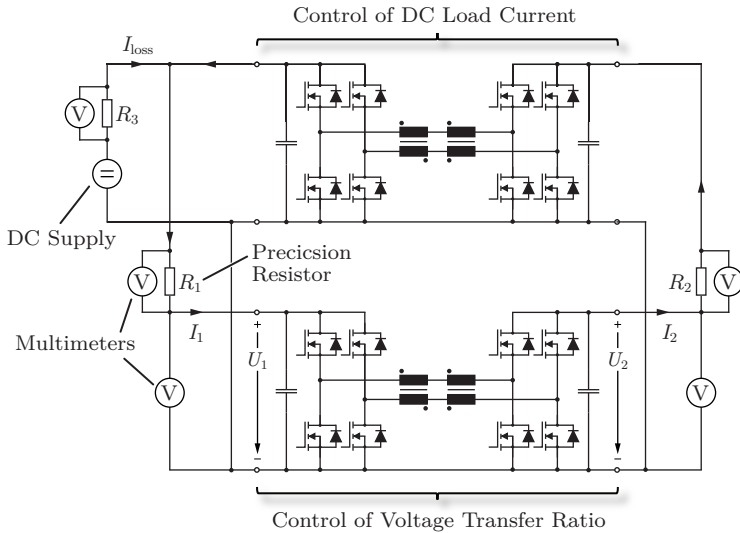


Fig. 6.4: Back-to-back setup of two identical DC-DC converter modules for direct power loss and efficiency measurements. One module operates at a fixed duty cycle, while the second module controls the circulating DC load current.

analysis and calculation models.

For the experimental performance evaluation of the buck+boost-type DC-DC converter modules, two of the realized modules are connected in the back-to-back measurement arrangement shown in **Fig. 6.4**. The input- and output-side DC-links of both converter modules are connected via the 10 m Ω precision shunt resistors R_1 and R_2 for measuring the input and output currents of the converters. For supplying the power losses to the back-to-back system, an external DC power supply is connected via another precision shunt resistor R_3 . For the measurement of the shunt voltages and of the DC-link voltages at the converter terminals, multimeters of type Agilent 34410A are used. In order to control the converter voltages, one of the DC-DC converters is operated with a fixed duty-cycle that is adjusted to obtain $U_2 = 800$ V at the output for $U_1 = 600$ V input voltage. All presented measurements are taken at these DC-link voltages. The second DC-DC converter is operated with activated current control. The reference current is manu-

ally varied to control the power flow in the back-to-back setup. During the power loss measurements, also the component temperatures at different spots of the converter are measured using thermocouples. All power loss measurements are taken only after the temperatures of all components have settled to their thermal steady-state values.

During this process, the total power losses of both converters together can be determined directly from the current I_{loss} measured at the power supply. Alternatively, an indirect loss measurement can be obtained by taking the difference of the measured input and output power of one of the converters. The results for the measured power losses of a single converter obtained from both methods are shown in **Fig. 6.5(a)** together with a second-order polynomial curve fit to the directly measured losses. As expected, the larger variance of the indirect measurements with respect to the fitted curve confirms that the direct loss measurement method is better conditioned. It is therefore the more appropriate method for measuring the losses of power electronic converters with high efficiencies.

The efficiency that results from the directly measured power losses for a single DC-DC converter module is shown in **Fig. 6.5(b)** as a function of the output power. The curve fit, which is also shown in the figure, is derived from the second order polynomial fitted to the directly measured power losses. This curve fit is used below to capture the efficiency of the DC-DC stage when assessing the accuracy of the calculation models for the IPT system. The peak efficiency of $\eta_{\text{max}} = 99.17\%$ is reached at 8.6 kW output power. The efficiency at the nominal power output of 20 kW is 98.80% (calculated are 98.85%, cf. Chapter 5).

The temperature measurement results are shown in **Fig. 6.6** as temperature differences $\Delta T = T - T_{\text{amb}}$ with respect to the measured ambient temperature $T_{\text{amb}} \approx 25^\circ\text{C}$ (approx. constant during the measurements, not shown in the figure). The most critical part is the power PCB, because it is only cooled by natural convection and experiences current densities of up to 15 A/mm^2 in the $100\text{ }\mu\text{m}$ thick copper traces. The magnetic core of the ICI exhibits a higher temperature rise than the DCI, because its positioning in the converter arrangement limits the air flow from the cooling system. Nevertheless, the highest operating temperature is only 32.7°C above ambient, which indicates that the power density of the magnetic components could be increased even further in a future design step.

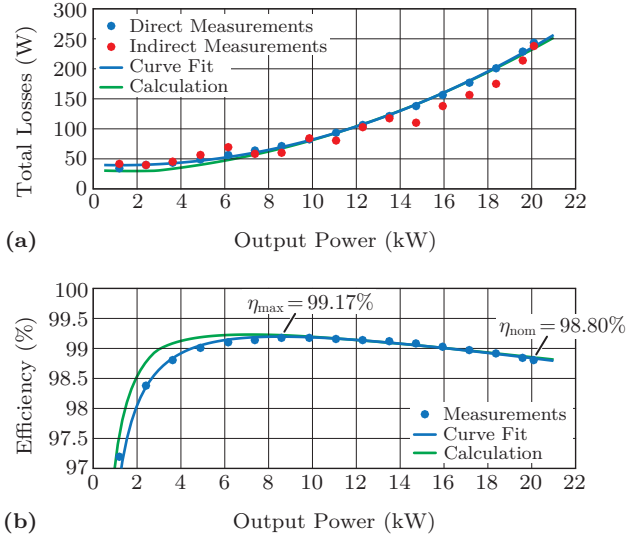


Fig. 6.5: (a) Direct and indirect measurements of the total losses of a single DC-DC converter module, curve fit for the directly measured power losses, and calculated total losses. (b) Measured and calculated efficiency of the DC-DC converter module.

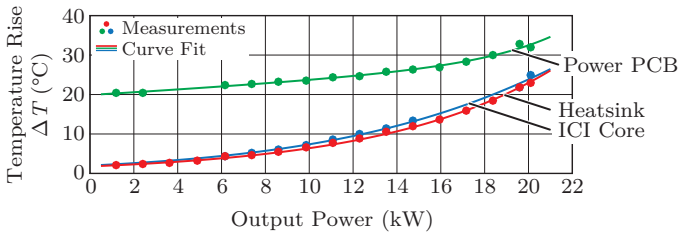


Fig. 6.6: Component temperature rise ΔT with reference to ambient temperature ($T_{\text{amb}} \approx 25^\circ\text{C}$) measured on the power PCB (current density up to 15 A/mm^2 in $100\ \mu\text{m}$ thick copper traces), the magnetic core of the ICI, and the aluminum heat sink of the forced-air cooling system.

From the measured heat sink temperature, the junction temperature of the MOSFETs can be estimated with a thermal model consisting of the thermal resistance from the junction to the case of the device, the thermal resistance of the electrical isolation between its housing and the heat sink, and the calculated power losses. For the worst case operating conditions², the calculated junction temperature is 110.8 °C at the ambient temperature of 25 °C, which was observed during the efficiency measurements. This estimation together with the discussed temperature measurement results indicates that the presented DC-DC converter is capable of operation at an ambient temperatures of 45 °C specified during the design process.

6.2 Experimental Verification of the IPT System Performance

In this section, comprehensive experimental results for the fully assembled IPT system are presented. In the first part, the used measurement setup with energy feedback for circulating the transferred power is described. Then, direct power loss measurements are performed and the DC-to-DC conversion efficiency of the IPT system is extracted. To conclude the experimental investigation, the magnetic stray field is measured with the magnetic field probe designed in Section 3.4.

6.2.1 IPT Test Setup with Energy Feedback

After the experimental validation of the power electronics design, a measurement setup for the 50 kW IPT system is constructed. Due to the high power level, again an arrangement with circulating power is preferred. Hence, two identical power converters are assembled according to the design presented in Section 5.5.2. Thereof, one converter is connected to the transmitter coil and used as the transmitter-side power converter. The second converter is used as the receiver-side power electronics and is connected to the receiver coil. In the second converter, the inverter-stage is used for synchronous rectification.

²Output voltage reduced to 590 V to compensate for maximum specified coil misalignment of ± 100 mm and transmission of the full output power of 20 kW per DC-DC converter module.

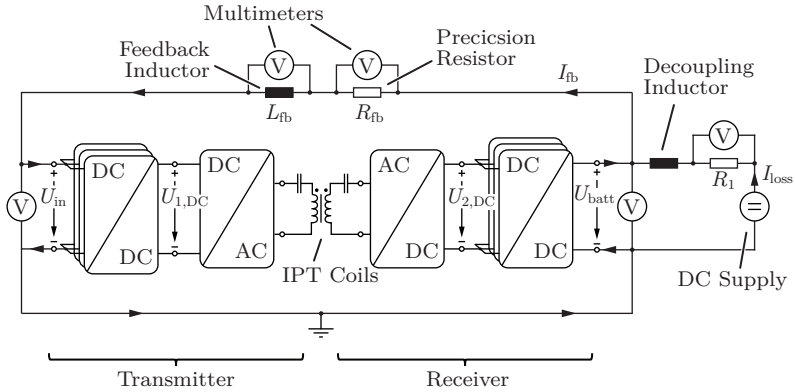


Fig. 6.7: Symmetrical IPT test setup with energy feedback for direct power loss and efficiency measurements with up to 50 kW circulating power.

The two power converters are arranged as shown in **Fig. 6.7**. The DC-links of the two identical converters are connected via the inductor $L_{fb} = 3.4 \text{ mH}$ for the energy feedback in the positive rail. The feedback inductor is realized as an air coil in order to avoid frequency-dependent hysteresis losses in a magnetic core. A multimeter is used to measure the voltage drop across the feedback inductor for subtracting its DC losses from the power loss measurements presented below. For measuring the feedback current I_{fb} , a $1 \text{ m}\Omega$ precision shunt resistor R_{fb} is connected in series to the feedback inductor. At the output of the receiver-side power electronics, a power supply that represents the EV battery is connected. The battery voltage is $U_{batt} = 600 \text{ V}$ for all of the shown measurements. The supply current I_{loss} is measured via the voltage drop across the $10 \text{ m}\Omega$ precision shunt resistor R_1 . An additional inductor is used for decoupling the power supply from the rest of the circuit. The multimeters that are used for measuring the shunt voltages, the voltage drop on the feedback inductor, and the DC-link voltages are Agilent 34410A devices.

In the laboratory, the IPT test equipment is installed in a Faraday cage for safety reasons. The measurement setup is shown in **Fig. 6.8**. Clearly, the grounded fence of the Faraday cage affects the field distribution inside the test chamber. Efforts are made to maximize the distance between the IPT coils and the fence. A wooden table is used in order to minimize eddy currents in metal parts as much as possible.

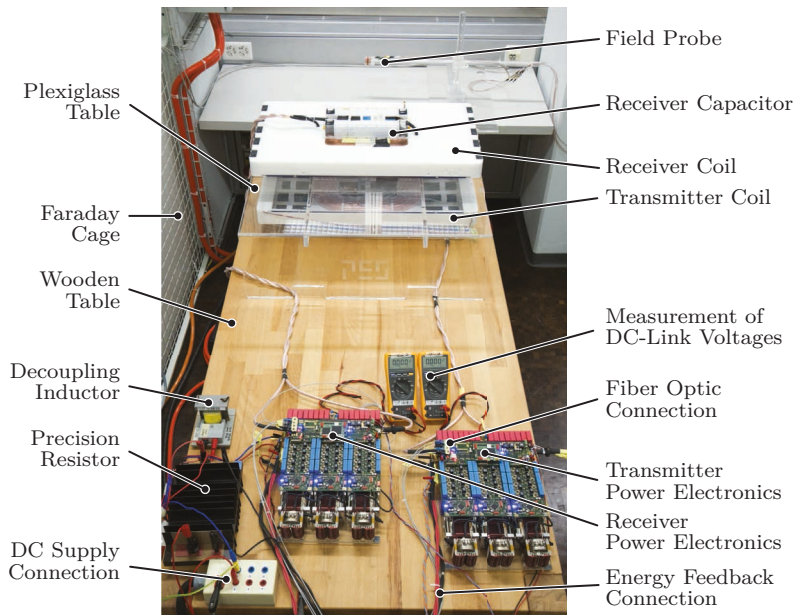


Fig. 6.8: Photograph of the IPT test setup installed on a wooden table inside a Faraday cage. The distances between the IPT coils, the grounded fence of the Faraday cage, and the power electronics are maximized to avoid interference with the electromagnetic fields (the distance from the power converters to the coils is approximately 750 mm).

On the table, the IPT coils, the power electronic converters, and the measurement equipment are separated as far apart as possible in order to avoid interference of the stray fields with the sensitive sensor and control electronics. A plexiglass table is used to support the receiver coil at a distance of 160 mm from the transmitter coil. Communication between the converters and a PC is possible via a fiber optic connection. The measurement equipment, the energy feedback inductor, and the DC power supply described above are placed next to the wooden table, at the lower end of the photograph (not shown).

To control the power flow across the air gap of the IPT system, the DC-DC converters are used to regulate the variable DC-link voltages $U_{1,DC}$ and $U_{2,DC}$ of the transmitter and receiver-side power converters. One of the three DC-DC converter modules acts as the master module

and is operated with a constant duty cycle to set the transmitter-side and receiver-side DC-link voltages $U_{1,DC}$ and $U_{2,DC}$. The duty cycles are manually adjusted from a user interface on a PC and sent to the power converters via the fiber optics interface. For simplicity of operation, the duty cycles are always set to the same value for the transmitter and the receiver-side power converter. Then, the power transfer is impressed by the IPT system and follows (2.34). The remaining two DC-DC converter modules in each power converter are operated as slaves in current control mode. The slave modules obtain current reference values from the master module. The master module calculates the average of the inductor currents of all active DC-DC converter modules (master and slaves) of the transmitter-side or receiver-side power converter. This value is continuously updated and sent to the slave modules as current reference. In steady-state, this process leads to a balanced sharing of the load current among all three modules. In the master modules, the CM current component is not actively controlled, in order to avoid instability at rapid load steps. However, the DM current control is used also for the master modules in order to avoid transient DM currents that could lead to saturation of the ICI and large currents in the semiconductor devices of the master module.

The waveforms of the currents and voltages at the terminals of the IPT resonant circuit are shown in **Fig. 6.9** during the transmission of 50 kW output power. The measured IPT coil currents have amplitudes of 121 A and 110 A for the transmitter and the receiver coil current, respectively. The small phase shift between the current i_1 in the transmitter coil and the inverter output voltage u_1 is necessary to ensure ZVS of the MOSFETs in the transmitter-side full-bridge.

6.2.2 Synchronous Rectification at the Receiver

To ensure minimum on-state conduction losses of the receiver-side rectifier, the operation of the synchronous rectification described in Section 5.4 is verified in the final IPT test setup. **Fig. 6.10** shows the measured receiver coil current i_2 and the rectifier output voltage u_2 during switching transitions of the rectifier. The smooth slopes of the voltage waveforms and the fact that the current crosses zero before the voltage transition confirms ZVS of the rectifier stage.

For this measurement, the receiver-side DC-link voltage $U_{2,DC}$ is adjusted to 250 V in order to capture the effect of the synchronous rectifi-

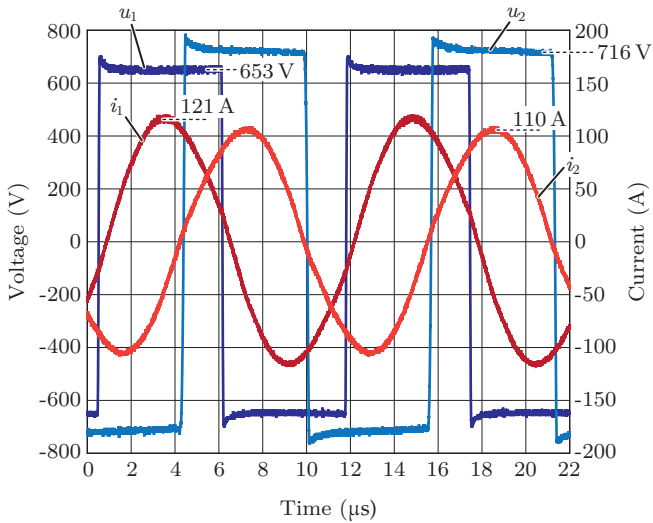


Fig. 6.9: Waveforms of the inverter output voltage u_1 , the transmitter coil current i_1 , the receiver coil current i_2 and the diode rectifier output voltage u_2 , measured at a power transmission of 50 kW.

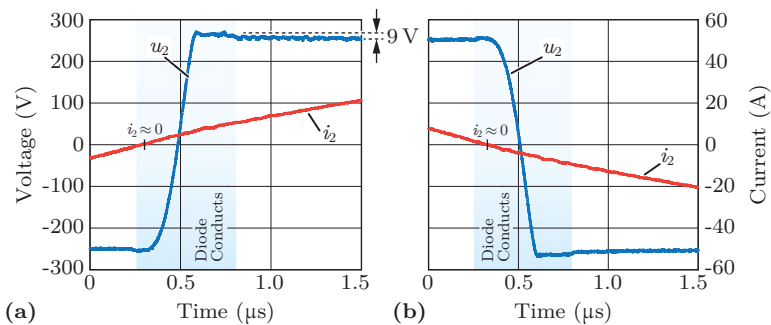


Fig. 6.10: (a) Positive and (b) negative transition of the switch node voltage at the input of the synchronous rectifier of the receiver-side converter. The forward voltage drop of $2 \cdot 4.5 \text{ V} = 9 \text{ V}$ of the two conducting bipolar SiC body diodes is clearly visible.

cation. This modification is necessary because of the limited resolution of the oscilloscope. With this setting, the two forward voltage drops of approximately 4.5 V (=9 V total) of the bipolar SiC body diodes are visible shortly before and after the voltage transition. The observed forward voltage drop is in good agreement with the data sheet value. The significant reduction of the forward voltage drop confirms that the synchronous turn-on of the MOSFET leads to a large efficiency improvement.

6.2.3 DC-to-DC Efficiency Measurement

For the efficiency measurements, the transmitted power is adjusted via the duty cycles of the voltage-controlling DC-DC converter modules in the transmitter- and the receiver-side power converters. At each operating point, the voltage at the DC links and at the shunt resistors are measured using an averaging over 0.5 s for noise filtering. Because the power is circulated and only the losses are supplied by the external DC supply, the input current I_{loss} can be used for a highly accurate direct measurement of the power losses. During the measurement process, the active-cooling systems of the converter and of the IPT transmission coils are constantly running. Thermal steady-state is always ensured for all components, before the samples are taken.

The measurement results for the total power losses from DC input U_{in} to the battery voltage U_{batt} (cf. **Fig. 6.7**) are shown in **Fig. 6.11(a)** together with a curve fit and the calculated power losses. The measurements include the complete power conversion chain, i. e., the DC-DC conversion stage and the ZVS full-bridge inverter stage of the transmitter-side power converter as well as the synchronous rectifier stage and the DC-DC conversion stage of the receiver-side power converter, the resonant capacitors, and the IPT coils. The measured DC-to-DC efficiency is shown in **Fig. 6.11(b)** with a curve fit and a comparison to the calculated efficiency. The measurements are taken with ideally aligned IPT coils and at an air gap of 160 mm. For the calculation of the exact current amplitudes and for calculating the losses in the power semiconductors of the transmitter- and receiver-side power electronics, the detailed models presented in [68] are employed. Measurements of the heat sink temperature are used to estimate the semiconductor junction temperature and the temperature-dependent semiconductor losses. For the calculation of the power losses in the IPT

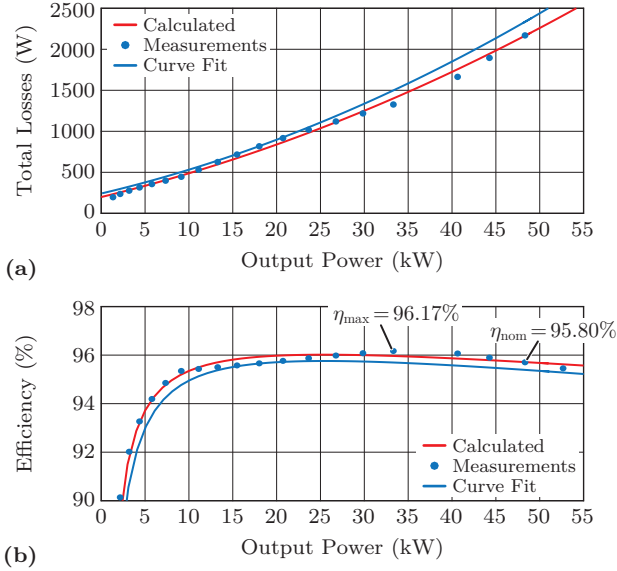


Fig. 6.11: (a) Measured total DC-to-DC conversion power losses including the DC-DC conversion as well as the ZVS full-bridge of the transmitter- and receiver-side power electronics, the resonant capacitors, and the IPT transmission coils. (b) Corresponding DC-to-DC conversion efficiency including all components of the power conversion chain for an air gap of 160 mm and ideal coil positioning.

transmission coils, the models presented in Section 4.2.1 are used. For the DC-DC conversion stage, the fitted curve obtained from the directly measured power losses discussed above is used instead of the calculation with the goal of documenting the accuracy of the calculation models for the IPT coils as good as possible.

The comparison of the measured power losses and efficiency of **Fig. 6.11** to the calculated curves demonstrates the accuracy of the proposed calculation models. Overall, the calculation results are equally accurate as for the previously presented scaled 5 kW prototype system (cf. Chapter 3). This particularly proves the validity of the simplifications that were made for the calculation of the IPT coil AC resistance and for the 3D FEM-based power loss estimation in the eddy current shielding and the ferrite cores.

Due to the high frequency of the power transmission and the high voltage and current amplitudes, a more direct measurement of the power losses of the components in the resonant circuit is not possible with acceptable accuracy with a typical power analyzer [150]. Even small measurement errors for the current and voltage phase shifts would lead to false results due to the high efficiency. In addition, a direct measurement of the AC resistance of the transmission coil is challenging. Based on the calculated AC resistance, a phase angle of 89.96° is expected for the coil impedance at 85 kHz. Thus, the angular difference of 0.04° to a phase angle of 90° needs to be resolved with an accuracy of 0.004° for a measurement of the AC resistance with 10% measurement error. This is beyond the capabilities of a typical impedance analyzer [151, 152]. In addition, given the low value of the AC resistance to be measured, the impedance of the physically large probe fixture or even contact resistances could adversely affect the accuracy of an impedance measurement. Therefore, the presented measurement of the total DC-to-DC conversion efficiency based on a direct power loss measurement in the setup with circulating power is considered the best option for the model verification.

The peak efficiency of 96.16% is measured at 33.2 kW and at 50 kW power transmission, an efficiency of 95.8% is reached for a 160 mm air gap and ideal alignment of the IPT coils. These numbers clearly demonstrate the capability of the IPT technology to reach similar efficiency levels than conventional conductive chargers.

6.2.4 DC-to-DC Efficiency Measurement with Coil Misalignment

After the experiments with ideally positioned IPT coils, measurements with horizontally misaligned coils are taken. The measurement results for the total power losses are shown in **Fig. 6.12(a)** together with the calculated values. The measured DC-to-DC conversion efficiency is shown in **Fig. 6.12(b)**. The efficiency is decreased by approximately 0.7%-points for a lateral or longitudinal coil misalignment of 100 mm. A coil misalignment of 150 mm in the lateral direction leads to an efficiency reduction of close to 2%-points. An efficiency reduction of 3.8%-points to approximately 92% is observed at a longitudinal coil misalignment of 150 mm.

As expected, the presented measurements confirm that the misalign-

ment tolerance of the IPT demonstrator is higher in the lateral direction than in the longitudinal direction. As outlined in Section 4.2.6, the desired orientation of the transmission coil with respect to the EV is such that the longitudinal direction is the direction of motion of the EV. In the direction of motion of the vehicle, guiding the driver to an accurate parking position is straightforward, e. g., with small bumpers installed on the road surface. In the lateral direction of the vehicle, corrections of the parking position are more difficult and a higher tolerance with respect to the coil positioning is therefore needed.

6.2.5 Component Temperatures During Continuous Operation

In order to validate the forced-air cooling system of the IPT transmission coil, thermal measurements are conducted while the IPT system is continuously operating with 50 kW power transmission and ideally positioned IPT coils. The core and winding temperatures are measured with thermocouples that are glued to the litz wire winding and to the core. In addition, the air temperatures are measured with two additional thermocouples at the inlet and at the outlet of the cooling system. The sensor positions are indicated in **Fig. 6.13(a)**. The air temperature at the inlet, approximately 24 °C during the measurement, is used as reference temperature for the calculation of the temperature rise $\Delta T = T - T_{\text{inlet}}$.

The measured component temperatures are shown in **Fig. 6.13(b)**. The measurements are in good agreement with the thermal simulations presented in Section 4.3.2. The temperatures of the litz wire and the cores stay well below the maximum ratings of the materials, which validates the thermal management of the transmission coil.

6.2.6 Measurement of the Magnetic Stray Field

For the verification of the magnetic stray field, the magnetic field probe designed in Section 3.4 is used. The field probe is consecutively positioned at three different observation points on a horizontal axis in the lateral direction, starting in the center of the air gap as shown in **Fig. 6.14**. Then, the power transfer of the IPT system is increased stepwise. The signals obtained from all three sense windings of the probe are recorded and the amplitude of the induced voltage is extracted by

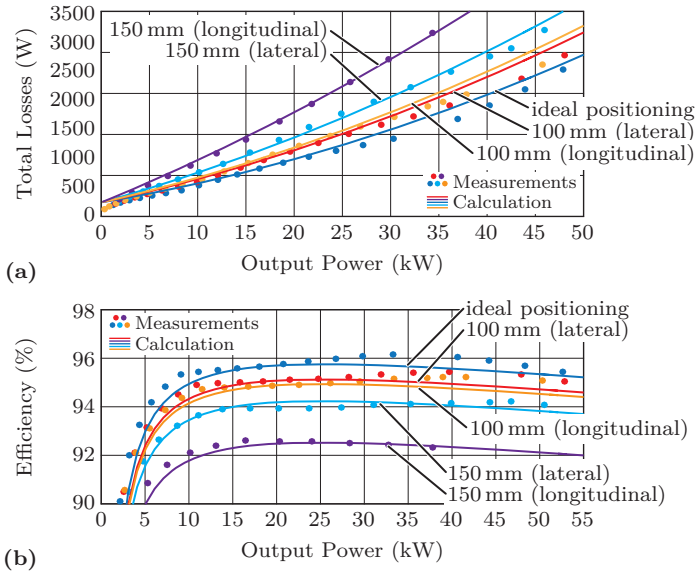


Fig. 6.12: (a) Measured total DC-to-DC power losses and (b) corresponding DC-to-DC conversion efficiency for an air gap of 160 mm and a variable lateral and longitudinal coil misalignment.

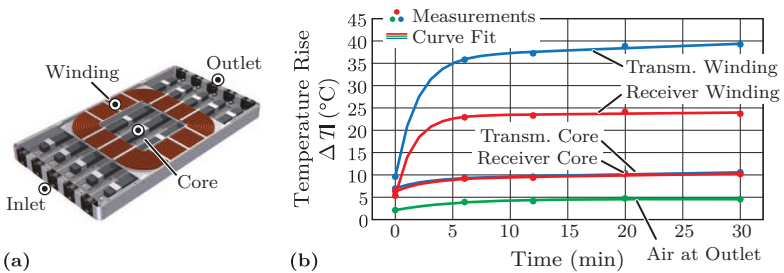


Fig. 6.13: (a) Positions of the thermocouples for the measurement of the component temperatures. (b) Measured transmitter and receiver winding and core temperatures and air temperature at the outlet of the cooling system during continuous operation with 50 kW power transmission.

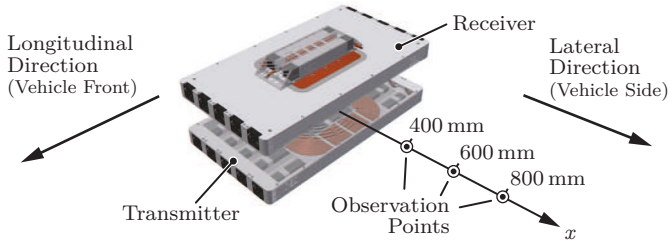


Fig. 6.14: Measurement setup for the evaluation of the magnetic stray field.

performing a FFT on the measured waveforms. With the measured induced voltages and the probe dimensions, the RMS magnetic flux density is calculated as described in Section 3.4.

In **Figs. 6.15(a)-(b)**, the obtained measurement results are compared to the FEM calculations for the selected observation points. The calculated magnetic stray fields exhibit a calculation error of around 15% with respect to the measured values, which is a satisfactory result. However, the error is larger than for the measurements presented in Section 3.4.3. Several aspects could explain the deviation. Firstly, the measurements for the 50 kW system are conducted in a Faraday cage for safety reasons (cf. **Fig. 6.8**), while the measurements with the scaled 5 kW prototype were conducted in open space. This means that the experimental setup is arranged in a relatively narrow area surrounded by a grounded metal fence at a distance of approximately 500 mm. Additional metals are present in the power supply, the cabling, and the measurement equipment. Eddy currents are induced in all of these metal parts, which distort the magnetic field distribution. These effects are not modeled in the FEM simulation. Secondly, the FEM model contains a number of simplifications, which could adversely affect the calculation accuracy. For instance, the resonant capacitor module mounted to the backside of the IPT coil is not modeled to accelerate the convergence of the FEM calculation. Lastly, in the physically larger measurement setup for the 50 kW system, the positioning of the field probe is not as accurately possible as for the smaller setup of the 5 kW system.

The presented measurements show that the designed IPT transmission coils fulfill the ICNIRP 2010 guidelines [39] for the magnetic field exposure of the general public at a lateral distance of 800 mm from the coil center. In addition, the measurements of **Fig. 6.15(b)** show

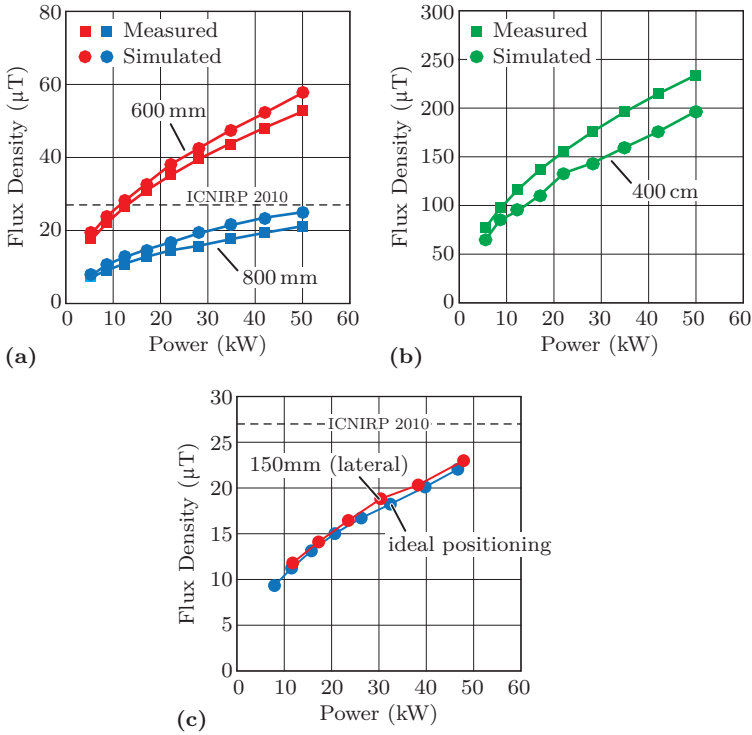


Fig. 6.15: (a) Measured and FEM-calculated RMS magnetic flux density at 800, 600, and (b) 400 mm lateral distance from the air gap center point. (c) RMS magnetic flux density at 800 mm for ideally positioned IPT coils and with 150 mm lateral misalignment in negative x -direction.

that the magnetic stray field at the considered observation point is relatively independent of the lateral coil misalignment. This demonstrates the prototype system presented in this thesis is suitable for a practical application where compliance with the upcoming standard SAE J2954 [41] is required.

6.3 Summary of the Chapter

In this chapter, a comprehensive experimental analysis of the 50 kW IPT system was presented. In the first part, detailed measurements

that document the current sharing between the parallel connected SiC MOSFET devices in the ZVS full-bridge of the power electronic converter were conducted. Thereafter, the DC-DC conversion stage was experimentally tested and the efficiency was assessed with a direct power loss measurement obtained from a back-to-back test configuration of two identical converter modules. Then, an measurement setup with energy feedback was built for conducting experiments with the complete IPT system. The energy feedback allowed circulating the transmitted power in the system, and enabled direct power loss and efficiency measurements with high accuracy. Finally, the magnetic stray field of the prototype was measured to validate the compliance of the presented demonstrator system with the ICNIRP 2010 guidelines [39]. All of the presented measurement results were compared to the values estimated during the design phase in the previous chapters and the employed calculation models were successfully validated.

The main results obtained from the experimental investigation of the IPT demonstrator system are summarized as follows:

- ▶ The current sharing between the parallel connected SiC MOSFETs of the full-bridge inverter is balanced during continuous conduction. The asymmetries observed during switching transients do not have an impact on the system performance as long as ZVS of the full-bridge is maintained.
- ▶ The peak efficiency of the designed DC-DC converter modules is measured as 99.17% at 8.6 kW. At the rated power of 20 kW, an efficiency of 98.80% is reached.
- ▶ For the complete IPT system, a maximum efficiency of 96.16% is measured at 33.2 kW and the efficiency at the rated power of 50 kW is 95.8% at an air gap of 160 mm, including the power losses of the power electronic converters at the transmitter and the receiver side, the resonant capacitors, and the IPT transmission coils.
- ▶ The designed 50 kW IPT system fulfills the ICNIRP 2010 [39] guidelines for the magnetic field exposure of the general public at a lateral distance of 800 mm from the coil center with up to 150 mm lateral coil misalignment. In addition, it is designed for operation at a transmission frequency of 85 kHz. This makes the

demonstrator suitable for applications where compliance with the upcoming standard SAE J2954 [41] is required.

- ▶ The presented measurements for the efficiency, the total power losses, and for the magnetic stray field are in good agreement with the predicted values. This verifies the proposed calculation models for the IPT coils and the power converter. In addition, the measured results and the achieved overall performance highlight the validity of the proposed optimization approach.

The presented experimental verification completes the design of the 50 kW IPT demonstrator system. Final conclusions regarding IPT system design and the application of IPT technology for EV battery charging are given in the next chapter.

7

Conclusion & Outlook

CONTACTLESS battery charging systems for automotive applications must satisfy multiple performance requirements simultaneously. The main performance indicators are the charging efficiency and the power density of the converter system. Other factors include the tolerance to coil misalignment and low electromagnetic emissions. The presented study seeks to provide a fundamental understanding of the interdependencies among the different performance aspects with the aim of providing a framework for a multi-objective optimization of IPT systems. A summary of the individual findings is given at the end of each chapter. Therefore, only the main conclusions are presented in the following. Suggestions for future research topics are given at the end of the chapter.

7.1 Results & Conclusions

In this thesis, the fundamental working principles of IPT systems are introduced in analogy to a conventional conductive EV charger. The key design challenges are outlined and the encountered trade-offs between different performance factors such as the charging efficiency, the component size, and the stray fields are discussed in detail. A multi-objective IPT optimization process is proposed that allows taking into account the interdependencies between the different performance factors during the design phase. The experimental investigation of hardware prototypes designed for 5 kW and for 50 kW charging power demonstrate the accuracy of the employed models and the proposed optimization approach. The presented demonstrator systems are designed with the goal

of driving the performance to the physical boundaries. They provide a benchmark for what performance is achievable for an IPT battery charger if every component is optimized to its limits, using the best available materials and device technologies.

The obtained results highlight that for a contactless EV battery charging system based on IPT, similar efficiencies¹ as for conventional conductive chargers can be achieved, if all sub-systems are appropriately designed. Therefore, IPT is a viable candidate charging technology not only for private vehicles, but also for public transportation. There, the lower and less volatile energy costs of EV in comparison to fossil fueled vehicles are fully recognized as a technological advantage. The unique advantages that result from the contactless power transmission additionally enable the design of *opportunity charging* installations without moving mechanical parts. The seamless integration of the charging process into the regular operation of the vehicles reduces dwell time for recharging at the depot and thereby allows lowering the number of fleet vehicles. In addition, the more frequent charging reduces the depth of discharge of the battery. This allows optimizing the volume, weight, and lifetime cost of the on-board energy storage.

Because EV charging stations are fully exposed to the environment, conventional systems, which are able to automatically establish a galvanic connection with moving mechanical parts, suffer from corrosion of open electrical contacts in addition to the wear and fatigue that results from the mechanical motion. For an IPT system all components can be fully enclosed, because no exposed electrical contacts are needed. Moreover, no mechanical contacting system is required as a result of the power transmission via the magnetic field. Therefore, IPT systems require reduced maintenance compared to conventional conductive charging systems. These aspects make further operating cost reductions possible.

However, these advantages are tied to a trade-off as shown schematically in **Fig. 7.1**. The presented analysis has shown that a compact design of a contactless charger is a major design challenge. As a result of the large air gap over which the power must be transmitted in EV applications, large transmission coils are invariably required to achieve a high efficiency. Therefore, the required component volume, weight, and also the material cost are significantly higher than for a conventional solution. In fact, the volumetric and gravimetric power density of

¹Measured DC-to-DC efficiency: 95.8% for 50 kW at 160 mm air gap.

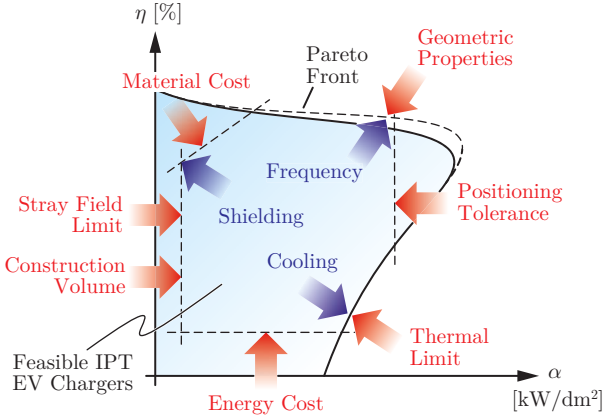


Fig. 7.1: Schematic representation of the feasible performance space of contactless EV chargers based on IPT including the effects of the technological constraints and potential ways for future improvement.

the designed IPT transmission coil is already approximately 50% lower than that of a state-of-the-art conductive EV charger², where the complete power conversion chain from the mains to the battery is already included. On one hand, a drastic drop in efficiency, the challenging thermal management of the IPT coils, and an inferior coil positioning tolerance restrict an increase of the power density. On the other hand, small coils are required to limit the necessary construction volume and material cost of the vehicle-side components, as well as for minimizing the magnetic stray fields of IPT systems that is measured at a defined distance measured from the coil center.

The design parameter with the highest potential for breaking the technical barriers is the transmission frequency. The presented analysis suggests that an increase in power density and a reduction of the magnetic stray field can be achieved by increasing the frequency of operation of the contactless power transmission. However, the design of the power electronics becomes more and more challenging at higher switching frequencies due to the increasing impact of component parasitics. Eventually, the approach is also limited by losses in the power semiconductors, the magnetic cores, and the resonant capacitors. In addition,

²2.7 kW/dm³ and 2 kW/kg for the presented prototype in comparison to 5 kW/dm³ and 3.8 kW/kg for the system in [28].

interoperability requirements encourage the definition of a common operating frequency in an industry standard. The transmission frequency is therefore not necessarily available as a degree-of-freedom to the designer.

Alternative ways to increase the power density could result from advanced cooling techniques that make operation with a lower efficiency possible by an improved heat removal from the IPT transmission coils. However, if the power density of the IPT coils is increased, care has to be taken with regard to the coil misalignment tolerance. For a smaller size of the receiver coil, maintaining a high tolerance to coil misalignment becomes more an more challenging. A possible countermeasure is to install a larger coil at the transmitter-side or to employ multiple small transmitters at the cost of an increased complexity of the system.

In addition to the lower power density of IPT systems, the considerable complexity of the realized demonstrator solutions must be noted. In particular, the number of on-board system components is larger for IPT systems than for a conductive charger. For a conventional EV charging system with a DC connection to the vehicle, a high-frequency isolation transformer is typically located in the stationary part and only a DC-DC converter without galvanic isolation is needed on-board. For the contactless EV charger, the IPT receiver coil and the rectifier-stage have to be located on the vehicle in addition to the DC-DC conversion stage. Moreover, comparably complex high-frequency power electronic converters and advanced control systems are required for the contactless charger. For a realization as a commercial product, a number of possible simplifications were outlined in the thesis. Particularly modifications of the power electronics topology and the control scheme have the potential to increase reliability and reduce cost. However, while in this way a realization with lower complexity is possible, the simplifications are expected to impair the system performance significantly.

As demonstrated by the presented hardware prototype, a practical realization of the presented contactless charging concept at a power level as high as 50 kW is feasible while keeping the magnetic stray fields below the relevant limits. However, the stray fields become more and more of a limiting factor when scaling the concept to even higher power levels, because of the increased currents in the IPT coils. As countermeasures, higher nominal DC-link voltages can be considered. Since the series resonant voltages scale as a multiple of the applied DC-link voltage, insulation becomes an additional design challenge. For instance,

multiple resonant capacitors connected in series, possibly at the end of each turn of the IPT coil, might be required to limit the individual device voltages. Alternatively, high operating frequencies achievable with fast-switching power semiconductors help reducing the stray field. However, high-frequency operation becomes more and more challenging as the power level increases, partly due to the limited availability of devices with sufficient current carrying capability at low switching losses³ and partly because of the ever higher impact of system parasitics. As a final option, advanced passive or active shielding methods may be used to limit the stray field at higher charging power levels. However, such methods typically lead to additional power losses and increase the system complexity even further.

All in all, it has become clear that trade-offs between multiple competing objectives dominate the design of an IPT system for EV battery charging. The proposed multi-objective IPT optimization process provides a framework for addressing these objectives in a systematic manner. It enables the development of a fundamental understanding of the underlying interdependencies between the different performance factors, which is an inherent requirement for finding an optimal solution to a multi-objective design problem.

7.2 Future Research Areas

The main goal of the presented work was to provide an in-depth understanding of the interdependencies and trade-offs between the different factors describing the performance of IPT systems for EV battery charging. Based on the results that were obtained during this study, the following topics are suggested as future research areas:

- ▶ Beneficial effects are expected from an increase of the transmission frequency beyond the 85 kHz specified by the upcoming standard SAE J2954 [41]. Based on this hypothesis, future research could aim for a high power density solution as a counterpart to the high efficiency system presented in this thesis. An analysis of how much could be gained from a frequency increase could provide further insight into the interdependencies between the design of the transmission coils and the design of the power electronics.

³For IGBTs, the ZCS losses due to the stored charge become a limiting factor at high switching frequencies [110–112].

- ▶ Advanced cooling techniques for the IPT coils could enable operation at a lower efficiency and make a design with increased power density possible. Therefore, future research could be directed towards improved cooling concepts for IPT systems with the aim of increasing the power density at the receiver-side. As an additional factor, forced-air cooling systems are typically not favored in automotive applications due to the limited lifetime of the rotating parts. The investigated solutions could therefore also include design options without active cooling in order to increase the lifetime of the system components.
- ▶ Magnetic and electric stray fields are an inherent concern with regards to IPT systems, particularly at the high power levels required for EV battery charging. A topic for future research could be an in-depth investigation of advanced measures for a reduction of the electromagnetic emissions. This could include measures based on passive or active shielding of the stray fields. Additionally, also converter topology optimizations and EMC filtering of the currents and voltages applied to the resonant circuit can be investigated.
- ▶ For a further reduction of the vehicle-side component volume and cost, an integration of the receiver-side power converter with other on-board power electronic systems could be considered. For instance, the presented DC-DC converter modules could be connected to a conductive DC charger. If necessary, they could be realized with a high-frequency isolation transformer instead of the coupled inductors to provide galvanic isolation. Alternatively, also an integration of the inverter stage of the IPT power electronics with the traction inverter could be investigated if similar power levels are used for both systems.

Contactless EV battery charging as an innovative technology as well as power electronics in general have the potential to promote public adoption of electric energy instead of fossil fuels for transportation. It is left to hope that research in this area is rewarded with a more sustainable stewardship of available resources.

List of Publications

Different parts of the research findings presented in this thesis have already been published or will be published in international scientific journals, conference proceedings, tutorials, or have been protected by multi-national patents. The publications and patents developed in the course of this thesis are listed below.

Journal Papers

- ▶ R. Bosshard, J. W. Kolar, J. Mühlethaler, I. Stevanović, B. Wunsch and F. Canales, "Modeling and η - α -Pareto Optimization of Inductive Power Transfer Coils for Electric Vehicles," *IEEE J. Emerg. Sel. Topics Power Electron.*, vol. 3, no. 1, pp. 50–64, Mar. 2015. DOI: [10.1109/JESTPE.2014.2311302](https://doi.org/10.1109/JESTPE.2014.2311302)
- ▶ R. Bosshard, J. W. Kolar, "Multi-Objective Optimization of 50 kW/85 kHz IPT System for Public Transport," under review at *IEEE J. Emerg. Sel. Topics Power Electron.*, 2016.
- ▶ R. Bosshard, J. W. Kolar, "All-SiC 9.5 kW/dm³ On-Board Power Electronics for 50 kW/85 kHz Automotive IPT System," under review at *IEEE J. Emerg. Sel. Topics Power Electron.*, 2016.
- ▶ R. Bosshard, U. Iruretagoyena, J. W. Kolar, "Comprehensive Evaluation of Rectangular and Double-D Coil Geometry for 50 kW/85 kHz IPT System," under review at *IEEE J. Emerg. Sel. Topics Power Electron.*, 2016.
- ▶ R. Bosshard, T. Guillod, J. W. Kolar, "Electromagnetic Field Patterns and Energy Flux of Efficiency Optimal IPT Systems," under review at *Springer Electrical Engineering*, 2016.

Magazine Articles

- ▶ R. Bosshard, J. W. Kolar, "On the Technical Challenges and Trade-Offs of Inductive Power Transfer for EV Charging," *IEEE Power Electron. Mag.*, planned publ. 2016.

Conference Papers

- ▶ R. Bosshard, J. W. Kolar, and B. Wunsch, "Control Method for Inductive Power Transfer with High Partial-Load Efficiency and Resonance Tracking," in *Proc. Int. Power Electron. Conf. (IPEC - ECCE Asia)*, Hiroshima, Japan, May 2014, pp. 2167–2174. DOI: [10.1109/IPEC.2014.6869889](https://doi.org/10.1109/IPEC.2014.6869889)
- ▶ R. Bosshard, J. W. Kolar, and B. Wunsch, "Accurate Finite-Element Modeling and Experimental Verification of Inductive Power Transfer Coil Design," in *Proc. 29th Appl. Power Electron. Conf. and Expo. (APEC)*, Fort Worth, USA, Mar. 2014, pp. 1648–1653. DOI: [10.1109/APEC.2014.6803527](https://doi.org/10.1109/APEC.2014.6803527)
- ▶ R. Bosshard, J. Mühlethaler, J. W. Kolar, and I. Stevanović, "Optimized Magnetic Design for Inductive Power Transfer Coils," in *Proc. 28th Appl. Power Electron. Conf. and Expo. (APEC)*, Long Beach, USA, Mar. 2013, pp. 1812–1819. DOI: [10.1109/APEC.2013.6520541](https://doi.org/10.1109/APEC.2013.6520541)
- ▶ R. Bosshard, U. Badstübner, J. W. Kolar, and I. Stevanović, "Comparative Evaluation of Control Methods for Inductive Power Transfer," in *Proc. 1st Int. Conf. Renewable Energy Research and Appl. (ICRERA)*, Nagasaki, Japan, Nov. 2012, pp. 1–6. DOI: [10.1109/ICRERA.2012.6477400](https://doi.org/10.1109/ICRERA.2012.6477400)
- ▶ R. Bosshard, J. Mühlethaler, J. W. Kolar, and I. Stevanović, "The η - α -Pareto Front of Inductive Power Transfer Coils," in *Proc. 38th Annu. Conf. IEEE Ind. Electron. Soc. (IECON)*, Montreal, CA, Oct. 2012, pp. 4270–4277. DOI: [10.1109/IECON.2012.6389203](https://doi.org/10.1109/IECON.2012.6389203)

Tutorials

- ▶ R. Bosshard and J. W. Kolar, "Fundamentals and Multi-Objective Design of Inductive Power Transfer Systems," Tutorial at *Euro-pean Conf. Power Electron. and Appl. (EPE - ECCE Europe)*, Geneva, CH, Sept. 2015.
- ▶ R. Bosshard and J. W. Kolar, "Fundamentals and Multi-Objective Design of Inductive Power Transfer Systems," Tutorial at *9th Int.*

Conf. Power Electron. (ICPE - ECCE Asia), Seoul, KR, June 2015.

- ▶ R. Bosshard and J. W. Kolar, "Fundamentals and Multi-Objective Design of Inductive Power Transfer Systems," Tutorial at *Conf. for Power Conversion and Intelligent Motion (PCIM Europe)*, Nuremberg, DE, May 2015.
- ▶ R. Bosshard and J. W. Kolar, "Fundamentals and Multi-Objective Design of Inductive Power Transfer Systems," Tutorial at *30th Appl. Power Electron. Conf. and Expo. (APEC)*, Charlotte, USA, Mar. 2015.
- ▶ J. W. Kolar and R. Bosshard, "Mains Interfaces for Future 400 Vdc Distribution Systems and Electric Vehicle Battery Charging," Tutorial at *5th Int. Symp. on Power Electron. for Distributed Generation Syst. (PEDG)*, Galway, IE, June 2014.

Patents

- ▶ R. Bosshard, J. W. Kolar, F. Canales., B. Guggisberg, G. Gong., and B. Wunsch, "Inductive Power Transfer System and Method for Operating an Inductive Power Transfer System,"
 - European Patent Application No. 14162789.3, Filed Mar. 31, 2014, Published Dec. 24, 2014.
 - United States Patent Application No. 14/672,803, Filed Mar. 30, 2015, Published Oct. 1, 2015.
 - Chinese Patent Application No. CN104953683, Filed Mar. 31, 2015, Published Sept. 30, 2015.

Further Scientific Contributions

- ▶ O. Knecht, R. Bosshard, J. W. Kolar, "High Efficiency Transcutaneous Energy Transfer for Implantable Mechanical Heart Support Systems," *IEEE Trans. Power Electron.*, vol. 30, no. 11, pp. 6221–6236, Nov. 2015. DOI: [10.1109/TPEL.2015.2396194](https://doi.org/10.1109/TPEL.2015.2396194)

- ▶ O. Knecht, R. Bosshard, J. W. Kolar, C. T. Starck, "Optimization of Transcutaneous Energy Transfer Coils for High Power Medical Applications," in *Proc. 15th IEEE Workshop on Control and Modeling of Power Electron. (COMPEL)*, Santander, ES, June 2014. DOI: [10.1109/COMPEL.2014.6877190](https://doi.org/10.1109/COMPEL.2014.6877190)
- ▶ A. Tüysüz, R. Bosshard, J. W. Kolar, "Performance Comparison of a GaN GIT and a Si IGBT for High-Speed Drive Applications," in *Proc. Int. Power Electron. Conf. (IPEC - ECCE Asia)*, Hiroshima, JP, June 2014, pp. 1904–1911. DOI: [10.1109/IPEC.2014.6869845](https://doi.org/10.1109/IPEC.2014.6869845)

Bibliography

- [1] T. Trigg, “The third age of electric vehicles,” *J. Int. Energy Agency*, no. 2, Spring 2012. [Online] Available: www.iea.org. [Accessed: Sept. 15, 2015].
- [2] *Global EV outlook: understanding the electric vehicle landscape to 2020*. Electric Vehicles Initiative of the International Energy Agency, 2013 [Online]. Available: www.iea.org/evi. [Accessed: Sept. 11, 2015].
- [3] D. Hug, *In der Oberklasse wird vor allem Tesla gefahren*. Neue Zürcher Zeitung (NZZ), 18.10.2015.
- [4] *Global EV outlook 2015*. Electric Vehicles Initiative of the International Energy Agency, 2015 [Online]. Available: www.iea.org/evi. [Accessed: Sept. 11, 2015].
- [5] *CO₂ emissions from new passenger cars in the EU: car manufacturers’ performance in 2014*. International Council on Clean Transportation, 2015 [Online]. Available: www.theicct.org. [Accessed: Sept. 11, 2015].
- [6] *Kyoto protocol to the United Nations framework convention on climate change*. United Nations, 1998 [Online]. Available: www.unfccc.int. [Accessed: Sept. 15, 2015].
- [7] *Supercharger: The world’s fastest charging station*. Tesla Motors, Inc., 2015 [Online]. Available: www.teslamotors.com/supercharger. [Accessed: Sept. 15, 2015].
- [8] *Highway and en route fast chargers*. ABB, Ltd., 2015 [Online]. Available: <http://new.abb.com/ev-charging/highway-fast-chargers>. [Accessed: Sept. 15, 2015].
- [9] J. Bolger, F. Kirsten, and L. Ng, “Inductive power coupling for an electric highway system,” in *Proc. 28th Vehicular Tech. Conf.*, vol. 28, Denver, USA, Mar. 1978, pp. 137–144. DOI: [10.1109/VTC.1978.1622522](https://doi.org/10.1109/VTC.1978.1622522)
- [10] J. Bolger, L. Ng, D. Turner, and R. Wallace, “Testing a prototype inductive power coupling for an electric highway system,” in *Proc. 29th Vehicular Tech. Conf.*, vol. 29, Arlington Heights, USA, Mar. 1979, pp. 48–56. DOI: [10.1109/VTC.1979.1622664](https://doi.org/10.1109/VTC.1979.1622664)

- [11] K. Lashkari, S. E. Schladober, and E. H. Lechner, "Inductive power transfer to an electric vehicle," in *Proc. 8th Int. Electric Vehicle Symp.*, Washington, USA, Oct. 1986.
- [12] E. H. Lechner and S. E. Schladober, "The roadway powered electric vehicle - an all-electric hybrid system," in *Proc. 8th Int. Electric Vehicle Symp.*, Washington, USA, Oct. 1986.
- [13] S. E. Schladober, "Systems engineering of the roadway powered electric vehicle technology," in *Proc. 9th Int. Electric Vehicle Symp.*, Toronto, CA, Nov. 1988.
- [14] A. W. Green and J. T. Boys, "10 kHz inductively coupled power transfer-concept and control," in *Proc. 5th Int. Conf. Power Electron. and Variable-Speed Drives*, London, UK, Oct. 1994, pp. 694–699. DOI: [10.1049/cp:19941049](https://doi.org/10.1049/cp:19941049)
- [15] G. Elliott, J. Boys, and A. Green, "Magnetically coupled systems for power transfer to electric vehicles," in *Proc. Int. Conf. Power Electron. and Drive Systems (PEDS)*, vol. 2, Feb. 1995, pp. 797–801. DOI: [10.1109/PEDS.1995.404968](https://doi.org/10.1109/PEDS.1995.404968)
- [16] D. Magnor, J. B. Gerschler, M. Ecker, P. Merk, and D. U. Sauer, "Concept of a battery aging model for lithium-ion batteries considering the lifetime dependency on the operation strategy," in *Proc. 24th European Photovoltaic Solar Energy Conf.*, Hamburg, DE, Sept. 2009, pp. 3128 – 3134. DOI: [10.4229/24thEUPVSEC2009-4BO.11.3](https://doi.org/10.4229/24thEUPVSEC2009-4BO.11.3)
- [17] K. van Schuylenbergh and R. Puers, *Inductive Powering: Basic Theory and Application to Biomedical Systems*, 1st edition. Dordrecht, NL: Springer Science+Business Media, 2009. DOI: [10.1007/978-90-481-2412-1](https://doi.org/10.1007/978-90-481-2412-1)
- [18] *10 years of electric buses with IPT charge*. Conductix Wampfler/Delachaux SA, 2012 [Online]. Available: www.conductix.com. [Accessed: Sept. 16, 2015].
- [19] *Primove - Introducing true electric mobility for a sustainable future*. Bombardier Transportation, 2013 [Online]. Available: <http://primove.bombardier.com>. [Accessed: Sept. 16, 2015].

- [20] *Wave IPT - Wirelessly charging electric vehicles*, [Online]. Available: www.waveipt.com. [Accessed: Sept. 16, 2015].
- [21] S. Choi, B. Gu, S. Jeong, and C. Rim, "Advances in wireless power transfer systems for roadway-powered electric vehicles," *IEEE J. Emerg. Select. Topics Power Electron.*, vol. 3, no. 1, pp. 18–36, 2015. DOI: [10.1109/JESTPE.2014.2343674](https://doi.org/10.1109/JESTPE.2014.2343674)
- [22] J. Kim, J. Kim, S. Kong, H. Kim, I.-S. Suh, N. P. Suh, D.-H. Cho, J. Kim, and S. Ahn, "Coil design and shielding methods for a magnetic resonant wireless power transfer system," *Proc. IEEE*, vol. 101, no. 6, pp. 1332–1342, June 2013. DOI: [10.1109/JPROC.2013.2247551](https://doi.org/10.1109/JPROC.2013.2247551)
- [23] B. Warner, O. Augé, and A. Moglestue, "Taking charge - flash charging is just the ticket for clean transportation," *ABB Review*, no. 4, 2013 [Online]. Available: www.abb.com. [Accessed: Feb. 24, 2016].
- [24] *TOSA Projekt - Allgemeine Angaben*. Projekt TOSA, 2013 [Online]. Available: www.tosa2013.com. [Accessed: Sept. 16, 2015].
- [25] *ABB automated e-bus fast chargers to power Namur, Belgium's new emissions-free electric hybrid bus system*. ABB, Ltd., 2016 [Online]. Available: www.abb.com. [Accessed: Feb. 29, 2016].
- [26] *Charging your future - with the Siemens eBus charging infrastructure*. Siemens AG, 2015 [Online]. Available: www.siemens.com/mobility. [Accessed: Sept. 16, 2015].
- [27] *EDDA - Schnellladefähiger Batteriebus für den Linienbetrieb in Städten*. Projekt EDDA Bus, 2015 [Online]. Available: www.edda-bus.de. [Accessed: Sept. 16, 2015].
- [28] B. Whitaker, A. Barkley, Z. Cole, B. Passmore, D. Martin, T. McNutt, A. Lostetter, J. S. Lee, and K. Shiozaki, "A high-density, high-efficiency, isolated on-board vehicle battery charger utilizing silicon carbide power devices," *IEEE Trans. Power Electron.*, vol. 29, no. 5, pp. 2606–2617, Mar. 2014. DOI: [10.1109/TPEL.2013.2279950](https://doi.org/10.1109/TPEL.2013.2279950)
- [29] J. Everts, "Modeling and optimization of bidirectional dual active bridge DC-DC converter topologies," Ph.D. dissertation, KU Leuven, Belgium, 2014.

- [30] D. Gautam, F. Musavi, M. Edington, W. Eberle, and W. Dunford, "An automotive onboard 3.3-kW battery charger for PHEV application," *IEEE Trans. Veh. Technol.*, vol. 61, no. 8, pp. 3466–3474, Oct. 2012. DOI: [10.1109/TVT.2012.2210259](https://doi.org/10.1109/TVT.2012.2210259)
- [31] M. Chinthavali, O. C. Onar, S. L. Campbell, and L. M. Tolbert, "Integrated charger with wireless charging and boost functions for PHEV and EV applications," in *Proc. IEEE Transportation Electrification Conf. and Expo. (ITEC)*, Dearborn, USA, June 2015, pp. 1–8. DOI: [10.1109/ITEC.2015.7165813](https://doi.org/10.1109/ITEC.2015.7165813)
- [32] T. Burress, *Benchmarking EV and HEV technologies*, 2014. [Online]. Available: <http://energy.gov> [Accessed: Nov. 24, 2015].
- [33] B. Goeldi, S. Reichert, and J. Tritschler, "Design and dimensioning of a highly efficient 22 kW bidirectional inductive charger for e-mobility," in *Proc. Int. Exhibition and Conf. for Power Electronics (PCIM Europe)*, Nuremberg, DE, 2013, pp. 1496–1503.
- [34] *Inductive charging system ICS115 - data sheet*. Brusa Elektronik AG, [Online]. Available: www.brusa.eu. [Accessed: Sept. 16, 2015].
- [35] *WiT-3300 resonator pair R2.3 - data sheet*. WiTricity Corp., [Online]. Available: www.witricity.com. [Accessed: Sept. 16, 2015].
- [36] T. Diekhans and R. De Doncker, "A dual-side controlled inductive power transfer system optimized for large coupling factor variations and partial load," *IEEE Trans. Power Electron.*, vol. 30, no. 11, pp. 6320–6328, Nov. 2015. DOI: [10.1109/TPEL.2015.2393912](https://doi.org/10.1109/TPEL.2015.2393912)
- [37] T. Friedli, M. Hartmann, and J. W. Kolar, "The essence of three-phase PFC rectifier systems - part II," *IEEE Trans. Power Electron.*, vol. 29, no. 2, pp. 543–560, Feb. 2014. DOI: [10.1109/TPEL.2013.2258472](https://doi.org/10.1109/TPEL.2013.2258472)
- [38] International Commission on Non-Ionizing Radiation Protection (ICNIRP), "Guidelines for limiting exposure to time-varying electric, magnetic and electromagnetic fields (up to 300 GHz)," *Health Phys.*, vol. 74, no. 4, pp. 494–522, 1998.

-
- [39] International Commission on Non-Ionizing Radiation Protection (ICNIRP), “Guidelines for limiting exposure to time-varying electric and magnetic fields (1 Hz to 100 kHz),” *Health Phys.*, vol. 99, no. 6, pp. 818–836, 2010.
- [40] *IEEE Standard for safety levels with respect to human exposure to radio frequency electromagnetic fields, 3 kHz to 300 GHz*, International Committee on Electromagnetic Safety, IEEE Std. C95.1-2005.
- [41] *Wireless charging of electric and plug-in hybrid vehicles*, Society of Automotive Engineers, SAE Std. J2954 (unpublished) [Online]. Available: <http://standards.sae.org/wip/j2954/>. [Accessed: Sept. 16, 2015].
- [42] J. Schneider, *SAE J2954 overview and path forward*, 2012. [Online] Available: www.sae.org. [Accessed: Sept. 18, 2015].
- [43] *Press release ID 2296*. Society of Automotive Engineers (SAE), 2013 [Online]. Available: www.sae.org. [Accessed: Sept. 16, 2015].
- [44] I. Jitaru, “A 3 kW soft switching DC-DC converter,” in *Proc. 15th Appl. Power Electron. Conf. and Expo. (APEC)*, New Orleans, USA, Feb. 2000, pp. 86–92. DOI: [10.1109/APEC.2000.826088](https://doi.org/10.1109/APEC.2000.826088)
- [45] Y. Charon, *Soft Commutation*, 1st edition. London, UK: Chapman & Hall, 1992.
- [46] R. Steigerwald, “A comparison of half-bridge resonant converter topologies,” *IEEE Trans. Power Electron.*, vol. 3, no. 2, pp. 174–182, 1988. DOI: [10.1109/63.4347](https://doi.org/10.1109/63.4347)
- [47] A. Esser, “Berührungslose kombinierte Energie und Informationsübertragung für bewegliche Systeme,” Ph.D. dissertation, Rheinisch-Westfälische Technische Hochschule (RWTH), Aachen, DE, 1992.
- [48] D. Bortis, L. Fässler, A. Looser, and J. W. Kolar, “Analysis of rotary transformer concepts for high-speed applications,” in *Proc. 28th Appl. Power Electron. Conf. and Expo. (APEC)*, Long Beach, USA, 2013, pp. 3262–3269. DOI: [10.1109/APEC.2013.6520768](https://doi.org/10.1109/APEC.2013.6520768)

- [49] C. Marxgut, J. Biela, J. W. Kolar, R. Steiner, and P. Steimer, “DC-DC converter for gate power supplies with an optimal air transformer,” in *Proc. 25th Appl. Power Electron. Conf. and Expo. (APEC)*, Palm Springs, USA, Feb. 2010, pp. 1865–1870. DOI: [10.1109/APEC.2010.5433487](https://doi.org/10.1109/APEC.2010.5433487)
- [50] B. Wunsch, J. Bradshaw, I. Stevanovic, F. Canales, W. Van-der Merwe, and D. Cottet, “Inductive power transfer for auxiliary power of medium voltage converters,” in *Proc. 30th Appl. Power Electron. Conf. and Expo. (APEC)*, Charlotte, USA, Mar. 2015, pp. 2551–2556. DOI: [10.1109/APEC.2015.7104710](https://doi.org/10.1109/APEC.2015.7104710)
- [51] P. E. K. Donaldson, “Frequency hopping in r.f. energy-transfer links,” *Electronics & Wireless World*, pp. 24–26, Aug. 1986.
- [52] C.-S. Wang, G. Covic, and O. Stielau, “Power transfer capability and bifurcation phenomena of loosely coupled inductive power transfer systems,” *IEEE Trans. Ind. Electron.*, vol. 51, no. 1, pp. 148–157, Feb. 2004. DOI: [10.1109/TIE.2003.822038](https://doi.org/10.1109/TIE.2003.822038)
- [53] C.-S. Wang, O. Stielau, and G. Covic, “Design considerations for a contactless electric vehicle battery charger,” *IEEE Trans. Ind. Electron.*, vol. 52, no. 5, pp. 1308–1314, Oct. 2005. DOI: [10.1109/TIE.2005.855672](https://doi.org/10.1109/TIE.2005.855672)
- [54] R. Bosshard, U. Badstübner, J. W. Kolar, and I. Stevanović, “Comparative evaluation of control methods for inductive power transfer,” in *Proc. 1st Int. Conf. Renewable Energy Research and Appl. (ICRERA)*, Nagasaki, JP, 2012, pp. 1–6. DOI: [10.1109/ICRERA.2012.6477400](https://doi.org/10.1109/ICRERA.2012.6477400)
- [55] E. Waffenschmidt and T. Staring, “Limitation of inductive power transfer for consumer applications,” in *Proc. 13th European Conf. on Power Electronics and Applications (EPE - ECCE Europe)*, Barcelona, ES, Sept. 2009, pp. 1–10.
- [56] R. Bosshard, J. W. Kolar, J. Mühlethaler, I. Stevanović, B. Wunsch, and F. Canales, “Modeling and η - α -Pareto optimization of inductive power transfer coils for electric vehicles,” *IEEE J. Emerg. Select. Topics Power Electron.*, vol. 3, no. 1, pp. 50–64, Mar. 2015. DOI: [10.1109/JESTPE.2014.2311302](https://doi.org/10.1109/JESTPE.2014.2311302)

-
- [57] R. W. Erickson and D. Maksimovic, *Fundamentals of Power Electronics*, 2nd edition. New York, USA: Springer Science+Business Media, 2001. DOI: [10.1007/b100747](https://doi.org/10.1007/b100747)
- [58] *Toyota to begin wireless vehicle charging verification testing*. Toyota Motor Corp., 2014 [Online]. Available: <http://newsroom.toyota.co.jp>. [Accessed: Sept. 21, 2015].
- [59] A. Kurs, A. Karalis, R. Moffatt, J. D. Joannopoulos, P. Fisher, and M. Soljačić, “Wireless power transfer via strongly coupled magnetic resonances,” *Science*, vol. 317, no. 5834, pp. 83–86, July 2007. DOI: [10.1126/science.1143254](https://doi.org/10.1126/science.1143254)
- [60] R. Bosshard, J. Mühlethaler, J. W. Kolar, and I. Stevanović, “The η - α -Pareto front of inductive power transfer coils,” in *Proc. 38th Annu. Conf. IEEE Ind. Electron. Soc. (IECON)*, Montreal, CA, 2012, pp. 4270–4277. DOI: [10.1109/IECON.2012.6389203](https://doi.org/10.1109/IECON.2012.6389203)
- [61] R. Bosshard, J. W. Kolar, and B. Wunsch, “Control method for inductive power transfer with high partial-load efficiency and resonance tracking,” in *Proc. Int. Power Electron. Conf. (IPEC - ECCE Asia)*, Hiroshima, JP, May 2014, pp. 2167–2174. DOI: [10.1109/IPEC.2014.6869889](https://doi.org/10.1109/IPEC.2014.6869889)
- [62] O. Knecht and J. W. Kolar, “Impact of transcutaneous energy transfer on the electric field and specific absorption rate in the human tissue,” in *Proc. 41st Annu. Conf. IEEE Ind. Electron. Soc. (IECON)*, Yokohama, JP, Nov. 2015. DOI: [10.1109/IECON.2015.7392881](https://doi.org/10.1109/IECON.2015.7392881)
- [63] K. Klontz, D. Divan, D. Novotny, and R. Lorenz, “Contactless power delivery system for mining applications,” in *Conf. Rec. IEEE Ind. Appl. Soc. (IAS) Annu. Meeting*, Dearborn, USA, Oct. 1991, pp. 1263–1269. DOI: [10.1109/IAS.1991.178024](https://doi.org/10.1109/IAS.1991.178024)
- [64] A. W. Green and J. T. Boys, “An inductively coupled high-frequency power system for material handling application,” in *Proc. Int. Power Eng. Conf. (IPEC)*, Singapore, Mar. 1993, pp. 821–826.
- [65] J. Boys, G. Covic, and A. Green, “Stability and control of inductively coupled power transfer systems,” *IEE Proc. - Electric*

- Power Appl.*, vol. 147, no. 1, pp. 37–43, Jan. 2000. DOI: [10.1049/ip-epa:20000017](https://doi.org/10.1049/ip-epa:20000017)
- [66] F. Krismer, “Modeling and optimization of bidirectional dual active bridge DC–DC converter topologies,” Ph.D. dissertation, ETH Zurich, Switzerland, 2010.
- [67] M. Kasper, R. Burkart, J. W. Kolar, and G. Deboy, “ZVS of power MOSFETs revisited,” *IEEE Trans. Power Electron.* (*accepted for publication*), 2016.
- [68] O. Knecht, R. Bosshard, and J. W. Kolar, “High-efficiency transcutaneous energy transfer for implantable mechanical heart support systems,” *IEEE Trans. Power Electron.*, vol. 30, no. 11, pp. 6221–6236, Nov. 2015. DOI: [10.1109/TPEL.2015.2396194](https://doi.org/10.1109/TPEL.2015.2396194)
- [69] J. W. Kolar and T. Friedli, “The essence of three-phase PFC rectifier systems - part I,” *IEEE Trans. Power Electron.*, vol. 28, no. 1, pp. 176–198, Jan. 2013. DOI: [10.1109/TPEL.2012.2197867](https://doi.org/10.1109/TPEL.2012.2197867)
- [70] J. Tritschler, S. Reichert, and B. Goeldi, “A practical investigation of a high power, bidirectional charging system for electric vehicles,” in *Proc. 16th European Conf. Power Electron. and Appl. (EPE - ECCE Europe)*, Lappeenranta, FI, 2014, pp. 1–7. DOI: [10.1109/EPE.2014.6910809](https://doi.org/10.1109/EPE.2014.6910809)
- [71] T. Soeiro, T. Friedli, and J. W. Kolar, “SWISS rectifier - a novel three-phase buck-type PFC topology for electric vehicle battery charging,” in *Proc. 27th Appl. Power Electron. Conf. and Expo. (APEC)*, Orlando, USA, Feb. 2012, pp. 2617–2624. DOI: [10.1109/APEC.2012.6166192](https://doi.org/10.1109/APEC.2012.6166192)
- [72] T. R. Crompton, *Battery Reference Book*, 3rd edition. Oxford, UK: Newnes, 1990.
- [73] M. Broussely, *Industrial Applications of Batteries: From Cars to Aerospace and Energy Storage*, 1st edition. Amsterdam, NL: Elsevier Science, 2012.
- [74] U. Madawala, M. Neath, and D. Thrimawithana, “A power-frequency controller for bidirectional inductive power transfer systems,” *IEEE Trans. Ind. Electron.*, vol. 60, no. 1, pp. 310–317, Jan. 2013. DOI: [10.1109/TIE.2011.2174537](https://doi.org/10.1109/TIE.2011.2174537)

-
- [75] G. Covic and J. Boys, “Inductive power transfer,” *Proc. IEEE*, vol. 101, no. 6, pp. 1276–1289, June 2013. DOI: [10.1109/JPROC.2013.2244536](https://doi.org/10.1109/JPROC.2013.2244536)
- [76] J. Sabate, M. Jovanovic, F. Lee, and R. Gean, “Analysis and design-optimization of LCC resonant inverter for high-frequency AC distributed power system,” *IEEE Trans. Ind. Electron.*, vol. 42, no. 1, pp. 63–71, Feb. 1995. DOI: [10.1109/41.345847](https://doi.org/10.1109/41.345847)
- [77] H. Pinheiro, P. Jain, and G. Joos, “Self-sustained oscillating resonant converters operating above the resonant frequency,” *IEEE Trans. Power Electron.*, vol. 14, no. 5, pp. 803–815, Aug. 1999. DOI: [10.1109/63.788476](https://doi.org/10.1109/63.788476)
- [78] F. da Silveira Cavalcante, “High output voltage series-parallel resonant DC-DC converter for medical x-ray imaging applications,” Ph.D. dissertation, ETH Zurich, Switzerland, 2006.
- [79] T. Soeiro, “High efficiency electrostatic precipitator systems with low effects on the mains,” Ph.D. dissertation, ETH Zurich, Switzerland, 2012.
- [80] U. Badstübner, “Ultra-high performance telecom DC-DC converter,” Ph.D. dissertation, ETH Zurich, Switzerland, 2012.
- [81] R. Bosshard, J. W. Kolar, and B. Wunsch, “Accurate finite-element modeling and experimental verification of inductive power transfer coil design,” in *Proc. 29th Appl. Power Electron. Conf. and Expo. (APEC)*, Fort Worth, USA, 2014, pp. 1648–1653. DOI: [10.1109/APEC.2014.6803527](https://doi.org/10.1109/APEC.2014.6803527)
- [82] *Film capacitors - data handbook*. EPCOS, 2009. Available: <http://de.tdk.eu/tdk-de/155496/tech-library/publikationen>.
- [83] J. W. Kolar, J. Biela, S. Waffler, T. Friedli, and U. Badstübner, “Performance trends and limitations of power electronic systems,” in *Proc. 6th Int. Conf. on Integrated Power Electronics Systems (CIPS)*, Nuremberg, DE, Mar. 2010, pp. 1–20.
- [84] J. C. Schuder, “Powering an artificial heart: birth of the inductively coupled-radio frequency system in 1960,” *Artificial Organs*, vol. 26, no. 11, pp. 909–915, June 2002.

- [85] C. Zierhofer and E. Hochmair, “Geometric approach for coupling enhancement of magnetically coupled coils,” *IEEE Trans. Biomed. Eng.*, vol. 43, no. 7, pp. 708–714, July 1996. DOI: [10.1109/10.503178](https://doi.org/10.1109/10.503178)
- [86] F. W. Grover, *Inductance Calculation*. New York, USA: Dover, 1964.
- [87] S. Babic and C. Akyel, “Calculating mutual inductance between circular coils with inclined axes in air,” *IEEE Trans. Magn.*, vol. 44, no. 7, pp. 1743–1750, July 2008. DOI: [10.1109/TMAG.2008.920251](https://doi.org/10.1109/TMAG.2008.920251)
- [88] W. Hurley, M. Duffy, J. Zhang, I. Lope, B. Kunz, and W. Wolfe, “A unified approach to the calculation of self- and mutual-inductance for coaxial coils in air,” *IEEE Trans. Power Electron.*, vol. 30, no. 11, pp. 6155–6162, Nov. 2015. DOI: [10.1109/TPEL.2015.2413493](https://doi.org/10.1109/TPEL.2015.2413493)
- [89] M. Budhia, G. Covic, and J. Boys, “Design and optimization of circular magnetic structures for lumped inductive power transfer systems,” *IEEE Trans. Power Electron.*, vol. 26, no. 11, pp. 3096–3108, Nov. 2011. DOI: [10.1109/TPEL.2011.2143730](https://doi.org/10.1109/TPEL.2011.2143730)
- [90] D. Kürschner, C. Rathge, and U. Jumar, “Design methodology for high efficient inductive power transfer systems with high coil positioning flexibility,” *IEEE Trans. Ind. Electron.*, vol. 60, no. 1, pp. 372–381, Jan. 2013. DOI: [10.1109/TIE.2011.2181134](https://doi.org/10.1109/TIE.2011.2181134)
- [91] L. K. L. Cheng, J. W. Hay, and P. G. W. Beart, “Contact-less power transfer,” US Patent 6906 495 B2, 2005.
- [92] J. T. Boys, G. A. Covic, and M. B. Budhia, “Inductive power transfer apparatus,” WO Patent 2012018 268 A1, 2012.
- [93] C.-Y. Huang, “Design of IPT EV battery charging systems for variable coupling applications,” Ph.D. dissertation, University of Auckland, Auckland, NZ, 2011.
- [94] M. Budhia, J. Boys, G. Covic, and C.-Y. Huang, “Development of a single-sided flux magnetic coupler for electric vehicle IPT charging systems,” *IEEE Trans. Ind. Electron.*, vol. 60, no. 1, pp. 318–328, Jan. 2013. DOI: [10.1109/TIE.2011.2179274](https://doi.org/10.1109/TIE.2011.2179274)

-
- [95] M. Budhia, G. Covic, and J. Boys, “A new IPT magnetic coupler for electric vehicle charging systems,” in *Proc. 36th Annu. Conf. IEEE Ind. Electron. Soc. (IECON)*, Glendale, USA, Nov. 2010, pp. 2487–2492. DOI: [10.1109/IECON.2010.5675350](https://doi.org/10.1109/IECON.2010.5675350)
- [96] J. McLean and R. Sutton, “On the nature of the electromagnetic field in the immediate vicinity of inductive power transfer system,” in *Proc. IEEE Int. Symp. Electromagnetic Compatibility*, Denver, USA, Aug. 2013, pp. 60–65. DOI: [10.1109/ISEMC.2013.6670382](https://doi.org/10.1109/ISEMC.2013.6670382)
- [97] F. Turki, R. Wiengarten, V. Reising, and A. Kratser, “Impact of the working frequency on wireless power transfer systems,” in *Proc. Conf. for Power Conversion and Intelligent Motion (PCIM Europe)*, Nuremberg, DE, May 2014, pp. 1–6.
- [98] R. Bosshard, J. Mühlethaler, J. W. Kolar, and I. Stevanović, “Optimized magnetic design for inductive power transfer coils,” in *Proc. 28th Appl. Power Electron. Conf. and Expo. (APEC)*, Long Beach, USA, 2013, pp. 1812–1819. DOI: [10.1109/APEC.2013.6520541](https://doi.org/10.1109/APEC.2013.6520541)
- [99] D. Meeker, *FEMM 4.2 Magnetostatic Tutorial*. Waltham, USA: Finite Element Method Magnetics, [Online]. Available: www.femm.info/Archives/doc/tutorial-magnetic.pdf. [Accessed: Sept. 25, 2015].
- [100] J. Mühlethaler, “Modeling and multi-objective optimization of inductive power components,” Ph.D. dissertation, ETH Zurich, Switzerland, 2012.
- [101] J. Lammeraner and M. Štafl, *Eddy Currents*. London, UK: Iliffe Books Ltd., 1966.
- [102] J. Biela, “Optimierung des elektromagnetisch integrierten Serien-Parallel Resonanzkonverters mit eingepprägtem Ausgangsstrom,” Ph.D. dissertation, ETH Zurich, Switzerland, 2005.
- [103] A. Urling, V. Niemela, G. Skutt, and T. Wilson, “Characterizing high-frequency effects in transformer windings - a guide to several significant articles,” in *Proc. 4th Appl. Power Electron. Conf. and Expo. (APEC)*, Baltimore, USA, Mar. 1989, pp. 373–385. DOI: [10.1109/APEC.1989.36989](https://doi.org/10.1109/APEC.1989.36989)

- [104] C. Sullivan, “Optimal choice for number of strands in a litz-wire transformer winding,” *IEEE Trans. Power Electron.*, vol. 14, no. 2, pp. 283–291, Mar. 1999. DOI: [10.1109/63.750181](https://doi.org/10.1109/63.750181)
- [105] W. Hurley, E. Gath, and J. Breslin, “Optimizing the AC resistance of multilayer transformer windings with arbitrary current waveforms,” *IEEE Trans. Power Electron.*, vol. 15, no. 2, pp. 369–376, Mar. 2000. DOI: [10.1109/63.838110](https://doi.org/10.1109/63.838110)
- [106] Z. Ouyang, J. Zhang, and W. Hurley, “Calculation of leakage inductance for high-frequency transformers,” *IEEE Trans. Power Electron.*, vol. 30, no. 10, pp. 5769–5775, Oct. 2015. DOI: [10.1109/TPEL.2014.2382175](https://doi.org/10.1109/TPEL.2014.2382175)
- [107] *VDI Heat Atlas*, 2nd edition. Berlin, DE: Springer-Verlag Berlin Heidelberg, 2010. DOI: [10.1007/978-3-540-77877-6](https://doi.org/10.1007/978-3-540-77877-6)
- [108] J. Biela and J. W. Kolar, “Cooling concepts for high power density magnetic devices,” in *Proc. Power Conversion Conf. (PCC)*, Nagoya, JP, Apr. 2007, pp. 1–8. DOI: [10.1109/PCCON.2007.372915](https://doi.org/10.1109/PCCON.2007.372915)
- [109] G. Ortiz, “High-power dc-dc converter technologies for smart grid and traction applications,” Ph.D. dissertation, ETH Zurich, Switzerland, 2014.
- [110] P. Ranstad and H.-P. Nee, “On dynamic effects influencing IGBT losses in soft-switching converters,” *IEEE Trans. Power Electron.*, vol. 26, no. 1, pp. 260–271, Jan. 2011. DOI: [10.1109/TPEL.2010.2055581](https://doi.org/10.1109/TPEL.2010.2055581)
- [111] G. Ortiz, H. Uemura, D. Bortis, J. W. Kolar, and O. Apeldoorn, “Modeling of soft-switching losses of IGBTs in high-power high-efficiency dual-active-bridge DC/DC converters,” *IEEE Trans. Electron Devices*, vol. 60, no. 2, pp. 587–597, Feb. 2013. DOI: [10.1109/TED.2012.2223215](https://doi.org/10.1109/TED.2012.2223215)
- [112] J. Huber, G. Ortiz, F. Krismer, N. Widmer, and J. W. Kolar, “ η - ρ Pareto optimization of bidirectional half-cycle discontinuous-conduction-mode series-resonant DC/DC converter with fixed voltage transfer ratio,” in *Proc. 28th Appl. Power Electron. Conf. and Expo. (APEC)*, Long Beach, USA, Mar. 2013, pp. 1413–1420. DOI: [10.1109/APEC.2013.6520484](https://doi.org/10.1109/APEC.2013.6520484)

-
- [113] J. Lenz and A. S. Edelstein, “Magnetic sensors and their applications,” *IEEE Sensors J.*, vol. 6, no. 3, pp. 631–649, June 2006. DOI: [10.1109/JSEN.2006.874493](https://doi.org/10.1109/JSEN.2006.874493)
- [114] T. Nussbaumer, M. Baumann, and J. W. Kolar, “Comprehensive design of a three-phase three-switch buck-type PWM rectifier,” *IEEE Trans. Power Electron.*, vol. 22, no. 2, pp. 551–562, Mar. 2007. DOI: [10.1109/TPEL.2006.889987](https://doi.org/10.1109/TPEL.2006.889987)
- [115] *ION-DRIVE 630V Battery System*. Saft SAS, 2015 [Online]. Available: www.saftbatteries.com. [Accessed: Oct. 1, 2015].
- [116] *Primove Battery - Optimized battery system for urban mobility*. Bombardier Transportation, 2015 [Online]. Available: <http://primove.bombardier.com>. [Accessed: Oct. 1, 2015].
- [117] B. Cougo, A. Tüysüz, J. Mühlethaler, and J. Kolar, “Increase of tape wound core losses due to interlamination short circuits and orthogonal flux components,” in *Proc. 37th Annu. Conf. IEEE Ind. Electron. Soc. (IECON)*, Melbourne, AU, Nov. 2011, pp. 1372–1377. DOI: [10.1109/IECON.2011.6119508](https://doi.org/10.1109/IECON.2011.6119508)
- [118] H. W. Ott, *Noise Reduction Techniques in Electronic Systems*, 2nd edition. New York, USA: Wiley-Interscience, 1988.
- [119] C. R. Paul, *Introduction to Electromagnetic Compatibility*, 2nd edition. Hoboken, USA: John Wiley & Sons, Inc., 2005. DOI: [10.1002/0471758159](https://doi.org/10.1002/0471758159)
- [120] D. Geselowitz, Q. Hoang, and R. Gaumond, “The effects of metals on a transcutaneous energy transmission system,” *IEEE Trans. Biomed. Eng.*, vol. 39, no. 9, pp. 928–934, Sept. 1992. DOI: [10.1109/10.256426](https://doi.org/10.1109/10.256426)
- [121] A. van den Bossche and V. C. Valchev, *Inductors and Transformers for Power Electronics*. New York: Taylor & Francis, 2005.
- [122] R. J. Moffat, “Modeling air-cooled heat sinks as heat exchangers,” in *Proc. 23rd Annu. IEEE Semiconductor Thermal Measurement and Management Symp. (SEMI-THERM)*, San Jose, USA, Mar. 2007, pp. 200–207. DOI: [10.1109/stherm.2007.352424](https://doi.org/10.1109/stherm.2007.352424)

- [123] Y. S. Muzychka, “Generalized models for laminar developing flows in heat sinks and heat exchangers,” *Heat Transfer Eng.*, vol. 34, no. 2-3, pp. 178–191, Jan. 2013. DOI: [10.1080/01457632.2013.703517](https://doi.org/10.1080/01457632.2013.703517)
- [124] C. Gammeter, F. Krismer, and J. W. Kolar, “Weight optimization of a cooling system composed of fan and extruded-fin heat sink,” *IEEE Trans. Ind. Appl.*, vol. 51, no. 1, pp. 509–520, Jan. 2015. DOI: [10.1109/TIA.2014.2336977](https://doi.org/10.1109/TIA.2014.2336977)
- [125] R. Bosshard, U. Iruretagoyena, and J. W. Kolar, “Comprehensive evaluation of rectangular and double-d coil geometry for 50 kW/85 kHz IPT system,” publ. under review at IEEE JESTPE, 2016.
- [126] S. Waffler and J. W. Kolar, “A novel low-loss modulation strategy for high-power bidirectional buck+boost converters,” *IEEE Trans. Power Electron.*, vol. 24, no. 6, pp. 1589–1599, June 2009. DOI: [10.1109/TPEL.2009.2015881](https://doi.org/10.1109/TPEL.2009.2015881)
- [127] M. März, A. Schletz, B. Eckardt, S. Egelkraut, and H. Rauh, “Power electronics system integration for electric and hybrid vehicles,” in *Proc. 6th Int. Conf. on Integrated Power Electronics Systems (CIPS)*, Nuremberg, DE, Mar. 2010, pp. 1–10.
- [128] M. Yilmaz and P. Krein, “Review of battery charger topologies, charging power levels, and infrastructure for plug-in electric and hybrid vehicles,” *IEEE Trans. Power Electron.*, vol. 28, no. 5, pp. 2151–2169, May 2013. DOI: [10.1109/TPEL.2012.2212917](https://doi.org/10.1109/TPEL.2012.2212917)
- [129] U. Madawala and D. Thrimawithana, “A bidirectional inductive power interface for electric vehicles in V2G systems,” *IEEE Trans. Ind. Electron.*, vol. 58, no. 10, pp. 4789–4796, Oct. 2011. DOI: [10.1109/TIE.2011.2114312](https://doi.org/10.1109/TIE.2011.2114312)
- [130] R. Wang, D. Boroyevich, P. Ning, Z. Wang, F. Wang, P. Mattavelli, K. D. T. Ngo, and K. Rajashekara, “A high-temperature SiC three-phase AC-DC converter design for $\geq 100^{\circ}\text{C}$ ambient temperature,” *IEEE Trans. Power Electron.*, vol. 28, no. 1, pp. 555–572, Jan. 2013. DOI: [10.1109/TPEL.2012.2199131](https://doi.org/10.1109/TPEL.2012.2199131)
- [131] B. Wrzecionko, D. Bortis, and J. W. Kolar, “A 120°C ambient temperature forced air-cooled normally-off SiC JFET automotive

- inverter system,” *IEEE Trans. on Power Electron.*, vol. 29, no. 5, pp. 2345–2358, May 2014. DOI: [10.1109/TPEL.2013.2294906](https://doi.org/10.1109/TPEL.2013.2294906)
- [132] J. Biela, M. Schweizer, S. Waffler, and J. W. Kolar, “SiC versus Si—evaluation of potentials for performance improvement of inverter and DC-DC converter systems by SiC power semiconductors,” *IEEE Trans. Ind. Electron.*, vol. 58, no. 7, pp. 2872–2882, July 2011. DOI: [10.1109/TIE.2010.2072896](https://doi.org/10.1109/TIE.2010.2072896)
- [133] B. Eckardt and M. März, “A 100 kW automotive powertrain DC/DC converter with 25 kW/dm³ by using SiC,” in *Proc. 4th Int. Conf. on Integrated Power Electronics Systems (CIPS)*, Naples, IT, June 2006, pp. 1–6.
- [134] T. Diekhans and R. De Doncker, “A Pareto-based comparison of power electronic topologies for inductive power transfer,” in *Proc. Conf. for Power Conversion and Intelligent Motion (PCIM Europe)*, Nuremberg, DE, May 2015, pp. 1–9.
- [135] M. Hirakawa, M. Nagano, Y. Watanabe, K. Andoh, S. Nakatomi, and S. Hashino, “High power density DC/DC converter using the close-coupled inductors,” in *Proc. IEEE Energy Conversion Congr. and Expo. (ECCE)*, San Jose, USA, Sept. 2009, pp. 1760–1767. DOI: [10.1109/ECCE.2009.5316389](https://doi.org/10.1109/ECCE.2009.5316389)
- [136] B. Cougo, T. Friedli, D. Boillat, and J. W. Kolar, “Comparative evaluation of individual and coupled inductor arrangements for input filters of PV inverter systems,” in *Proc. 7th Int. Conf. on Integrated Power Electronics Systems (CIPS)*, Nuremberg, DE, Mar. 2012.
- [137] D. Boillat and J. W. Kolar, “Modeling and experimental analysis of a coupling inductor employed in a high performance AC power source,” in *Proc. 1st Int. Conf. Renewable Energy Research and Appl. (ICRERA)*, Nagasaki, JP, Nov. 2012, pp. 1–18. DOI: [10.1109/ICRERA.2012.6477401](https://doi.org/10.1109/ICRERA.2012.6477401)
- [138] S. Utz and J. Pforr, “Current-balancing controller requirements of automotive multi-phase converters with coupled inductors,” in *Proc. IEEE Energy Conversion Congr. and Expo. (ECCE)*, Raleigh, USA, Sept. 2012, pp. 372–379. DOI: [10.1109/ECCE.2012.6342798](https://doi.org/10.1109/ECCE.2012.6342798)

- [139] F. Forest, T. A. Meynard, J.-J. Huselstein, D. Flumian, C. Rizet, and A. Lacarnoy, "Design and characterization of an eight-phase-137-kW intercell transformer dedicated to multicell DC-DC stages in a modular UPS," *IEEE Trans. Power Electron.*, vol. 29, no. 1, pp. 45–55, Jan. 2014. DOI: [10.1109/TPEL.2013.2248755](https://doi.org/10.1109/TPEL.2013.2248755)
- [140] F. Marvi, E. Adib, and H. Farzanehfard, "Zero voltage switching interleaved coupled inductor synchronous buck converter operating at boundary condition," *IET Power Electron.*, vol. 9, no. 1, pp. 126–131, Jan. 2016. DOI: [10.1049/iet-pel.2014.0960](https://doi.org/10.1049/iet-pel.2014.0960)
- [141] J. Lutz, H. Schlangenotto, U. Scheuermann, and R. De Doncker, *Semiconductor Power Devices: Physics, Characteristics, Reliability*. Berlin, DE: Springer-Verlag Berlin Heidelberg, 2011.
- [142] Z. Chen, Y. Yao, W. Zhang, D. Boroyevich, K. Ngo, P. Mattavelli, and R. Burgos, "Development of a 1200 V, 120 A SiC MOSFET module for high-temperature and high-frequency applications," in *Proc. IEEE Workshop on Wide Bandgap Power Devices and Appl. (WiPDA)*, Columbus, USA, Oct. 2013, pp. 52–59. DOI: [10.1109/WiPDA.2013.6695561](https://doi.org/10.1109/WiPDA.2013.6695561)
- [143] *Paralleling Power MOSFETs (Appl. Note AN-941)*. International Rectifier, [Online]. Available: www.irf.com. [Accessed: Oct. 12, 2015].
- [144] D. Pefitsis, R. Baburske, J. Rabkowski, J. Lutz, G. Tolstoy, and H.-P. Nee, "Challenges regarding parallel connection of SiC JFETs," *IEEE Trans. Power Electron.*, vol. 28, no. 3, pp. 1449–1463, Mar. 2013. DOI: [10.1109/TPEL.2012.2206611](https://doi.org/10.1109/TPEL.2012.2206611)
- [145] H. Li, S. Munk-Nielsen, X. Wang, R. Maheshwari, S. Beczkowski, C. Uhrenfeldt, and W. Franke, "Influences of device and circuit mismatches on paralleling silicon carbide MOSFETs," *IEEE Trans. Power Electron.*, vol. 31, no. 1, pp. 621–634, Jan. 2016. DOI: [10.1109/TPEL.2015.2408054](https://doi.org/10.1109/TPEL.2015.2408054)
- [146] M. Kasper, D. Bortis, and J. W. Kolar, "Scaling and balancing of multi-cell converters," in *Proc. Int. Power Electron. Conf. (IPEC - ECCE Asia)*, Hiroshima, JP, May 2014, pp. 2079–2086. DOI: [10.1109/IPEC.2014.6869875](https://doi.org/10.1109/IPEC.2014.6869875)

- [147] W. G. Hurley and W. H. Wölflé, *Transformers and Inductors for Power Electronics*, 1st edition. Hoboken, USA: John Wiley & Sons, Inc., 2013.
- [148] W. Hurley, W. Wolfle, and J. Breslin, “Optimized transformer design: inclusive of high-frequency effects,” *IEEE Trans. Power Electron.*, vol. 13, no. 4, pp. 651–659, July 1998. DOI: [10.1109/63.704133](https://doi.org/10.1109/63.704133)
- [149] R. Burkart, “Advanced modeling and multi-objective optimization of power electronic converter systems,” Ph.D. dissertation, ETH Zurich, Switzerland, 2015.
- [150] *WT3000 Precision Power Analyzer User’s Manual*. Yokogawa Electric Corp., 2015. [Online]. Available: <http://tmi.yokogawa.com>. [Accessed: Oct. 20, 2015].
- [151] *Agilent Precision Impedance Analyzer 4294A Data Sheet*. Keysight Technologies Inc., 2003. [Online]. Available: www.keysight.com. [Accessed: Oct. 20, 2015].
- [152] S. Prabhakaran and C. Sullivan, “Impedance-analyzer measurements of high-frequency power passives: techniques for high power and low impedance,” in *Conf. Rec. 37th Annu. Meeting IEEE Ind. Appl. Soc. (IAS)*, vol. 2, Pittsburgh, USA, Oct. 2002, pp. 1360–1367. DOI: [10.1109/IAS.2002.1042734](https://doi.org/10.1109/IAS.2002.1042734)

Curriculum Vitae

Personal Information



Name	Roman BOSSHARD
Date of birth	December 20, 1986
Nationality	Swiss
Citizen of	Oetwil am See, Switzerland
Contact	roman.bosshard@gmail.com +41 (0)79 446 50 12

Education

2011 – 2015	Doctorate at the Power Electronic Systems Laboratory (PES), ETH Zurich
2011	Master Thesis at Celeroton, Zurich
2006 – 2011	BSc and MSc studies in Information Technology and Electrical Engineering, ETH Zurich
1999 – 2005	Kantonsschule Zürcher Oberland, Wetzikon (passed with distinction)
1993 – 1999	Primary school, Oetwil am See

Work Experience

2011 – 2015	Research assistant at the Power Electronic Systems Laboratory (PES), ETH Zurich
2009 – 2010	Internship at ABB Switzerland, Turgi
2007 – 2009	Teaching Assistant at ETH Zurich